Università degli Studi di Genova

Corso di Dottorato in Fluidodinamica e Processi dell' Ingegneria Ambientale

Homogenized-based modeling of flows over and through poroelastic media

Thesis submitted for the degree of Doctor of Philosophy

Candidate:
Giuseppe Antonio Zampogna

Advisor:
Professor Alessandro Bottaro

Contents

Abstract

The main goal of this work is to study the interactions between fluids and porous (rigid and elastic) media, inspired by biological organs and functions, with the long-term objective of developing poroelastic coatings for aeronautical purposes. Since the poroelastic media considered are characterized by a microscopic porous matrix, a homogenization technique is used to describe the separation of scales which characterizes the phenomenon. This technique is used together with a study of the interface conditions needed to match the solutions at the boundary between the pure-fluid and the porous regions. Homogenization leads us in two directions, the microscopic and the macroscopic one, yielding the governing equations for the mixture fluid-solid, considered as a new continuum. The first point of view allows to understand the microscopic characteristics (permeability and elasticity), influencing the latter, which describes the macroscopic behavior of the flow. Problems in different flow regimes (laminar and turbulent) are considered to validate the model, which includes inertia in the leading order equations for the permeability tensor through a Oseen approximation. The components of the permeability and elasticity are reasonably well estimated by the theory, both in the laminar and the turbulent case. This is demonstrated by comparing the model's results to both experimental measurements and direct numerical simulations of the equations which solve for the flow also through the pores of the medium. Some limits of the technique used are shown considering different microscopic skeletons, isotropic and anisotropic. The appropriateness of the conditions at the macroscopic boundaries of the medium is enquired also performing a linear stability analysis of the computed profile of velocity in the particular application of canopy flows.

Chapter 1

Introduction

1.1 Half a century of research in biomimetics

Even if Leonardo da Vinci, Orville and Wilbur Wright, George de Mestral (the inventor of Velcro, fig. 1a) and many others have been inspired by Nature in their work, the term "biomimetics" entered the Webster's dictionary only in 1974 after biophysicist Otto Schmitt who used it for the first time at the International Biophysics Congress in Boston in 1969. From that moment on much progress has been made in biomimetics. Among the works which contain a more complete review of the common attempts to apply Nature's principles to technology we can cite Vincent *et al.* (2006) and Lakhtakia & Martín–Palma (2013). We present below a concise list of works on biomimetics, which constituted also the stimulus us to undertake the present study. In most of the phenomena commonly studied in biomimetics, the presence of a separation of characteristic scales (e.g. the characteristic dimensions of some physical structures or phenomena) is very important. To appreciate both scales, it is often necessary to consider two different points of view: the microscopic and the macroscopic one. The former allow us to appreciate differences over a small scale, although we do not see sufficiently far to appreciate differences at the large scale; with the latter we can see physic over a large scale but cannot appreciate anything of the microscopic world. Some of the works which have in common these two ways of viewing things are listed below, with reference to activities pursued in the last 50 years or so.

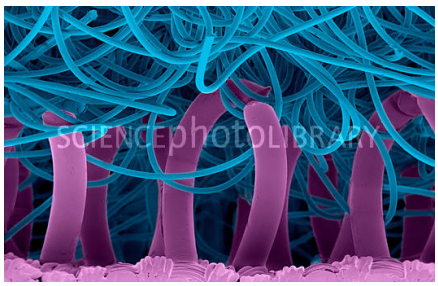

(a) Velcro device consists of two different parts, upper and lower. The lower part has coils of plastic thread which form hooks.

(b) The structures on the top of the lotus leaf, along with a waxy coating, help to efficiently repel water droplets.

(c) Feet of geckos are covered with ridges and microscopic hairs, which enable it to cling to very smooth surfaces.

(d) Owls have the benefit of silent flight due to the filamentous extensions of their anterior barbules on their feathers.

(e) The sharply pointed, placoid scales on the skin of sharks, also known as dermal teeth, reduce drag.

Figure 1.1: Example of microscopic structures in biological organisms. Without a microscopic visualization of these geometries and an understanding of their effect, the corresponding macroscopic result would not be available.

- The microscopic observation of the leaves of the lotus (Barthlott & Neinhuis, 1997) or of the wings of some species of insects (Wagner *et al.*, 1996) identified a relationship between the superficial microstructures, their wettability and behavior under the influence of contamination. The resulting conclusions of these works led to the production of paints for self-cleaning surfaces.

- The study of the microstructures which compose the surface of insects' eyes and wings (Bernhard *et al.*, 1965; Stoddart *et al.*, 2006), and the leaves of some tropical plants (Lee, 1986) was helpful to produce antireflective polyethilene sheets.

- Autumn & Peattie (2001) and Geim *et al.* (2003) have shown that hairs of the gecko foot adhere to hydrophobic and hydrophilic surfaces thanks only to the size and shape of the microscopic structures of the hairs, without any kind of chemical addictive. Dry adhesive tapes, such as GeckSkin^{TM}, are now produced using this principle.

- In the '60 the first studies on the shark skin were conducted, proving that these fast inhabitants of the oceans have peculiar placoid scales on their skins. These microscopic structures induce vortices that cut down friction drag significantly. Bio-inspired V-shaped riblets (inspired by such scales) have been originally developed by NASA Langley Research Center technology (and then produced by the 3M Company, `http://www.nasa.gov/centers/langley/news/factsheets/Riblets.html`), in order to improve airplane fuel efficiency, by reducing the drag caused by the friction of turbulent airflow over the airplane. After its development in the '80, the film was used both in aeronautical and naval fields. More recent applications are, for instance, in the production of professional swimwear. Much literature exists for quantifying the drag reduction and optimize the shape of the riblets which modify the boundary layer of the fluid flow interacting with them (e.g. Luchini *et al.*, 1991). A recent review has been done by Bechert *et al.* (2000) with a particular focus on the drag reduction assessment.Work on this topic is still undergoing: Wen *et al.* (2014) are developing a synthetic 3D-printed shark skin.

- Aeroacoustic studies by Kroeger *et al.* (1972) and Sarradj *et al.* (2011) have shown that owls eliminate self-noises when they hunt. These studies inspired a wide literature on the acoustics of fluid-structure interactions near poroelastic surfaces (e.g. Sueki *et al.*, 2010).

On the other side, there are studies in which we find only macroscopical and mechanical inspiration from Nature; it is the case, for instance, of earth-moving machinery which can be optimized with ridges and bumps inspired by soil-moving animals (Li *et al.*, 2004). One more example of one-scale-biomimetics is the development of microflyers (Sirohi, 2013), ornithopters (Park & Yoon, 2008) or appendices inspired by wings and feathers which optimize the flight of traditional airplanes and operate an active or passive control of the flight.

Our work aims to put together these two aspects of biomimicry, proposing a mathematical model which will be used to simulate porous and poroelastic coatings which can then be applied to mobile wings devices for passive control and optimization of the flight. Why porous and elastic coatings? Observing riblets one need porosity, observing birds' feathers also elasticity is required. Furthermore, the presence of poroelastic surfaces or coatings is proven to modify significantly the flow field near them (cf. Battiato *et al.*, 2010; Luhar & Nepf, 2011; Gosselin & de Langre, 2011; Rosti *et al.*, 2015).

Our main goal is to develop a simple and computationally cheap model to simulate the behavior of the coatings and the fluid which flows near and inside them, in order to use it to evaluate and optimize some fundamental measures like skin friction or drag. Two important constraints can be immediately outlined:

- the skeleton which constitutes the coating should have at least two principal characteristic scales (and likewise for the phenomenon which we are simulating);
- the model should be able to take into account the microscopic skeleton (which we cannot express explicitly if we have the constraint of computational economy) as well as the macroscopic configuration, and on its basis, one should be able to locally change a given microscopic property in a simple way (Wen *et al.*, 2014, already observed that the microscopic geometrical properties of the riblets are different in different regions of the shark skin).

In order to attain our objectives, in a preliminary analysis two things should be understood:

- how to model the presence of a solid structure;
- how a fluid flow develops inside and near the porous medium.

A study of the literature, presented in the next sections, has been pursued to achieve the two objectives listed above.

1.2 Models for poroelastic materials

As already outlined earlier, when a fluid flows in a porous medium, there is usually a strong separation of scales between the macroscopic scale defined by the global size of the problem and the microscopic length typical of the solid inclusions of the porous medium (cf. figures 1.2 and 1.3). We present an overview of some methods which can be used to model a porous and elastic medium.

1.2.1 Microscopic and macroscopic approaches

Two approaches are generally employed to treat flows in porous media: the first one is to implement a pore-scale numerical simulation of the flow in the medium, reproducing closely the geometry of the solid skeleton. The second consists in an effective macroscopic simulation where the microscopic structure is lost, but some auxiliary problem is introduced to characterize the pore-scale behavior. The first path has been followed, for instance, by Breugem & Boersma (2005), Kuttanikkad (2009) and Matsumura & Jackson (2014). One of the difficulties of this kind of analysis is the computational cost of the simulation: the smaller is the ratio between the microscopic and the macroscopic length scale, the larger is the resolution which must be used to discretize the geometry of the skeleton. From a technical point of view, if on the one hand, for rigid porous media, it is relatively simple to perform a direct numerical simulation because the presence of the porous medium requires only to modify the domain over which we are solving the equations of motion for the fluid, on the other hand, when one deals with media which are also elastic, things become more difficult: the domain over which the equations should be solved changes in time and two systems of equations (one for the fluid and the other for the solid) must be coupled via an interface condition which holds on the microscopic, moving boundaries of the poroelastic structure. Much effort is devoted to this direction of research: different technique have been implemented (e.g. the immersed boundary method), but there are still great limitations (whether computational or of applicability, due by the simplifications of some models). Such a big effort presents the additional disadvantage of providing a solution to only a particular configuration of the porous medium. With the second choice, based on homogenization, we have a concise and rapid description of the fluid behavior, satisfactory from a macroscopic point of view. A precursory idea of this method consists in assuming that simulating a fluid flowing through a porous medium is the same as thinking of the coupled fluid-solid medium as a continuum for which an effective conductivity, permeability

or viscosity, different from that of the fluid, can be defined. These effective medium approaches were first postulated, for rigid media, from an empirical point of view by Darcy (1856) and then modified using analytical considerations (Brinkman, 1949). In the elastic case, instead, a similar model has been deduced by Biot (1955) which found a well posed system of partial differential equations coupling the Darcy's law with the equilibrium equations for the elastic material. Even if the equations were born as empirical laws, several strategies have been developed in time in order to derive these equations analytically, deducing the macroscopic behavior from the local description (Davit *et al.*, 2013). This procedure is called upscaling. Different techniques are available for upscaling: they start from a representative elementary volume (REV, cf. figure 1.2) and generate an equivalent macroscopic continuous model called homogenized model.

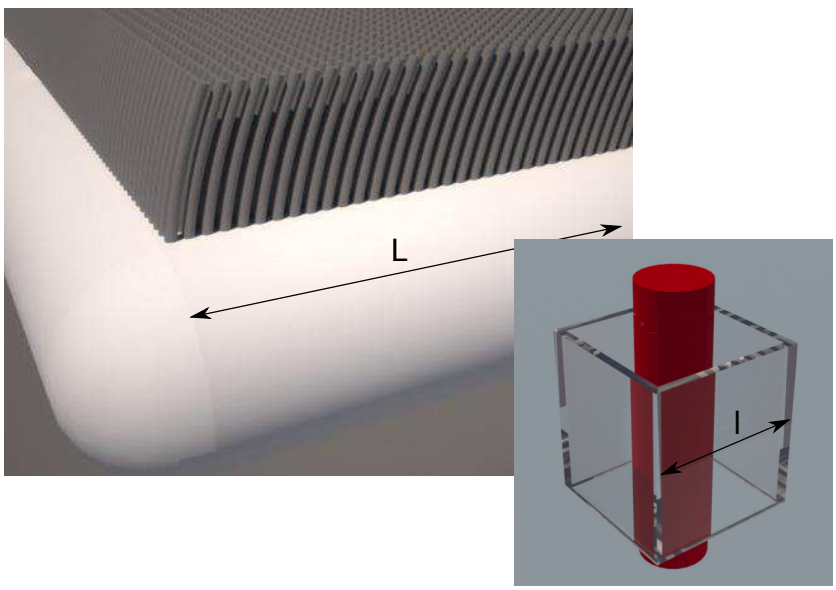

Figure 1.2: Macroscopic design of a poroelastic coating (left), and microscopic zoom over one cylindrical fiber inside a cubic representative elementary volume (defined by the upscaling technique). L and l are the macroscopic and microscopic length scales, respectively.

1.2.2 Volume averaging technique

One of the most used approaches is the volume averaging method thoroughly described by Whitaker (1998). It consists in considering an elementary cell representative of the porous structure (V in figure 1.3); the size of the REV is of the order of the pore size. A fundamental assumption is that of periodicity, over V, for the unknown quantities. Starting from the Navier-Stokes equations (NSE), it is assumed that the solution (velocity and pressure fields) can be decomposed into a mean part plus a fluctuation (Gray, 1975). The fluctuation represents how much the solution is far from its mean part and it must satisfy a zero average condition over the REV, that is fundamental to deduce the effective equations. After substituting the decomposition of the unknown fields inside the NSE and considering the spatial average of the equations over the REV, one obtains the momentum equation for the mean flow, with forcing terms related to the fluctuations. In this way, the Darcy's law (Whitaker, 1986), its Brinkman's correction (Quintard & Whitaker, 1994) and the Forchheimer's equation (Whitaker, 1996) have been deduced theoretically. Even if Whitaker did not developed any model for elastic media (cf. Whitaker, 1998), there are also works which propose models for poroelastic media based on volume averaging (e.g. Le Bars & Worster, 2006), but in this case a closure relation for the motion of the structure is introduced.

1.2.3 Homogenized model

Another strategy widely used is described by Mei & Vernescu (2010) and consists in implementing a homogenization technique based on a multiple scale analysis. The starting point of this technique is the same as the volume averaging method: the Navier-Stokes equations are taken to be valid over V_f in figure 1.3 and a proper expansion of the unknown fields in terms of powers of a small parameter is assumed. If the convective term is sufficiently small (of the order of the ratio between length scales) the resulting equations at leading order are self-contained, i.e. there is no need to introduce a closure relation. Darcy's, Brinkman's and Forchheimer's equations can be deduced analytically also in this case. The generalization to the deformable elastic case requires some effort because also the equation for the elastic material must be accounted for. Both approaches briefly outlined above require *closure* relations when nonlinear terms are present. Much work is present in the literature: in particular, Mei & Auriault (1991) have examined the effect of weak fluid inertia in the porous medium, finding that Forchheimer's correction to Darcy's law

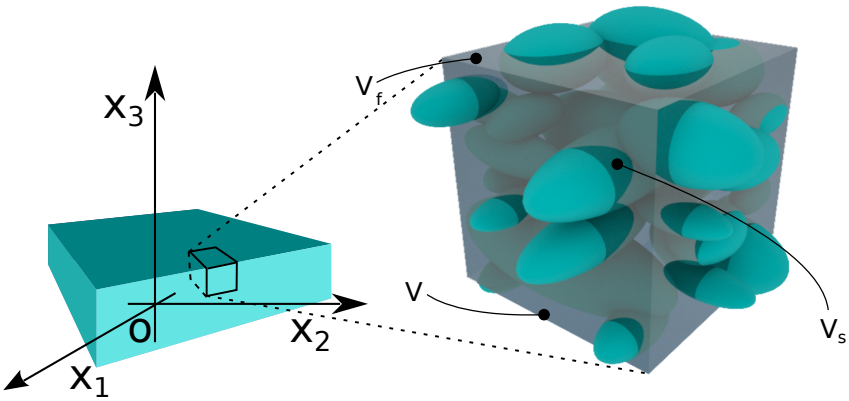

Figure 1.3: View of a generic porous medium within an elementary cell V. V_f is the volume occupied by the fluid and V_s is that occupied by the solid, so that $V = V_f + V_s$. Γ is the fluid-solid microscopic interface.

should be at least cubic (instead of quadratic) for isotropic media. This has been confirmed by Firdaouss *et al.* (1997). The same occurs for orthotropic media (Skjetne & Auriault, 1999). Auriault (2009) investigated the domain of validity of Brinkman's equation, finding that it is valid for swarms of fixed particles or a fixed bed of fibers at very low concentration and under precise conditions which depend on the separation of scale parameter $\epsilon = l/L$, with l and L two different, representative length scales. Homogenization provides a point of contact between the microscopic and the macroscopic worlds, and permits to transfer information from one point of view to the other. In this, it differs from purely microscopic approaches such as those by Tamayol & Bahrami (2009), van der Westhuizen & du Plessis (1996), Jackson & James (1986) and Yazdchi *et al.* (2011), and it is also different from purely macroscopic points of view, such as that by Battiato (2012) in which analytical forms of the permeability are taken from the literature.

Both volume averaging method and homogenization theory are suitable for the development of mathematical models in poroelasticity. Many works in this field have been pursued on the basis of these two techniques: some example are Rice & Cleary (1976); Burridge & Keller (1981); Sharma (2007); Penta & Ambrosi (2013). Actually, even if the two methods are different, they have several points of contact

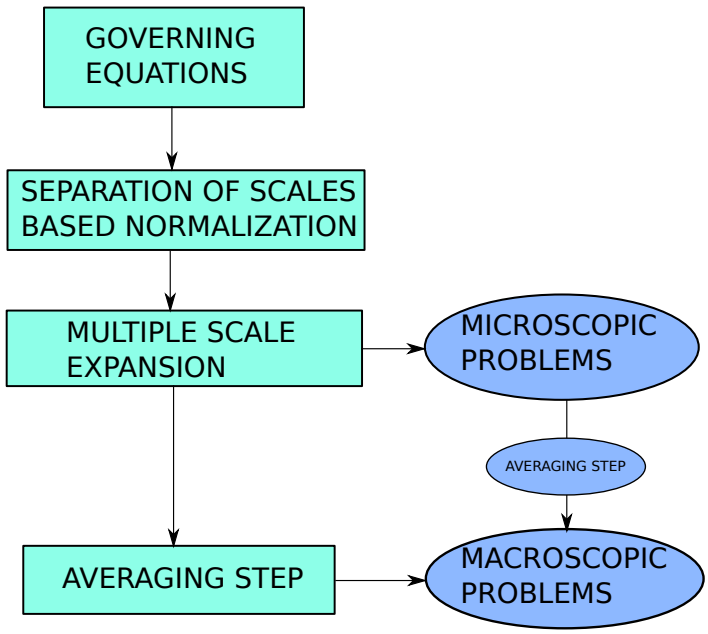

Figure 1.4: Diagram of the workflow for the homogenization technique. Rectangle represents the theoretical steps to develop a model equation. Ovals represent the operative steps where the equations are solved. The multiple scale expansion and the averaging step give us the microscopic and macroscopic equations, respectively. Furthermore, the averaging is also used to transfer information between the two sets of equations.

which are explained in detail by Davit *et al.* (2013).

1.3 Interface conditions and coupling methods

All the works and the methods cited up to now refer to the solution of the flow deeply inside a porous medium, far from the boundaries. The problem of the interface conditions between the pure fluid and the porous region is crucial and amply discussed in the literature. The scene is rather complex already in case of rigid porous media: Jäger & Mikelić (1996, 2000) spent much effort on this problem, concluding, through functional analysis and introducing an auxiliary problem based on homogenization, that the widely used condition of Beavers & Joseph (1967) and its modification by Saffman (1971) have a mathematical justification. Beavers & Joseph (1967) observed that the penetration of the velocity into the porous bed extends over a length proportional to $\sqrt{\mathcal{K}}$, with $\mathcal{K}$ the bed's permeability. This is equivalent to specifying a jump in the average velocity at the interface. More elaborate conditions have also been proposed, simulating the flow inside the porous medium with the Darcy-Brinkman equation, introducing an effective viscosity μ_e (Givler & Altobelli, 1994), and imposing continuity of the normal and tangential components of the stress tensor at the interface (Hill & Straughan, 2008). Another interface condition has been developed by Ochoa-Tapia & Whitaker (1995) via the definition of the excess surface and bulk stress tensors to be obtained from the governing equations holding in the porous and pure fluid regions. This condition becomes, under certain hypotheses, the continuity of the effective velocity and pressure over the macroscopic interface. Finally, a strategy often used to couple two different media is the penalization method. It consists in solving the Navier-Stokes equations in the whole domain, with a forcing term added in the porous region to take into account the presence of the structure. This forcing term is multiplied by the characteristic equation of the porous domain and it goes to zero smoothly outside of it. This approach has been pursued, among others, by Bruneau & Mortazavi (2008) and Angot *et al.* (1999). Cimolin & Discacciati (2013) have shown that even if the penalization method is stable and easy to implement, the comparison of the solution against experimental data near the interface is not satisfactory. Concerning the interface conditions for elastic media, one difficult consists on the motion of the macroscopic interface. This difficult is often avoided by imposing interface conditions at a fixed interface (usually that one identified from an initial resting state of the medium), assuming that the deformations are small, or equivalently, that the phenomenon is observed from a macroscopic point of view. The usual choice for the conditions to be imposed at the fixed interface appears to be the continuity of the effective velocities and of effective normal stresses, as stated in Barry *et al.* (1991); Hoffmann *et al.*

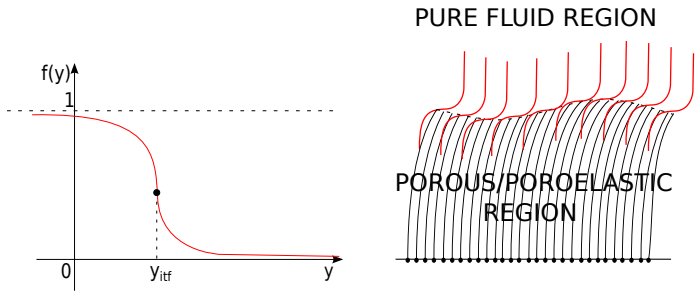

Figure 1.5: Sketch of a smooth filter f centered at the height of the interface y_{itf}, of possible use in a penalization method.

(2004); Gopinath & Mahadevan (2011); Alexiou & Kapellos (2013).

Summing up, the interface conditions can be essentially classified in three classes: the first one involves pressure and velocities which are linked over the interface directly (continuity or jump); the second one involves them indirectly, linking the normal to the interface components of the stress tensor. The second class cannot be employed if the equation to be solved in the porous medium is Darcy's law. The third class includes all those methods which use a filter to go from the porous region to the fluid region; a drawback of this latter approach is that there is no general physical justification for the choice of the filter. Some authors Breugem *et al.* (2004); Jamet & Chandesris (2009) have proven that the variation of the permeability near the interface is not an intrinsic property of the porous medium, but depends on the properties of the flow.

1.4 Solid mechanics: transversely isotropic structures

Our bio-inspired coating is assumed to be composed by cylindrical fibres; we are thus interested in the fluid-structure interaction of transversely isotropic porous media such as those sketched in fig. 1.6. A transversely isotropic material is characterized by the fact that all the geometric and physical properties are symmetric about an axis that is normal to a plane of isotropy (properties along x_3 in fig. 1.6 are constant if the cylinders are infinitely long). This means that, if $\mathbf{A}$ is a second order tensor only depending on the topological and physical properties of the structure, it

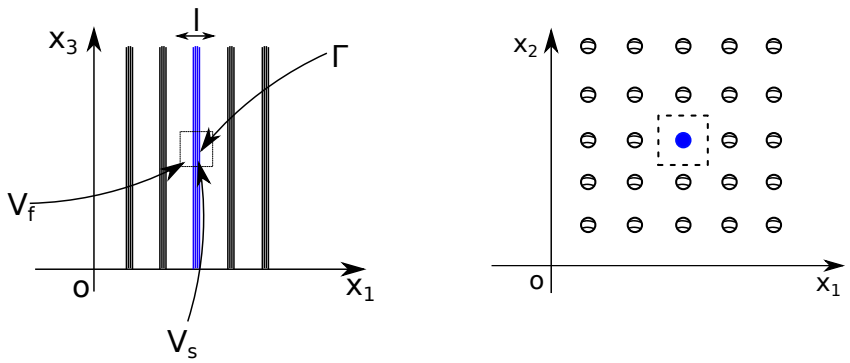

Figure 1.6: View of a transversely isotropic porous medium, made by fibers shown in the (x_1, x_3) and (x_1, x_2) plane, respectively. The dotted rectangle in the two frames represents the elementary cell V. V_f is the volume occupied by the fluid and V_s is that occupied by the solid, so that $V = V_f + V_s$. Γ is the fluid-solid microscopic interface.

can be written in the form:

$$\mathbf{A} = \begin{pmatrix} A_1 & 0 & 0 \\ 0 & A_1 & 0 \\ 0 & 0 & A_3 \end{pmatrix},$$

so that $\mathbf{A}$ is fully determined by two constants instead of nine. The proof of this fact is very simple: if $\mathbf{A}$ is a generic material matrix related to the medium and $\mathbf{f}$, $\mathbf{d}$ are material properties such that

$$\mathbf{f} = \mathbf{A}\mathbf{d},$$

in a medium which is transversely isotropic, the material properties are invariant with respect to an orthogonal transformation $\mathbf{R}$ along the axis of symmetry, i.e.

$$\mathbf{R}\mathbf{f} = \mathbf{A}\mathbf{R}\mathbf{d};$$

combining the equations we obtain that

$$\mathbf{A} = \mathbf{R}^{-1}\mathbf{A}\mathbf{R}.$$

For transversely isotropic materials $\mathbf{R}$ is a rotation over the plane (x_1, x_2) and hence it has the form

$$\mathbf{R} = \begin{pmatrix} \cos\theta & \sin\theta & 0 \\ -\sin\theta & \cos\theta & 0 \\ 0 & 0 & 1 \end{pmatrix};$$

for the special case $\theta = \pi$ we obtain that $A_{13} = A_{31} = A_{12} = A_{21} = 0$ and for $\theta = \frac{\pi}{2}$ it is found that $A_{23} = A_{32} = 0$ and $A_{11} = A_{22}$. Analyzing elastic media, higher rank tensors will be introduced (like the stiffness tensor); also for these tensor some symmetry properties can be demonstrated because of transverse isotropicity (Cowin, 2013). The homogenization theory presented in the following holds both in the case of isotropic and anisotropic porous media, and thus also for transversely isotropic porous media. In the last case it is useful to define the concept of unit (or elementary) cell; a cubic unit cell is defined in fig. 1.6 by the dotted lines. This choice of the elementary cell is equivalent to developing homogenization for an infinitely wide lattice of infinitely long cylinders or, equivalently, the theory holds if we are far from the boundaries of the porous medium; to take into account the boundaries some strategies will have to be devised, both at a macroscopic and at a microscopic level as briefly anticipated in section 1.3.

Chapter 2

Homogenized model for rigid and elastic porous media

In this chapter the models developed with the homogenization theory introduced in chapter 1, to simulate flows through porous media, are presented. The whole theory considered here in the case of two-scale is suitable for infinitely wide domains; we do not deal for now with boundary or interface conditions which are the subject of the next chapter. To not confuse the reader we show the options which can be chosen for the model. Table 2.1 represents all the possible choices which can be made on the basis of the characteristics of the structure and of the flow and the tools to analyze the system. We present the two-scale approach for both rigid and elastic porous media, distinguishing for the flow regimes in table 2.1 and then the three-scales approach for the rigid case. The latter approach is useful for certain particular structures where three length scales are present and it represents an attempt to extend the standard technique to macroscopically or mesoscopically confined media. It transform the three-dimensional microscopic problems into more tractable two-dimensional problems (which are not depending on the mesoscopic variable). This fact depends on the nature of the equations to which the technique is applied: for poroelastic media, even if we apply a three-scale theory, we does not obtain equations independent on the mesoscopic direction (x_3 in this case), reason for that the three-scale theory is omitted.

	RIGID	ELASTIC
$\mathrm{Re} = \mathcal{O}(\epsilon)$	2-SCALE / 3-SCALE	2-SCALE
$\mathrm{Re} = \mathcal{O}(1)$	2-SCALE / 3-SCALE	2-SCALE

Table 2.1: Table showing the possible choices to model flow through porous and poroelastic media.

2.1 Two-scale approach for rigid porous media

Let us consider a rigid porous medium saturated by an incompressible Newtonian fluid of constant density ρ. The velocity and pressure fields in the fluid domain are ruled by the Navier Stokes equations (NSE):

$$\frac{\partial \hat{u}_i}{\partial \hat{x}_i} = 0, \tag{2.1.1}$$

$$\rho \frac{\partial \hat{u}_i}{\partial \hat{t}} + \rho \hat{u}_j \frac{\partial \hat{u}_i}{\partial \hat{x}_j} = -\frac{\partial \hat{p}}{\partial \hat{x}_i} + \mu \hat{\nabla}^2 \hat{u}_i, \tag{2.1.2}$$

defined on V_f, with $\hat{u}_i = 0$ on Γ which is the solid-fluid interface. In order to highlight the order of each term in the governing equations we need to introduce two length scales: the microscale l which represents a characteristic dimension of the solid inclusions, and the macroscale L which is associated with the global pressure gradient (the pressure scale is denoted with P). This fact allows us to define an ordering symbol

$$\epsilon = \frac{l}{L} \ll 1.$$

Under the hypothesis that the global pressure gradient is balanced by the local viscous term, we obtain an order relation that defines the velocity scale U:

$$\frac{P}{L} = \frac{\mu U}{l^2}. \tag{2.1.3}$$

The scaled dimensionless variables are related to the dimensional ones by:

$$\hat{t} = \frac{l}{U} t = \frac{\mu}{\epsilon P} t, \quad \hat{\mathbf{x}} = l\mathbf{x}, \quad \hat{p} = Pp, \quad \hat{\mathbf{u}} = U\mathbf{u} = \frac{\epsilon l P}{\mu}\mathbf{u}.$$

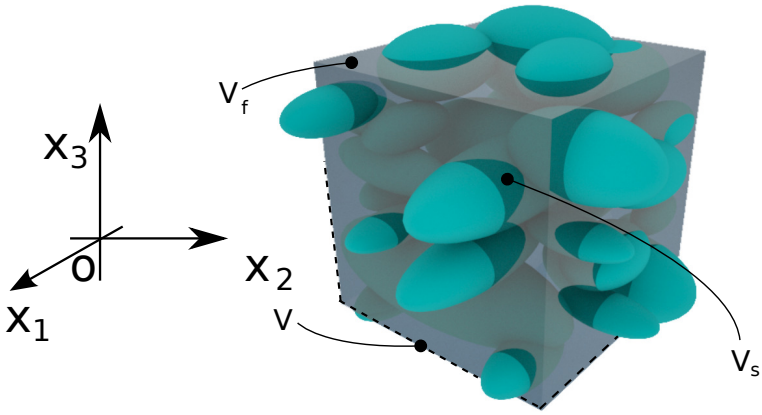

Figure 2.1: View of a generic porous medium within an elementary cell V. V_f is the volume occupied by the fluid and V_s is that occupied by the solid, so that $V = V_f + V_s$. Γ is the fluid-solid microscopic interface.

The governing equations thus become:

$$\frac{\partial u_i}{\partial \hat{x}_i} = 0,$$

$$\rho \frac{\Delta P^2 l^3}{\mu^2 L^2} \frac{\partial u_i}{\partial t} + \rho \frac{\Delta P^2 l^3}{\mu^2 L^2} u_j \frac{\partial u_i}{\partial x_j} = -\frac{\Delta P}{l} \frac{\partial p}{\partial x_i} + \frac{\Delta P}{L} \nabla^2 u_i.$$

Defining the Reynolds number on the microscale as:

$$\mathrm{Re} = \frac{\rho U l}{\mu} = \epsilon \rho \frac{\Delta P l^2}{\mu^2},$$

and multiplying the last equation by $\frac{L}{\Delta P}$, the dimensionless NSE can be rewritten as

$$\mathrm{Re} \frac{\partial u_i}{\partial t} + \mathrm{Re} u_j \frac{\partial u_i}{\partial x_j} = -\frac{1}{\epsilon} \frac{\partial p}{\partial x_i} + \nabla^2 u_i. \tag{2.1.4}$$

As already noted there are two possibilities about the Reynolds number:

$$\mathrm{Re} \ll 1 \quad \text{and} \quad \mathrm{Re} = \mathcal{O}(1).$$

2.1.1 Small Reynolds number

We start by choosing the case $\mathrm{Re} \ll 1$ and consider the dimensionless NSE

$$\frac{\partial u_i}{\partial x_i} = 0$$

$$\epsilon \mathrm{Re} \frac{\partial u_i}{\partial t} + \epsilon \mathrm{Re} u_j \frac{\partial u_i}{\partial x_j} = -\frac{\partial p}{\partial x_i} + \epsilon \nabla^2 u_i.$$

Before applying the homogenization method we have to specify that we consider a medium which is periodic over a cell V, and focus our attention on this cell (the microscopic volume, cf. fig. 2.1). We introduce the fast (microscopic) and slow (macroscopic) variables $\mathbf{x}$ and $\mathbf{x}' = \epsilon \mathbf{x}$ and the expansions

$$\mathbf{u} = \mathbf{u}^{(0)} + \epsilon \mathbf{u}^{(1)} + \ldots, \quad p = p^{(0)} + \epsilon p^{(1)} + \ldots \tag{2.1.5}$$

where $\mathbf{u}^{(i)}$ and $\mathbf{p}^{(i)}$ are functions of $(\mathbf{x}, \mathbf{x}', t)$. Note that

$$\frac{\partial}{\partial x_i} \to \frac{\partial}{\partial x_i} + \epsilon \frac{\partial}{\partial x_i'} \tag{2.1.6}$$

and

$$\frac{\partial^2}{\partial x_i \partial x_i} \to \frac{\partial^2}{\partial x_i \partial x_i} + 2\epsilon \frac{\partial^2}{\partial x_i \partial x_i'} + \epsilon^2 \frac{\partial^2}{\partial x_i' \partial x_i'}. \tag{2.1.7}$$

Now we can rewrite the equations substituting expansions (2.1.5) and using (2.1.6) and (2.1.7):

$$\sum_{j=0}^{N} \left(\epsilon^j \frac{\partial u_i^{(j)}}{\partial x_i} + \epsilon^{j+1} \frac{\partial u_i^{(j)}}{\partial x_i'} \right) = 0, \tag{2.1.8}$$

$$\begin{aligned} \mathrm{Re} \sum_{l=0}^{N} \left[\epsilon^{l+1} \frac{\partial u_i^{(l)}}{\partial t} + \epsilon^{l+1} u_j^{(l)} \sum_{m=0}^{N} \left(\epsilon^m \frac{\partial u_i^{(m)}}{\partial x_j} + \epsilon^{m+1} \frac{\partial u_i^{(m)}}{\partial x_j'} \right) \right] = \\ - \sum_{l=0}^{N} \left(\epsilon^l \frac{\partial p^{(l)}}{\partial x_i} + \epsilon^{l+1} \frac{\partial p^{(l)}}{\partial x_i'} \right) + \\ + \left(\sum_{l=0}^{N} \epsilon^{l+1} \frac{\partial^2 u_i^{(l)}}{\partial x_j^2} + 2 \sum_{l=0}^{N} \epsilon^{l+2} \frac{\partial^2 u_i^{(l)}}{\partial x_j \partial x_j'} + \sum_{l=0}^{N} \epsilon^{l+3} \frac{\partial^2 u_i^{(l)}}{\partial x_j'^2} \right). \end{aligned} \tag{2.1.9}$$

Collecting like-order terms, we obtain at order ϵ^0:

$$\frac{\partial u_i^{(0)}}{\partial x_i} = 0, \tag{2.1.10}$$

$$0 = -\frac{\partial p^{(0)}}{\partial x_i}, \tag{2.1.11}$$

and at order ϵ^1:

$$0 = -\frac{\partial p^{(1)}}{\partial x_i} - \frac{\partial p^{(0)}}{\partial x'_i} + \frac{\partial^2 u_i^{(0)}}{\partial x_j \partial x_j}, \tag{2.1.12}$$

under the hypothesis that Re is at most of order ϵ. From equation (2.1.11) we have that $p^{(0)} = p^{(0)}(\mathbf{x}', t)$, i.e. the leading order term of the pressure varies only over the macroscale (and time in general). Equations (2.1.10) and (2.1.12) constitute a Stokes problem for $u_i^{(0)}$ and $p^{(1)}$ forced by the macroscopic pressure $p^{(0)}$ and the solution can be written formally as

$$u_i^{(0)} = -K_{ij}\frac{\partial p^{(0)}}{\partial x'_j}, \qquad p^{(1)} = -A_j\frac{\partial p^{(0)}}{\partial x'_j} + p_0^{(1)}(\mathbf{x}', t), \tag{2.1.13}$$

where K_{ij} is a tensor, A_j is a vector and $p_0^{(1)}$ is an integration constant (with respect to the integration variable $\mathbf{x}$). Substituting (2.1.13) into (2.1.10) and (2.1.12) and dividing by $\partial p^{(0)}/\partial x'_j$, it follows that the coefficients should satisfy the relations:

$$\frac{\partial K_{ij}}{\partial x_i} = 0, \qquad -\frac{\partial A_j}{\partial x_i} + \nabla^2 K_{ij} = -\delta_{ij}, \tag{2.1.14}$$

which is a forced Stokes problem in the unknowns K_{ij} and A_j for $i, j = 1, 2, 3$ (in principle a system of 12 equations and 12 unknowns) with boundary condition

$$K_{ij} = 0 \quad \text{on } \Gamma,$$

and K_{ij} and A_j which are V-periodic. Moreover, to ensure uniqueness of the solution we can impose

$$\langle A_j \rangle = 0 \tag{2.1.15}$$

for each j, where the volume average over a unit cell $\langle \cdot \rangle$ is defined by:

$$\langle f \rangle := \frac{1}{V}\int_{V_f} f \, dV. \tag{2.1.16}$$

By taking the volume average of (2.1.13), noting that $p^{(0)}$ and $p_0^{(1)}$ do not depend on $\mathbf{x}$ and using (2.1.15), we obtain

$$\langle u_i^{(0)} \rangle = -\mathcal{K}_{ij}\frac{\partial p^{(0)}}{\partial x'_j}, \quad \text{with } \mathcal{K}_{ij} = \langle K_{ij} \rangle, \tag{2.1.17}$$

$$\langle p^{(1)} \rangle = \vartheta p_0^{(1)}, \quad \text{with } \vartheta = \frac{V_f}{V},$$

where $\mathcal{K}_{ij}$ is the dimensionless permeability tensor and ϑ the porosity. The equation above is Darcy's law, which is thus a first order approximation of the NSE in ϵ. In dimensional variables, eq. (2.1.17) reads:

$$\langle \hat{u}_i^{(0)} \rangle = -\frac{\mathcal{K}_{ij} l^2}{\mu} \frac{\partial \hat{p}^{(0)}}{\partial \hat{x}_j} = -\frac{\hat{\mathcal{K}}_{ij}}{\mu} \frac{\partial \hat{p}^{(0)}}{\partial \hat{x}_j}. \tag{2.1.18}$$

2.1.2 Going beyond leading order

A strategy to account for inertia is to consider the next order terms in eqs. (2.1.8) and (2.1.9), and thus write:

$$\frac{\partial u_j^{(1)}}{\partial x_j} + \frac{\partial u_j^{(0)}}{\partial x'_j} = 0 \tag{2.1.19}$$

$$u_j^{(0)} \frac{\partial u_i^{(0)}}{\partial x_j} = -\frac{\partial p^{(2)}}{\partial x_i} - \frac{\partial p^{(1)}}{\partial x'_i} + \frac{\partial^2 u_i^{(1)}}{\partial x_j \partial x_j} + 2\frac{\partial^2 u_i^{(0)}}{\partial x'_j \partial x_j} \tag{2.1.20}$$

$$u_i^{(1)} = 0 \quad \text{on } \Gamma \quad \text{and } u_i^{(1)} \quad V - \text{periodic.}$$

where the time derivative of $u_i^{(0)}$ is absent in the momentum equation because $u_i^{(0)}$ is obtained in the previous section as the solution of a steady problem; we have now assumed also that Re is exactly of order ϵ. Substituting eq. (2.1.13) in (2.1.19) and (2.1.20), the equations read:

$$\frac{\partial u_j^{(1)}}{\partial x_j} = K_{ij} \frac{\partial^2 p^{(0)}}{\partial x'_i \partial x'_j} \tag{2.1.21}$$

$$\frac{\partial p^{(2)}}{\partial x_i} - \frac{\partial^2 u_i^{(1)}}{\partial x_j \partial x_j} = A_j \frac{\partial^2 p^{(0)}}{\partial x'_i \partial x'_j} - \frac{\partial p_0^{(1)}}{\partial x'_i} - K_{jl} \frac{\partial K_{ik}}{\partial x_j} \frac{\partial p^{(0)}}{\partial x'_k} \frac{\partial p^{(0)}}{\partial x'_l} - 2\frac{\partial K_{ij}}{\partial x_k} \frac{\partial^2 p^{(0)}}{\partial x'_j \partial x'_k}, \tag{2.1.22}$$

where the terms in the LHS are unknown. Because of linearity of equations (2.1.21) and (2.1.22) we can formally write a particular solution as:

$$u_i^{(1)} = -L_{ijk} \frac{\partial p^{(0)}}{\partial x'_j} \frac{\partial p^{(0)}}{\partial x'_k} - M_{ijk} \frac{\partial^2 p^{(0)}}{\partial x'_j \partial x'_k} - S_{ij} \frac{\partial p_0^{(1)}}{\partial x'_j} \tag{2.1.23}$$

$$p^{(2)} = -B_{jk}\frac{\partial p^{(0)}}{\partial x'_j}\frac{\partial p^{(0)}}{\partial x'_k} - C_{jk}\frac{\partial^2 p^{(0)}}{\partial x'_j \partial x'_k} - T_j\frac{\partial p_0^{(1)}}{\partial x'_j} + p_0^{(2)}, \tag{2.1.24}$$

where $p_0^{(2)}$ depends only on the macroscale variable. Substituting (2.1.23) and (2.1.24) into (2.1.19) and (2.1.20) we obtain

$$\frac{\partial}{\partial x_i}\left(-B_{jk}\frac{\partial p^{(0)}}{\partial x'_j}\frac{\partial p^{(0)}}{\partial x'_k} - C_{jk}\frac{\partial^2 p^{(0)}}{\partial x'_j \partial x'_k} - T_j\frac{\partial p_0^{(1)}}{\partial x'_j}\right)$$
$$-\frac{\partial^2}{\partial x_g \partial x_g}\left(-L_{ijk}\frac{\partial p^{(0)}}{\partial x'_j}\frac{\partial p^{(0)}}{\partial x'_k} - M_{ijk}\frac{\partial^2 p^{(0)}}{\partial x'_j \partial x'_k} - S_{ij}\frac{\partial p_0^{(1)}}{\partial x'_j}\right) =$$
$$= A_j\frac{\partial^2 p^{(0)}}{\partial x'_i \partial x'_j} - \frac{\partial p_0^{(1)}}{\partial x'_i} - K_{jl}\frac{\partial K_{ik}}{\partial x_j}\frac{\partial p^{(0)}}{\partial x'_k}\frac{\partial p^{(0)}}{\partial x'_l} - 2\frac{\partial K_{ij}}{\partial x_k}\frac{\partial^2 p^{(0)}}{\partial x'_j \partial x'_k},$$

$$\frac{\partial}{\partial x_i}\left(-L_{ijk}\frac{\partial p^{(0)}}{\partial x'_j}\frac{\partial p^{(0)}}{\partial x'_k} - M_{ijk}\frac{\partial^2 p^{(0)}}{\partial x'_j \partial x'_k} - S_{ij}\frac{\partial p_0^{(1)}}{\partial x'_j}\right) = K_{ij}\frac{\partial^2 p^{(0)}}{\partial x'_i \partial x'_j}$$

which are satisfied if the relation below hold:

$$\frac{\partial L_{ijk}}{\partial x_i}\frac{\partial p^{(0)}}{\partial x'_j}\frac{\partial p^{(0)}}{\partial x'_k} = 0,$$
$$\frac{\partial B_{jk}}{\partial x_i}\frac{\partial p^{(0)}}{\partial x'_j}\frac{\partial p^{(0)}}{\partial x'_k} - \frac{\partial L_{ijk}}{\partial x_g \partial x_g}\frac{\partial p^{(0)}}{\partial x'_j}\frac{\partial p^{(0)}}{\partial x'_k} = K_{jl}\frac{\partial K_{ik}}{\partial x_j}\frac{\partial p^{(0)}}{\partial x'_k}\frac{\partial p^{(0)}}{\partial x'_l},$$
$$\frac{\partial M_{ijk}}{\partial x_i}\frac{\partial^2 p^{(0)}}{\partial x'_j \partial x'_k} = -K_{kj}\frac{\partial^2 p^{(0)}}{\partial x'_j \partial x'_k},$$
$$\frac{\partial C_{jk}}{\partial x_i}\frac{\partial^2 p^{(0)}}{\partial x'_j \partial x'_k} - \frac{\partial M_{ijk}}{\partial x_g \partial x_g}\frac{\partial^2 p^{(0)}}{\partial x'_j \partial x'_k} = -A_j\frac{\partial^2 p^{(0)}}{\partial x'_i \partial x'_j} + 2\frac{\partial K_{ij}}{\partial x_k}\frac{\partial^2 p^{(0)}}{\partial x'_j \partial x'_k},$$
$$\frac{\partial S_{ij}}{\partial x_i}\frac{\partial p_0^{(1)}}{\partial x'_j} = 0,$$
$$\frac{\partial T_j}{\partial x_i}\frac{\partial p_0^{(1)}}{\partial x'_j} - \frac{\partial S_{ij}}{\partial x_g \partial x_g}\frac{\partial p_0^{(1)}}{\partial x'_j} = -\frac{\partial p_0^{(1)}}{\partial x'_i}.$$

Simplifying all the macroscopic terms related to the pressure, we obtain the following set of microscopic equations:

$$\frac{\partial L_{ijk}}{\partial x_i} = 0 \tag{2.1.25}$$

$$\frac{\partial B_{jk}}{\partial x_i} - \frac{\partial L_{ijk}}{\partial x_g \partial x_g} = K_{lj} \frac{\partial K_{ik}}{\partial x_l} \tag{2.1.26}$$

$$\frac{\partial M_{ijk}}{\partial x_i} = -K_{kj} \tag{2.1.27}$$

$$\frac{\partial C_{jk}}{\partial x_i} - \frac{\partial M_{ijk}}{\partial x_g \partial x_g} = -A_j \delta_{ik} + 2 \frac{\partial K_{ij}}{\partial x_k} \tag{2.1.28}$$

$$\frac{\partial S_{ij}}{\partial x_i} = 0 \tag{2.1.29}$$

$$\frac{\partial T_j}{\partial x_i} - \frac{\partial S_{ij}}{\partial x_g \partial x_g} = -\delta_{ij} \tag{2.1.30}$$

$$L_{ijk} = S_{ij} = T_j = 0,\ M_{ijk} = -\frac{V}{|\Gamma|} \langle K_{kj} \rangle n_i \quad \text{on } \Gamma,$$

$$L_{ijk},\ M_{ijk},\ B_{jk},\ C_{jk},\ S_{ij}, T_j \ V\text{-periodic}$$

plus the conditions $\langle C_{ij} \rangle = \langle B_{ij} \rangle = \langle T_j \rangle = 0$ in order to guarantee uniqueness of the solution. S_{ij} and T_j are the same as K_{ij} and A_j because they satisfy the same problem. Something has to be explained about the condition on Γ for M_{ijk}: the inhomogeneous boundary value problem for M_{ijk} is needed in order to counterbalance the source term in equation (2.1.27) inside the elementary cell. Moreover, this choice for M_{ijk} satisfies the no-slip condition for $u_i^{(1)}$: using equations (2.1.23) and the boundary condition for M_{ijk} we obtain

$$u_i^{(1)} = \frac{V}{|\Gamma|} \langle K_{kj} \rangle \frac{\partial^2 p^{(0)}}{\partial x'_j \partial x'_k} n_i = 0 \quad \text{on } \Gamma. \tag{2.1.31}$$

Since we are interested in the macroscopic velocity and pressure, we can take the average of (2.1.23) and (2.1.24):

$$\langle u_i^{(1)} \rangle = -\mathcal{L}_{ijk} \frac{\partial p^{(0)}}{\partial x'_j} \frac{\partial p^{(0)}}{\partial x'_k} - \mathcal{M}_{ijk} \frac{\partial^2 p^{(0)}}{\partial x'_j \partial x'_k} - \mathcal{K}_{ij} \frac{\partial p_0^{(1)}}{\partial x'_j}, \tag{2.1.32}$$

$$\langle p^{(2)} \rangle = \vartheta p_0^{(2)}, \tag{2.1.33}$$

where $\mathcal{L}_{ijk} = \langle L_{ijk} \rangle$ and $\mathcal{M}_{ijk} = \langle M_{ijk} \rangle$. Combining equation (2.1.17) with (2.1.33), we obtain an anisotropic version of the non-linear correction of Darcy's

law (the so-called Forchheimer equation):

$$\begin{aligned}\langle u_i \rangle = \langle u_i^{(0)} \rangle + \epsilon \langle u_i^{(1)} \rangle = \\ = -\mathcal{K}_{ij} \frac{\partial p^{(0)}}{\partial x'_j} - \epsilon \left(\mathcal{L}_{ijk} \frac{\partial p^{(0)}}{\partial x'_j} \frac{\partial p^{(0)}}{\partial x'_k} - \mathcal{M}_{ijk} \frac{\partial^2 p^{(0)}}{\partial x'_j \partial x'_k} - \mathcal{K}_{ij} \frac{\partial p_0^{(1)}}{\partial x'_j} \right) = \\ = -\mathcal{K}_{ij} \frac{\partial p_0}{\partial x'_j} - \epsilon \left(\frac{\mathcal{L}_{ijk}}{\mathcal{K}_{lj} \mathcal{K}_{gk}} u_l^{(0)} u_g^{(0)} - \frac{\mathcal{M}_{ijk}}{\mathcal{K}_{lk}} \frac{\partial u_l^{(0)}}{\partial x'_j} \right),\end{aligned}$$

where $p_0 = p^{(0)} + \epsilon p_0^{(1)}$. We highlight the fact that the equation above, at least in theory, does not hold in the case of non-negligible inertia. A paper by Skjetne & Auriault (1999) shows that this non linear correction of Darcy's law is valid for $\mathrm{Re} \in (\sqrt{\epsilon}, 1)$. A strategy to consider, at least in theory, higher values of Re is presented in the following section.

2.1.3 Finite Reynolds number

The system is different when $\mathrm{Re} = \mathcal{O}(1)$. The dimensionless NSE are the same as in section 2.1.1 (eqs. (2.1.8) and (2.1.9)) and expanding as before we have the following equations at different orders in ϵ:

$$\frac{\partial u_i^{(0)}}{\partial x_i} = 0, \tag{2.1.34}$$

$$0 = -\frac{\partial p^{(0)}}{\partial x_i}, \tag{2.1.35}$$

$$\mathrm{Re} \left(\frac{\partial u_i^{(0)}}{\partial t} + u_j^{(0)} \frac{\partial u_i^{(0)}}{\partial x_j} \right) = -\frac{\partial p^{(1)}}{\partial x_i} - \frac{\partial p^{(0)}}{\partial x'_i} + \frac{\partial^2 u_i^{(0)}}{\partial x_j \partial x_j}, \tag{2.1.36}$$

where the presence of the nonlinear term on the $\mathcal{O}(\epsilon)$ momentum equation complicates matters. Still, from (2.1.35) we have $p^{(0)} = p^{(0)}(\mathbf{x}', t)$; further analytical progress can be made under an Oseen-like approximation, i.e. assuming that

$$u_j^{(0)} \frac{\partial u_i^{(0)}}{\partial x_j} \approx U_j \frac{\partial u_i^{(0)}}{\partial x_j}$$

where U_j is a mean fluid velocity through the pores defined via a spatial average:

$$U_j := \frac{1}{V_{Tot}} \int_{V_{Tot}} \langle u_j^{(0)} \rangle \, dV; \tag{2.1.37}$$

with V_{Tot} the macroscopic volume of the porous medium (fluid plus solid). Initially we search for a steady solution of equations (2.1.34) and (2.1.36). The Oseen approximation has been proposed for cases with Re $= \mathcal{O}(1)$ by Gustafsson & Protas (2013), with satisfactory results. We adopt it here in order to maintain a linear problem, yielding (2.1.17).The choice of a global estimate of the velocity $\overline{U}$, defined via equation (2.1.37), is important to establish a two-way link between the microscopic and the macroscopic set of equations.

Steady solution

If the time derivative in equation (2.1.36) is negligible, after linearization we obtain the following problem

$$\mathrm{Re}U_j \frac{\partial u_i^{(0)}}{\partial x_j} = -\frac{\partial p^{(1)}}{\partial x_i} - \frac{\partial p^{(0)}}{\partial x_i'} + \frac{\partial^2 u_i^{(0)}}{\partial x_j^2} \tag{2.1.38}$$

and

$$\frac{\partial u_i^{(0)}}{\partial x_i} = 0; \tag{2.1.39}$$

writing the solution as in eq. (2.1.13), we are actually searching for K_{ij} and A_j which satisfy

$$-\mathrm{Re}U_g \frac{\partial K_{ij}}{\partial x_g} = \frac{\partial A_j}{\partial x_i} - \delta_{ij} - \frac{\partial^2 K_{ij}}{\partial x_g^2} \tag{2.1.40}$$

and

$$\frac{\partial K_{ij}}{\partial x_i} = 0 \tag{2.1.41}$$

which can be obtained as in section 1.1.1. After $u_i^{(0)}$ and $p^{(0)}$ are found, U_j in (2.1.37) must be updated until convergence.

2.2 Two-scale approach for poroelastic media

If the inclusions in fig. 2.1 are not rigid, but are made of a deformable material, the theory described up to now does not hold and we need to take into account the deformation of the structure. One of the problems is that, although the unit cell is fixed in time and centered in $\mathbf{x}$, $V_s = V_s(t)$ and $V_f = V_f(t)$ because of the deformation and so, in general, it follows that

$$V(\mathbf{x}) = V_s(\mathbf{x}, t) \cup V_f(\mathbf{x}, t),$$

where the dependence on time and on the centroid $\mathbf{x}$ of each cell appears; for ease of notation we will omit both of these dependencies. Another difficulty is that the equation for the solid motion must now be coupled with the equations for the fluid. Thus, we consider the dimensional equation for the structure, i.e.

$$\rho_s \frac{\partial^2 \hat{v}_i}{\partial \hat{t}^2} = \frac{\partial \hat{\sigma}_{ij}}{\partial \hat{x}_j} \quad \text{on } V_s, \tag{2.2.1}$$

where $\hat{\mathbf{v}}$ is the solid displacement vector and $\hat{\sigma}_{ij}$ are the components of the solid stress tensor. Under the assumption that the structure is linearly elastic, for infinitesimally small strain the following equation holds

$$\hat{\sigma}_{ij} = \hat{C}_{ijkl}\hat{\varepsilon}_{kl}(\hat{\mathbf{v}}) = \frac{1}{2}\hat{C}_{ijkl}\left(\frac{\partial \hat{v}_k}{\partial \hat{x}_l} + \frac{\partial \hat{v}_l}{\partial \hat{x}_k}\right) \tag{2.2.2}$$

with $\hat{C}_{ijkl}$ the fourth order elasticity tensor. This equation must be coupled to the dimensional NSE for the velocity field $\hat{\mathbf{u}}$ and the pressure field $\hat{p}$, written in the form:

$$\rho_f \left(\frac{\partial \hat{u}_i}{\partial \hat{t}} + \hat{u}_j \frac{\partial \hat{u}_i}{\partial \hat{x}_j}\right) = \frac{\partial \hat{\Sigma}_{ij}}{\partial \hat{x}_j} \quad \text{on } V_f, \tag{2.2.3}$$

$$\frac{\partial \hat{u}_i}{\partial \hat{x}_i} = 0 \quad \text{on } V_f, \tag{2.2.4}$$

where $\hat{\Sigma}_{ij}$ is the canonical fluid stress tensor

$$\hat{\Sigma}_{ij} = -\hat{p}\delta_{ij} + 2\mu\hat{\varepsilon}_{ij}(\hat{\mathbf{u}}), \tag{2.2.5}$$

with $\hat{\varepsilon}$ the strain tensor for the fluid, formally defined like for the structure. The boundary conditions on the solid-fluid interface Γ are the continuity of velocities and normal stresses:

$$\hat{u}_i = \frac{\partial \hat{v}_i}{\partial \hat{t}} \quad \text{and} \quad \hat{\Sigma}_{ij} n_j = \hat{\sigma}_{ij} n_j, \tag{2.2.6}$$

where $\mathbf{n}$ is the unit normal vector pointing from the solid to the fluid; moreover, we impose V-periodicity. As in the rigid case, we need to understand the order (in ϵ) of each term in the governing equations. If U, V and T_S are the fluid velocity, solid displacement and solid time scales, respectively, from equation (2.2.6) it is:

$$U = \frac{V}{T_S}. \tag{2.2.7}$$

Moreover, we use Young's modulus of elasticity, E, to scale the elastic tensor and denote by P the pressure scale. If we assume that macroscopic solid stresses are balanced by pressure on the interface, we have

$$E\frac{Pl^2}{\mu L^2}T_S = P, \tag{2.2.8}$$

provided that macroscopic pressure forces are equilibrated by macroscopic viscous dissipation i.e. equation (2.1.3) holds also in this case. Thus, the solid time scale is defined as

$$T_S = \frac{\mu L^2}{El^2} = \frac{\mu}{\epsilon^2 E}, \tag{2.2.9}$$

with $\epsilon = l/L \ll 1$. Furthermore, from (2.2.1) we can introduce the relation

$$\frac{\rho_s}{T_S^2} = \frac{E}{L^2}, \tag{2.2.10}$$

on the assumptionn that inertia of the solid is of the same order of the solid stress over the macroscale. Combining equations (2.2.9) and (2.2.10) we obtain:

$$\frac{\rho_s E l^2}{\mu^2} = \frac{1}{\epsilon^2}. \tag{2.2.11}$$

Relation (2.1.3) implies that the fluid velocity scale can be written as

$$U = \epsilon\frac{Pl}{\mu}. \tag{2.2.12}$$

Using the last equation together with equations (2.2.7) and (2.2.9) we obtain the solid displacement scale:

$$V = \epsilon\frac{PL^2}{El} = \frac{PL}{E}. \tag{2.2.13}$$

Evaluation of the characteristic time scales In order to understand if the assumptions on the order of magnitude for the physical constants of the medium make sense, we calculate them in case of different elastic materials and fluids. Table 2.2 shows a few possible values of characteristic time scales for some combinations of the chosen materials. In all the cases $\epsilon = 10^{-3}$. As we can see, T_S is at least three orders of magnitude smaller than T_F for each fluid-solid combination. This fact suggests that the model described here applies when the solid phase reacts instaneously to stresses imposed by the fluid i.e. when the solid phase is in equilibrium

	steel $E = 205GPa$, $\nu_P = 0.282$	polyurethane elastomer $E = 0.002GPa$, $\nu_P = 0.499$	silicon $E = 110GPa$ $\nu_P = 0.240$	graphite $E = 1.5GPa$ $\nu_P = 0.280$
water $\mu = 1.002 \cdot 10^{-3} Pa\, s$	$T_S = 0.49 \cdot 10^{-8} s$, $T_F = 10s$	$T_S = 5 \cdot 10^{-4}$, $T_F = 10s$	$T_S = 9.1 \cdot 10^{-9}$, $T_F = 10s$	$T_S = 6.7 \cdot 10^{-7}$, $T_F = 10s$
air $\mu = 1.983 \cdot 10^{-5} Pa\, s$	$T_S = 0.97 \cdot 10^{-10} s$, $T_F = 0.5s$	$T_S = 1 \cdot 10^{-3}$, $T_F = 0.5s$	$T_S = 1.8 \cdot 10^{-10}$, $T_F = 0.5s$	$T_S = 1.32 \cdot 10^{-8}$, $T_F = 0.5s$

Table 2.2: Values of the characteristic time scales for solid and fluid phase, for four different materials. Here ν_P is the Poisson's ratio. The characteristic fluid time scale is always the same because it is not dependent on the type of solid material we are considering. The values of E and ν_P used in this table are taken from Jones & Ashby (2005)

over the characteristic time-scale of the fluid system. However, since the homogenization theory is valid also in the limit of infinitesimally small ϵ and $T_S \propto \epsilon^{-2}$, the solid time scale becomes comparable to the fluid one if ϵ is sufficient small.

We are now ready to introduce the relations between the dimensional and dimensionless variables (the latter without hat):

$$\hat{t} = \frac{lt_f}{U}, \text{ for the fluid time scale, and } \hat{t} = \frac{\mu t_s}{E\epsilon^2}, \text{ for the solid time scale,} \quad (2.2.14)$$

$$\hat{\mathbf{x}} = l\mathbf{x}, \quad \hat{p} = Pp, \quad \hat{\mathbf{u}} = \epsilon\frac{Pl}{\mu}\mathbf{u}, \quad \hat{\mathbf{v}} = \frac{PL}{E}\mathbf{v}. \quad (2.2.15)$$

Substituting these definitions in the fluid equation we obtain equation (2.1.4) which can be written as

$$\epsilon \mathrm{Re}\left(\frac{\partial u_i}{\partial t_f} + u_j\frac{\partial u_i}{\partial x_j}\right) = -\frac{\partial p}{\partial x_i} + 2\epsilon\frac{\partial \varepsilon_{ij}(\mathbf{u})}{\partial x_j}, \quad (2.2.16)$$

where, also in this case $\mathrm{Re} = (\rho_f U l)/\mu$. Applying the same procedure to the equation for the solid we obtain:

$$\epsilon^4\rho_s\frac{El^2}{\mu^2}\frac{\partial^2 v_i}{\partial t_s^2} = \frac{\partial \sigma_{ij}}{\partial x_j} \quad \text{on } V_s. \quad (2.2.17)$$

which becomes

$$\epsilon^2\frac{\partial^2 v_i}{\partial t_s^2} = \frac{\partial \sigma_{ij}}{\partial x_j} \quad \text{on } V_s. \quad (2.2.18)$$

thanks to (2.2.11). The boundary condition on the normal stresses becomes:

$$-p\,n_i + 2\epsilon\,\varepsilon_{ij}(\mathbf{u})n_j = \left[\frac{1}{\epsilon}C_{ijkl}\varepsilon_{kl}(\mathbf{v})\right]n_j \quad \text{on } \Gamma. \quad (2.2.19)$$

The continuity equation for the fluid, the boundary conditions and V-periodicity remain unchanged. At this point we can perform a multiple scale expansion as in the rigid case introducing the fast and slow variables, $\mathbf{x}$ and $\mathbf{x}' = \epsilon\mathbf{x}$, respectively, and the expansions

$$f = f^{(0)} + \epsilon f^{(1)} + \epsilon^2 f^{(2)} + \ldots \quad \text{where } f = \{u_i, v_i, p, \Sigma_{ij}, \sigma_{ij}\}. \quad (2.2.20)$$

Moreover we note that the strain tensor (for either the solid or the fluid) becomes

$$\varepsilon_{ij} + \epsilon\varepsilon'_{ij} \quad (2.2.21)$$

where

$$\varepsilon_{ij}(w) = \frac{1}{2}\left(\frac{\partial w_i}{\partial x_j} + \frac{\partial w_j}{\partial x_i}\right)$$

and

$$\varepsilon'_{ij}(w) = \frac{1}{2}\left(\frac{\partial w_i}{\partial x'_j} + \frac{\partial w_j}{\partial x'_i}\right).$$

2.2.1 Small Reynolds number

Using equations (2.2.20) and (2.2.21), and supposing that $\mathrm{Re} = \mathcal{O}(\epsilon)$, we obtain the following system for the fluid:

$$\frac{\partial u_i^{(0)}}{\partial x_i} = 0, \tag{2.2.22}$$

$$\frac{\partial u_i^{(1)}}{\partial x_i} + \frac{\partial u_i^{(0)}}{\partial x'_i} = 0, \tag{2.2.23}$$

$$0 = -\frac{\partial p^{(0)}}{\partial x_i}, \tag{2.2.24}$$

$$0 = \frac{\partial \Sigma_{ij}^{(0)}}{\partial x'_j} + \frac{\partial \Sigma_{ij}^{(1)}}{\partial x_j} = -\frac{\partial p^{(1)}}{\partial x_i} - \frac{\partial p^{(0)}}{\partial x'_i} + \frac{\partial^2 u_i^{(0)}}{\partial x_j \partial x_j}, \tag{2.2.25}$$

on V_f, and for solid:

$$\frac{\partial \sigma_{ij}^{(0)}}{\partial x_j} = 0, \tag{2.2.26}$$

$$0 = \frac{\partial \sigma_{ij}^{(1)}}{\partial x_j} + \frac{\partial \sigma_{ij}^{(0)}}{\partial x'_j}, \tag{2.2.27}$$

$$\frac{\partial^2 v_i^{(0)}}{\partial t_s^2} = \frac{\partial \sigma_{ij}^{(2)}}{\partial x_j} + \frac{\partial \sigma_{ij}^{(1)}}{\partial x'_j}, \tag{2.2.28}$$

on V_s, plus the boundary conditions:

$$u_i^{(0)} = \frac{\partial v_i^{(0)}}{\partial t_s}, \tag{2.2.29}$$

$$u_i^{(1)} = \frac{\partial v_i^{(1)}}{\partial t_s}, \tag{2.2.30}$$

$$\sigma_{ij}^{(0)} n_j = 0, \tag{2.2.31}$$

$$\sigma_{ij}^{(1)} n_j = \Sigma_{ij}^{(0)} n_j = -p^{(0)} n_i, \tag{2.2.32}$$

$$\sigma_{ij}^{(2)} n_j = \Sigma_{ij}^{(1)} n_j, \tag{2.2.33}$$

on Γ. It is useful to specify the form of the tensors σ and Σ at leading powers in ϵ:

$$\sigma_{ij}^{(0)} = C_{ijkl}(\varepsilon_{kl}(\mathbf{v}^{(0)})), \tag{2.2.34}$$

$$\sigma_{ij}^{(1)} = C_{ijkl}(\varepsilon_{kl}(\mathbf{v}^{(1)})) + C_{ijkl}(\varepsilon'_{kl}(\mathbf{v}^{(0)})), \tag{2.2.35}$$

$$\Sigma_{ij}^{(0)} = -p^{(0)} \delta_{ij}, \tag{2.2.36}$$

$$\Sigma_{ij}^{(1)} = -p^{(1)} \delta_{ij} + 2\varepsilon_{ij}(\mathbf{u}^{(0)}). \tag{2.2.37}$$

We now observe that, from equation (2.2.24), we have $p^{(0)} = p^{(0)}(\mathbf{x}', t)$; the system made by (2.2.26) and (2.2.31) implies that

$$\sigma_{ij}^{(0)} = 0 \; \forall \; i, j \quad \text{i.e.} \;\; C_{ijkl}(\varepsilon_{kl}(\mathbf{v}^{(0)})) = 0 \; \forall \; i, j, \tag{2.2.38}$$

and from this we have

$$\varepsilon_{kl}(\mathbf{v}^{(0)}) = 0 \; \forall \; k, l \quad \text{which implies that } \mathbf{v}^{(0)} = \mathbf{v}^{(0)}(\mathbf{x}', t).$$

Effective elasticity tensor Coupling the order ϵ solid momentum equation (2.2.27) with the boundary condition (2.2.32) we obtain a system which, using (2.2.35) and (2.2.38), can be rewritten in the following way:

$$\frac{\partial}{\partial x_j} \left\{ C_{ijkl} \left[\varepsilon_{kl}(\mathbf{v}^{(1)}) + \varepsilon'_{kl}(\mathbf{v}^{(0)}) \right] \right\} = 0 \quad \text{on } V_s, \tag{2.2.39}$$

$$\left\{ C_{ijkl} \left[\varepsilon_{kl}(\mathbf{v}^{(1)}) + \varepsilon'_{kl}(\mathbf{v}^{(0)}) \right] \right\} n_j = -p^{(0)} n_i \quad \text{on } \Gamma, \tag{2.2.40}$$

plus V-periodicity. Since the system above can be viewed as a linear differential equation for $\mathbf{v}^{(1)}$ forced by $\mathbf{v}^{(0)}$ and $p^{(0)}$, we formally express $\mathbf{v}^{(1)}$ in terms of $\mathbf{v}^{(0)}$ and $p^{(0)}$:

$$\mathbf{v}^{(1)}(\mathbf{x}, \mathbf{x}', t) = \chi_i^{pq}(\mathbf{x}) \varepsilon'_{pq}(\mathbf{v}^{(0)})(\mathbf{x}', t) - \eta_i(\mathbf{x}) p^{(0)}(\mathbf{x}', t) \quad \text{on } V_s, \tag{2.2.41}$$

where $\boldsymbol{\chi}$ is a third order tensor and $\boldsymbol{\eta}$ a vector. Substituting (2.2.41) into (2.2.39) and (2.2.40) we have:

$$\frac{\partial}{\partial x_j}\left\{C_{ijkl}\left[\varepsilon_{kl}(\chi^{pq})\varepsilon'_{pq}(\mathbf{v}^{(0)})\right] - C_{ijkl}\left[\varepsilon_{kl}(\eta)p^{(0)}\right] + \right.$$
$$\left. + C_{ijkl}\left[\varepsilon'_{kl}(\mathbf{v}^{(0)})\right]\right\} = 0 \quad \text{on } V_s, \tag{2.2.42}$$

$$\left\{C_{ijkl}\left[\varepsilon_{kl}(\chi^{pq})\varepsilon'_{pq}(\mathbf{v}^{(0)})\right] - C_{ijkl}\left[\varepsilon_{kl}(\eta)p^{(0)}\right] + \right.$$
$$\left. + C_{ijkl}\left[\varepsilon'_{kl}(\mathbf{v}^{(0)})\right]\right\} n_j = -p^{(0)}n_i \quad \text{on } \Gamma. \tag{2.2.43}$$

A particular solution of this system solves the two problems:

$$\frac{\partial}{\partial x_j}\left\{C_{ijkl}\left[\varepsilon_{kl}(\chi^{pq}) + \delta_{kp}\delta_{lq}\right]\right\} = 0 \quad \text{on } V_s, \tag{2.2.44}$$

$$\left\{C_{ijkl}\left[\varepsilon_{kl}(\chi^{pq}) + \delta_{kp}\delta_{lq}\right]\right\} n_j = 0 \quad \text{on } \Gamma, \tag{2.2.45}$$

and

$$\frac{\partial}{\partial x_j}\left[C_{ijkl}\,\varepsilon_{kl}(\eta)\right] = 0 \quad \text{on } V_s, \tag{2.2.46}$$

$$\left[C_{ijkl}\,\varepsilon_{kl}(\eta)\right] n_j = -n_i \quad \text{on } \Gamma. \tag{2.2.47}$$

Generalizing the averaging operator to the solid phase within the unit cell, we define

$$\langle f_s\rangle = \frac{1}{V}\int_{V_s} f_s\, dV,$$

where the function f_s is defined on V_s. From this moment on we will not distinguish between the solid or fluid averaging unless the distinction is ambiguous. Our target is to deduce a set of equations to determine the solution up to order ϵ. In order to do this we can take the solid-phase average to express the solid stress:

$$\langle\sigma^{(1)}_{ij}\rangle = \tag{2.2.48}$$
$$= \langle C_{ijkl}\,\varepsilon_{kl}(\mathbf{v}^{(1)})\rangle + \langle C_{ijkl}\rangle\varepsilon'_{kl}(\mathbf{v}^{(0)}) =$$
$$= \left[\langle C_{ijkl}\,\varepsilon_{kl}(\chi^{pq})\rangle + \langle C_{ijkl}\rangle\delta_{kp}\delta_{lq}\right]\varepsilon'_{pq}(\mathbf{v}^{(0)}) - \langle C_{ijkl}\,\varepsilon_{kl}(\eta)\rangle p^{(0)} =$$
$$= \mathcal{C}_{ijpq}\,\varepsilon'_{pq}(\mathbf{v}^{(0)}) - \langle C_{ijkl}\,\varepsilon_{kl}(\eta)\rangle p^{(0)},$$

where

$$\mathcal{C}_{ijpq} = \langle C_{ijkl}\,\varepsilon_{kl}(\chi^{pq})\rangle + \langle C_{ijpq}\rangle. \tag{2.2.49}$$

Momentum balance for the composite Equation (2.2.48) is the macroscale Hooke's law in the solid phase forced by the fluid pressure. To deduce the momentum equation for the composite we can define a new tensor

$$T_{ij} = \begin{cases} \Sigma_{ij} & \text{on } V_f \\ \epsilon^{-1}\sigma_{ij} & \text{on } V_s. \end{cases} \tag{2.2.50}$$

where σ is divided by ϵ because we take into account the scaling relation (2.2.19) between σ and Σ. It is useful at this point, to compute the average of $T_{ij}^{(0)}$, i.e. $\langle T_{ij}^{(0)} \rangle = \int_V T_{ij}^{(0)}\, dV/\mathbb{V}$:

$$\langle T_{ij}^{(0)} \rangle = \langle \sigma_{ij}^{(1)} \rangle + \langle \Sigma_{ij}^{(0)} \rangle = \langle \sigma_{ij}^{(1)} \rangle - \vartheta p^{(0)} \delta_{ij} =$$

$$= [\langle C_{ijkl}\, \varepsilon_{kl}(\chi^{pq}) \rangle + \langle C_{ijkl} \rangle \delta_{kp}\delta_{lq}]\, \varepsilon'_{pq}(\mathbf{v}^{(0)}) - (\langle C_{ijkl}\, \varepsilon_{kl}(\eta) \rangle + \vartheta \delta_{ij}) p^{(0)} =$$

$$\mathcal{C}_{ijpq}\, \varepsilon'_{pq}(\mathbf{v}^{(0)}) - \alpha'_{ij} p^{(0)}, \tag{2.2.51}$$

where α'_{ij} is defined by

$$\alpha'_{ij} = \vartheta \delta_{ij} + \langle C_{ijkl}\, \varepsilon_{kl}(\eta) \rangle. \tag{2.2.52}$$

Adding the averages of (2.2.25) and (2.2.28) we get

$$\langle \frac{\partial^2 v_i^{(0)}}{\partial t_s^2} \rangle = \langle \frac{\partial T_{ij}^{(0)}}{\partial x'_j} \rangle + \langle \frac{\partial \Sigma_{ij}^{(1)}}{\partial x_j} \rangle + \langle \frac{\partial \sigma_{ij}^{(2)}}{\partial x_j} \rangle. \tag{2.2.53}$$

Observing that we can exchange integral and derivative only if the integration domain and variables do not depend on the differentiation variable we obtain

$$(1-\vartheta)\frac{\partial^2 v_i^{(0)}}{\partial t_s^2} = \frac{\partial \langle T_{ij}^{(0)} \rangle}{\partial x'_j} + \frac{1}{V}\int_{V_f} \frac{\partial \Sigma_{ij}^{(1)}}{\partial x_j}\, dV + \frac{1}{V}\int_{V_s} \frac{\partial \sigma_{ij}^{(2)}}{\partial x_j}\, dV,$$

which, using Gauss theorem, becomes

$$(1-\vartheta)\frac{\partial^2 v_i^{(0)}}{\partial t_s^2} = \frac{\partial \langle T_{ij}^{(0)} \rangle}{\partial x'_j} + \frac{1}{V}\int_{\Gamma} \left(\sigma_{ij}^{(2)} - \Sigma_{ij}^{(1)}\right) n_j\, d\Omega.$$

The last integral in the equation above is zero by the boundary condition (2.2.33), so that the average momentum balance of the composite can be rewritten as

$$(1-\vartheta)\frac{\partial^2 v_i^{(0)}}{\partial t_s^2} = \frac{\partial}{\partial x'_j}\left[\mathcal{C}_{ijpq}\varepsilon'_{pq}(\mathbf{v}^{(0)}) - \alpha'_{ij} p^{(0)}\right]. \tag{2.2.54}$$

Equation (2.2.54) can be solved, if $\mathcal{C}$ is assigned, after solving the equations for $\boldsymbol{\chi}$ and $\boldsymbol{\eta}$.

Continuity equation for the composite Another important equation is deduced using the continuity equation for the fluid at order ϵ. Let us take the fluid-phase average of (2.2.23):

$$\langle \frac{\partial u_i^{(0)}}{\partial x_i'} \rangle = -\frac{1}{V} \int_{V_f} \frac{\partial u_i^{(1)}}{\partial x_i} \, dV.$$

As before we can exchange derivative and integral; using Gauss theorem, we obtain that the equation above is equivalent to

$$\frac{\partial \langle u_i^{(0)} \rangle}{\partial x_i'} = \frac{1}{V} \int_\Gamma u_i^{(1)} n_i \, d\Omega = \frac{1}{V} \int_\Gamma \dot{v}_i^{(1)} n_i \, d\Omega = \frac{1}{V} \int_{V_s} \frac{\partial \dot{v}_i^{(1)}}{\partial x_i} \, dV = \langle \frac{\partial \dot{v}_i^{(1)}}{\partial x_i} \rangle, \tag{2.2.55}$$

by the boundary condition (2.2.30). Equation (2.2.41) tells us that

$$\langle \frac{\partial \dot{v}_i^{(1)}}{\partial x_i} \rangle = \langle \frac{\partial}{\partial x_i} \frac{\partial}{\partial t_s} \left[\chi_i^{pq}(\mathbf{x}) \varepsilon'_{pq}(\mathbf{v}^{(0)})(\mathbf{x}', t_s) - \eta_i(\mathbf{x}) p^{(0)}(\mathbf{x}', t_s) \right] \rangle =$$

$$= \langle \frac{\partial}{\partial x_i} \chi_i^{pq}(\mathbf{x}) \varepsilon'_{pq}(\dot{\mathbf{v}}^{(0)})(\mathbf{x}', t_s) \rangle - \langle \frac{\partial}{\partial x_i} \eta_i(\mathbf{x}) \dot{p}^{(0)}(\mathbf{x}', t_s) \rangle =$$

$$= \langle \frac{\partial \chi_i^{pq}}{\partial x_i} \rangle \varepsilon'_{pq}(\dot{\mathbf{v}}^{(0)}) - \langle \frac{\partial \eta_i}{\partial x_i} \rangle \dot{p}^{(0)}.$$

The only time scale left is the solid time scale t_s, indicated simply as t in the following. A dot above a variable denotes derivation with respect to t. Substituting the equation above in (2.2.55) we obtain a relation between the solid stress and the pressure:

$$\frac{\partial \langle u_i^{(0)} \rangle}{\partial x_i'} = \langle \frac{\partial \chi_i^{pq}}{\partial x_i} \rangle \varepsilon'_{pq}(\dot{\mathbf{v}}^{(0)}) - \langle \frac{\partial \eta_i}{\partial x_i} \rangle \dot{p}^{(0)}. \tag{2.2.56}$$

Also this equation can be solved, once we know $\boldsymbol{\chi}$ and $\boldsymbol{\eta}$.

Momentum equation for the effective flow In order to obtain a momentum equation for the fluid phase we consider the problem formed by (2.2.22), (2.2.25), the boundary condition (2.2.29) plus periodicity over V. This problem can be viewed as a Stokes problem for $\mathbf{u}^{(0)}$ and $p^{(1)}$ forced by $p^{(0)}$ and $\dot{\mathbf{v}}^{(0)}$, so that the most general solution can be written as

$$u_i^{(0)} = -K_{ij} \frac{\partial p^{(0)}}{\partial x_j'} + H_{ij} \dot{v}_j^{(0)} \quad \text{and} \quad p^{(1)} = -A_j \frac{\partial p^{(0)}}{\partial x_j'} + B_j \dot{v}_j^{(0)}. \tag{2.2.57}$$

Substituting this form of the solution in equations (2.2.22), (2.2.25), (2.2.29) we obtain

$$\frac{\partial H_{ij}}{\partial x_i}\dot{v}_j^{(0)} = \frac{\partial K_{ij}}{\partial x_i}\frac{\partial p^{(0)}}{\partial x_j}, \tag{2.2.58}$$

$$\left(\frac{\partial B_j}{\partial x_i} - \frac{\partial^2 H_{ij}}{\partial x_k \partial x_k}\right)\dot{v}_j^{(0)} = \left(\frac{\partial A_j}{\partial x_i} - \delta_{ij} - \frac{\partial K_{ij}}{\partial x_k \partial x_k}\right)\frac{\partial p^{(0)}}{\partial x'_j}, \tag{2.2.59}$$

and

$$(H_{ij} - \delta_{ij})\,\dot{v}_j^{(0)} = K_{ij}\frac{\partial p^{(0)}}{\partial x'_j} \quad \text{on } \Gamma. \tag{2.2.60}$$

A solution of this problem can be found imposing the left-hand-side and the right-hand-side of equations (2.2.58) and (2.2.59) to vanish. Then, simplifying by $\dot{v}_j^{(0)}$ or $\partial p^{(0)}/\partial x_j$ the equations obtained, we find two different problems which must be solved in the unit cell:

$$\frac{\partial A_j}{\partial x_i} - \frac{\partial K_{ij}}{\partial x_k \partial x_k} = \delta_{ij}, \quad \frac{\partial K_{ij}}{\partial x_i} = 0, \quad K_{ij} = 0 \quad \text{on } \Gamma, \tag{2.2.61}$$

and

$$\frac{\partial B_j}{\partial x_i} - \frac{\partial H_{ij}}{\partial x_k \partial x_k} = 0, \quad \frac{\partial H_{ij}}{\partial x_i} = 0, \quad H_{ij} = \delta_{ij} \quad \text{on } \Gamma. \tag{2.2.62}$$

In order to guarantee the unicity of the solution, since only the gradient of A_j and B_j appears in equations (2.2.61), (2.2.62), we impose $\langle A_j \rangle = 0$ and $\langle B_j \rangle = 0$. Finally, we consider the volume average of equations (2.2.57) obtaining the macroscopic governing equation for the fluid phase

$$\langle u_i^{(0)} \rangle - \mathcal{H}_{ij}\dot{v}_j^{(0)} = -\mathcal{K}_{ij}\frac{\partial p^{(0)}}{\partial x'_j}, \tag{2.2.63}$$

$$\langle p^{(1)} \rangle = -\mathcal{A}_j\frac{\partial p^{(0)}}{\partial x'_j} + \mathcal{B}_j\dot{v}_j^{(0)}. \tag{2.2.64}$$

Equation (2.2.63) can be viewed as a Darcy's law for the unknown $\langle u_i^{(0)} \rangle - \mathcal{H}_{ij}\dot{v}_j^{(0)}$.

2.2.2 Finite Reynolds number

For $\mathrm{Re} = \mathcal{O}(1)$ the equations to solve are different. In this case, after substituting the expansion in ϵ in the governing equations (2.2.16) and (2.2.18), the new set of equations for each order of ϵ is composed by equations (2.2.22) to (2.2.33)

where equation (2.2.25) is substituted by (4.2.1). The development of the effective equations remains unaltered up to eq. (2.2.53) which must be replaced by

$$\langle\frac{\partial^2 v_i^{(0)}}{\partial t_s^2}\rangle + \mathrm{Re}\bar{U}_j\langle\frac{\partial u_i^{(0)}}{\partial x_j}\rangle = \langle\frac{\partial T_{ij}^{(0)}}{\partial x_j'}\rangle + \langle\frac{\partial \Sigma_{ij}^{(1)}}{\partial x_j}\rangle + \langle\frac{\partial \sigma_{ij}^{(2)}}{\partial x_j}\rangle, \tag{2.2.65}$$

so that the new effective equation for the solid structure is

$$(1-\vartheta)\frac{\partial^2 v_i^{(0)}}{\partial t_s^2} + \mathrm{Re}\bar{U}_j\langle\frac{\partial u_i^{(0)}}{\partial x_j}\rangle = \frac{\partial}{\partial x_j'}\left[\mathcal{C}_{ijpq}\varepsilon_{pq}'(\mathbf{v}^{(0)}) - \alpha_{ij}' p^{(0)}\right]. \tag{2.2.66}$$

In the same way we obtain equation (2.2.56) which represents the effective continuity equation for the composite. Focusing now on the development of Darcy's law for the effective velocity, we consider the problem formed by (2.2.22), (4.2.1), boundary condition (2.2.29) plus periodicity over V. After averaging, we obtain that the effective equations for $u_i^{(0)}$ are exactly (2.2.63) and (2.2.64) where $\mathcal{H}_{ij}$ and $\mathcal{B}_i$ are the solution of the same system as in the $\mathrm{Re} = \mathcal{O}(\epsilon)$ case, and $\mathcal{K}_{ij}$ and $\mathcal{A}_i$ are the solution of a system formed by (4.2.1) and (2.1.41).

2.3 Three-scale approach for rigid porous media

In consideration of the peculiarity of our porous medium we can also perform a three-scale analysis. In addition to the microscale l and the macroscale L defined before, we introduce a mesoscale h which is a characteristic distance along the longitudinal axis of the filaments. The order relation among these three scales are:

$$\frac{l}{h} = \mathcal{O}(\epsilon), \quad \frac{h}{L} = \mathcal{O}(\epsilon), \quad \Rightarrow \frac{l}{L} = \mathcal{O}(\epsilon^2). \tag{2.3.1}$$

We thus introduce a new elementary cell, shown in Fig. 2.2. The velocity and pressure fields are governed by equations (2.1.1) and (2.1.2). In the previous case we had that the velocity and pressure field were V-periodic; in this case, instead, we can only impose periodicity along the x_1 and x_2 directions. In the x_3 direction the condition needed are

$$\hat{u}_i(x_1, x_2, 0, t) = 0 \text{ and } \hat{u}_i(x_1, x_2, h, t) = U_i^h \tag{2.3.2}$$

where U_i^h is the velocity in the pure fluid region (unknown a priori).

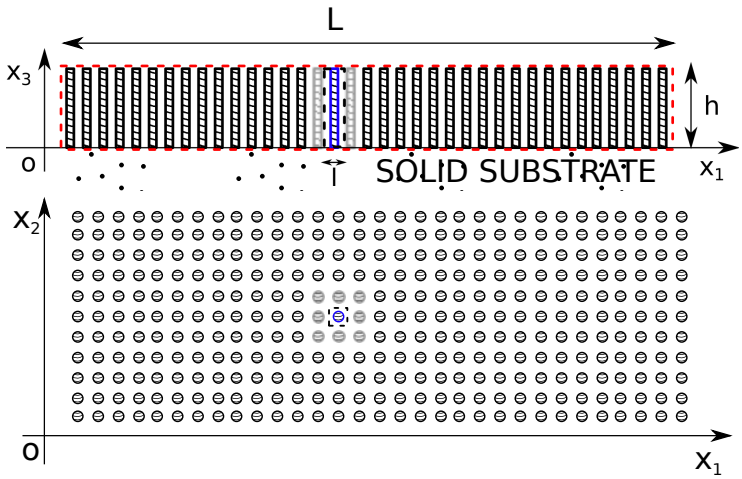

Figure 2.2: View of the particular porous medium, made by fibers shown in the (x_1, x_3) and (x_1, x_2) plane, respectively, for which a three-scale study is suitable. The dotted rectangle in the two frames represents the elementary cell. Notations are the same as in the two-scale approach.

As in the previous case, under the hypothesis that the global pressure gradient is balanced by the local viscous term, the pressure scale is found by equation (2.1.3). The dimensionless variables are related to the dimensional ones by:

$$\hat{x}_i = l x_i \quad \text{for } i = 1, 2 \quad \hat{x}_3 = h x_3 \quad \hat{t} = \frac{l}{U} t$$

$$\hat{u}_i = U u_i \quad \text{for } i = 1, 2 \quad \text{and } \hat{u}_3 = \epsilon U u_3$$

Considering these normalizations, we observe that two scales define the pressure gradient, i.e.

$$\frac{\partial \hat{p}}{\partial \hat{x}_i} = \frac{\mu U L}{l^3} \frac{\partial p}{\partial x_i} \quad \text{for } i = 1, 2 \quad \text{and} \quad \frac{\partial \hat{p}}{\partial \hat{x}_3} = \frac{\mu U L}{l^2 h} \frac{\partial p}{\partial x_3} = \epsilon \frac{\mu U L}{l^3} \frac{\partial p}{\partial x_3}.$$

Substituting in the governing equations we obtain

$$\frac{U}{l} \frac{\partial u_i}{\partial x_i} + \frac{\epsilon U}{h} \frac{\partial u_3}{\partial x_3} = 0 \quad \text{for } i = 1, 2, \tag{2.3.3}$$

$$\rho\left(\frac{U^2}{l}\frac{\partial u_i}{\partial t}+\frac{U^2}{l}u_j\frac{\partial u_i}{\partial x_j}+\frac{\epsilon U^2}{h}u_3\frac{\partial u_i}{\partial x_3}\right)= \tag{2.3.4}$$
$$=-\frac{\mu UL}{l^3}\frac{\partial p}{\partial x_i}+\frac{\mu U}{l^2}\frac{\partial^2 u_i}{\partial x_j^2}+\frac{\mu U}{h^2}\frac{\partial^2 u_i}{\partial x_3^2}\quad \text{for } i,j=1,2$$

$$\rho\left(\frac{\epsilon U^2}{l}\frac{\partial u_3}{\partial t}+\frac{\epsilon U^2}{l}u_j\frac{\partial u_3}{\partial x_j}+\frac{\epsilon^2 U^2}{h}u_3\frac{\partial u_3}{\partial x_3}\right)= \tag{2.3.5}$$
$$=-\epsilon\frac{\mu UL}{l^3}\frac{\partial p}{\partial x_3}+\epsilon\frac{\mu U}{l^2}\frac{\partial^2 u_3}{\partial x_j^2}+\epsilon\frac{\mu U}{h^2}\frac{\partial^2 u_3}{\partial x_3^2}\quad \text{for } j=1,2$$

Defining the Reynolds number in the usual way and multiplying equations (2.3.4) and (2.3.5) by $l/\rho U^2$ and $l/\epsilon\rho U^2$, respectively, the normalized momentum equation is

$$\frac{\partial u_i}{\partial t}+u_j\frac{\partial u_i}{\partial x_j}+\epsilon^2 u_3\frac{\partial u_i}{\partial x_3}= \tag{2.3.6}$$
$$=-\frac{1}{\epsilon^2\text{Re}}\frac{\partial p}{\partial x_i}+\frac{1}{\text{Re}}\frac{\partial^2 u_i}{\partial x_j^2}+\epsilon^2\frac{1}{\text{Re}}\frac{\partial^2 u_i}{\partial x_3^2}\quad \text{for } j=1,2 \text{ and } i=1,2,3.$$

The continuity equation becomes

$$\frac{\partial u_i}{\partial x_i}+\epsilon^2\frac{\partial u_3}{\partial x_3}=0\quad \text{for } i=1,2. \tag{2.3.7}$$

As in the two-scale analysis we consider two possibilities for the Reynolds number:

$$\text{Re}=\mathcal{O}(\epsilon)\quad \text{and}\quad \text{Re}=\mathcal{O}(1).$$

2.3.1 Small Reynolds numbers

If we choose $\text{Re}=\mathcal{O}(\epsilon)$ the momentum equation can be rewritten as

$$\epsilon^3\left(\frac{\partial u_i}{\partial t}+u_j\frac{\partial u_i}{\partial x_j}+\epsilon^2 u_3\frac{\partial u_i}{\partial x_3}\right)= \tag{2.3.8}$$
$$=-\frac{1}{\text{Re}^*}\frac{\partial p}{\partial x_i}+\epsilon^2\frac{1}{\text{Re}^*}\frac{\partial^2 u_i}{\partial x_j^2}+\epsilon^4\frac{1}{\text{Re}^*}\frac{\partial^2 u_i}{\partial x_3^2}\quad \text{for } j=1,2 \text{ and } i=1,2,3,$$

where $\text{Re}^*=\mathcal{O}(1)$. The continuity equation remains unchanged. We introduce the microscopic variables (x_1,x_2) in the x_1- and x_2-directions, the mesoscopic

variable $x_3' = \epsilon x_3$ in the x_3-direction, the macroscopic variables $(x_1'', x_2'', x_3'') = \epsilon^2(x_1, x_2, 0)$ and the expansions

$$\mathbf{u} = \mathbf{u}^{(0)} + \epsilon \mathbf{u}^{(1)} + \ldots, \quad p = p^{(0)} + \epsilon p^{(1)} + \ldots \tag{2.3.9}$$

where $\mathbf{u}^{(i)}$ and $\mathbf{p}^{(i)}$ are functions of $(x_1, x_2, x_3', x_1'', x_2'', t)$. The derivative operators assume the following form

$$\frac{\partial}{\partial x_i} \to \frac{\partial}{\partial x_i} + \epsilon^2 \frac{\partial}{\partial x_i''} \quad \text{for } i = 1, 2 \tag{2.3.10}$$

$$\frac{\partial}{\partial x_3} \to \epsilon \frac{\partial}{\partial x_3'}, \tag{2.3.11}$$

and

$$\frac{\partial^2}{\partial x_i \partial x_i} \to \frac{\partial^2}{\partial x_i \partial x_i} + 2\epsilon^2 \frac{\partial^2}{\partial x_i \partial x_i''} + \epsilon^4 \frac{\partial^2}{\partial x_i'' \partial x_i''} \quad \text{for } i = 1, 2, \tag{2.3.12}$$

$$\frac{\partial^2}{\partial x_3 \partial x_3} \to \epsilon^2 \frac{\partial^2}{\partial x_3' \partial x_3'}. \tag{2.3.13}$$

Substituting all these expansions in the governing equations and collecting like-order terms, we obtain at $\mathcal{O}(\epsilon^0)$

$$u_i^{(0)} = 0 \text{ on } \Gamma \tag{2.3.14}$$

$$\frac{\partial u_i^{(0)}}{\partial x_i} = 0 \quad \text{for } i = 1, 2, \tag{2.3.15}$$

$$\frac{\partial p^{(0)}}{\partial x_i} = 0 \quad \text{for } i = 1, 2, \tag{2.3.16}$$

at $\mathcal{O}(\epsilon)$

$$\frac{\partial p^{(1)}}{\partial x_i} = 0 \quad \text{for } i = 1, 2 \quad \text{and } \frac{\partial p^{(0)}}{\partial x_3'} = 0, \tag{2.3.17}$$

and at $\mathcal{O}(\epsilon^2)$

$$0 = -\frac{\partial p^{(0)}}{\partial x_i''} - \frac{\partial p^{(2)}}{\partial x_i} + \frac{\partial^2 u_i^{(0)}}{\partial x_j^2} \text{ for } i, j = 1, 2, \tag{2.3.18}$$

$$0 = -\frac{\partial p^{(1)}}{\partial x_3'} + \frac{\partial^2 u_3^{(0)}}{\partial x_j^2} \text{ for } j = 1, 2. \tag{2.3.19}$$

Equations (2.3.16) and (2.3.17) imply that $p^{(0)} = p^{(0)}(\mathbf{x}'')$ (the leading order pressure term depends only on macroscale) and

$$p^{(1)} = p^{(1)}(x_3', x_1'', x_2'') \tag{2.3.20}$$

(the order ϵ term of the pressure does not depends on the microscale). Equation (2.3.19) is linear for $u_3^{(0)}$, forced by $\partial p^{(1)}/\partial x_3'$. By linearity we can write the solution as

$$u_3^{(0)} = -K_{33}\frac{\partial p^{(1)}}{\partial x_3'}. \tag{2.3.21}$$

Substituting (2.3.21) in (2.3.14) and (2.3.19) we obtain the equations for K_{33}:

$$\frac{\partial K_{33}}{\partial x_1^2} + \frac{\partial K_{33}}{\partial x_2^2} = -1. \tag{2.3.22}$$

$$K_{33} = 0 \text{ on } \Gamma. \tag{2.3.23}$$

In the same way we can conclude that the solution of equations (2.3.18) can be written as

$$u_i^{(0)} = -K_{ij}\frac{\partial p^{(0)}}{\partial x_j''} \text{ for } i,j = 1,2 \tag{2.3.24}$$

and

$$p^{(2)} = -A_j\frac{\partial p^{(0)}}{\partial x_j''} + p_0^{(2)} \text{ for } j = 1,2, \tag{2.3.25}$$

where $p_0^{(2)}$ is constant with respect to $x_j,\ j = 1,2$. The equations which must be satisfied by K_{ij}, A_j are obtained by substituting (2.3.24) and (2.3.25) in (2.3.18), (2.3.15) and (2.3.14), i.e.

$$\frac{\partial A_j}{\partial x_i} - \frac{\partial^2 K_{ij}}{\partial x_k^2} = \delta_{ij} \text{ for } i,j,k = 1,2, \tag{2.3.26}$$

$$\frac{\partial K_{ij}}{\partial x_j} = 0 \text{ for } i,j = 1,2, \tag{2.3.27}$$

$$K_{ij} = 0 \text{ on } \Gamma \text{ for } i,j = 1,2. \tag{2.3.28}$$

In order to find the equations for the velocity field at the macroscale we define the following averaging

$$\langle f \rangle_{\mathscr{P}} = \frac{1}{A}\int_{\mathscr{P}(V_f)} f dA \tag{2.3.29}$$

where $\mathscr{P}(V_f)$ is the projection of V_f over the (x_1, x_2)-plane so that $dA = dx_1 dx_2$ and A is the area of $\mathscr{P}(V_f)$. Summing up we have the following seven unknowns

$$K = \begin{pmatrix} k_{11} & k_{12} & 0 \\ k_{21} & k_{22} & 0 \\ 0 & 0 & k_{33} \end{pmatrix} \text{ and } A = \begin{pmatrix} A_1 & A_2 & 0 \end{pmatrix} \tag{2.3.30}$$

which can be found solving the problem defined over the projection of the elementary cell V over the (x_1, x_2) plane

$$\begin{cases} \dfrac{\partial A_j}{\partial x_i} - \dfrac{\partial^2 K_{ij}}{\partial x_1^2} - \dfrac{\partial^2 K_{ij}}{\partial x_2^2} = \delta_{ij} \\ \dfrac{\partial K_{i1}}{\partial x_1} + \dfrac{\partial K_{i2}}{\partial x_2} = 0 \\ K_{ij} = 0 \text{ on } \Gamma \\ K_{ij}, A_j \ (x_1, x_2)\text{-periodic} \end{cases} \tag{2.3.31}$$

for the unknowns K_{ij}, A_j, $i, j = 1, 2$. K_{33}, instead, can be found solving the following problem over the whole cell V

$$\begin{cases} \dfrac{\partial K_{33}}{\partial x_1^2} + \dfrac{\partial K_{33}}{\partial x_2^2} = -1 \\ K_{33} = 0 \text{ on } \Gamma \\ K_{33} \ (x_1, x_2)\text{-periodic} \end{cases} \tag{2.3.32}$$

Once we have found all the coefficients, after averaging (2.3.21) and (2.3.24), the equations for the velocity field at the macroscale read

$$\langle u_3^{(0)} \rangle_{\mathscr{P}} = -\langle K_{33} \rangle_{\mathscr{P}} \frac{\partial p^{(1)}}{\partial x_3'}; \quad \langle u_i^{(0)} \rangle_{\mathscr{P}} = -\langle K_{ij} \rangle_{\mathscr{P}} \frac{\partial p^{(0)}}{\partial x_j''} \tag{2.3.33}$$

since $\partial p^{(0)} / \partial x_j''$ does not depend on the variables of integration in the definition of $\langle \cdot \rangle_{\mathscr{P}}$. Equations (2.3.33) are mesoscopic. To obtain the macroscopic equations we have to consider the average with respect to the mesoscopic variable x_3' defined as

$$\langle \cdot \rangle_3 = \int_0^{1/\epsilon} \cdot \, dx_3' \tag{2.3.34}$$

where x_3' varies between 0 and $1/\epsilon$ since we are considering problems over a unitary square. The resulting equations are

$$\langle \langle u_3^{(0)} \rangle_{\mathscr{P}} \rangle_3 = -\langle \langle K_{33} \rangle_{\mathscr{P}} \frac{\partial p^{(1)}}{\partial x_3'} \rangle_3, \quad \langle \langle u_i^{(0)} \rangle_{\mathscr{P}} \rangle_3 = -\langle K_{ij} \rangle_{\mathscr{P}} \frac{\partial p^{(0)}}{\partial x_j''} \tag{2.3.35}$$

which macroscopically are defined only for a fixed x_3'' (indeed, as already noted, the macroscopic variable in the third direction is not defined, and this means precisely that the porous medium is macroscopically confined in that direction). This last fact is equivalent to stating that, in a fluid-structure interaction problem, the presence of a porous medium, can be written as a modified boundary condition at a fixed x_3.

2.3.2 Finite Reynolds numbers

If we choose $\mathrm{Re} = \mathcal{O}(1)$ the dimensionless governing equations are

$$\frac{\partial u_i}{\partial t} + u_j \frac{\partial u_i}{\partial x_j} + \epsilon^2 u_3 \frac{\partial u_i}{\partial x_3} =$$

$$= -\frac{1}{\epsilon^2 \mathrm{Re}} \frac{\partial p}{\partial x_i} + \frac{1}{\mathrm{Re}} \frac{\partial^2 u_i}{\partial x_j^2} + \epsilon^2 \frac{1}{\mathrm{Re}} \frac{\partial^2 u_i}{\partial x_3^2} \quad \text{for } j = 1, 2 \text{ and } i = 1, 2, 3,$$

and

$$\frac{\partial u_i}{\partial x_i} + \epsilon^2 \frac{\partial u_3}{\partial x_3} = 0 \quad \text{for } i = 1, 2.$$

The procedure is the same as in the small Re case; collecting like-order terms in ϵ, equations found previously at $\mathcal{O}(\epsilon^0)$ and $\mathcal{O}(\epsilon)$ still hold, but at $\mathcal{O}(\epsilon^2)$ we obtain

$$\frac{\partial u_i^{(0)}}{\partial t} + u_j^{(0)} \frac{\partial u_i^{(0)}}{\partial x_j} = -\frac{1}{\mathrm{Re}} \left(\frac{\partial p^{(0)}}{\partial x_i''} + \frac{\partial p^{(2)}}{\partial x_i} \right) + \frac{1}{\mathrm{Re}} \frac{\partial^2 u_i^{(0)}}{\partial x_j^2} \text{ for } i, j = 1, 2, \tag{2.3.36}$$

$$\frac{\partial u_3^{(0)}}{\partial t} + u_j^{(0)} \frac{\partial u_3^{(0)}}{\partial x_j} = -\frac{1}{\mathrm{Re}} \frac{\partial p^{(1)}}{\partial x_3'} + \frac{1}{\mathrm{Re}} \frac{\partial^2 u_3^{(0)}}{\partial x_j^2} \text{ for } j = 1, 2. \tag{2.3.37}$$

instead of equations (2.3.18) and (2.3.19). As before, $p^{(0)} = p^{(0)}(x_1'', x_2'')$ and $p^{(1)} = p^{(1)}(x_3', x_1'', x_2'')$. Before solving equations (2.3.36) and (2.3.37), they must be linearized using the definition (2.1.37). Once the equations are linearized, the solution of (2.3.36) and (2.3.37) can be written as in equations (2.3.24), (2.3.25) and (2.3.21), respectively. However, the tensor $\mathbf{K}$ satisfies the following systems

$$\begin{cases} \mathrm{Re} U_l \dfrac{\partial K_{ij}}{\partial x_l} + \dfrac{\partial A_j}{\partial x_i} - \dfrac{\partial^2 K_{ij}}{\partial x_1^2} - \dfrac{\partial^2 K_{ij}}{\partial x_2^2} = \delta_{ij} \\ \dfrac{\partial K_{i1}}{\partial x_1} + \dfrac{\partial K_{i2}}{\partial x_2} = 0 \\ K_{ij} = 0 \text{ on } \Gamma \\ K_{ij}, A_j \ (x_1, x_2)\text{-periodic} \end{cases} \tag{2.3.38}$$

for the unknowns K_{ij}, A_j, $i, j, l = 1, 2$. K_{33}, instead, can be found solving the following problem over the whole cell V

$$\begin{cases} -\mathrm{Re}U_j \dfrac{\partial K_{33}}{\partial x_j} + \dfrac{\partial K_{33}}{\partial x_1^2} + \dfrac{\partial K_{33}}{\partial x_2^2} = -1 \\ K_{33} = 0 \text{ on } \Gamma \\ K_{33} \ (x_1, x_2)\text{-periodic} \end{cases} \tag{2.3.39}$$

with $j = 1, 2$. The macroscopic equations can be deduced as in the small Re case (equations 2.3.35).

Chapter 3

Treatment of heterogeneities

As already noted in chapter 1, our goal is to develop a model for a fluid flow which interacts with porous and elastic structures. In order for our work to have some relevance in real physical applications, we have to be able to deal with sudden changes in the physical characteristics of the domain over which we solve. This is the case, for instance, of macroscopic boundaries in the porous medium, beyond which there are zero-permeability zones (walls) or fully permeable regions (pure fluid). It must be pointed out that all of these occurences should be treated with the homogenization technique with great care, since the fundamental hypothesis in homogenization is that we are dealing with infinite domains in order to identify some sort of micro–periodicity in the structure. Thus, different sets of equations must be solved over different domains neighboring, for example, a region of different physical properties. These same equations should be coupled with interface conditions valid at the intersections of the domains. NSE hold in the pure fluid region, while in the porous region the macroscopic equations developed in the previous chapter are assumed to be valid.

In this chapter we show the basis of the *domain decomposition method*, highlighting how these interface conditions are treated. Then we present a different normalization of the macroscopic equations in order to make them comparable with NSE. Eventually, we introduce the interface conditions used to couple the two sets of equations in the rigid case. Several interface conditions are present in the literature and a recent review can be found in Carraro *et al.* (2013). They can be essentially classified in three classes: the first one involves pressure and velocities which are

linked over the interface directly (continuity or jump); the second one involves them indirectly, linking the normal to the interface components of the stress tensor. The second class cannot be employed if the equation to be solved in the porous medium is Darcy's law. The third class includes all those methods which use a filter to go from the porous region to the fluid region; a drawback of this latter approach is that there is no general physical justification for the choice of the filter. We have tested the most representative of each class comparatively; all conditions contain a certain degree of arbitrariness (since they must account for the lack of homogenization) and require the *a posteriori* calibration of one or more parameters.

For clarity, we denote in the following with $\cdot|_F$ the unknown fields in the pure fluid region, and with $\cdot|_P$ the unknown fields in the porous medium, as sketched in figure 3.2.

Whereas the microscopic fluid-structure interface Γ has a physical counterpart and it is unequivocally defined by the microscopic structure of the porous medium, the interface related to the boundaries of a porous medium (which has a pointwise or local characterization if we use a macroscopic or mesoscopic approach, respectively, as already explained in section 1.2.1) is an idealization which does not have a physical counterpart and its introduction is necessary if we want to observe the phenomenon from both the points of view just cited. To formalize its definition we restrict our macroscopic problems on a plane, so that the interface is a curve. The coordinates of this curve on a plane are $\mathbf{x}_{ITF}(\gamma)$ where γ is the curvilinear abscissa which parametrizes the curve. The subsequent question is: how can we identify this curve? The answer cannot be formalized for every structure, but in general one should consider a smooth line which overlies the portions of Γ, whose normal unit vector points outside the porous medium. This definition is visualized in figure 3.1. Similarly, the interfacial region (highlighted in figure 3.1) can be realized as an offset of the pointwise interface, of width a priori unknown.

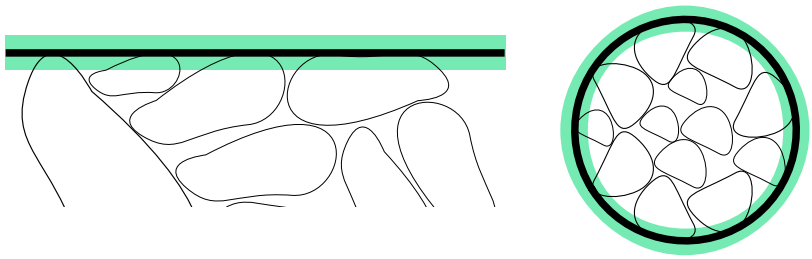

Figure 3.1: The solid thick lines represent the microscopic pointwise interface defined as before; the highlighted regions, instead, are the local macroscopic interfaces (or interfacial zones).

3.1 Heterogeneous domain decomposition method

In order to make immediately clear why we have written about interface conditions and coupling sets of equations, we briefly show the idea of domain decomposition method. In terms of differential problems we want to solve two different boundary value problems over two disjoined neighboring domains Ω_F and Ω_P such that $\Omega_F \cap \Omega_P = \Gamma_{FP}$ as represented in figure 3.2. We denote with g_F and g_P the families of unknowns which live on Ω_F and Ω_P, respectively. Using these notations from the macroscopic fluid-structure interaction problem the following system of equations arises:

$$\begin{cases} L_F g_F = f_F & \text{over } \Omega_F, \\ L_P g_P = f_P & \text{over } \Omega_P, \\ \Phi_F(g_F) = h_F & \text{over } \partial\Omega_F \backslash \Gamma_{FP}, \\ \Phi_P(g_P) = h_P & \text{over } \partial\Omega_P \backslash \Gamma_{FP}, \\ \Psi_F(g_F) = \Psi_P(g_P) & \text{over } \Gamma_{FP}, \\ \Xi_P(g_P) = \Xi_F(g_F) & \text{over } \Gamma_{FP}, \end{cases} \tag{3.1.1}$$

where f_F and f_P are the knowns terms, Φ_F and Φ_P, h_F and h_P are the boundary conditions and Ψ_F, Ψ_P and Ξ_F, Ξ_P are the exchange conditions related to the respective problems F and P. We note that in order to have two well posed boundary values problems, two exchange conditions are needed, one for the F-problem and

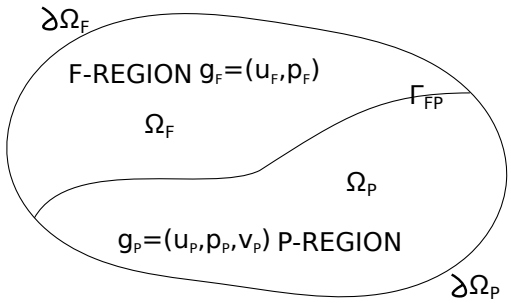

Figure 3.2: Sketch of a generic domain over which the domain decomposition method is applied. In each region we have a different solution.

one for the P-problem. For an in-depth analysis we refer to Quarteroni & Valli (1999).

3.2 Macroscopic and pointwise equations

In each region of the domain constituted only by the fluid phase (Ω_F), the NSE are valid. They have been non-dimensionalized on the basis of a macroscopic Reynolds number $\mathrm{Re}_{\mathcal{L}}$ defined as

$$\mathrm{Re}_{\mathcal{L}} = \frac{\rho U \mathcal{L}}{\mu}, \tag{3.2.1}$$

where a priori $\mathcal{L}$ is not necessarily equal to L, is the macroscopic length used in the homogenization method. With this choice we call $\mathbf{X}$ the long-scale spatial variable and $\delta = l/\mathcal{L}$ the characteristic small parameter of the elementary cell with the new normalization. For simplicity, from this point on, we assume that $\mathcal{L} = L$, $\delta = \epsilon$ and $\mathbf{X} = \mathbf{x}'$ (for the two-scale approach, or $\mathbf{X} = \mathbf{x}''$ for the three-scale approach). Moreover, we note that the microscopic problems introduced in chapter 2 are referred to the microscopic domain and deduced using a different Reynolds number, based on the length l. The relation between the two Reynolds numbers is

$$\mathrm{Re} = \epsilon \mathrm{Re}_L;$$

we now have to normalize the microscopic domain using the following transformation:

$$\mathbf{X} = \epsilon \mathbf{x}$$

i.e., if the microscopic variable in the $L-$normalization varies in $[0,\epsilon]^3$ then $\mathbf{x}$ varies in $[0,1]^3$, so that K_{ij} and A_j are dimensionless variables computed on the unitary cube (or on the unitary square in the case of three scales). We underline here that only the order zero terms are considered in our homogenization technique, i.e. $\mathbf{u} = \mathbf{u}^{(0)}$. For this reason we can compare the effective equations, deduced in chapter 2, with the pointwise NSE and, to not confuse the reader, we omit the brackets and the superscript (0) in the effective equations, with the understanding that each time that we encounter an unknown denoted by $\cdot|_P$, it is the solution of the homogenized governing equations.

Darcy's equation The second normalization stems from the need to couple Darcy's equation with the NSE. The dimensional Darcy's equation is

$$\hat{u}_i = -\frac{\hat{\mathcal{K}}_{ij}}{\mu}\frac{\partial \hat{p}}{\partial \hat{x}_j}; \tag{3.2.2}$$

to find the non-dimensional Darcy's law we consider the same normalization of the Navier-Stokes equation:

$$\hat{\mathbf{x}} = L\mathbf{x}, \quad \hat{p} = \rho U^2 p, \quad \hat{\mathbf{u}} = U\mathbf{u}. \tag{3.2.3}$$

Writing Darcy's law in non-dimensional form we get

$$u_i = -\mathrm{Re}_L \frac{\hat{\mathcal{K}}_{ij}}{L^2}\frac{\partial p}{\partial x_j}, \tag{3.2.4}$$

which can be written as

$$u_i = -\epsilon^2 \mathrm{Re}_L \frac{\hat{\mathcal{K}}_{ij}}{l^2}\frac{\partial p}{\partial x_j} = -\epsilon^2 \mathrm{Re}_L \mathcal{K}_{ij}\frac{\partial p}{\partial x_j}. \tag{3.2.5}$$

We note that $\hat{\mathcal{K}}_{ij}/l^2$ is the non-dimensional permeability tensor, normalized by l^2, i.e. the permeability tensor found via homogenization ($\mathcal{K}_{ij}$ in eq. (2.1.17)).

Brinkman's equation We consider here also Brinkman's equation, which has not been introduced up to now. This equation can be obtained from homogenization theory (cf. Mei & Vernescu (2010)), adopting slightly different normalizations of the starting equations, on the assumption that the fibers are sufficiently sparse. The dimensional form of this equation is

$$\hat{u}_i = -\frac{\hat{\mathcal{K}}_{ij}}{\mu}\frac{\partial \hat{p}}{\partial \hat{x}_j} + \frac{\hat{\mathcal{K}}_{ij}}{\mu}\mu_e \frac{\partial^2 \hat{u}_j}{\partial \hat{x}_k^2},$$

where μ_e is an effective viscosity, a priori unknow (cf. Givler & Altobelli (1994)). Using the normalizations in equation (3.2.3), the non-dimensional form of the equation above is

$$u_i = -\mathcal{K}_{ij}\epsilon^2 \mathrm{Re}_L \frac{\partial p}{\partial x_j} + \mathcal{K}_{ij}\epsilon^2 \frac{\mu_e}{\mu}\frac{\partial^2 u_j}{\partial x_k^2}. \tag{3.2.6}$$

Poroelastic equations We recall here the poroelastic equations:

$$\begin{cases} (1-\vartheta)\dfrac{\partial^2 v_i}{\partial t^2} = \dfrac{\partial}{\partial x'_j}\left[\mathcal{C}_{ijpq}\varepsilon'_{pq}(\mathbf{v}) - \alpha'_{ij}p\right], \\ \dfrac{\partial u_i}{\partial x'_i} = \langle \dfrac{\partial \chi_i^{pq}}{\partial x_i}\rangle \varepsilon'_{pq}(\dot{\mathbf{v}}) - \langle \dfrac{\partial \eta_i}{\partial x_i}\rangle \dot{p}, \\ u_i - \mathcal{H}_{ij}\dot{v}_j = -\mathcal{K}_{ij}\dfrac{\partial p}{\partial x'_j}. \end{cases} \tag{3.2.7}$$

In this case we choose the normalization employed in the homogenization technique to couple (3.2.7) with NSE, which read as in equation (2.2.16), i.e.

$$\epsilon \mathrm{Re}\left(\frac{\partial u_i}{\partial t_f} + u_j\frac{\partial u_i}{\partial x_j}\right) = -\frac{\partial p}{\partial x_i} + 2\epsilon\frac{\partial \varepsilon_{ij}(\mathbf{u})}{\partial x_j}. \tag{3.2.8}$$

3.3 First approach: the fictitious interface condition

The first interface condition is suitable when we want to couple the Darcy's law with the NSE; it consists of imposing

$$p|_P = p|_F + constant \tag{3.3.1}$$

at a fictitious interface positioned a small distance δ, which we call *penetration depth*, below the physical interface, in order to transfer information from the fluid region to the porous region. The presence of the constant term has no influence on the solution of Darcy's equation, since the pressure is always specified (both in P and F) up to an arbitrary constant; the *constant* is however maintained, at least formally, in (3.3.1) to highlight the fact that pressure may be non-continuous across the interface. More specifically, a pressure jump has been predicted by Marciniak-Czochra & Mikelić (2012) and Carraro *et al.* (2013) when the porous medium is anisotropic or in the presence of flow inertia, and it varies along the interface direction. On the other hand, continuity of pressure across the interface, up to the order

of the pore size, was strongly advocated by Ene & Sánchez-Palencia (1975). To have adequate conditions for the Navier-Stokes equation, we use

$$u_i|_F = u_i|_P \,, \tag{3.3.2}$$

applied at the same fictitious interface as above. Here $u_i|_F$ is not averaged because it is the effective velocity, computed over a grid in which each point corresponds to a microscopic cell. Enforcing the continuity of both pressure and velocity *below* the real interface has been proposed and tested by Le Bars & Worster (2006), with the scope of accounting for inertia within the porous layer in the immediate vicinity of the fluid domain. Le Bars & Worster (2006) have shown that this is essentially equivalent to the interface condition by Beavers & Joseph (1967), which is applied at the physical interface, and have estimated the distance δ to vary as

$$\delta = c\sqrt{\frac{\mathcal{K}}{\vartheta}}, \tag{3.3.3}$$

where $\mathcal{K}$ represents the permeability (in their case a scalar since the medium is isotropic) and c is a constant to be determined ($c = 1$ in their work). By enforcing the conditions at δ, we are sufficiently far from the interface for the periodicity assumption of the theory to remain tenable.

3.4 Second approach: Brinkman–Navier–Stokes coupling at the interface

The second approach Kaviany (1995) consists in modifying Darcy's equation adding a viscous term through which we can impose continuity of the velocity and the tangential and normal components of the stress tensor over the interface. The resulting equation is Brinkman's equation (3.2.6). If μ_e were available we could impose the following conditions at the fluid-porous interface:

$$(\sigma_{ij}n_j)n_i|_F = (\sigma_{ij}n_j)n_i|_P \quad \text{and} \quad (\sigma_{ij}n_j)t_i|_F = (\sigma_{ij}n_j)t_i|_P \tag{3.4.1}$$

to transfer data from the fluid domain to the porous medium P ruled by Brinkman's equation, and

$$u_i|_F = u_i|_P \tag{3.4.2}$$

to go from the porous domain to the fluid domain. In equations (3.4.1), σ_{ij} is the stress tensor, n_i and t_i are, respectively, the unit vectors normal and tangent to the

interface. Such conditions can be written in the present case as

$$\left(\frac{\partial u_1}{\partial x_3}+\frac{\partial u_3}{\partial x_1}\right)\bigg|_F = \frac{\mu_e}{\mu}\left(\frac{\partial u_1}{\partial x_3}+\frac{\partial u_3}{\partial x_1}\right)\bigg|_P \tag{3.4.3}$$

and

$$\left(-p+\frac{2}{\mathrm{Re}_L}\frac{\partial u_3}{\partial x_3}\right)\bigg|_F = \left(-p+\frac{2\mu_e}{\mu\mathrm{Re}_L}\frac{\partial u_3}{\partial x_3}\right)\bigg|_P . \tag{3.4.4}$$

We note that the stress from the pure fluid region F is transmitted to the homogenized region P, and is distributed to both the inclusions (the fibers) ad the fluid contained within them.

3.5 Third approach: the apparent permeability near the interface

It is important to state the concept that the permeability is an apparent property of a porous skeleton (cf. Edwards *et al.* (1990); Breugem *et al.* (2004)), i.e. it does not depend only on the geometrical structure of the porous medium, but also on the flow regime inside it whenever we want to include (at least some) inertia. Up to a certain regime, the permeability can be assumed to be an intrinsic property; outside of this regime it depends mostly on the flow's properties (cf. figure 3.3). For this reason, if we look at the problem from a mesoscopic point of view the third interface condition used consists in applying the same strategy as in section 3.3 with $\delta = 0$, i.e. the matching is enforced precisely at the physical interface, but the permeability components are driven smoothly to a large absolute value near the interface, through a filter function which forces the permeability to vary rapidly over a distance of the order of ϵ. This strategy has been proposed by Chandesris & Jamet (2008) and Jamet & Chandesris (2009). The difficulties of imposing this condition arise during the estimation of the filter which allows the permeability to vary. Unfortunately there is no general law which describes the variation; if we have a numerical solution of a test case, the values of the permeability must be calibrated point by point (as shown for $\mathcal{K}_{11}$ in figure 3.4). This has been done in the hope of finding insight for the evaluation of the filter.

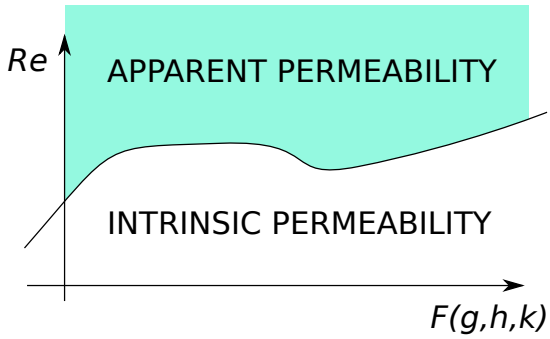

Figure 3.3: Intrinsic or apparent behavior of the permeability for varying regimes of the flow (expressed as function of Re) and the parameters g, h, k which represent some geometrical properties of the structure (e.g. porosity, shape of the solid inclusions or geometry of the macroscopic configuration).

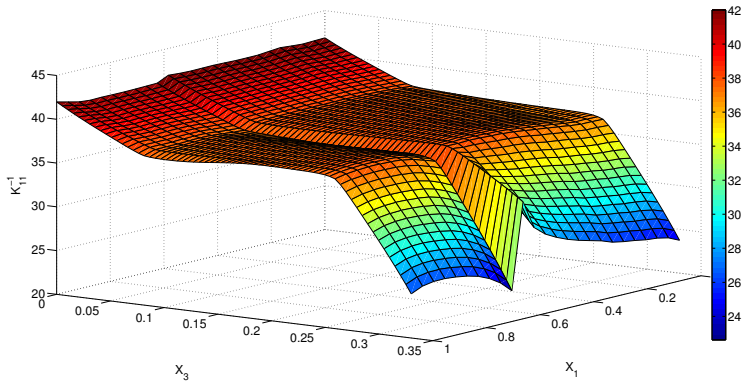

Figure 3.4: Inverse of the pointwise permeability $\mathcal{K}_{11}$ in a macroscopic region computed applying Darcy's law to the results of a direct numerical simulation *a posteriori*. The macroscopic configuration considered is described in chapter 5.

3.6 The equivalent boundary condition for the three-scale approach

If we apply a three-scale approach, in macroscopic terms, equation (2.3.35) reads as boundary condition because it holds only for a fixed x_3. In analogy with the conditions imposed in the first case presented in this chapter, we suppose that equation (3.3.1) is valid. Then, the horizontal velocity is deduced by equation (2.3.35), which is not dependent on x_3''. The slip horizontal velocity with the current notation reads

$$u_1|_F = -\mathcal{K}_{11}\left.\frac{\partial p}{\partial x_1}\right|_F . \tag{3.6.1}$$

Combining equation (3.6.1) with the continuity equation we obtain a second relation that can be used as an interface condition for u_3:

$$\left.\frac{\partial u_3}{\partial x_3}\right|_F = \mathcal{K}_{11}\left.\frac{\partial^2 p}{\partial x_1}\right|_F . \tag{3.6.2}$$

The hypotheses upon which this condition is applicable are essentially two:

- the porous medium has three characteristic length scales;
- the microscopic structure of the porous medium is isotropic or transversely isotropic, or, at least, $\mathcal{K}_{12} = 0$, otherwise the gradient of p in the vertical direction appears in the effective boundary condition (and this cannot be computed because the pressure inside the porous medium should be known).

Chapter 4

Microscopic results

As it can be evinced from chapter 2, there are two categories of equations, which lead us to different results, for the microscopic and macroscopic variables. The former category of results will be presented in the following chapter. Also in this case we divide the results on the basis of Table 2.1. The microscopic equations are solved over different domains, i.e. we have considered porous media with different periodic microstructures. The solid inclusions inside an elementary cell are represented in figure 5.42 These inclusions can be distinguished using the following classification:

- unconnected structures: detached spheres;
- partially connected structures (only in one direction): cylinders;
- totally connected structures (in all directions): touching spheres, linked cylinders.

Moreover, the same structures can be classified as isotropic (spheres, touching spheres) and transversely isotropic structures (cylinders, linked cylinders). The choice of the three categories listed above is not casual and, as we show in the present chapter, it causes fundamental differences in the effective tensors, making sometime unsuitable the homogenization technique. The microscopic tensors field computed over the unitary cubic cell, as noted in section 3.2, are presented. Then, special attention is devoted to the averaged fields, since only these values are used in the macroscopic governing equations for the flow and displacement. All the Cauchy's problems associated to the microscopic world are computed using OpenFOAM, an opensource

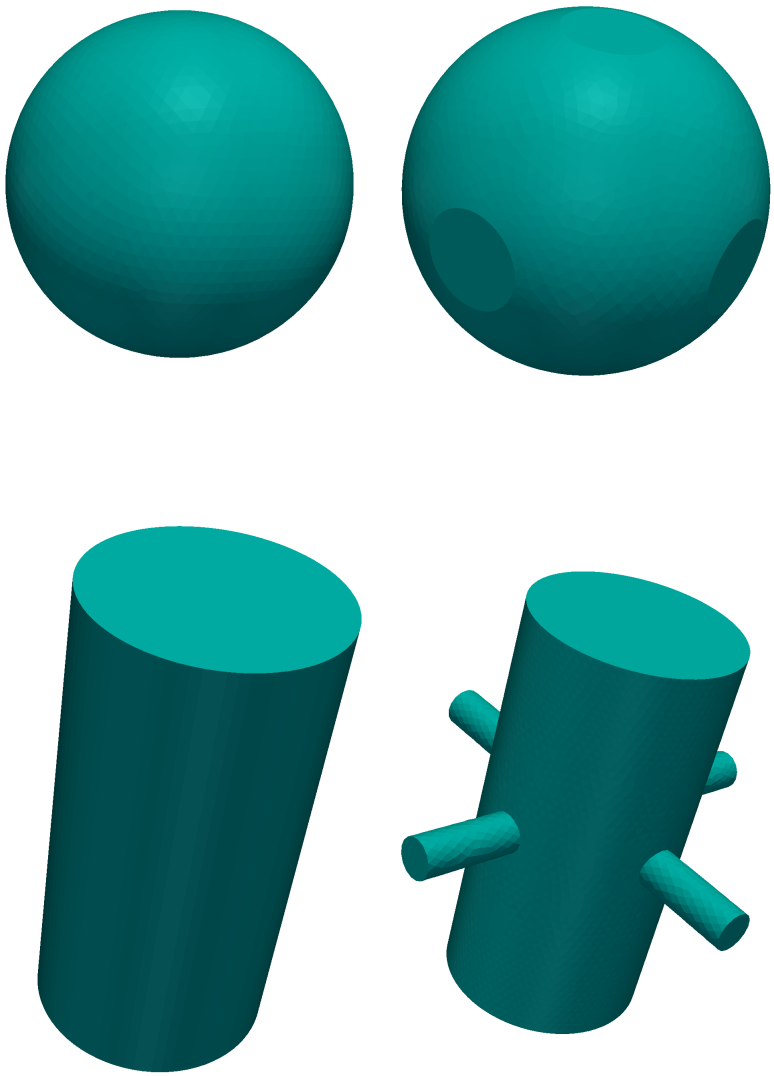

Figure 4.1: Four different solid inclusions which characterize the porous medium inside the elementary cell: spheres, touching spheres, cylinders and linked cylinders.

	radius of the sphere	radius of the cylinder
$\vartheta = 0.3$	0.5508	0.4720
$\vartheta = 0.35$	0.5374	0.4549
$\vartheta = 0.4$	0.5232	0.4370
$\vartheta = 0.45$	0.5083	0.4184
$\vartheta = 0.5$	0.4924	0.3989
$\vartheta = 0.55$	0.4754	0.3785
$\vartheta = 0.6$	0.4571	0.3568
$\vartheta = 0.65$	0.4372	0.3338
$\vartheta = 0.7$	0.4153	0.3090
$\vartheta = 0.75$	0.3908	0.2821
$\vartheta = 0.8$	0.3628	0.2523
$\vartheta = 0.85$	0.3296	0.2185
$\vartheta = 0.9$	0.2879	0.1784
$\vartheta = 0.95$	0.2285	0.1262
$\vartheta = 0.99$	0.1337	0.0564

Table 4.1: The table shows how the radii of a spherical or cylindrical inclusion vary for varying porosity ϑ. The porosities 0.3 to 0.45 cannot be realized if we do not allow for intersecting spheres.

tool for solving partial differential equations; for a detailed explanation of the numerical methods we refer to Appendix A.1.

The tensor $\mathcal{H}_{ij}$ and the vector $\mathcal{B}_j$ A general consideration must be made for $\mathcal{H}_{ij}$ and $\mathcal{B}_j$: they are deduced by system (2.2.62) for which a particular solution is $H_{ij} = \delta_{ij}$ and B_j constant, for each of the tested geometries. This fact can be proven analytically by simply substituting δ_{ij} in the system, as confirmed by Mei & Vernescu (2010) and by our numerical calculations over the microscopic cell. The value of B_j is not important to determine the flow and displacement fields because it expresses the dependence of $p^{(1)}$ onto $\dot{v}^{(0)}$, which does not appear in the effective equations at leading order.

4.0.1 Summary of the microscopic problems

We recall first the systems of PDE's to be solved for the microscopic quantities $\boldsymbol{\chi}$, $\boldsymbol{\eta}$, $\mathbf{K}$, $\mathbf{H}$, $\mathbf{A}$ and $\mathbf{B}$:

$$\begin{cases} \dfrac{\partial}{\partial x_j}\left\{C_{ijkl}\left[\varepsilon_{kl}(\chi^{pq})+\delta_{kp}\delta_{lq}\right]\right\}=0, \\ \left\{C_{ijkl}\left[\varepsilon_{kl}(\chi^{pq})+\delta_{kp}\delta_{lq}\right]\right\}n_j=0 \quad \text{on } \Gamma, \end{cases} \tag{4.0.1}$$

$$\begin{cases} \dfrac{\partial}{\partial x_j}\left[C_{ijkl}\,\varepsilon_{kl}(\eta)\right]=0, \\ \left[C_{ijkl}\,\varepsilon_{kl}(\eta)\right]n_j=n_i \quad \text{on } \Gamma, \end{cases} \tag{4.0.2}$$

$$\begin{cases} \dfrac{\partial A_j}{\partial x_i}-\dfrac{\partial^2 K_{ij}}{\partial x_k^2}=\delta_{ij}, \\ \dfrac{\partial K_{ij}}{\partial x_i}=0, \\ K_{ij}(\mathbf{x},t)=0 \quad \text{on } \Gamma, \end{cases} \tag{4.0.3}$$

$$\begin{cases} \dfrac{\partial B_j}{\partial x_i}-\dfrac{\partial^2 H_{ij}}{\partial x_k^2}=0, \\ \dfrac{\partial H_{ij}}{\partial x_i}=0, \\ H_{ij}(\mathbf{x},t)=\delta_{ij} \quad \text{on } \Gamma \end{cases} \tag{4.0.4}$$

plus $V-$periodicity for all the unknowns. When $\mathrm{Re}=\mathcal{O}(1)$ all the problems remain unchanged except for system (4.0.3) which is substituted by

$$\begin{cases} -\mathrm{Re}U_g\dfrac{\partial K_{ij}}{\partial x_g}=\dfrac{\partial A_j}{\partial x_i}-\delta_{ij}-\dfrac{\partial^2 K_{ij}}{\partial x_g^2}, \\ \dfrac{\partial K_{ij}}{\partial x_i}=0, \\ K_{ij}(\mathbf{x},t)=0 \quad \text{on } \Gamma. \end{cases} \tag{4.0.5}$$

4.1 Packed spheres

The case of packed spheres has been widely studied in the literature (cf. Carman (1939); Zick & Homsy (1982); Martys *et al.* (1994)) and is presented here as a first validation case for the permeability tensor.

4.1.1 The permeability tensor $\mathcal{K}_{ij}$ and $\mathcal{A}_i$

In figure 4.2 the component of the fields $\mathcal{K}_{ij}$ and $\mathcal{A}_i$ computed over the unitary cubic cell are shown. For spherical structures we find that $\mathcal{K}_{11} = \mathcal{K}_{22} = \mathcal{K}_{33}$, and $\mathcal{K}_{ij}$ with $i \neq j$ are antisymmetric with respect to the center of the sphere. Given that a spherical structure is isotropic, it is easy to prove that $\langle \mathcal{K}_{ij} \rangle = \mathcal{K}\delta_{ij}$ (cf. Goldstein (1980)), where $\mathcal{K}$ is a constant. Thanks to the antisymmetry of the microscopic fields, we obtain that $\langle \mathcal{K}_{ij} \rangle = 0$ for $i \neq j$. Figure 4.2 shows also that K_{ii} is perfectly symmetric with respect the center of the sphere. A particular consideration must be made for A_j: it is clear that, since it plays the role of the pressure in Stokes equations, it is determined up to a constant, so that also A_j is antisymmetric up to a translation. Actually, we are searching for a macroscopic solution at leading order in ϵ: whereas $\langle K_{ij} \rangle$ appears in the macroscopic equations for $u_i^{(0)}$, $\langle A_j \rangle$ is used only in the macroscopic equation for $p^{(1)}$, thus, it is not used in the determination of the leading order approximation of the flow field.

Comparison with the Kozeny and Carman equation

Since we are interested in the averaged values of the microscopic fields, we have compared the permeability tensor K_{ij} computed via equations (2.1.14) in the case of packed spheres ($\mathcal{K}_{ij} = \mathcal{K}\delta_{ij}$) with the Kozeny-Carman law given in Carman (1939):

$$\hat{\mathcal{K}} = \frac{1}{5}\left(\frac{V_s}{|\Gamma|}\right)^2 \frac{\theta^3}{(1-\theta)^2} \tag{4.1.1}$$

where V_s is the solid volume and $|\Gamma|$ is the area of the fluid structure interface (wetted surface); this equation is dimensional; in order to compare with the non-dimensional results we have to normalize the isotropic permeability $\hat{\mathcal{K}}$ with l^2 (cf. eq. 2.1.18). In the case of spheres, the dimensional Kozeny-Carman law becomes

$$\hat{\mathcal{K}} = \frac{1}{5}\left(\frac{\frac{4}{3}\pi r^3}{4\pi r^2}\right)^2 \frac{\theta^3}{(1-\theta)^2} = \frac{d^2}{180}\frac{\theta^3}{(1-\theta)^2}; \tag{4.1.2}$$

moreover, using the following relation which holds in the case of a cubic elementary cell with spherical inclusions;

$$d^2 = \left(\frac{6}{\pi}\right)^{\frac{2}{3}} l^2 (1-\theta)^{\frac{2}{3}}, \tag{4.1.3}$$

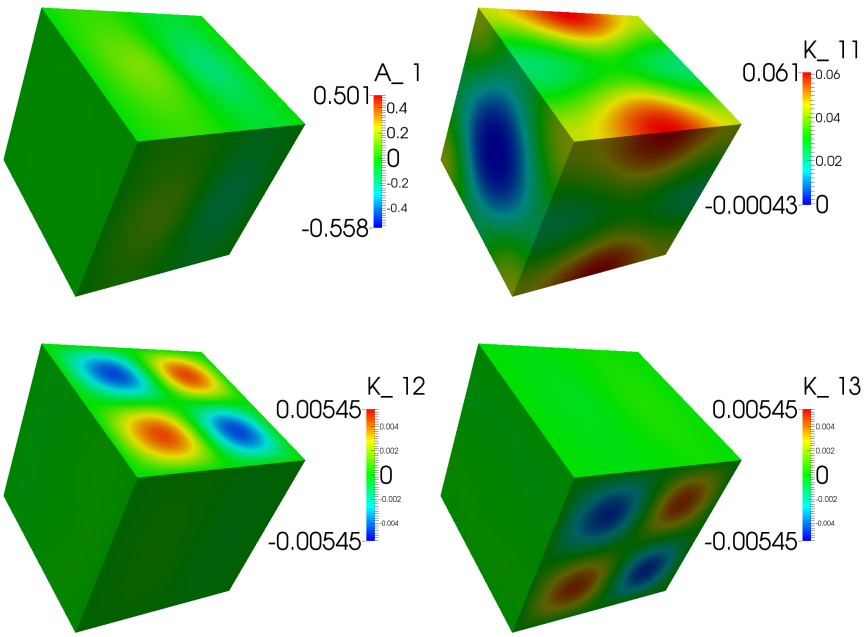

Figure 4.2: $\mathcal{K}$ and $\mathcal{A}$ fields in the unit cell,for the case of Stokes flow (eq. 2.1.14), porosity $\vartheta = 0.8$.

we obtain the following non dimensional form of the Kozeny-Carman law:

$$\mathcal{K} = \frac{\hat{\mathcal{K}}}{l^2} = \left(\frac{6}{\pi}\right)^{\frac{2}{3}} \frac{1}{180} \frac{\theta^3}{(1-\theta)^{\frac{4}{3}}}. \tag{4.1.4}$$

The results are reported in fig. 4.3, together with our numerical results and the theoretical solutions by Zick & Homsy (1982). Our results for $\mathcal{K}_{ij} = \langle K_{ij} \rangle$ averaged over space with the definition in equation (2.1.16), match perfectly those obtained by Zick & Homsy (1982) for varying values of the porosity ϑ (cf. fig. 4.3). The values of Zick & Homsy (1982) are Stokes flow results, obtained through the technique of integral equations, for different packings of uniform spheres. The much-quoted Kozeny-Carman (Carman (1939)) empirical formula is close to the theoretical findings only for ϑ around 0.5. A better fit through the data, to represent the isotropic

permeability as function of the porosity, is given by:

$$\hat{\mathcal{K}} = \frac{1}{5}\left(\frac{V_s}{|\Gamma|}\right)^2 \frac{\vartheta^{\frac{5}{2}}}{(1-\vartheta)^{\frac{47}{30}}} \tag{4.1.5}$$

(dashed red line in figure 4.3), valid in the range $0.476 < \vartheta < 1$.

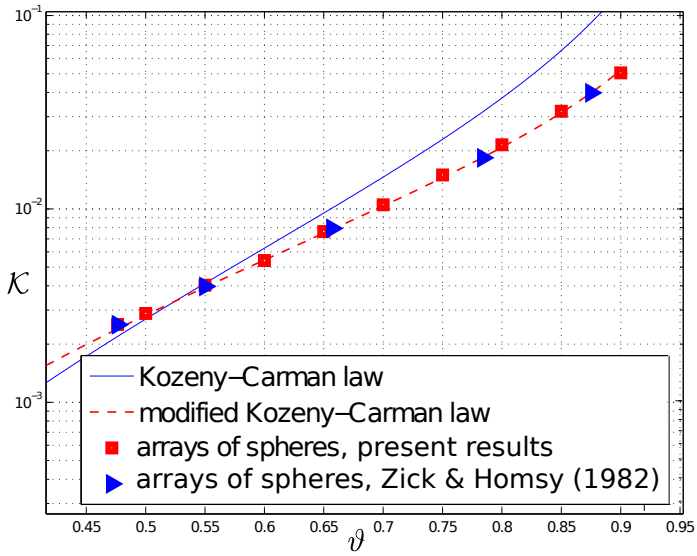

Figure 4.3: Permeability versus porosity for regular arrays of spheres: homogenization theory (■), empirical law of Kozeny-Carman (−), theoretical results by Zick & Homsy (1982) (▶).

Since the case of disjoined spheres has no physical meaning, as it will be shown later on section 4.2.3, we do not present the results for the other microscopic tensors.

4.2 Cylindrical fibres

As already discussed in the introduction, the case of cylindrical fibres is analyzed to model the behavior of biologically inspired coatings. We present the results for the permeability and for the effective elasticity tensor for this particular geometry. The results presented here are valid for an infinitely wide bed of infinitely long cylinders, or equivalently, for a region deep inside the porous medium.

4.2.1 The permeability tensor $\mathcal{K}_{ij}$

Since the structure is transversely isotropic, the components of the permeability tensor reduce to three: the transversal and longitudinal components K_{11} and K_{33}, respectively, and the extra diagonal component $K_{12} = K_{21}$. Once K_{ij} is found, we have a pointwise solution inside the elementary cell $V = [0, 1]^3$.

Case Re $= \mathcal{O}(\epsilon)$

If we are interested in the model for infinitesimally small Reynolds number we must solve system (4.0.3). The isocontours of each component of the solution are shown in figures (4.4) to (4.10) for the following porosities: $\vartheta = 0.4, 0.5, 0.6, 0.7, 0.8, 0.96$. Since the non-zero components of K_{ij} do not depend on x_3, we represent them over a fixed horizontal plane of equation $x_3 = 0.5$. We omit the results for K_{2j} because they are a permutation of K_{1j}. K_{11} and K_{22} have only one plane of symmetry ($x_1 = 0.5$), whereas K_{33} has two planes of symmetry ($x_1 = 0.5$ and $x_2 = 0.5$). As just observed for the case of packed spheres, K_{12} and K_{21} are not identically equal to zero, but antisymmetric. On the contrary, with this geometry, K_{13}, K_{23}, K_{31} and K_{32} are zero and the isocontours represented in figures 4.6, 4.8 and 4.9 are only due to discretization errors. As one expects, the maximum value of the main diagonal components increases when the porosity increases. To be thorough, in figures 4.7 and 4.11 also the results for A_j are presented even if they are not used in the effective equations. Obviously, also in this case A_j is determined up to a constant; in particular, we observe that A_1 and A_2 are antisymmetric with respect to the plane $x_1 = 0.5$ up to a translation of the whole field, and A_3 assumes a constant value in the whole domain. A_2 is not shown because it is a rotation of 90 degrees of A_1 around the x_3-axis.

As in the previous case, we carry out the weighted integral of K_{ij} over its microscopic domain, as by equation (2.1.16), to obtain $\mathcal{K}_{11}$, $\mathcal{K}_{33}$ and $\mathcal{K}_{12}$, the latter being zero by antisymmetry. The results are displayed in fig. 4.12 against a set of theoretical and experimental data from the literature (Sangani & Yao (1988); Skartsis & Kardos (1990); Sadiq *et al.* (1995); van der Westhuizen & du Plessis (1996); Mityushev & Adler (2002*a*)), with close agreement for ϑ ranging from 0.3 to 0.9. In the case Re $= \mathcal{O}(\epsilon)$ we obtain that K_{33} is about twice K_{11}, which ranges from about $\mathcal{O}(10^{-4})$ to $\mathcal{O}(10^{-1})$.

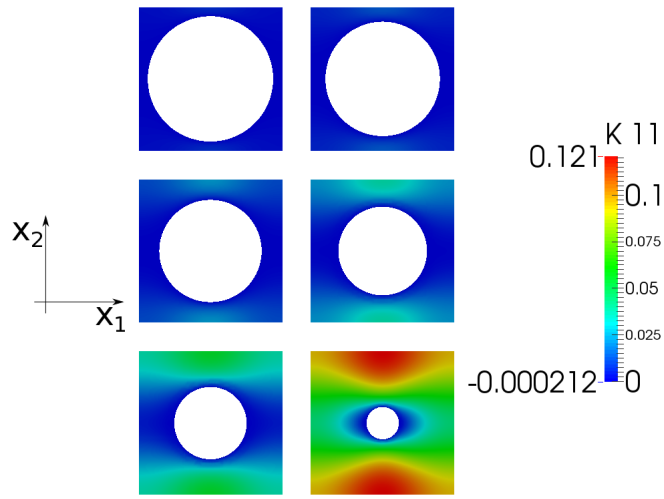

Figure 4.4: K_{11} for different radii of the cylinder. The porosity ranges in the interval [0.4,0.96].

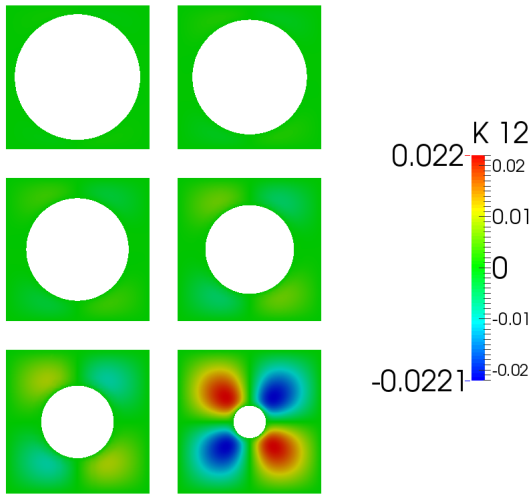

Figure 4.5: K_{12} for different radii of the cylinder. The porosity ranges in the interval [0.4,0.96].

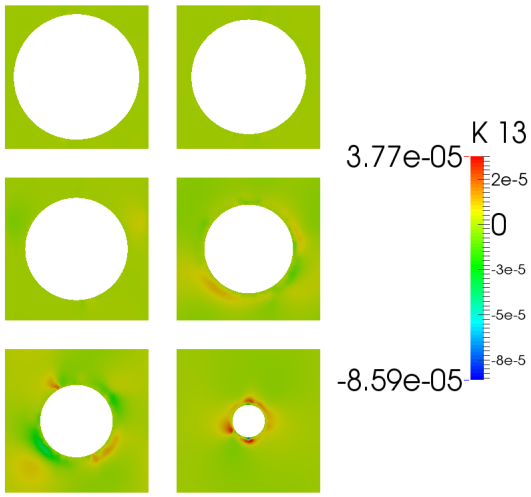

Figure 4.6: K_{13} for different radii of the cylinder. The porosity ranges in the interval [0.4,0.96].

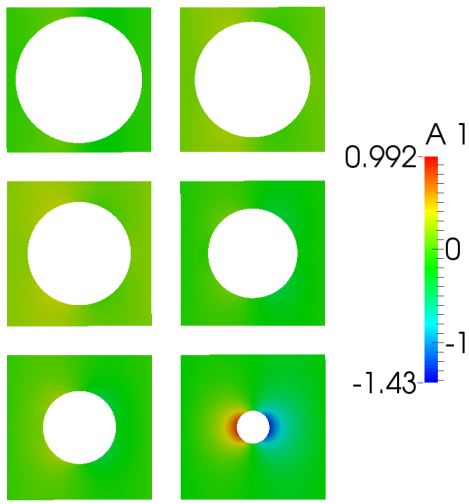

Figure 4.7: A_1 for different radii of the cylinder. The porosity ranges in the interval [0.4,0.96].

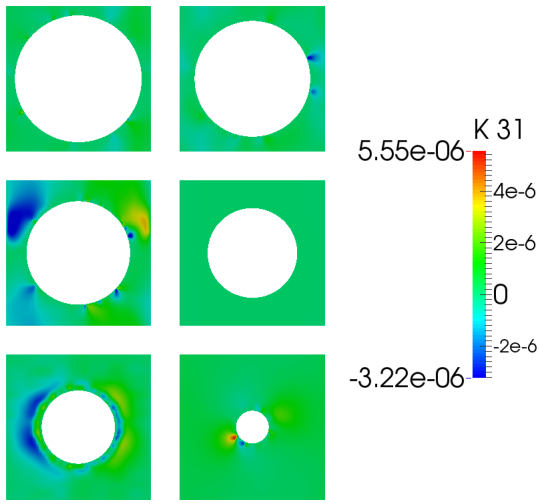

Figure 4.8: K_{31} for different radii of the cylinder. The porosity ranges in the interval [0.4,0.96].

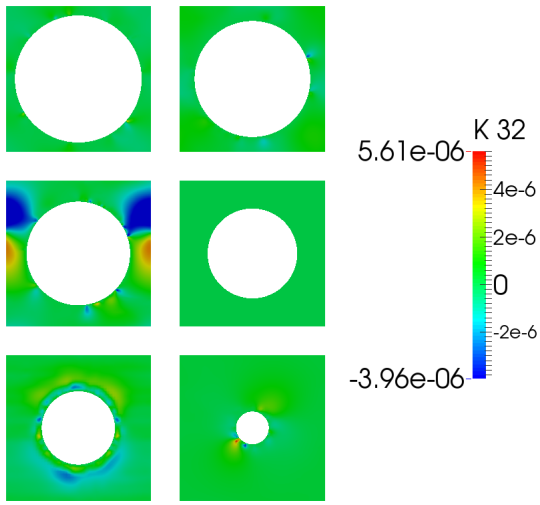

Figure 4.9: K_{32} for different radii of the cylinder. The porosity ranges in the interval [0.4,0.96].

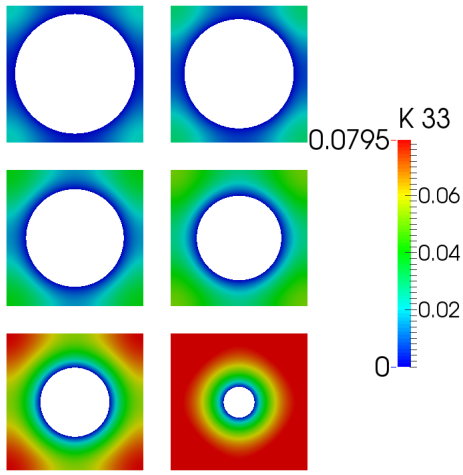

Figure 4.10: K_{33} for different radii of the cylinder. The porosity ranges in the interval [0.4,0.96].

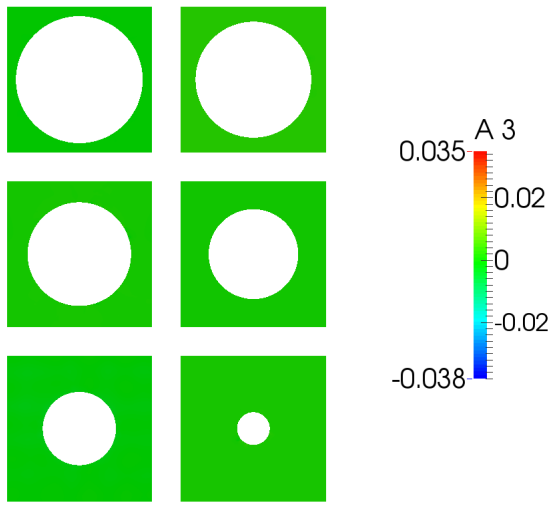

Figure 4.11: A_3 for different radii of the cylinder. The porosity ranges in the interval [0.4,0.96].

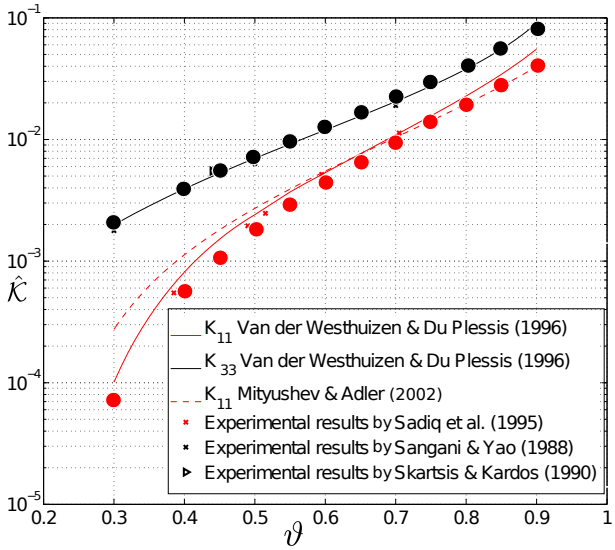

Figure 4.12: Components of the permeability tensor versus porosity for regular arrays of cylinders. The present results are represented by bullets, red for $\mathcal{K}_{11} = \mathcal{K}_{22}$, black for $\mathcal{K}_{33}$.

The three-scale approach As already noted, the particular cylindrical structure gives microscopic permeabilities which are invariant with respect to x_3. Moreover, if we suppose that the cylinders has two characteristic scale, l, comparable to its diameter and h, associated to its height which is different from the macroscopic length L, it makes sense to perform the three-scale approach described in section 2.3. The microscopic results are not shown here since they are analogous to those of the two-scale approach. The averaged results, in the sense of equation (2.3.29), are represented in figure 4.13, together with the results of the two-scale approach, already presented in figure 4.12. As one can see, the two theories are in good agreement. Actually, looking at the solution of the two-scale approach, the components of K_{ij} and A_j which are not present in the three-scale approach, are equal to zero in the two-scale approach, so that the equations are similar, but have been solved over different domains.

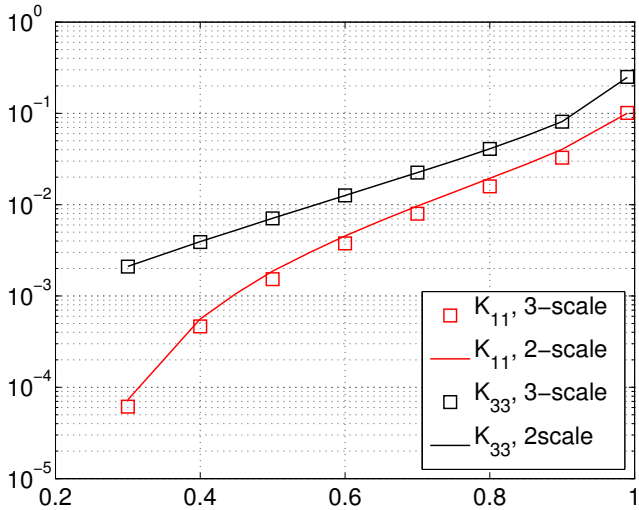

Figure 4.13: Components of the permeability tensor versus porosity for regular arrays of cylinders calculated with the three-scale (squares) and two-scale approaches.

Case Re $= \mathcal{O}(1)$

If we are interested in finite Reynolds numbers, instead, we must solve problem (4.0.5). The thing which should be immediately observed is that the permeability is not an intrinsic property of the structure, but it depends on the macroscopic characteristics of the flow, so that it can be termed *apparent* permeability. In order to understand how it is influenced by the flow, a parametric study for varying ϑ and Re$\mathbf{U}$ has been pursued. To verify if the Oseen's approximation adopted is suitable in this case, our results are compared with the results of Edwards *et al.* (1990) where the permeability is evaluated *a posteriori* inverting the Darcy's equation after solving for the flow. For comparison purposes, we rewrite equations (4.0.5) using a new notation. We define the mean fluid velocity vector through the pores as $\mathbf{v}^p = \mathbf{U}/\vartheta$ and the pore Reynolds number, $\mathrm{Re}_p = U_p l/\nu$, where U_p is the scale of the pore velocity $\mathbf{v}^p$. Hence, we can write the solution of the new linearized equations as in

(2.1.13) and search for K_{ij} and A_j which satisfy

$$\frac{\partial K_{ij}}{\partial x_i} = 0, \qquad -\vartheta \mathrm{Re}_p {v^p}_l \frac{\partial K_{ij}}{\partial x_l} = \frac{\partial A_j}{\partial x_i} - \frac{\partial^2 K_{ij}}{\partial x_g^2} - \delta_{ij}, \tag{4.2.1}$$

with the same boundary conditions as those used in problem (2.1.14). Thus, the permeability in this case is no longer a simple material property, but depends on the Reynolds number and the orientation of the velocity vector. In the simple case in which the fluid has a single main direction of motion x_1 with constant pore velocity (as in Edwards *et al.* (1990)), i.e. $\mathbf{v}^p = (1, 0, 0)$, equation (4.2.1) becomes:

$$\frac{\partial K_{ij}}{\partial x_i} = 0, \qquad -\vartheta \mathrm{Re}_p \frac{\partial K_{ij}}{\partial x_1} = \frac{\partial A_j}{\partial x_i} - \frac{\partial^2 K_{ij}}{\partial x_g^2} - \delta_{ij}. \tag{4.2.2}$$

Five different values of θ have been used, from 0.4 to 0.8. Important differences with respect to the $\mathrm{Re} = \mathcal{O}(\epsilon)$ case, whether in the microscopic pointwise permeability or in the averaged values, can be found. In figure 4.14 we see that the main effect of the presence of the Oseen's forcing term is the loss of the symmetries which characterize the microscopic fields associated to $\mathrm{Re} = \mathcal{O}(\epsilon)$. Figures from 4.15 to 4.17 show the loss of symmetry as function of the Oseen's closure term, for a fixed porosity of 0.7. The quantity $\mathrm{Re}U_1$ ranges in the interval $[0, 150]$. Furthermore the effect of a fixed forcing quantity $\mathrm{Re}U_1$ for varying porosity can be observed in figure 4.18 to 4.20, where $\theta \in [0.4, 0.8]$ and $\mathrm{Re}U_1 = 150$.

From a macroscopic point of view, in figure 4.21 we can observe the behavior of the averaged values of K_{ij} which decreases monotonically when the porosity decreases, as in the low Re case, and also when the Oseen term increases, thing that can be noted also observing the microscopic fields.

Another validation has been pursued using the experimental values of Ghisalberti & Nepf (2004; 2005; 2006) regarding a turbulent canopy flow. The averaged permeability is deduced *a posteriori* from their works, using equation (3.2.5), and has been compared with that deduced by our model. Since they assume to have a parallel flow, the only component of permeability that can be evaluated is $\mathcal{K}_{11}$. Figure 4.22 display the averaged values $\mathcal{K}_{11}$ for variable pore velocity. The gray band represents the range of permeability $\mathcal{K}_{11}$ computed using the homogenized model (4.2.2) for the corresponding porosities of each experiment. The experimental values are in reasonably good agreement with the homogenized values. More details on this problem are provided in section 5.3.

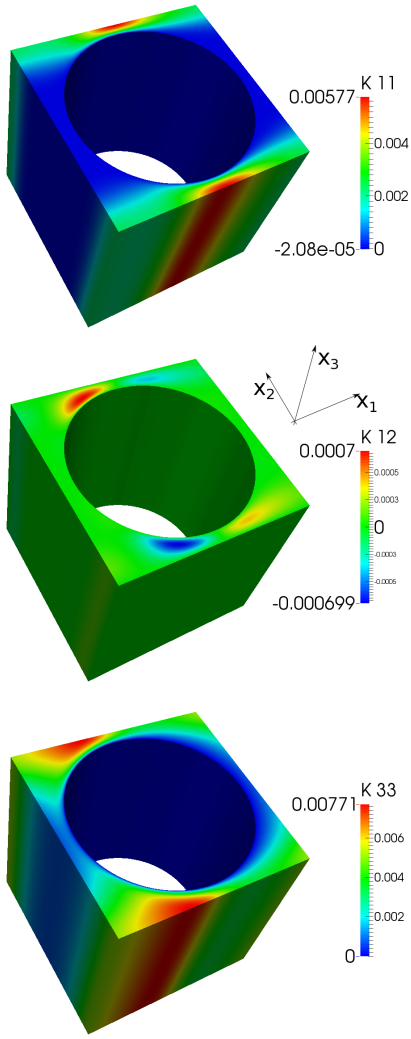

Figure 4.14: Relevant components of the permeability inside the microcell. $K_{12} = K_{21}$ and the remaining components are identically zero. In this case we have $\theta = 0.4$ and Re $= 150$ based on a reference velocity $U_1 = 1$. The solution is invariant with respect to x_3 and symmetry is lost.

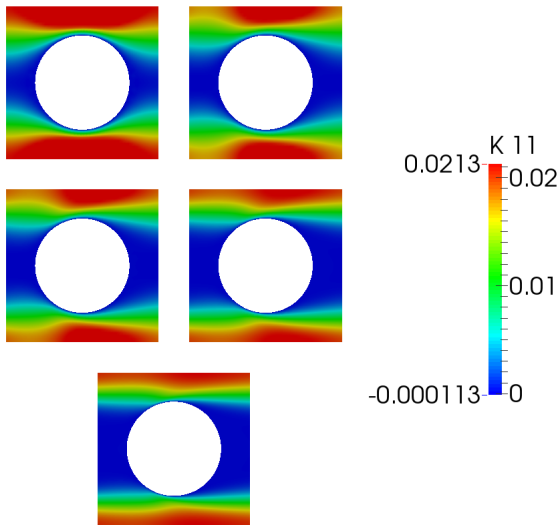

Figure 4.15: K_{11} for varying the Oseen forcing term from 0 to 150 in accordance to the values used in Edwards *et al.* (1990).

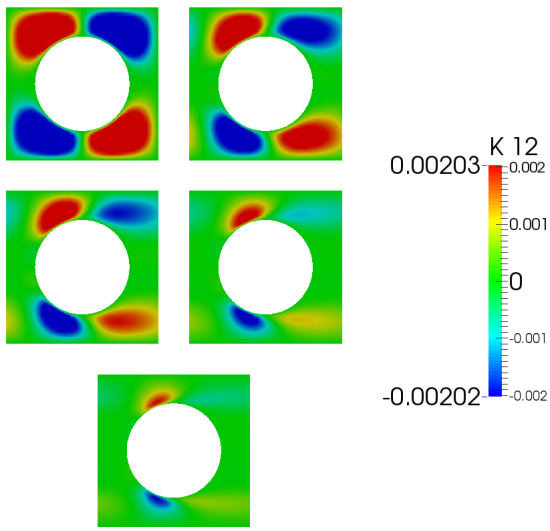

Figure 4.16: K_{12} for varying the Oseen forcing term from 0 to 150.

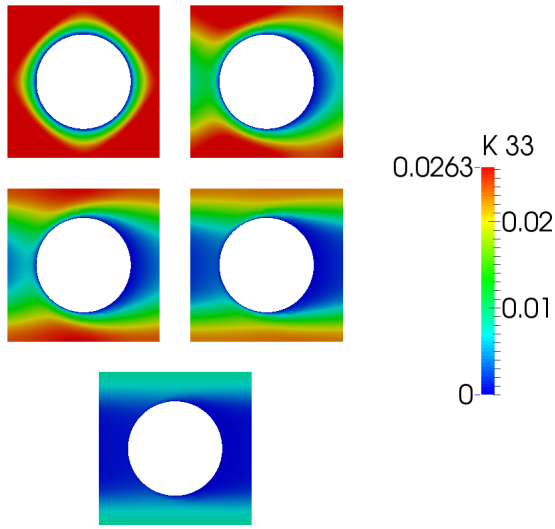

Figure 4.17: K_{33} for varying the Oseen forcing term from 0 to 150.

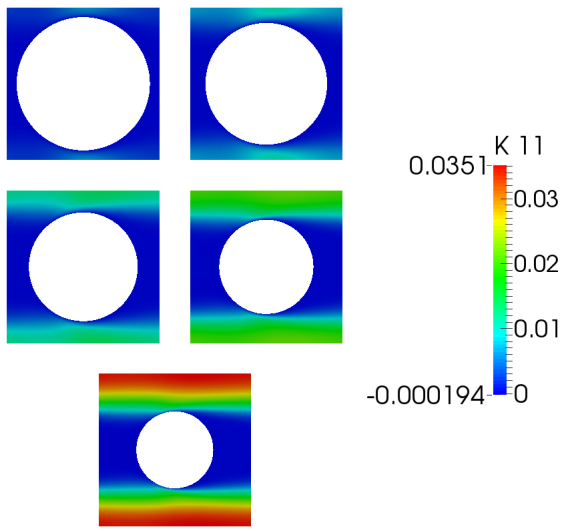

Figure 4.18: K_{11} for varying porosity at Re $= 150$.

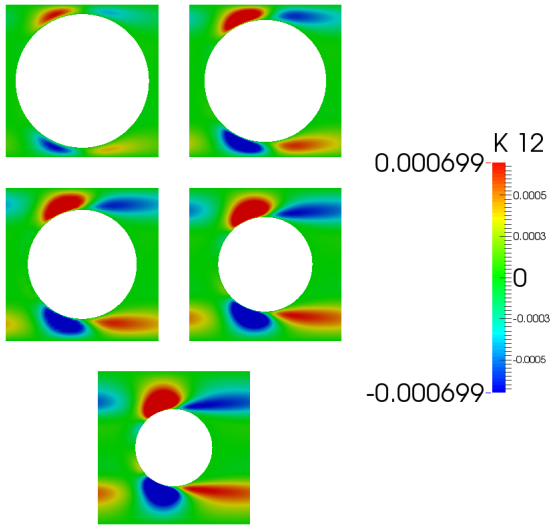

Figure 4.19: K_{12} for varying porosity at Re $= 150$.

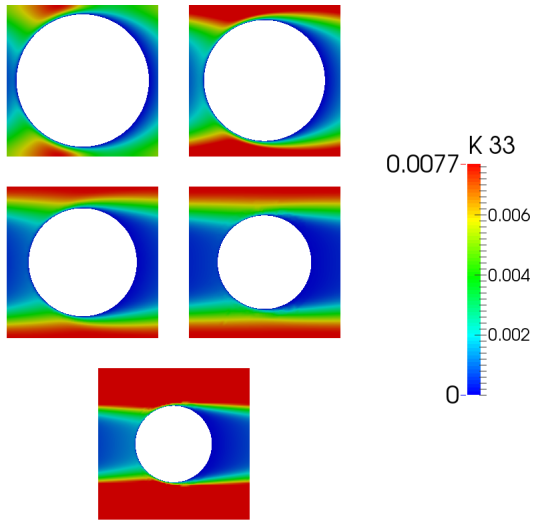

Figure 4.20: K_{33} for varying porosity at Re $= 150$.

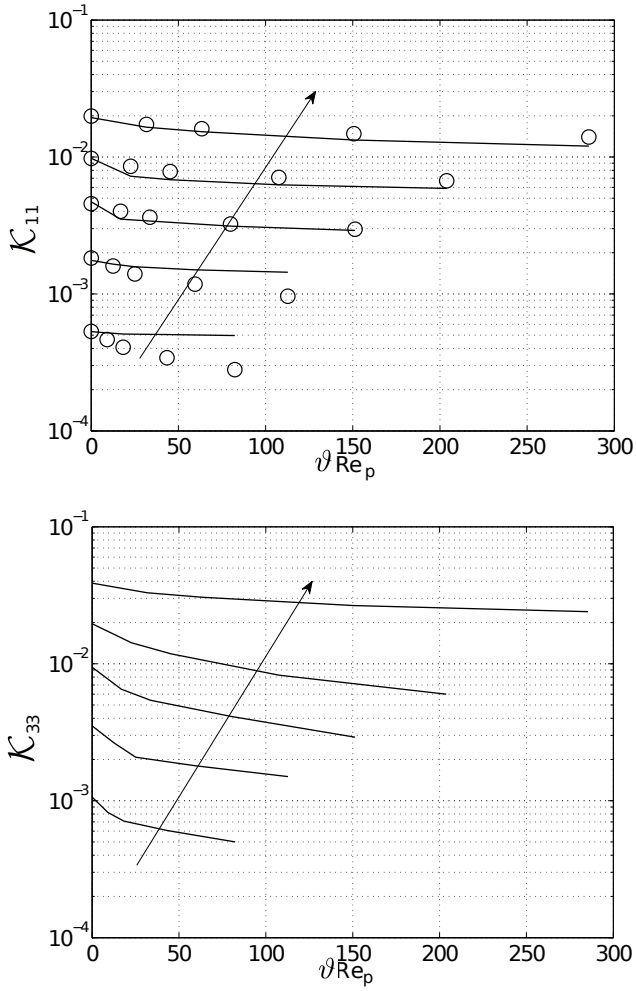

Figure 4.21: $\mathcal{K}_{11}$ and $\mathcal{K}_{33}$ for varying porosity from 0.4 to 0.8 for different values of the Oseen's term. The circles represents the values of $\mathcal{K}_{11}$ computed by Edwards *et al.* (1990); unfortunately, they studied a two dimensional problem over a horizontal plane so that $\mathcal{K}_{33}$ is not available.

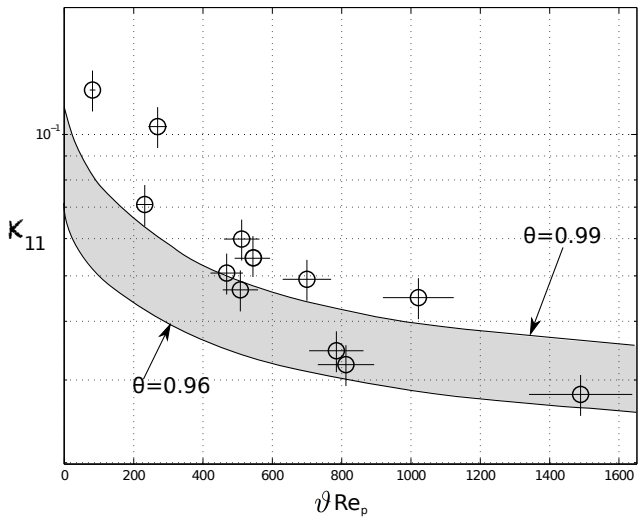

Figure 4.22: Horizontal component of the permeability $\mathcal{K}_{11}$ versus $\vartheta \mathrm{Re}_p$ of equation (4.2.2) from the measurements by Ghisalberti & Nepf (2004). Since the permeability is deduced from experimental data, the vertical and horizontal bars represent the uncertainty of the measurements which is about 10% for each value. The grey band represents the range of permeabilities calculated by the homogenized model for finite Reynolds numbers for $0.96 \leq \vartheta \leq 0.99$.

Effect of the flow direction on the apparent permeability

Even if the microscopic geometry of the porous medium that we are analyzing is transversely isotropic, since the apparent permeability depends also on the flow field some noticeable effects linked to non-isotropicity can be observed in the case of high Re numbers. In figure 4.23 we can see that if we impose an arbitrary value for the Oseen's term, e.g. $\mathrm{Re}\mathbf{U} = (10, 20, 15)$, the symmetries typical of a transversely isotropic medium are lost and a new form of the permeability tensor arises. For this particular flow direction and intensity we obtain an anisotropic permeability tensor equal to:

$$\mathcal{K}_{ij} = \begin{pmatrix} 0.0046 & 0.0003081 & \mathcal{O}(10^{-9}) \\ 0.0003079 & 0.0057 & \mathcal{O}(10^{-9}) \\ \mathcal{O}(10^{-9}) & \mathcal{O}(10^{-9}) & 0.01118 \end{pmatrix} \tag{4.2.3}$$

which can be compared with the corresponding permeability of the Stokes flow case:

$$\mathcal{K}_{ij} = \begin{pmatrix} 0.009 & \mathcal{O}(10^{-9}) & \mathcal{O}(10^{-9}) \\ \mathcal{O}(10^{-9}) & 0.009 & \mathcal{O}(10^{-9}) \\ \mathcal{O}(10^{-9}) & \mathcal{O}(10^{-9}) & 0.019 \end{pmatrix}. \tag{4.2.4}$$

Other tests which we have performed demonstrate that the greater the difference between the components of $\mathbf{U}$, the greater are the anisotropic effects on the microscopic and the averaged permeability.

4.2.2 Tensors $\mathcal{L}_{ijk}$ and $\mathcal{M}_{ijk}$

Computing the 27 component of $\mathcal{L}_{ijk}$, we have verified that they are equal to zero in accordance with Nield & Bejan (2013) and, in particular, with Skjetne & Auriault (1999) in which it is proven, using a variational form of the equations for K_{ij}, L_{ijk} and M_{ijk}, that for a certain range of $\mathrm{Re} \in (\epsilon^{\frac{1}{2}}\ 1)$, only a cubic correction of Darcy's law is relevant. In figure 4.24 and in table 4.2, for example, some components of the microscopic fields and the averaged values of the tensor L_{ijk} which appears in the quadratic correction of Darcy's law, are shown.

4.2.3 χ_i^{pq}, η_i, α'_{ij} and the effective elasticity tensor $\mathcal{C}_{ijpq}$

In this section we solve for the microscopic problems (4.0.1) – (4.0.2). In order for equations (4.0.1), (4.0.2) to make sense we introduce the microscopic elasticity

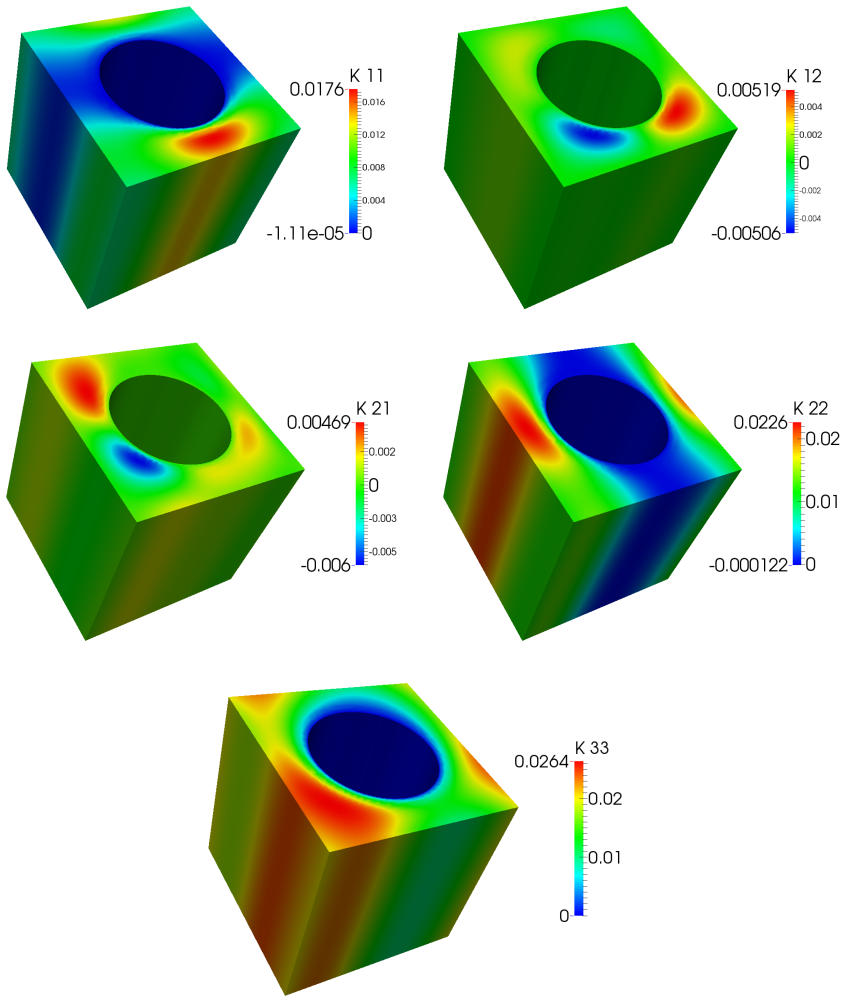

Figure 4.23: Components of the permeability tensor computed using an Oseen term with $\mathrm{Re}\mathbf{U} = (20, 10, 25)$.

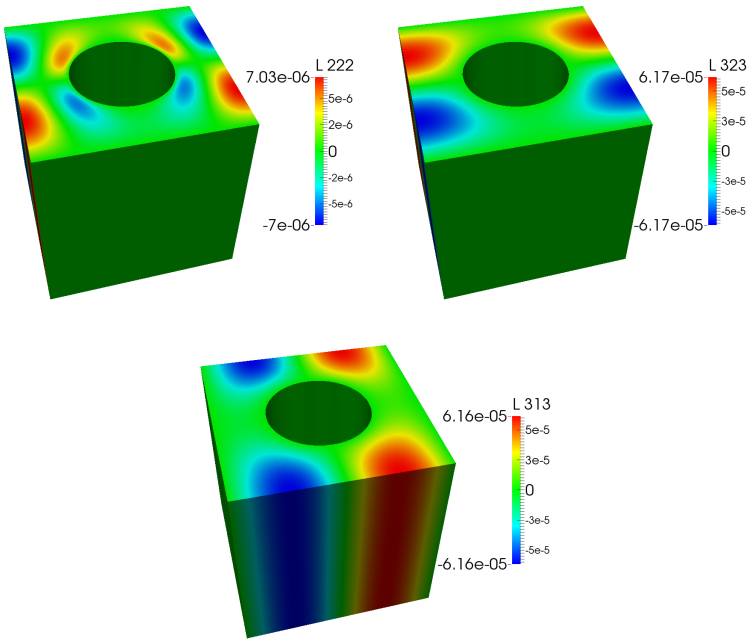

Figure 4.24: Some components of the tensor L_{ijk}. Looking at L_{323} and L_{313} a characteristic symmetry for transversely isotropic materials can be evinced.

$\times 10^9$	i=1	i=2	i=3
$\mathcal{L}_{i11}$	-8.26	1.89	-0.13
$\mathcal{L}_{i12}$	-0.47	-1.69	-0.11
$\mathcal{L}_{i13}$	$-0.51 \cdot 10^{-1}$	$-0.27 \cdot 10^{-1}$	-0.52
$\mathcal{L}_{i21}$	-4.47	2.30	$0.22 \cdot 10^{-2}$
$\mathcal{L}_{i22}$	-7.34	0.87	$-0.36 \cdot 10^{-1}$
$\mathcal{L}_{i23}$	$-0.31 \cdot 10^{-1}$	$0.96 \cdot 10^{-1}$	4.31
$\mathcal{L}_{i31}$	$0.65 \cdot 10^{-2}$	$-0.47 \cdot 10^{-2}$	$0.26 \cdot 10^{-1}$
$\mathcal{L}_{i32}$	$0.72 \cdot 10^{-2}$	$-0.91 \cdot 10^{-2}$	$0.4 \cdot 10^{-1}$
$\mathcal{L}_{i33}$	$0.85 \cdot 10^{-3}$	$-0.17 \cdot 10^{-1}$	$-0.71 \cdot 10^{-1}$

Table 4.2: Components of the tensor $\mathbf{L}$ computed using equation (2.1.25) and (2.1.26) and averaged over the elementary cell.

tensor C_{ijkl}, expressed as a 6×6 matrix in Voigt's contracted notation Voigt (1889). If we consider an isotropic elastic material, C_{ijkl} assumes the following form:

$$C_{ijkl} = \begin{pmatrix} \lambda+2\mu & \lambda & \lambda & 0 & 0 & 0 \\ \lambda & \lambda+2\mu & \lambda & 0 & 0 & 0 \\ \lambda & \lambda & \lambda+2\mu & 0 & 0 & 0 \\ 0 & 0 & 0 & \mu & 0 & 0 \\ 0 & 0 & 0 & 0 & \mu & 0 \\ 0 & 0 & 0 & 0 & 0 & \mu \end{pmatrix} \tag{4.2.5}$$

where λ and μ are the Lamé constants of the isotropic material, normalized by Young's modulus of elasticity. In terms of Young's modulus E and Poisson's ratio ν_P, the following relations hold:

$$\lambda = \frac{\nu_P E}{(1+\nu_P)(1-2\nu_P)} \quad \text{and} \quad \mu = \frac{E}{2(1+\nu_P)}. \tag{4.2.6}$$

We have analyzed three different materials plus the limit case of an incompressible polyurethane elastomer for which $\nu_P \to 0.5$. The different materials can be classified on the basis of ν_P:

- silicon carbide (SiC), $\nu_P = 0.15 \Rightarrow \lambda = 0.186, \mu = 0.435$;
- iron, $\nu_P = 0.28 \Rightarrow \lambda = 0.504, \mu = 0.390$;
- polycarbonate, $\nu_P = 0.42 \Rightarrow \lambda = 1.849, \mu = 0.352$;
- polyuretane elastomer, $\nu_P = 0.499 \Rightarrow \lambda = 166.403, \mu = 0.333$.

The tensor χ_i^{pq} and vector η_i

Tensor χ_i^{pq} represents a microscopic displacement. System (4.0.1) is formed by linear PDE's obtained as a combination of the entries of the pointwise elasticity tensor C_{ijkl} and of the jacobian of χ_i^{pq}, valid over the solid structure inside the microcell. Figure 4.25 shows the microscopic shape of χ_1^{11} for three values of ϑ. It is represented in the (x_1, x_2) plane because of its invariance with respect to x_3. The particular domain over which we are solving the equations causes a lot of symmetries and antisymmetries for χ_i^{pq}. In order not to be redundant we do not dwell on the microscopic structure of the 27 component of χ_i^{pq}, but provide directly the averaged values which appear in the effective equations. We observe also that η_i

solves the same differential equations as χ_i^{pq}, with a different boundary condition, and its microscopic shape is analogous to that of χ_i^{pq}, as can be seen comparing figures 4.25 and 4.26. From a macroscopic point of view we are interested in the

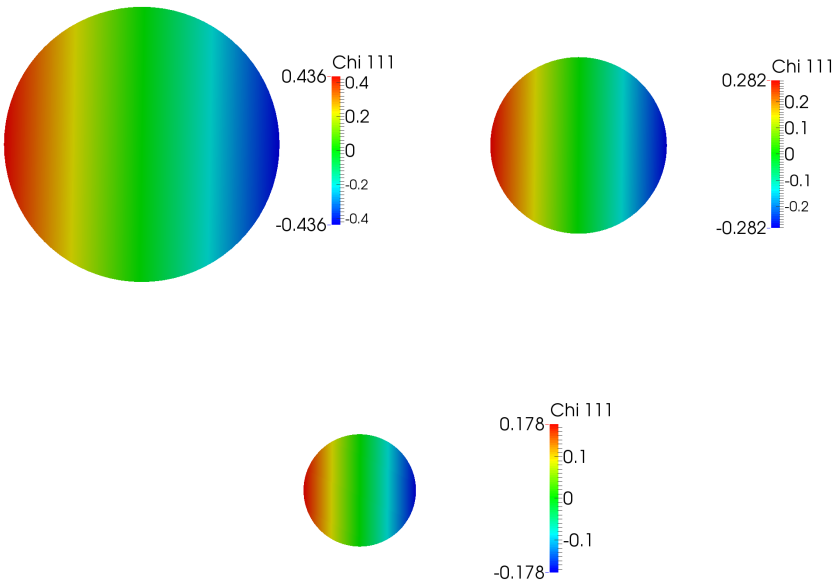

Figure 4.25: View of χ_1^{11}, for $\vartheta = 0.4, 0.7, 0.9$ ($r = 0.4370, 0.3090, 0.1784$), respectively. Since the vector field is constant along x_3, only a view over a horizontal midplane (x_1, x_2) is shown.

jacobian of χ_i^{pq} and η_i because they play a role in the definition of $\mathcal{C}_{ijpq}$, in the continuity equation for the composite, and in the matrix α'_{ij}, which appears in the balance equation for the effective displacement. In each of the cases studied for the four different material the following relations hold:

$$\left\langle \frac{\partial \chi_j^{11}}{\partial x_i} \right\rangle = -\delta_{i1}\delta_{1j}A, \quad \left\langle \frac{\partial \chi_j^{22}}{\partial x_i} \right\rangle = -\delta_{i2}\delta_{2j}A, \quad \left\langle \frac{\partial \chi_j^{33}}{\partial x_i} \right\rangle = -(\delta_{i1}\delta_{1j}+\delta_{i2}\delta_{2j})B,$$

$$\left\langle \frac{\partial \chi_j^{13}}{\partial x_i} \right\rangle = -\delta_{i1}\delta_{3j}A, \quad \left\langle \frac{\partial \chi_j^{12}}{\partial x_i} \right\rangle = -(\delta_{i1}\delta_{2j}+\delta_{i2}\delta_{1j})\frac{A}{2}, \quad \left\langle \frac{\partial \chi_j^{23}}{\partial x_i} \right\rangle = -\delta_{i2}\delta_{3j}A,$$

$$\left\langle \frac{\partial \chi_j^{31}}{\partial x_i} \right\rangle = \left\langle \frac{\partial \chi_i^{13}}{\partial x_j} \right\rangle, \quad \left\langle \frac{\partial \chi_j^{21}}{\partial x_i} \right\rangle = \left\langle \frac{\partial \chi_i^{12}}{\partial x_j} \right\rangle, \quad \left\langle \frac{\partial \chi_j^{32}}{\partial x_i} \right\rangle = \left\langle \frac{\partial \chi_i^{23}}{\partial x_j} \right\rangle. \tag{4.2.7}$$

The coefficients A and B depend a priori on the material properties and are listed in table 4.3 (in case of iron cylinders) for different porosities in the range of $[0.4, 0.9]$. Also, $\boldsymbol{\eta}$ can be written in an analogous way, i.e.

$$\left\langle \frac{\partial \eta_j}{\partial x_i} \right\rangle = -(\delta_{i1}\delta_{1j} + \delta_{i2}\delta_{2j})C \tag{4.2.8}$$

where C varies with ϑ as shown in table 4.3.

	iron		
	A	B	C
ϑ=0.4	0.600	0.172	0.328
ϑ=0.45	0.550	0.158	0.301
ϑ=0.5	0.500	0.144	0.274
ϑ=0.55	0.450	0.129	0.246
ϑ=0.6	0.400	0.115	0.219
ϑ=0.65	0.350	0.101	0.191
ϑ=0.7	0.300	0.086	0.164
ϑ=0.75	0.250	0.072	0.137
ϑ=0.8	0.200	0.058	0.109
ϑ=0.85	0.150	0.043	0.082
ϑ=0.9	0.100	0.029	0.055

Table 4.3: Values of the coefficients A, B and C to be used to find $\boldsymbol{\chi}$ and $\boldsymbol{\eta}$ in the case of a porous medium constituted by iron cylinders, computed solving system (4.0.1) and (4.0.2) for varying ϑ.

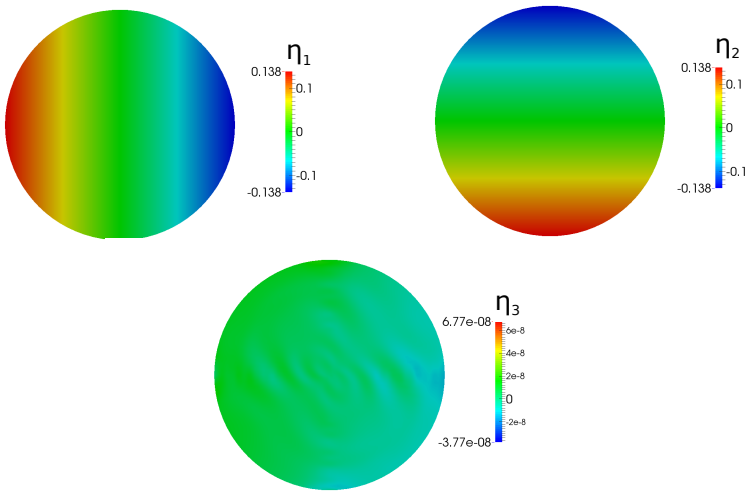

Figure 4.26: View of each component of the microscopic η_i field, $\vartheta = 0.8$. Since the vector field is constant in x_3, only a view over a horizontal midplane (x_1, x_2) is shown.

The effective elasticity $\mathcal{C}_{ijpq}$

The macroscopic stiffness tensor (equation 2.2.49) has the following non-zero entries:

$$\begin{aligned}
\mathcal{C}_{1111} = \mathcal{C}_{2222} &= (\lambda + 2\mu)(-A + 1 - \vartheta), \\
\mathcal{C}_{1122} = \mathcal{C}_{2211} = \mathcal{C}_{3311} = \mathcal{C}_{3322} &= \lambda(-A + 1 - \vartheta), \\
\mathcal{C}_{1133} = \mathcal{C}_{2233} &= -(2\lambda + 2\mu)B + (1 - \vartheta)\lambda, \\
\mathcal{C}_{3333} &= -2\lambda B + (1 - \vartheta)(\lambda + 2\mu), \\
\mathcal{C}_{1212} = \mathcal{C}_{1313} = \mathcal{C}_{2323} &= \mu(-A + 1 - \vartheta).
\end{aligned}$$

The microscopic simulations for the four materials considered show that A, B and C do not change if we change the Poisson's ratio of the material. This fact means that the properties of the material enter the model only when we consider the dimensional stiffness tensor $\mathcal{C}_{ijkl}$. We can conclude that for this particular shape of

the porous medium, $\mathcal{C}_{ijkl}$ has the following form:

$$\mathcal{C}_{ijkl} = \begin{pmatrix} 0 & 0 & 0 & 0 & 0 & 0 \\ 0 & 0 & 0 & 0 & 0 & 0 \\ 0 & 0 & \spadesuit & 0 & 0 & 0 \\ 0 & 0 & 0 & 0 & 0 & 0 \\ 0 & 0 & 0 & 0 & 0 & 0 \\ 0 & 0 & 0 & 0 & 0 & 0 \end{pmatrix} \tag{4.2.9}$$

where the symbol represents the only non zero entries of the matrix, which depends on porosity and Young's modulus. The matrix α'_{ij}, instead, assumes the form

$$\alpha'_{ij} = \begin{pmatrix} \vartheta & 0 & 0 \\ 0 & \vartheta & 0 \\ 0 & 0 & \vartheta \end{pmatrix}.$$

The non-dimensional value of ♠ can be deduced by table 4.3 and does not depend on λ and μ associated to the different materials tested. The real stiffness of each material enters the model when we consider its dimensional form: for a porosity equal to 0.8, ♠ varies from $\mathcal{O}(10^{-3})$ (polyurethane elastomer) to $\mathcal{O}(10^{2})$ (silicon carbide). Looking at $\mathcal{C}_{ijpq}$, it is clear that the homogenized material has rather strange properties, as already noted by Hoffmann *et al.* (2004). These authors have considered a poroelastic layer similar to ours, demonstrating that volume conserving deformations (shear deformations, in particular) do not produce elastic stresses. We ascribe this property to the fact that fibers are disconnected from one another. A strategy to deduce a *full* stiffness tensor is proposed in the following by slightly modifying the geometry of the fibers.

4.3 Linked fibres

A solution to the problem encountered in the previous section is to connect the porous inclusions in all the directions inside the microscopic cell, generating a geometry composed by a principal cylinder crossed by two secondary cylinders transversely to it as represented in figure 5.42. To make some comparison between the tensors deduced with this geometry and with that of the previous section, we consider a porosity which is almost the same as in the case of simple cylinders. This means that the diameter d_t of the crossing cylinders has to be much smaller than the diameter d of the main fiber. In table 4.4 we can see how the porosity changes for

main cyl.	$d/d_t = 7.5$	$d/d_t = 5$	$d/d_t = 2.5$	$d/d_t = 1$
$\vartheta = 0.8$	$\vartheta = 0.797$	$\vartheta = 0.793$	$\vartheta = 0.768$	$\vartheta = 0.583$
$r = 0.252$	$r_t = 0.034$	$r_t = 0.050$	$r_t = 0.101$	$r_t = 0.252$

Table 4.4: Behavior of the porosity for varying the ratio d_t/d for a fixed value of $\vartheta = 0.8$.

varying the ratio d_t/d. In order to not be redundant we present one sample case for which the problem for $\mathcal{C}_{ijkl}$ has been solved.

4.3.1 The permeability tensor $\mathcal{K}_{ij}$ and A_j

The results presented here are referred to a porosity of 0.79 realized using a main cylinder of radius 0.252 (in the case of simple cylinders ϑ would be 0.8) and $d/d_t = 5$. We observe that even if in this case ϑ varies only by about 1.3% the changes in the permeability are rather relevant. In figure 4.27 the microscopic fields of permeability are shown. The values assumed by the effective permeability are

$$\mathcal{K}_{ij}^{d=5d_t} = \begin{pmatrix} 2.5 \cdot 10^{-4} & \mathcal{O}(10^{-10}) & \mathcal{O}(10^{-10}) \\ \mathcal{O}(10^{-10}) & 2.5 \cdot 10^{-4} & \mathcal{O}(10^{-10}) \\ \mathcal{O}(10^{-10}) & \mathcal{O}(10^{-10}) & 4.7 \cdot 10^{-4} \end{pmatrix}.$$

These values are about two order of magnitude smaller than the values computed using a simple cylinder geometry with the same radius:

$$\mathcal{K}_{ij} = \begin{pmatrix} 1.9 \cdot 10^{-2} & \mathcal{O}(10^{-10}) & \mathcal{O}(10^{-10}) \\ \mathcal{O}(10^{-10}) & 2.0 \cdot 10^{-2} & \mathcal{O}(10^{-10}) \\ \mathcal{O}(10^{-10}) & \mathcal{O}(10^{-10}) & 3.9 \cdot 10^{-2} \end{pmatrix}.$$

The fact that the permeability tensor changes much even if the porosity does not, is desirable because it is an indication that the information related to the structure passed to the macroscopic equations are sufficiently detailed and do not depend only on the porosity. Calculating the permeability for different ratios of d/d_t the following results are obtained:

$$\mathcal{K}_{ij}^{d=d_t} = \begin{pmatrix} 9.4 \cdot 10^{-5} & \mathcal{O}(10^{-10}) & \mathcal{O}(10^{-10}) \\ \mathcal{O}(10^{-10}) & 9.4 \cdot 10^{-5} & \mathcal{O}(10^{-10}) \\ \mathcal{O}(10^{-10}) & \mathcal{O}(10^{-10}) & 9.4 \cdot 10^{-5} \end{pmatrix}$$

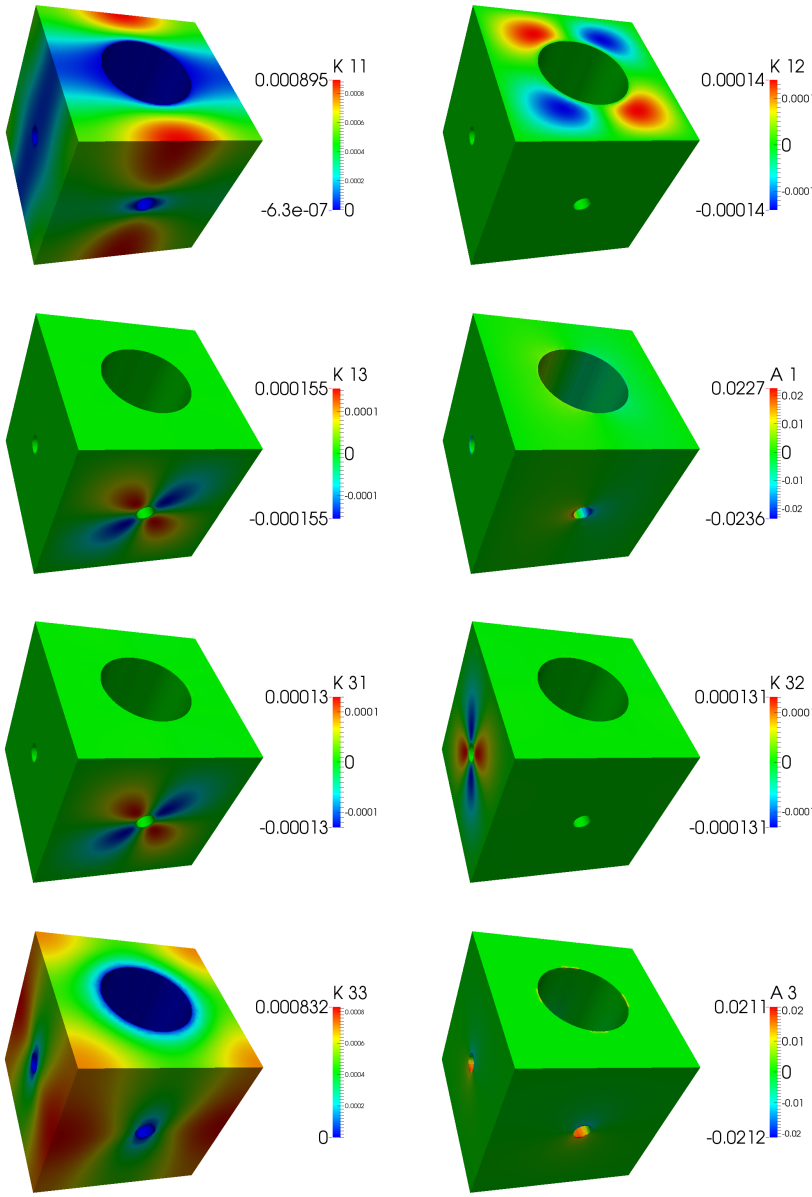

Figure 4.27: Component of the permeability tensor and vector $\mathcal{A}_j$ in case of linked cylinders. The second row of $\mathcal{K}_{ij}$ is not shown because it is a permutation of the elements in the first row.

and

$$\mathcal{K}_{ij}^{d=2.5d_t} = \begin{pmatrix} 2.0 \cdot 10^{-4} & \mathcal{O}(10^{-10}) & \mathcal{O}(10^{-10}) \\ \mathcal{O}(10^{-10}) & 2.0 \cdot 10^{-4} & \mathcal{O}(10^{-10}) \\ \mathcal{O}(10^{-10}) & \mathcal{O}(10^{-10}) & 4.1 \cdot 10^{-4} \end{pmatrix}.$$

As one can see, the permeability decreases monotonically decreasing the porosity, i.e. decreasing the ratio d/d_t; for the case $d = d_t$ the structure becomes isotropic and this is confirmed also by the shape of $\mathcal{K}_{ij}$ which is analogous to that in the case of sphere. For the other d/d_t the shape of the new effective permeability tensor confirms that the property of transverse isotropicity is conserved also with this geometry.

4.3.2 Tensors $\mathcal{L}_{ijk}$ and $\mathcal{M}_{ijk}$

Also in this case, in accordance with Skjetne & Auriault (1999), since the geometrical properties of the structure are maintained (transverse isotropicity), the averaged values of $\mathcal{L}_{ijk}$ and $\mathcal{M}_{ijk}$ are equal to zero. Some sample components are shown in figure 4.28.

4.3.3 χ_i^{pq}, η_i and the effective elasticity tensor $\mathcal{C}_{ijpq}$

The problem encountered with $\mathcal{C}_{ijkl}$ is relaxed with the "connected" geometry. In figures 4.29 to 4.32 the microscopic fields are shown. In particular figures 4.29 and 4.31 show the symmetry of the couples χ_i^{11}–χ_i^{22} and χ_i^{13}–χ_i^{23} which can then be observed also at a macroscopic level in the effective stiffness tensor ($\mathcal{C}_{1111} = \mathcal{C}_{2222}$, $\mathcal{C}_{1122} = \mathcal{C}_{2211}$, $\mathcal{C}_{1313} = \mathcal{C}_{2323}$ and $\mathcal{C}_{1133} = \mathcal{C}_{2233} = \mathcal{C}_{3322} = \mathcal{C}_{3311}$).

The new effective stiffness tensor has now the form

$$\mathcal{C}_{ijkl} = \begin{pmatrix} \bigcirc & \blacksquare & \otimes & 0 & 0 & 0 \\ \blacksquare & \bigcirc & \otimes & 0 & 0 & 0 \\ \otimes & \otimes & \bigstar & 0 & 0 & 0 \\ 0 & 0 & 0 & \clubsuit & 0 & 0 \\ 0 & 0 & 0 & 0 & \spadesuit & 0 \\ 0 & 0 & 0 & 0 & 0 & \spadesuit \end{pmatrix} \tag{4.3.1}$$

in accordance with Cheng (1997) and Cowin (2013); in particular, for the specific

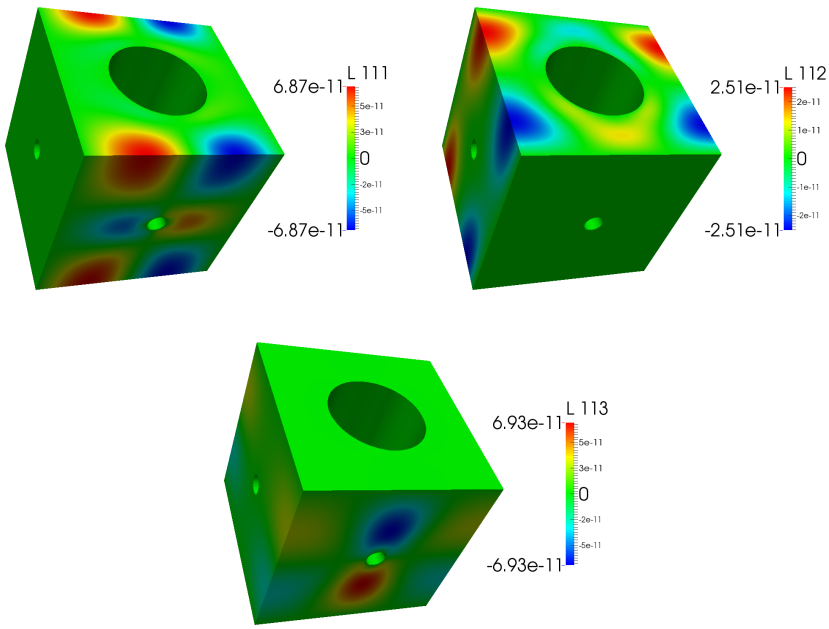

Figure 4.28: Three components of the tensor $\mathcal{L}_{ijk}$ are show. Since the structure is transversely isotropic, all the components of $\mathcal{L}_{ijk}$ and $\mathcal{M}_{ijk}$ vanish.

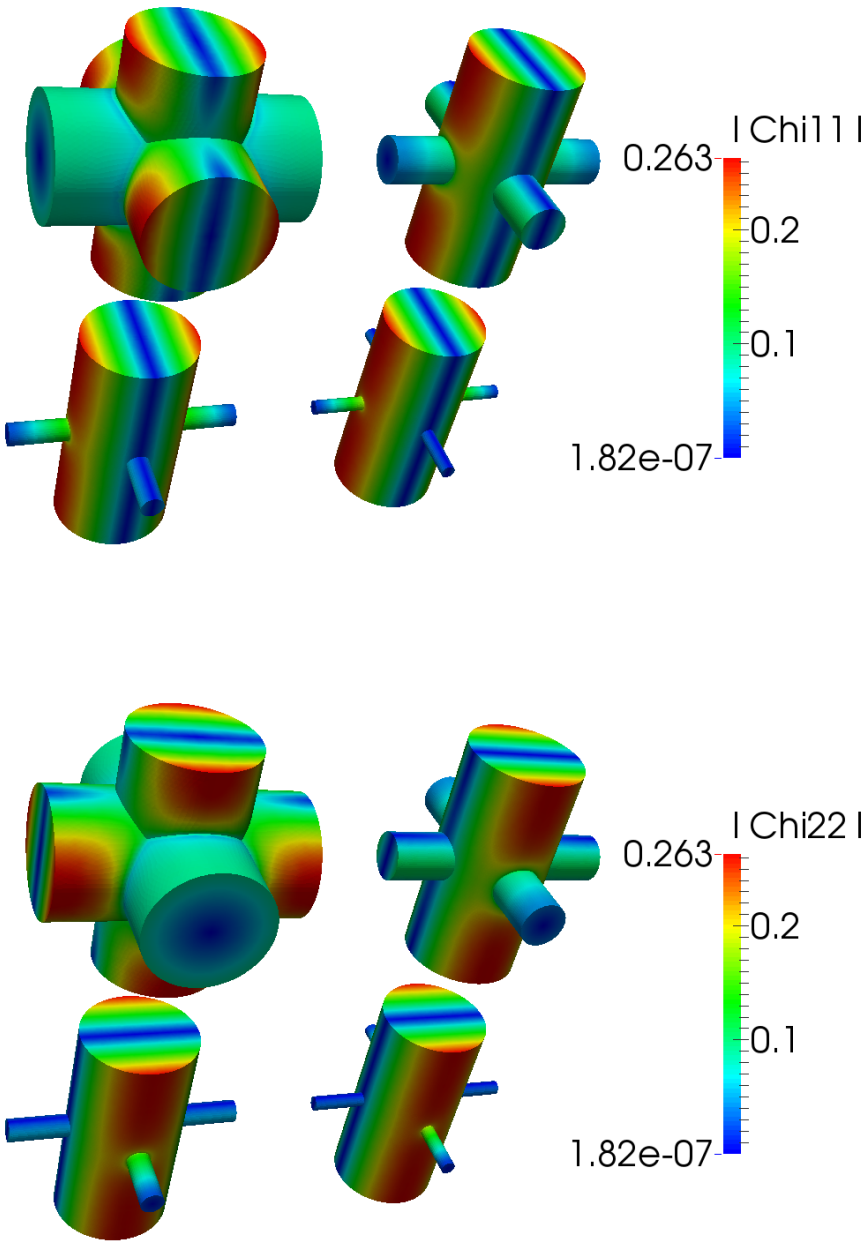

Figure 4.29: Magnitude of the vector field χ_i^{11} and χ_i^{22} for four different values of the ratio d/d_t: 1, 2.5, 5, 7.5.

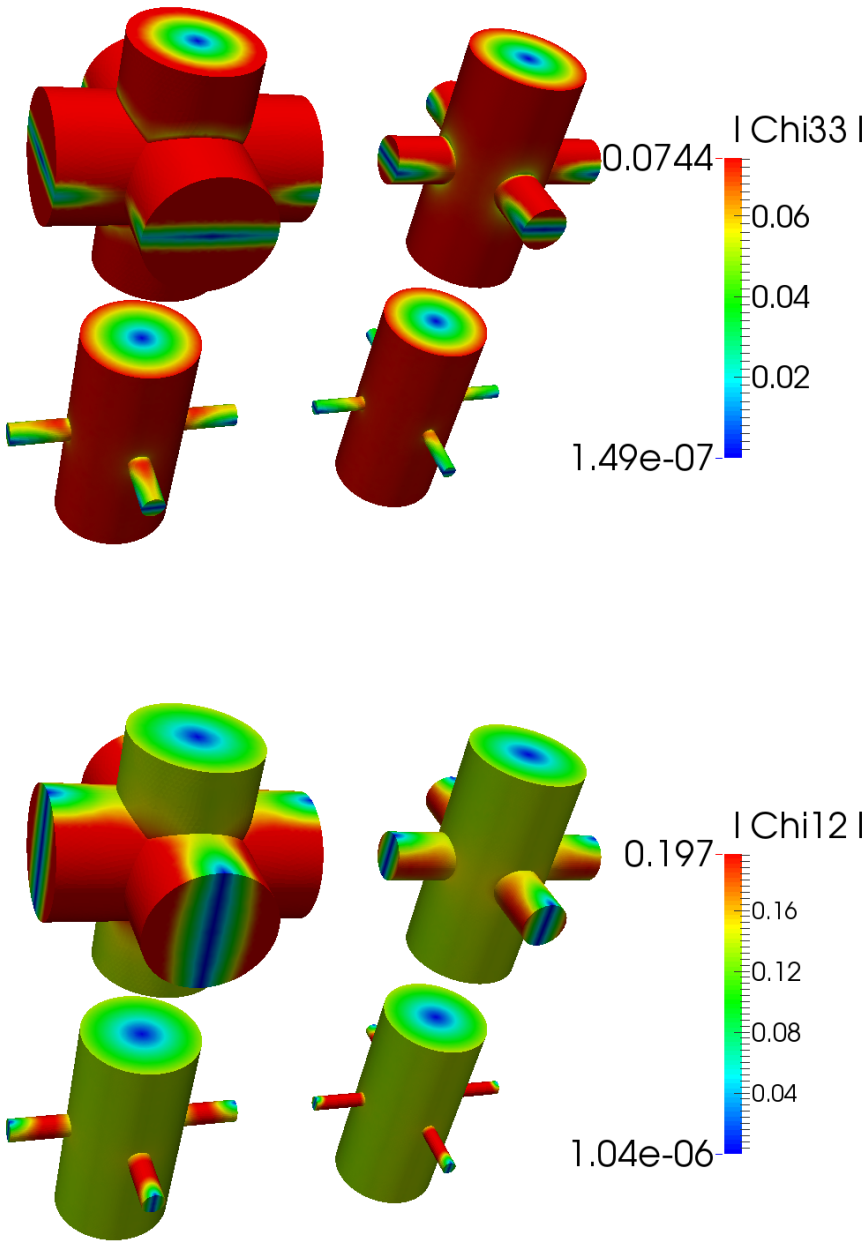

Figure 4.30: Magnitude of the vector field χ_i^{33} and χ_i^{12} for four different values of the ratio d/d_t: 1, 2.5, 5, 7.5.

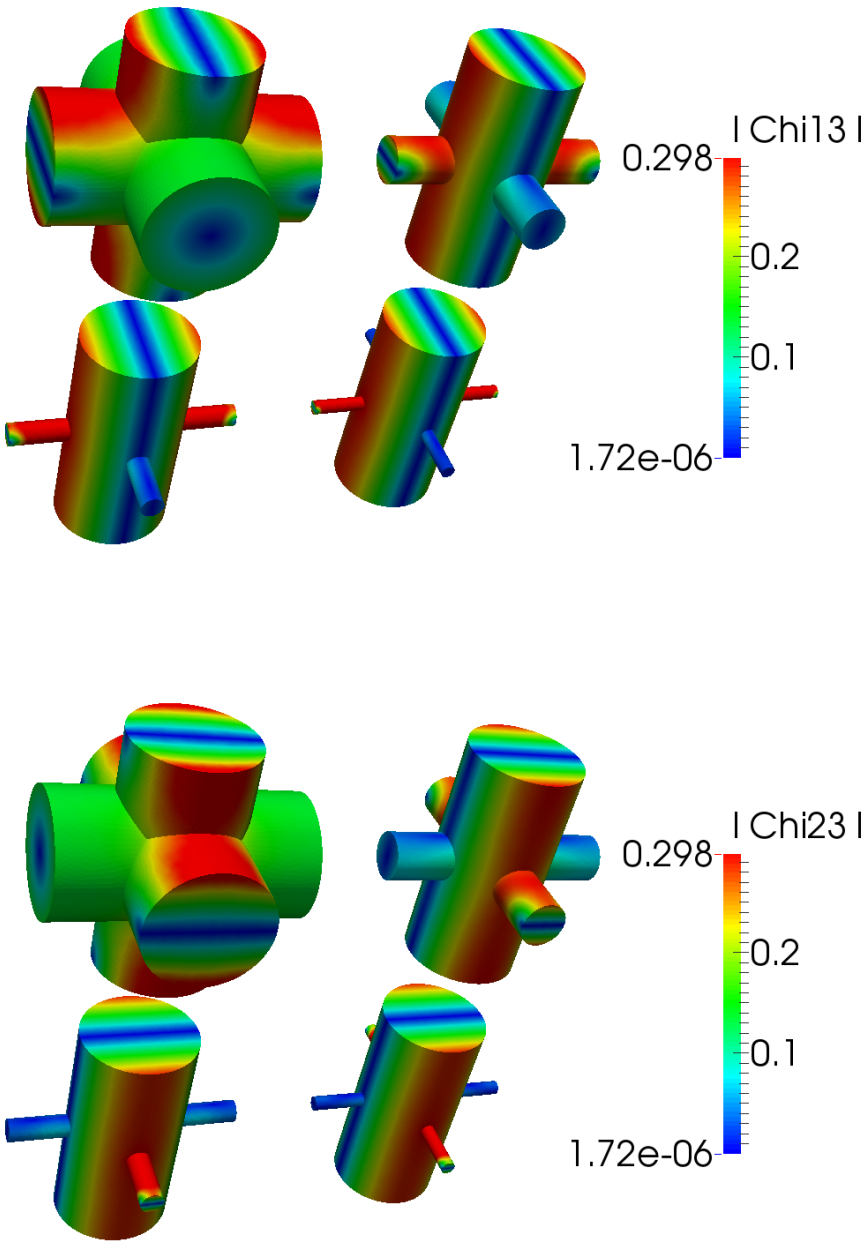

Figure 4.31: Magnitude of the vector field χ_i^{13} and χ_i^{23} for four different values of the ratio d/d_t: 1, 2.5, 5, 7.5.

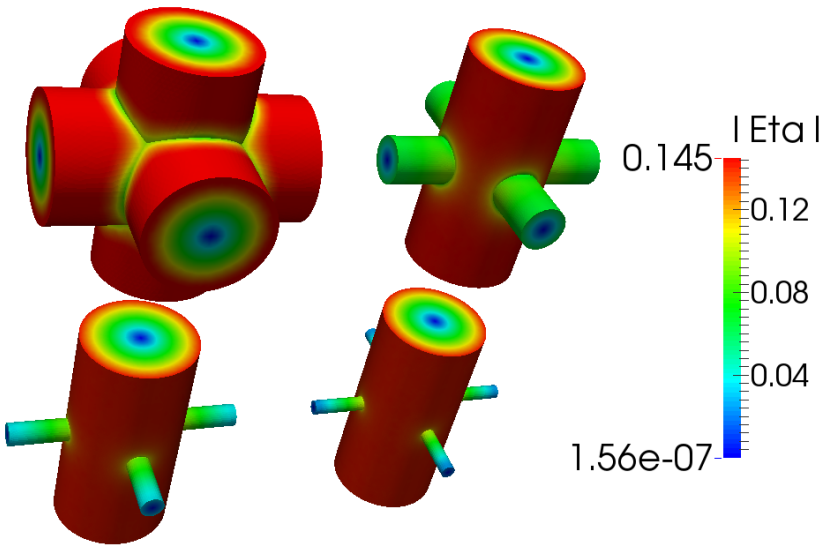

Figure 4.32: Magnitude of the vector field η for four different values of the ratio d/d_t: 1, 2.5, 5, 7.5.

values chosen for the linked cylinders geometry we have :

$$\mathcal{C}_{ijkl}^{d=d_t} = \begin{pmatrix} 0.2233 & 0.0314 & 0.0314 & 0 & 0 & 0 \\ 0.0314 & 0.2233 & 0.0314 & 0 & 0 & 0 \\ 0.0314 & 0.0314 & 0.2233 & 0 & 0 & 0 \\ 0 & 0 & 0 & 0.0117 & 0 & 0 \\ 0 & 0 & 0 & 0 & 0.0117 & 0 \\ 0 & 0 & 0 & 0 & 0 & 0.0117 \end{pmatrix},$$

$$\mathcal{C}_{ijkl}^{d=2.5d_t} = \begin{pmatrix} 0.0352 & 0.0020 & 0.0047 & 0 & 0 & 0 \\ 0.0020 & 0.0352 & 0.0047 & 0 & 0 & 0 \\ 0.0047 & 0.0047 & 0.2002 & 0 & 0 & 0 \\ 0 & 0 & 0 & -0.0072 & 0 & 0 \\ 0 & 0 & 0 & 0 & -0.0116 & 0 \\ 0 & 0 & 0 & 0 & 0 & -0.0116 \end{pmatrix},$$

$$\mathcal{C}_{ijkl}^{d=5d_t} = \begin{pmatrix} 0.0044 & 0.0010 & 0.0002 & 0 & 0 & 0 \\ 0.0010 & 0.0044 & 0.0002 & 0 & 0 & 0 \\ 0.0002 & 0.0002 & 0.1985 & 0 & 0 & 0 \\ 0 & 0 & 0 & -0.0060 & 0 & 0 \\ 0 & 0 & 0 & 0 & -0.0116 & 0 \\ 0 & 0 & 0 & 0 & 0 & -0.0116 \end{pmatrix}$$

and

$$\mathcal{C}_{ijkl}^{d=7.5d_t} = \begin{pmatrix} 0.0004 & 0.0020 & 0.0001 & 0 & 0 & 0 \\ 0.0020 & 0.0004 & 0.0001 & 0 & 0 & 0 \\ 0.0001 & 0.0001 & 0.1983 & 0 & 0 & 0 \\ 0 & 0 & 0 & -0.0048 & 0 & 0 \\ 0 & 0 & 0 & 0 & -0.0111 & 0 \\ 0 & 0 & 0 & 0 & 0 & -0.0111 \end{pmatrix}.$$

As one can observe, the structure realized with $d = d_t$ becomes isotropic because there are three planes of symmetry for the geometry, and the shape of $\mathcal{C}_{ijkl}$ is in accordance with the theory of solid mechanics (cf. Cowin (2013)). For the case $d = 2.5d_t$ the presence of the transverse cylinders is important, and this can be seen in the effective stiffness tensor which assumes the characteristic shape of transversely isotropic media. Increasing the ratio d/d_t, $\mathcal{C}_{ijkl}$ tends to that computed for the case of simple cylinders. The matrix α'_{ij} behaves in the same way (increasing d/d_t it tends to the α'_{ij} of the previous case):

$$\alpha_{ij}^{\prime d=d_t} = \begin{pmatrix} 0.5828 & 0 & 0 \\ 0 & 0.5828 & 0 \\ 0 & 0 & 0.5828 \end{pmatrix}, \alpha_{ij}^{\prime d=2.5d_t} = \begin{pmatrix} 0.7683 & 0 & 0 \\ 0 & 0.7683 & 0 \\ 0 & 0 & 0.7683 \end{pmatrix},$$

$$\alpha_{ij}^{\prime d=5d_t} = \begin{pmatrix} 0.7929 & 0 & 0 \\ 0 & 0.7929 & 0 \\ 0 & 0 & 0.7929 \end{pmatrix}, \alpha_{ij}^{\prime d=7.5d_t} = \begin{pmatrix} 0.7973 & 0 & 0 \\ 0 & 0.7973 & 0 \\ 0 & 0 & 0.7973 \end{pmatrix}.$$

Actually, also in this case, the values assumed by the diagonal components of α'_{ij} correspond to the porosities of each geometry, as clearly shown by table 4.4.

4.4 Touching spheres

One more geometry which relaxed the problem encountered for $\mathcal{C}_{ijkl}$ is an isotropic structure built as degeneration of the spherical case, by simply making the diameter of the sphere greater than the edge of the cubic elementary cell. The result is that the spheres touch each others, while maintaining a unique connected region of fluid.

4.4.1 The permeability tensor $\mathcal{K}_{ij}$

The effective values of permeability computed are obviously lower than the case of spheres and satisfies the properties due to the isotropicity of the microscopic structure. A sample case is shown in figure 4.33, realized using a radius for the sphere of 0.52, which gives a porosity of $\vartheta = 0.4159$. The averaged permeability is

$$\mathcal{K}_{ij} = 3.64 \cdot 10^{-5} \delta_{ij}$$

which is in accordance with the values obtained with the spheres for low porosities.

4.4.2 χ_i^{pq}, η_i, α'_{ij} and the effective elasticity tensor $\mathcal{C}_{ijpq}$

We have verified that also in this case the effective elasticity tensor satisfies isotropy. Figure 4.34 shows all the possible symmetries for χ_i^{pq} at a microscopic level; these symmetries can be verified at a macroscopic level observing that the off-diagonal components are equal to one another, and the diagonal components satisfy the equalities $\mathcal{C}_{1111} = \mathcal{C}_{2222} = \mathcal{C}_{3333}$ and $\mathcal{C}_{1212} = \mathcal{C}_{1313} = \mathcal{C}_{2323}$. The effective elasticity tensor is

$$\mathcal{C}_{ijkl} = \begin{pmatrix} 0.1493 & 0.0212 & 0.0212 & 0 & 0 & 0 \\ 0.0212 & 0.1493 & 0.0212 & 0 & 0 & 0 \\ 0.0212 & 0.0212 & 0.1493 & 0 & 0 & 0 \\ 0 & 0 & 0 & 0.0457 & 0 & 0 \\ 0 & 0 & 0 & 0 & 0.0457 & 0 \\ 0 & 0 & 0 & 0 & 0 & 0.0457 \end{pmatrix}.$$

Also in this case α'_{ij} can be written as $\vartheta\delta_{ij}$, i.e. $0.4159\delta_{ij}$.

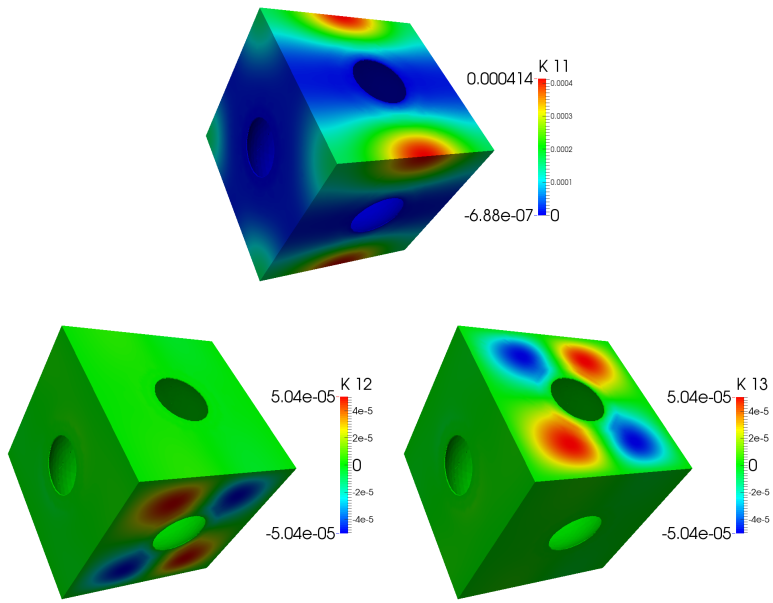

Figure 4.33: First row of $\mathcal{K}_{ij}$ for spherical inclusions of radius 0.52. The other rows can be realized by a permutation of the first one.

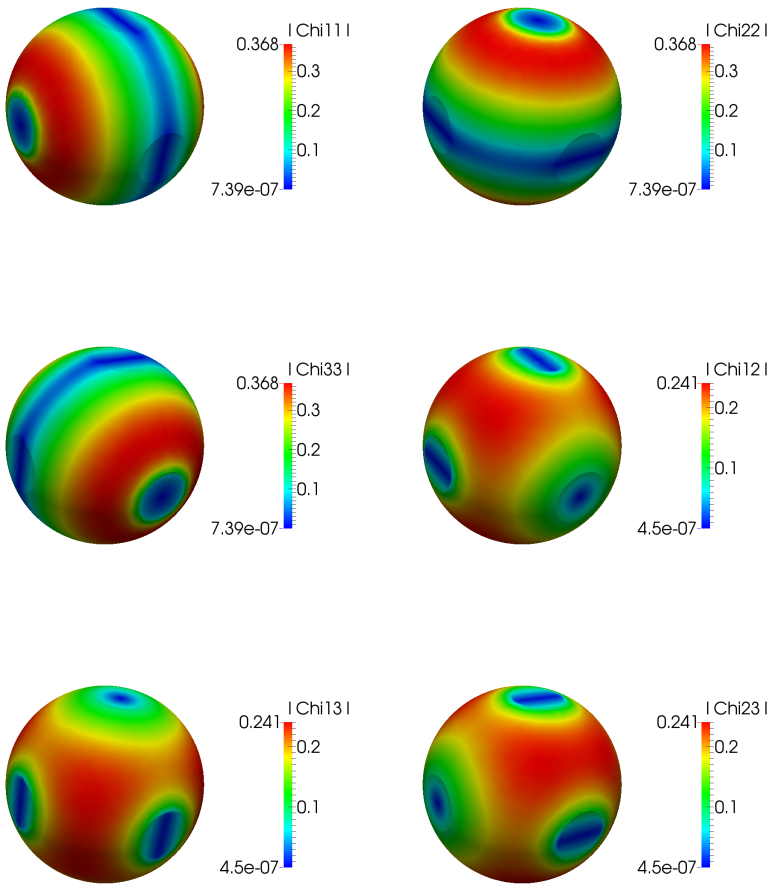

Figure 4.34: Magnitude of χ^{pq} for spherical inclusions of radius 0.52.

Chapter 5

Macroscopic results

Once the microscopic averaged quantities have been computed, the next step is to solve the effective equation of motion. The goal of the chapter is to show that the homogenized model is suitable also from a macroscopic point of view. In this chapter we present two applications, the first consists of lid-driven cavity filled in a certain zone by a homogeneous porous medium whether rigid or elastic, the latter is a canopy flow, only in the rigid case. All the results presented here are supposed to be invariant along x_2, i.e. they can be represented on the plane (x_1, x_3). From this moment on, the x_1 and x_3 directions are also named horizontal and vertical directions, respectively.

5.1 Summary of the macroscopic problems

For Re $= \mathcal{O}(\epsilon)$ the model is made by the following system of equations:

$$\begin{cases} (1-\vartheta)\dfrac{\partial^2 v_i^{(0)}}{\partial t^2} = \dfrac{\partial}{\partial x_j'}\left[\mathcal{C}_{ijpq}\varepsilon_{pq}'(\mathbf{v}^{(0)}) - \alpha_{ij}' p^{(0)}\right], \\ \dfrac{\partial \langle u_i^{(0)}\rangle}{\partial x_i'} = \langle \dfrac{\partial \chi_i^{pq}}{\partial x_i}\rangle \varepsilon_{pq}'(\dot{\mathbf{v}}^{(0)}) - \langle \dfrac{\partial \eta_i}{\partial x_i}\rangle \dot{p}^{(0)}, \\ \langle u_i^{(0)}\rangle - \mathcal{H}_{ij}\dot{v}_j^{(0)} = -\mathcal{K}_{ij}\dfrac{\partial p^{(0)}}{\partial x_j'}, \end{cases} \tag{5.1.1}$$

which is a system of three linear PDE's for the three macroscopic unknowns $\langle \mathbf{u}_i^{(0)} \rangle$, $\mathbf{v}^{(0)}$ and $p^{(0)}$ with respective boundary conditions. When $\mathrm{Re} = \mathcal{O}(1)$ system (5.1.1) can be replaced by

$$\begin{cases} (1-\vartheta)\dfrac{\partial^2 v_i^{(0)}}{\partial t_s^2} + \mathrm{Re}\bar{U}_j \langle \dfrac{\partial u_i^{(0)}}{\partial x_j} \rangle = \dfrac{\partial}{\partial x'_j}\left[\mathcal{C}_{ijpq}\varepsilon'_{pq}(\mathbf{v}^{(0)}) - \alpha'_{ij}p^{(0)}\right], \\ \dfrac{\partial \langle u_i^{(0)} \rangle}{\partial x'_i} = \langle \dfrac{\partial \chi_i^{pq}}{\partial x_i} \rangle \varepsilon'_{pq}(\dot{\mathbf{v}}^{(0)}) - \langle \dfrac{\partial \eta_i}{\partial x_i} \rangle \dot{p}^{(0)}, \\ \langle u_i^{(0)} \rangle - \mathcal{H}_{ij}\dot{v}_j^{(0)} = -\mathcal{K}_{ij}\dfrac{\partial p^{(0)}}{\partial x'_j}. \end{cases} \tag{5.1.2}$$

For the particular case of rigid structures, since $v_i^{(0)} = 0$, the equations above reduce to the system

$$\begin{cases} \langle u_i^{(0)} \rangle = -\mathcal{K}_{ij}\dfrac{\partial p^{(0)}}{\partial x'_j}, \\ \dfrac{\partial \langle u_i^{(0)} \rangle}{\partial x'_i} = 0. \end{cases} \tag{5.1.3}$$

In both cases the systems are coupled with the NSE normalized as in equation (3.2.8).

5.2 Lid-driven cavity

We focus our attention on anisotropic media and it is thus fundamental to consider a phenomenon characterized by at least two principal directions. We first solve for the flow in a composite domain, in which there is both a pure fluid region and a porous region formed by densely packed rigid fibres: the choice of considering a lid-driven cavity, filled up to a certain height (each fibre is long 0.33 times the side length of the square cavity) by the porous medium, as sketched in figure 5.1, allows us to analyze the orthotropic character of the medium. In fact, because of the non-negligible vertical velocity inside the porous region, we are able to quantify how much K_{33} affects the fluid flow and we can impose and compare different interface conditions. On the other hand, this case is more difficult than the classical pressure-driven channel flow with porous walls studied by many authors before. The configuration of the problem is shown in figure 5.1: a slip velocity is imposed on the top of a unitary square cavity and no-slip conditions are taken on the bottom and side walls.

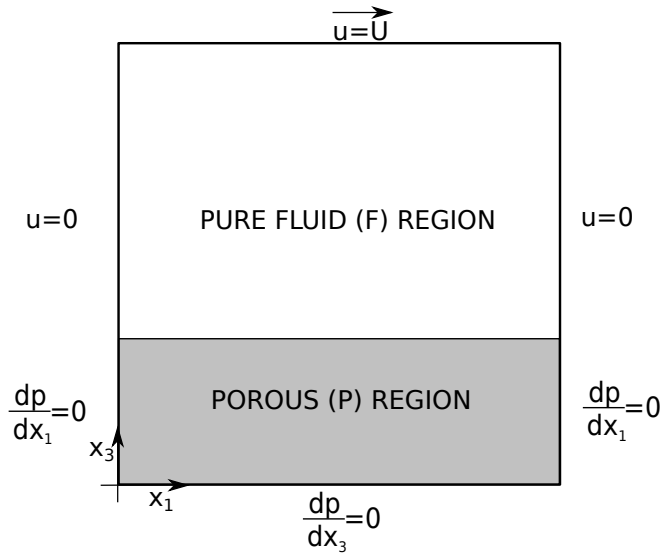

Figure 5.1: View of the macroscopic domain with the boundary conditions imposed when solving Darcy's equation in the P-region.

5.2.1 Rigid case

Many simulations have been done for varying ϑ and $\mathrm{Re}_L = LU/\nu$ where L (set equal to 1) is the side of the cavity and U (also equal to 1) is the slip velocity imposed at the top. Before doing a comparison for varying parameters, we must validate the macroscopic model and the interface conditions developed in chapter 3.

Validation with three dimensional direct numerical simulations which account for all fibers

In order to validate the homogenized model, compare the different interface conditions and assess which of them fits the problem analyzed in this work, three-dimensional direct numerical simulations (DNS) of the incompressible Navier-Stokes equations in the real geometry, accounting for all fibres (50 for the simulations presented here, so that $\epsilon = 0.02$) are performed with OpenFOAM. In the transverse direction (x_2) the size of the domain is taken equal to ϵ (in dimensionless terms)

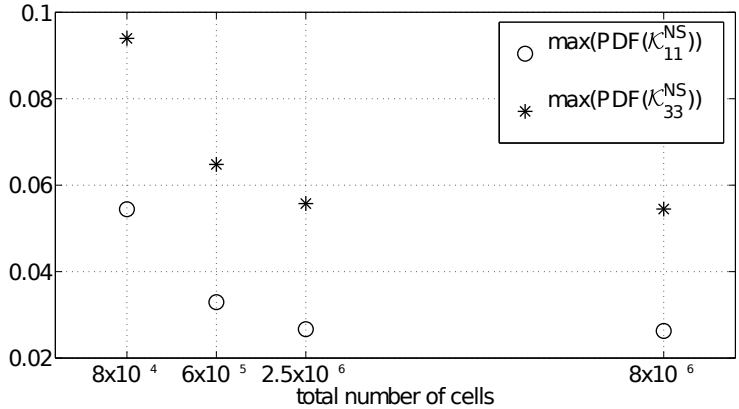

Figure 5.2: Spatial convergence study for the DNS in the case of $\mathrm{Re}_L = 100$. The different grids are built with the software snappyHexMesh (http://www.openfoam.org/version2.3.0/snappyHexMesh.php).

and periodic boundary conditions are enforced. The numerical mesh needed to have grid-converged solutions is formed by over 8 million cells for Re_L up to 1000; figure 5.2 provides an example of a convergence test for a measure (the PDF of the permeability components) introduced further on (§5.2.1). Figures 5.3, 5.4, 5.6 show a macroscopic view of the flow field in the cavity for the following parameters: $\mathrm{Re}_L = 1000$, $\epsilon = 0.02$ (i.e. 50 fibres), $\vartheta = 0.8$. The horizontal and vertical velocity are represented using two different scales: the fluid scale (upper frames of the corresponding figures) and the porous scale (lower frames). The presence of the fibers has a damping effect in the velocity field. So that, if we visualize the fields at a fluid scale the differences in the porous region cannot be appreciated. In these figures an oscillatory character of the velocity can be seen, due to the fact that no-slip condition has been imposed on the surface of each cylinder; this fact is also confirmed by figure 5.7 (which shows a sampling of u_1 and u_3 inside the porous region for a fixed x_3 and for varying x_2 in case of a simulation done using $\mathrm{Re}_L = 10$) and 5.5 where a slice of the steady converged solution for $\mathrm{Re}_L = 100$ at $x_3 = 0.25$ (thus within the porous medium) is shown, through isocontours of the first velocity component, near the solid boundaries and around $x_1 = 0.5$. The figure also shows a cut through the numerical grid.

With the results from the DNS we can:

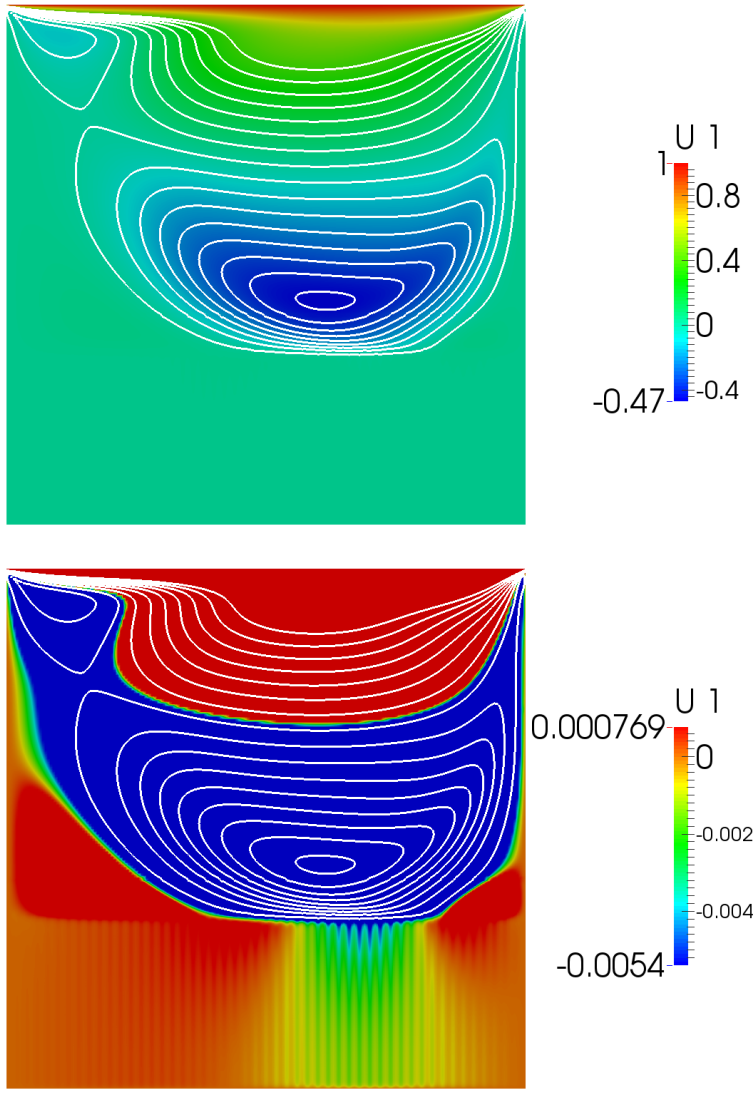

Figure 5.3: Isocontours of the horizontal velocity in the unitary square cavity for $\mathrm{Re}_L = 1000$, $\vartheta = 0.8$ and $\epsilon = 0.02$. Two different ranges of values are used to represent the same flow.

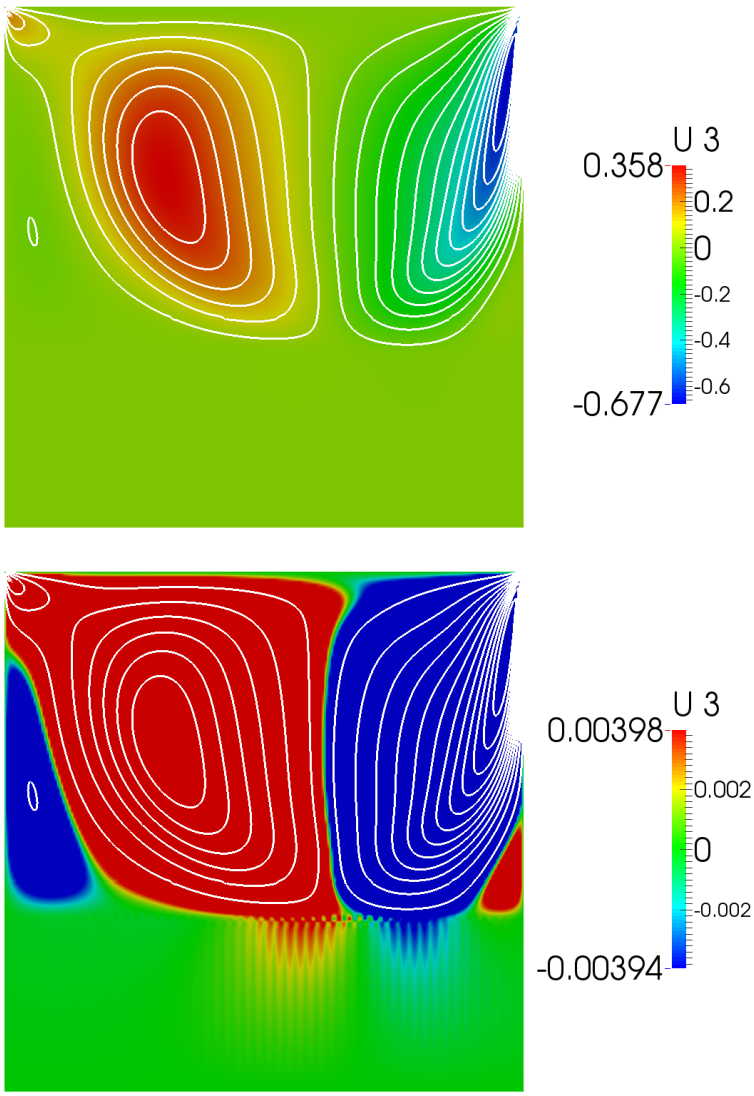

Figure 5.4: Isocontours of the vertical velocity in the unitary square cavity for $\mathrm{Re}_L = 1000$, $\vartheta = 0.8$ and $\epsilon = 0.02$.

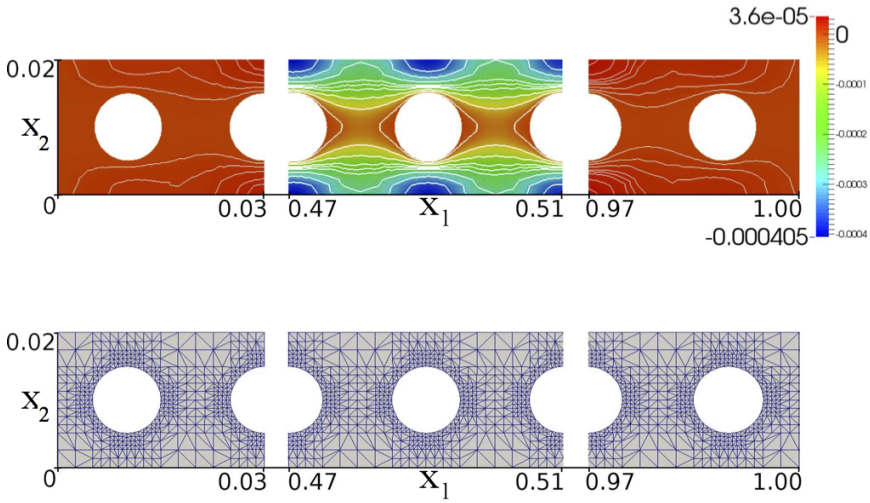

Figure 5.5: Zoom of the macroscopic domain of the DNS inside the porous medium with $\vartheta = 0.8$. Slice of the cavity at $x_3 = 0.25$. Only few cylinders (out of 50) are shown inside and at the extremities of the cavity. The colours and the white curves in the top frame represent the x_1-component of the velocity field and its isocontours. In the lower frame a cut through the grid is shown.

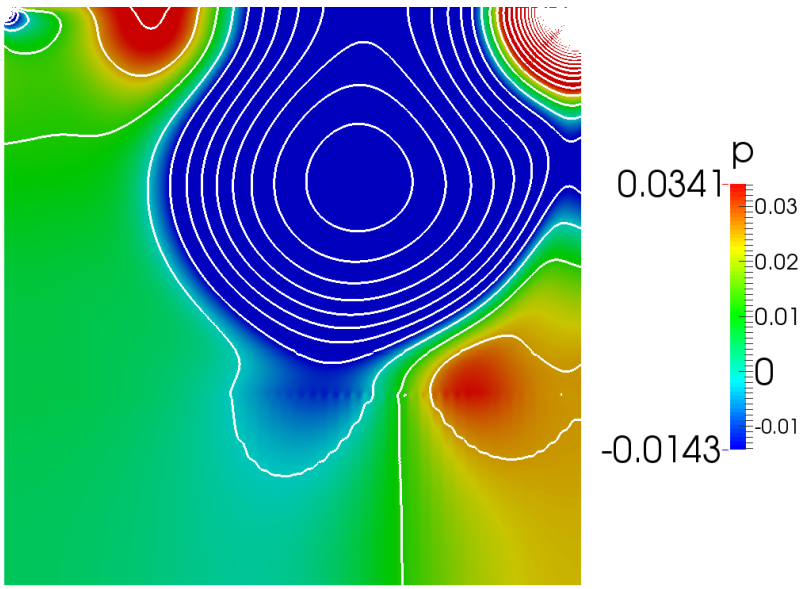

Figure 5.6: Isocontours of the pressure field in the unitary square cavity for $\mathrm{Re}_L = 1000$, $\vartheta = 0.8$ and $\epsilon = 0.02$.

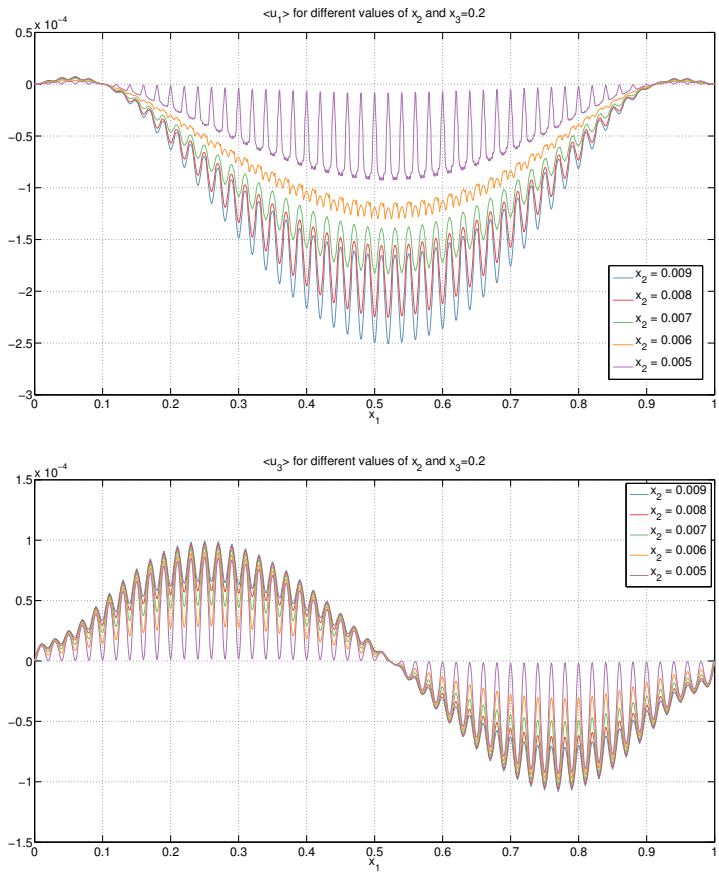

Figure 5.7: Pointwise values of the velocity components found through the DNS; the values are used to compute the average over each elementary cell of fig. 5.8) and to obtain K_{33}^{NS}. $x_3 = 0.2$, $Re = 10$, $\vartheta = 0.8$, $\epsilon = 0.02$. The oscillatory behavior of the velocity is due by the fact that the no-slip condition is imposed over each cylinder.

(*i*) evaluate the components of the permeability tensor and verify the results of homogenization theory;

(*ii*) test the different interface conditions and, for example, calibrate the constant c in the definition of δ (equation 3.3.3), calibrate the parameter μ_e in the Brinkman's equation and the shape of the filter in section 3.5;

(*iii*) validate the unknown fields at a macroscopic level, verifying the appropriateness of the homogenized equations.

To compare the DNS results with the two-dimensional simulations described in the previous section we must extract in a proper way the averaged values of the fields: the whole domain is thus decomposed into elementary cubic cells of size ϵ^3 (some of them are sketched in figure 5.8) and all fields are averaged over each micro-cell using the definition (2.1.16); in this way two-dimensional fields are obtained from the DNS results and, in particular, we have a sampling of the solution in the porous medium (in the case of a layer of N filaments of height 0.33 we have a cartesian grid, with velocity components and pressure centered in the cell, composed by $0.33\,N^2$ elements in P). The values of the averaged velocity field for a simulation with $\mathrm{Re}_L = 10$ is shown in figure 5.9. The spatial average has a smoothing effect on the solution. Furthermore, the averaged velocity near the walls of the cavity is not zero as its pointwise counterpart, fact that will be seen also in the solution of the homogenized model. Using the grid built, the pressure gradient is computed with fourth order finite differences with the scheme described in Appendix A.2. In the internal region of the porous medium, assuming that Darcy's approximation is valid (i.e. $\langle \mathbf{u}^{DNS} \rangle = \langle \mathbf{u}^{(0)} \rangle$ and $\langle p^{DNS} \rangle = p^{(0)}$), $\mathcal{K}_{ij}$ is computed using equation (3.2.5). Finally, we need to account for the influence of the wall/interface boundary layers and for the presence of isolated regions in which the pressure gradient becomes negligibly small; thus, the values of $\mathcal{K}_{ij}^{DNS}$ (superscript DNS is used to indicate that the value has been estimated on the basis of the full simulations) are evaluated on the basis of their probability density functions (PDF). To compute the PDF we divide the values of $\mathcal{K}_{ii}$ in a number of intervals such that each one of them has an extent equal to 10% of the value of $\mathcal{K}_{ii}$ for which we find the maximum of the PDF.

The components of the permeability tensor

Direct numerical simulations have been performed for Reynolds numbers Re_L varying from 1 to 1000, for fixed value of $\epsilon = 0.02$ and $\vartheta = 0.80$. The a-posteriori

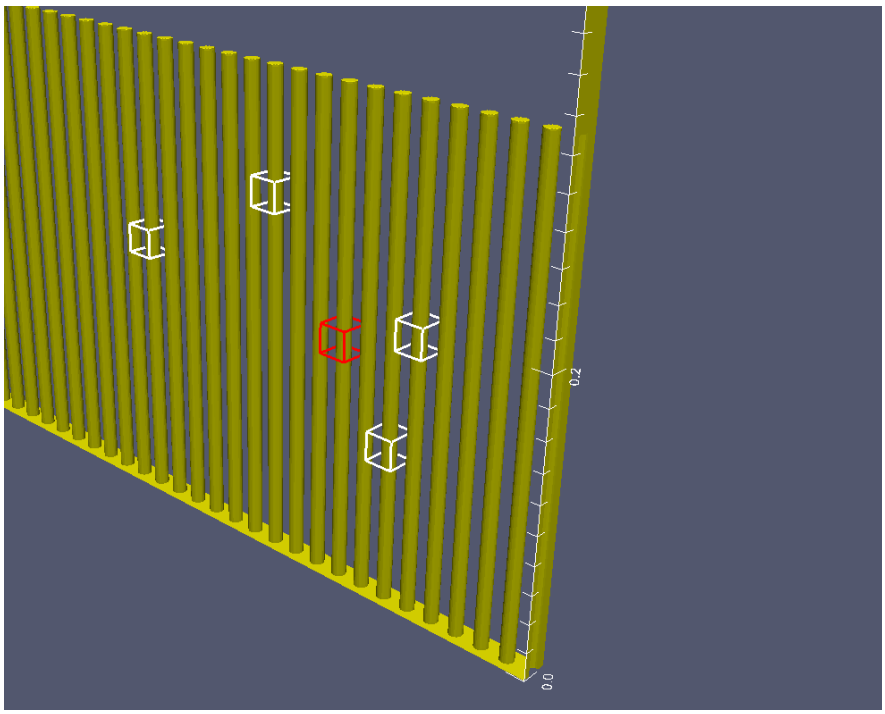

Figure 5.8: Sample case of the unitary cavity filled with $N = 50$ cylinders of height $h = 0.33$ and radius $r = 0.00504$ ($\vartheta = 0.8$). b) View of some elementary cells over which the fields are averaged. The dimension of the cubic cell is set by the dimension and number of the filaments.

treatment of the DNS results within the porous medium permits to extract the value of the permeability components over each elementary cubic cell, yielding the probability density functions displayed in fig. 5.10. It is immediately apparent that the PDF pinpoints sharply the values of $\mathcal{K}_{11}$ and $\mathcal{K}_{33}$ for Re_L up to 100, whereas for larger Re_L's the two components of the permeability display a broader variability. The peak values are nonetheless well defined and are reported in table 5.1, against corresponding results from the homogenization theory. The latter have been computed including inertial terms in the equations, with the same U_p found in the direct simulations of the full geometry. The values of the permeability components from the DNS are about 40% larger than those from the theory. We have seen (fig. 4.22)

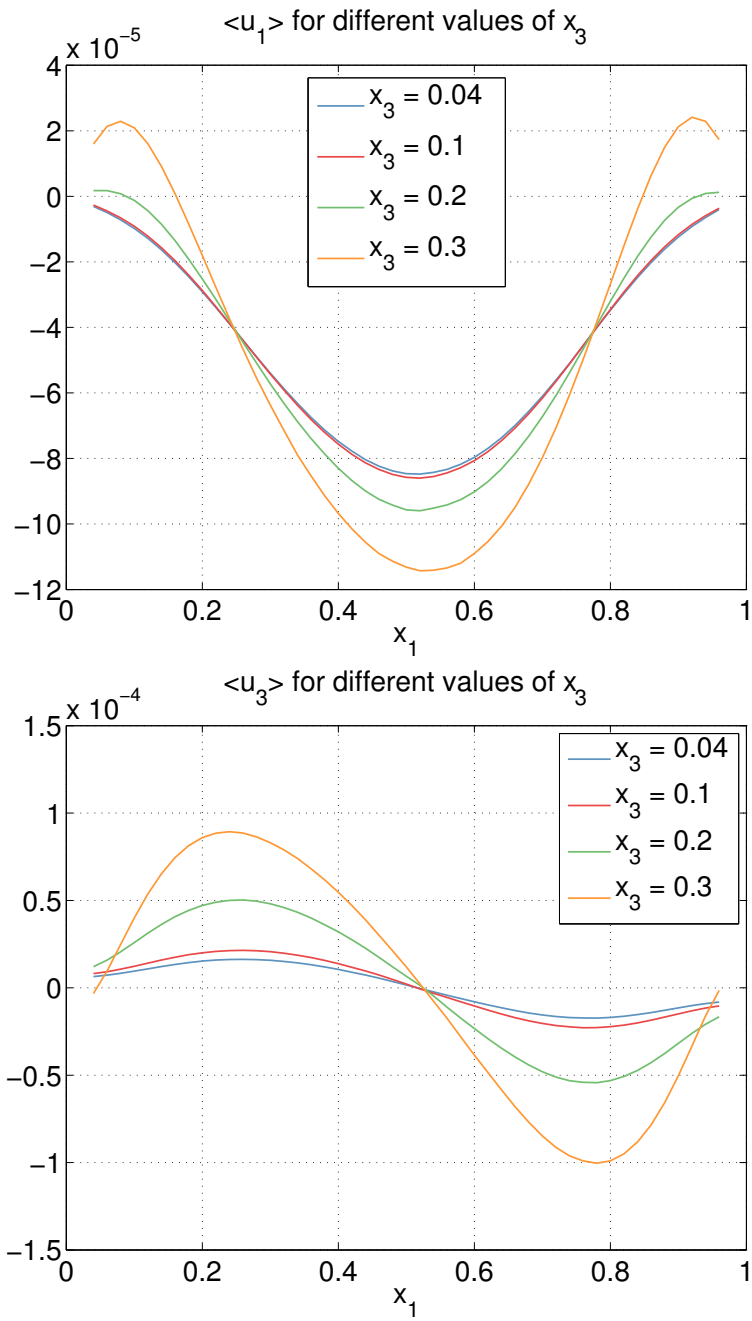

Figure 5.9: Averaged values of the velocity u_1 and u_3 computed from the data in figure 5.7. Smooth curves are obtained from the averaging procedure.

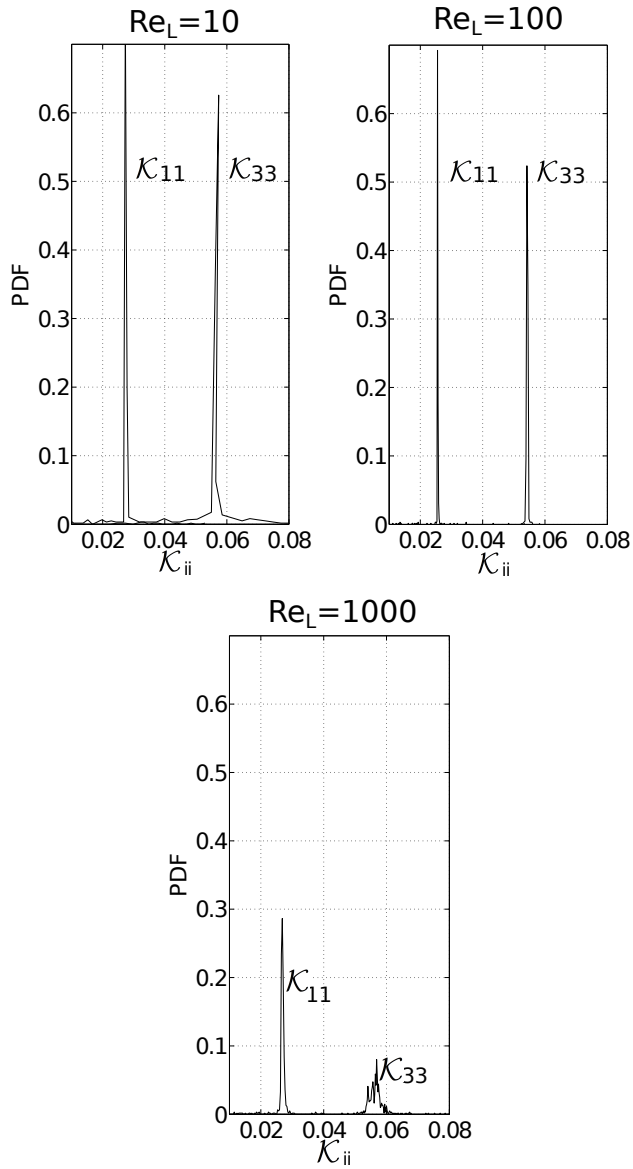

Figure 5.10: Probability density function of $\mathcal{K}_{11}$ and $\mathcal{K}_{33}$ for different values of Re_L. The apparent permeability is computed a posteriori applying Darcy's law to the averaged solution of the DNS.

that the same occurs also in the test case of canopy flow (which will presented later on), under turbulent conditions, for low values of $\vartheta \mathrm{Re}_p$. In the narrow range of pore Reynolds number considered here, the full simulations do not allow to extract a clear trend of how the permeability varies, whereas the theory indicates a slow decrease of both components with Re_p.

The disagreement between theory and direct simulations appears to be relatively mild, when seen in the scale of fig. 4.21, but nonetheless deserves to be clarified, since it occurs also for flow cases ($Re_L = 1$) in which the motion of the fluid through the pores is clearly ruled by Stokes equation. We believe that, on the one hand, the flow geometry plays a role here, since the two sidewalls constrain the fluid, forcing it to recirculate; a much better agreement would have been obtained had we considered a pressure-driven channel flow, like done by many authors Le Bars & Worster (2006); Hill & Straughan (2008); Battiato (2012). On the other hand, we would expect a closer match between the DNS results and the theory had we pushed the asymptotic development to third order, modifying Darcy's equation with a cubic Forchheimer term, as described by Mei & Vernescu (2010). This is indirectly supported by one direct simulation at $\mathrm{Re}_L = 100$, conducted with 200 fibres (instead of 50) – for which the small parameter ϵ of the expansion is small (and equal to 0.005), for the same porosity coefficient $\vartheta = 0.80$ – yielding values of the apparent permeability closer to the theoretical ones in table 5.1.

In the following, the results from the three-dimensional numerical simulations will be compared to results from the coupled two-dimensional Navier-Stokes/Darcy equation, where in the latter model the values used for the apparent permeability are those of the direct numerical simulations.

The macroscopic fields

A representative comparison between the DNS results and those from the model system is displayed in figure 5.11 and 5.12 in terms of the streamlines of the flow and the pressure field, respectively. In the model system we have enforced interface conditions described in 3.3, with $\delta = \varepsilon/5$, i.e. we have used the penetration depth δ that, as we will show, yields the best agreement between the model and the direct simulations. The results are very close to one another and, in particular, the complex behavior of the flow within the porous domain appears to be correctly captured by Darcy's equation (with a tensorial permeability). Also the pressure field of the homogenized model matches that of the DNS with the $constant$ term of equation (3.3.1) appropriately chosen.

	ϑU_p	$\vartheta \mathrm{Re}_p$	$\mathcal{K}_{11}^{DNS}$	$\mathcal{K}_{33}^{DNS}$	$\mathcal{K}_{11}$	$\mathcal{K}_{33}$	d_1/ϵ	d_3/ϵ
$\mathrm{Re}_L = 1$	$4.40 \cdot 10^{-5}$	$0.88 \cdot 10^{-6}$	$2.62 \cdot 10^{-2}$	$5.44 \cdot 10^{-2}$	$1.89 \cdot 10^{-2}$	$3.95 \cdot 10^{-2}$	3	1.5
$\mathrm{Re}_L = 10$	$4.50 \cdot 10^{-5}$	$0.90 \cdot 10^{-5}$	$2.66 \cdot 10^{-2}$	$5.57 \cdot 10^{-2}$	$1.89 \cdot 10^{-2}$	$3.95 \cdot 10^{-2}$	2.7	1.5
$\mathrm{Re}_L = 100$	$7.01 \cdot 10^{-5}$	$0.14 \cdot 10^{-3}$	$2.63 \cdot 10^{-2}$	$5.49 \cdot 10^{-2}$	$1.89 \cdot 10^{-2}$	$3.94 \cdot 10^{-2}$	2.5	1.5
$\mathrm{Re}_L = 1000$	$2.04 \cdot 10^{-4}$	$0.41 \cdot 10^{-2}$	$2.65 \cdot 10^{-2}$	$5.63 \cdot 10^{-2}$	$1.87 \cdot 10^{-2}$	$3.93 \cdot 10^{-2}$	2.5	1.5

Table 5.1: Values of the permeability components from the DNS and homogenization theory. U_p represents the dimensionless mean pore velocity in the whole porous medium. Because of continuity, the mean pore velocity is oriented only along x_1. d_1 and d_3 are the distances from the interface starting from which $\mathcal{K}_{11}$ and $\mathcal{K}_{33}$ can be assumed constant when condition **C** is applied (cf. figure 5.23).

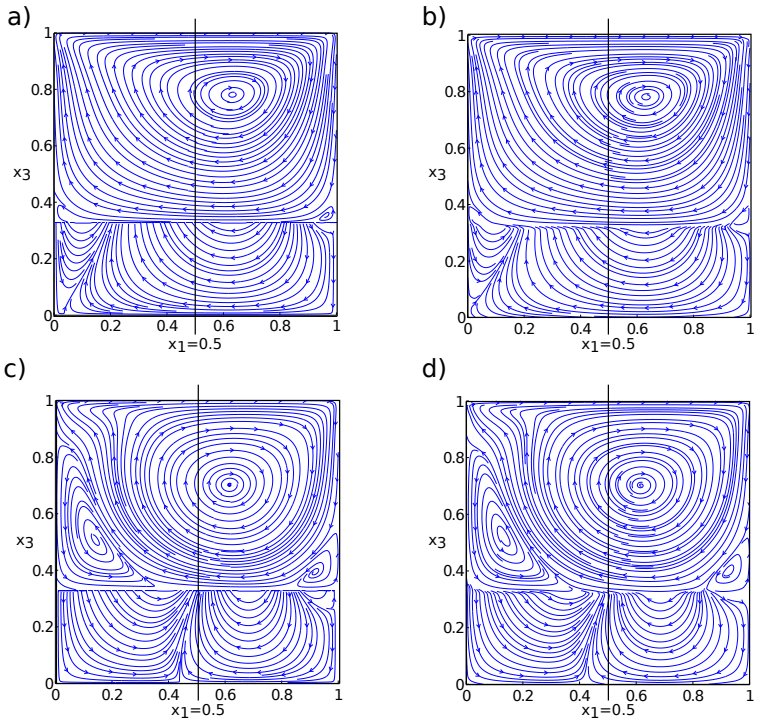

Figure 5.11: Streamlines in the composite domain. Frames $a)$ and $b)$ represent the solution for $\mathrm{Re}_L = 100$; $c)$ and $d)$ display results for $\mathrm{Re}_L = 1000$. In all cases the porosity is $\vartheta = 0.80$. The frames on the left show solutions of the homogenized model, the right frames are the DNS results. Representative velocity profiles will be later displayed along the vertical lines $x_1 = 0.5$.

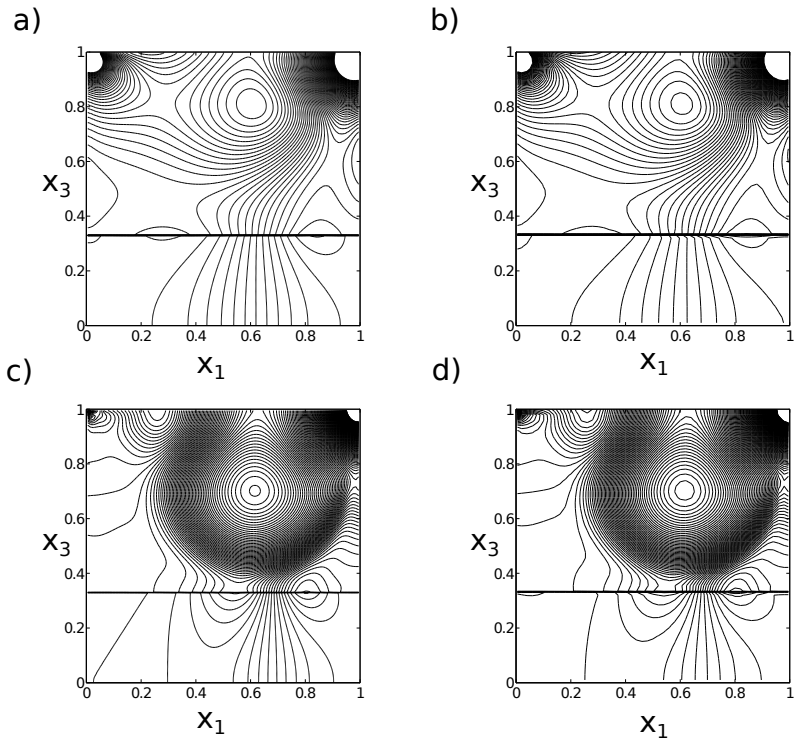

Figure 5.12: Isocontours of the pressure field in the composite domain. Frames $a)$ and $b)$ represent the solution for $\mathrm{Re}_L = 100$; $c)$ and $d)$ display results for $\mathrm{Re}_L = 1000$. In all cases the porosity is $\vartheta = 0.80$. The frames on the left are the solutions of the homogenized model, the right frames are the DNS results.

It is noticeable the fact that for different interface conditions the results are qualitatively similar, and all the model solutions look “correct", with minor differences noticeable. These differences can be appreciated near the interface and inside the porous medium. A closer look at the interfacial and porous zone is needed.

Focus on the interface

To assess the quality of the interface conditions we focus on $x_1 = 0.5$. The first condition presented in 3.3 yields the results displayed against the DNS solution in figures 5.13 and 5.14, for $\mathrm{Re}_L = 100$. A value of δ between 0 and $\epsilon/5$ provides a good fit with the DNS in the F-region and at the interface, whereas increasing δ above $\epsilon/2$ yields values of both velocity components near the interface which progressively overestimate the “true" values. Within the porous domain ($x_3 \leq 0.25$), the difference between the solutions computed for varying δ's and the DNS is negligible. When Re_L is equal to 1000, an excellent agreement with the DNS results is achieved for $\delta = \epsilon/5$, as shown in figures 5.15 and 5.16. It is important to notice that a poor choice of δ (e.g. $\delta \geq \varepsilon$) degrades the solution also in the fluid region F, as fig. 5.15 clearly demonstrates. As far as interface condition 3.3 is concerned, thus, we observe an increase of the penetration depth, δ, with Re_p, as one would intuitively expect. This fact will be confirmed also by the second application presented later on canopy flows.

We now turn to interface condition 3.4. Brinkman's equation has been discretized and directly matched to Navier-Stokes results in the F-region; the velocity profiles obtained at $x_1 = 0.5$ are compared to the reference profiles in figure 5.21, for $\mathrm{Re}_L = 100$ and different values of the effective viscosity, focusing on the region across the interface and within the porous domain. As μ_e approaches zero the Darcy limit is recovered; the upper value of μ_e/μ considered is 30, close to that determined experimentally by Givler & Altobelli (1994), which are similar to the values recovered by the DNS, applying the Brinkman's equation *a posteriori* (cf. figures 5.17 and 5.18). Furthermore, even the theoretical value, $\mu_e/\mu = (1-\vartheta)^{-1} = 5$, deduced on the basis of volume averaging theory by Ochoa-Tapia & Whitaker (1995), has been tested. We can observe that a value of the effective viscosity which is either too large (30) or too small (0.3) degrades significantly the solution in the F-region, as a direct consequence of the poor estimation of the velocity in the proximity of the interface. Conversely, when μ_e is a few times larger than the dynamic viscosity of the fluid, i.e. it is close to the theoretical approximation, the solution appears to behave better, when compared to the DNS, although close inspection

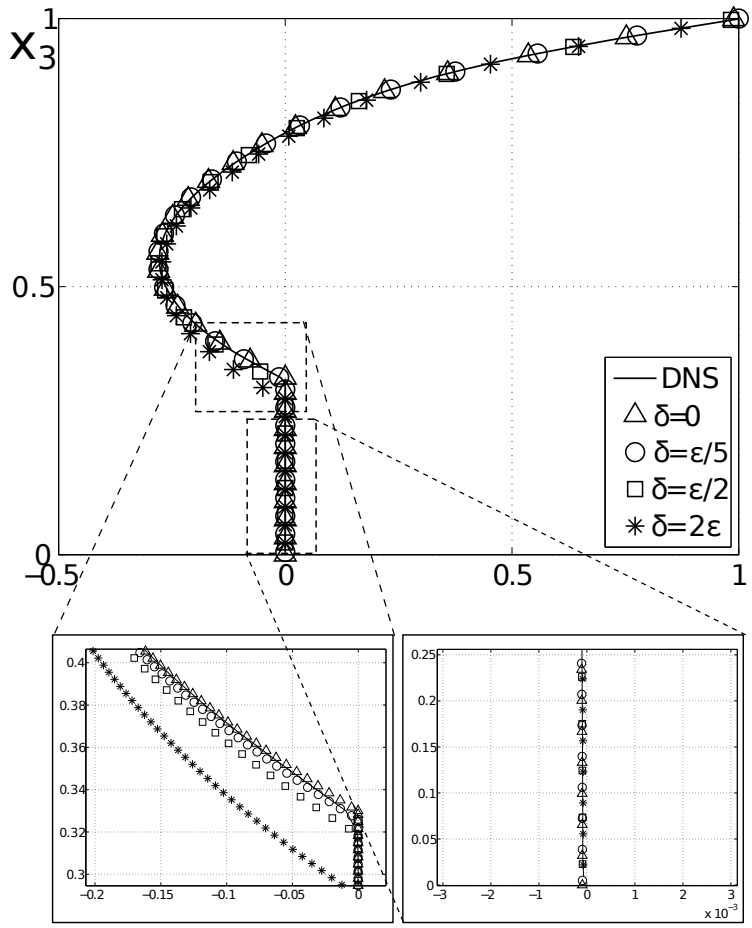

Figure 5.13: View of the macroscopic profile of u_1 and u_3 (lower frames) for $x_1 = 0.5$ (middle of the cavity) for the DNS and four choices of δ ($\mathrm{Re}_L = 100$). Two zooms are highlighted at the interface. Interface strategy: 3.3.

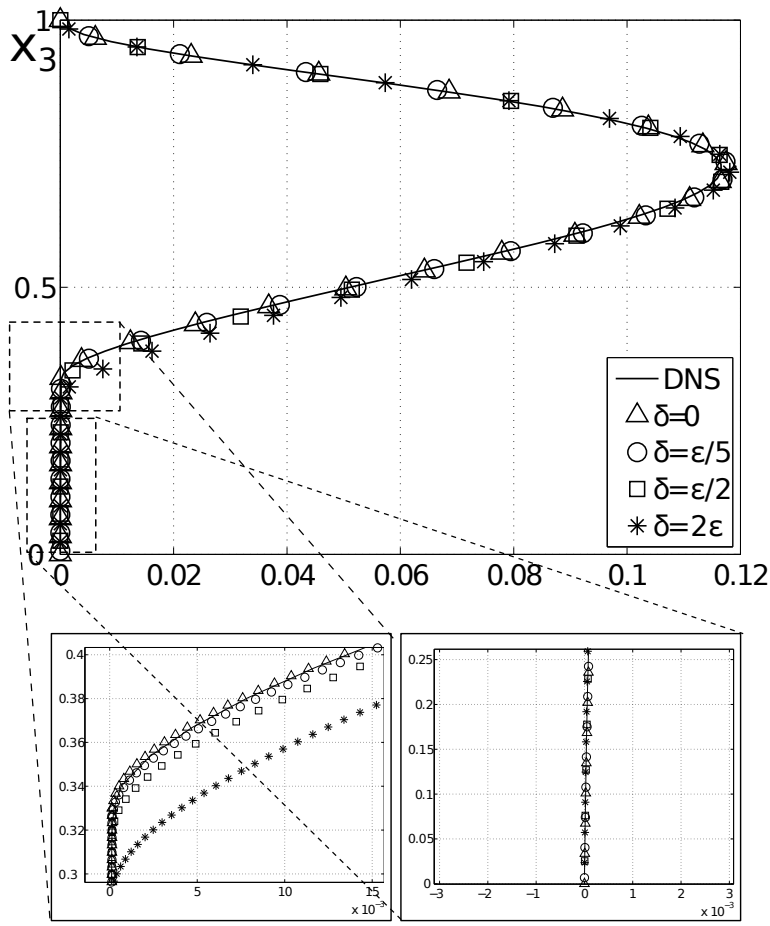

Figure 5.14: View of the macroscopic profile of u_3 for $x_1 = 0.5$ for the DNS and four choices of δ ($\mathrm{Re}_L = 100$).

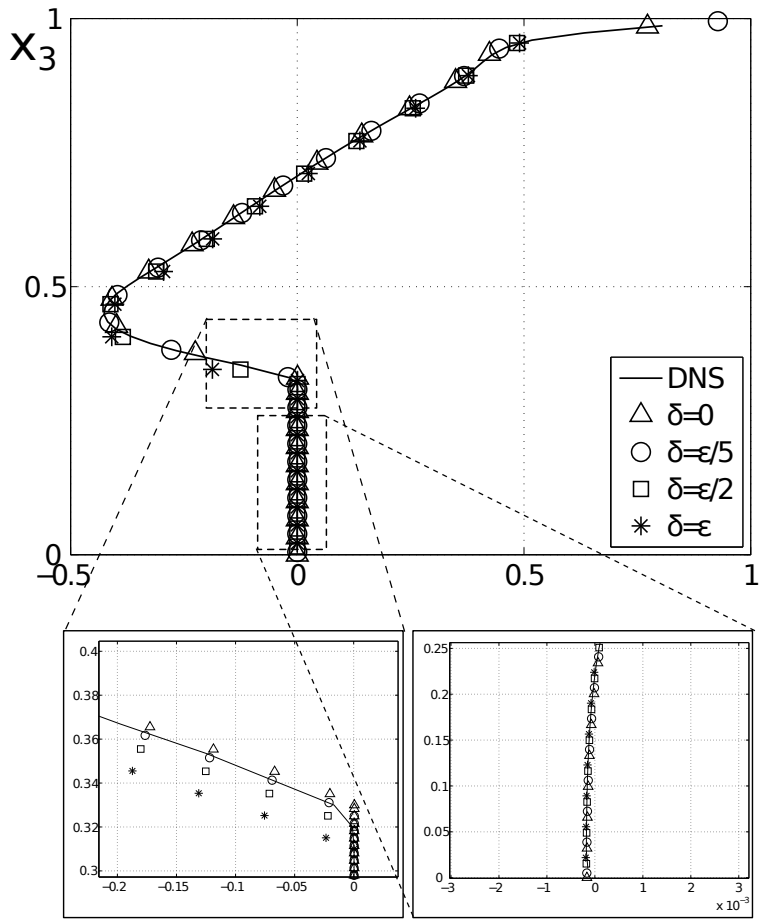

Figure 5.15: View of the macroscopic profile of u_1 and u_3 (lower frames) for $x_1 = 0.5$ for the DNS and four choices of δ ($\mathrm{Re}_L = 1000$). Interface strategy: 3.3.

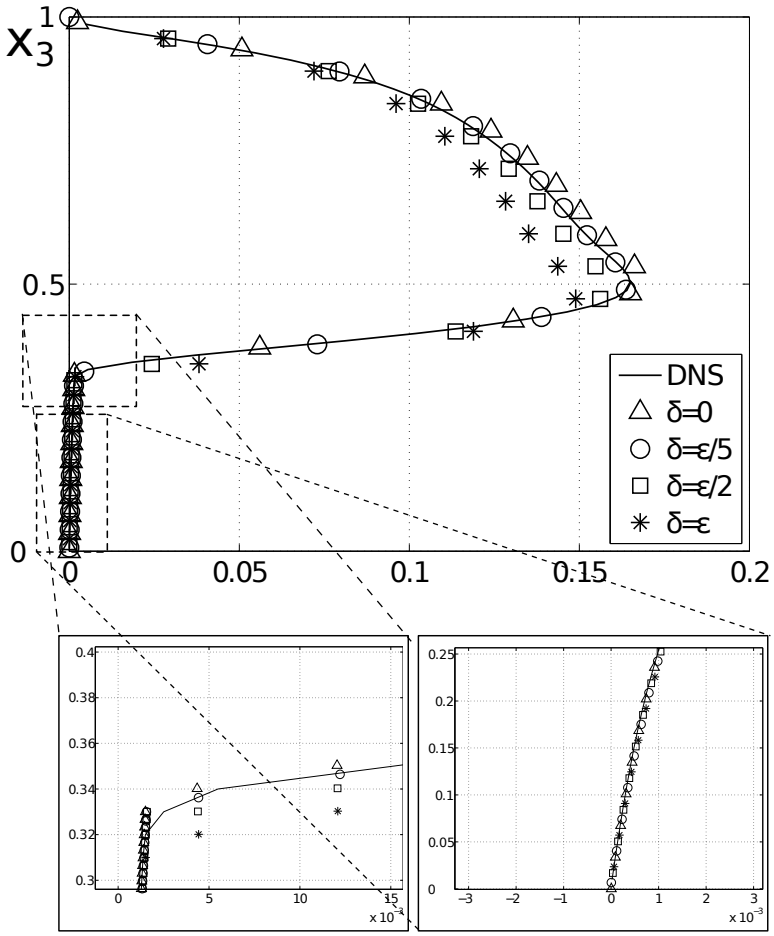

Figure 5.16: View of the macroscopic profile of u_3 for $x_1 = 0.5$ for the DNS and four choices of δ ($\mathrm{Re}_L = 1000$). Notice how for $\delta = \varepsilon$ the vertical velocity is significantly underestimated in the F-region at $x_1 = 0.5$, whereas $\delta = \varepsilon/5$ provides the best match between the two sets of results throughout the whole domain.

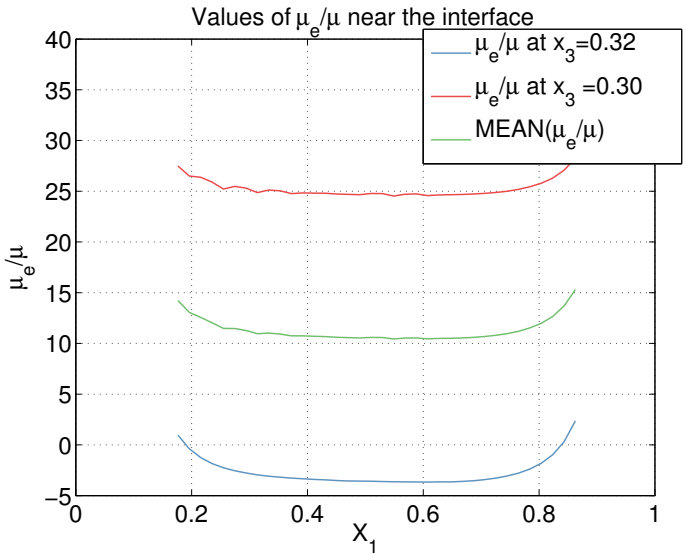

Figure 5.17: Values of the viscosity in the interface region, $\mathrm{Re}_L = 10$, $\theta = 0.8$. The values near the wall are neglected.

of the fields within the porous region (not shown) denote differences between the model solution and the "exact" result which are larger than those found with interface strategy 3.3. This negative aspect of Brinkman's model, coupled to the fact that the effective viscosity is not available a priori, can be somehow tempered by the fact that Brinkman's equation naturally creates boundary layers near the solid walls where the velocity is smoothly driven to zero. A similar conclusion on the poor performance of Brinkman's model in handling porous-fluid interfaces has also been reported by James & Davis (2001).

Results from the interface condition 3.5 are displayed in figure 5.23 and 5.24; here the permeability varies as the macroscopic interface (at $x_3^{ITF} = 0.33$) is approached. Whereas this is physically reasonable, it is unknown how the permeability should be taken to vary. In this specific case we use the DNS results to define the shape of the filter to apply on $\mathcal{K}$. The permeability inside the porous medium is recovered using Darcy's law as explained in the previous section. Figures 5.19 and 5.20 show the values of permeability found in the porous region. The peaks corresponds to the region where $\partial p/\partial x_1 = 0$ or $\partial p/\partial x_3 = 0$ due to the particular

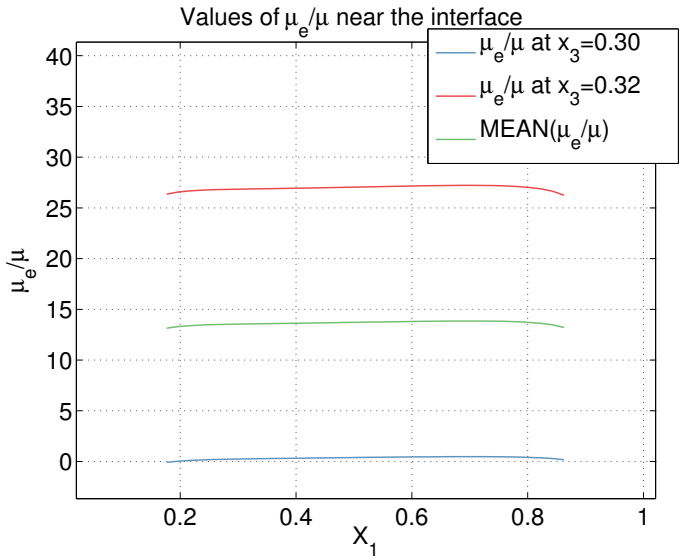

Figure 5.18: Values of the viscosity in the interface region, $\mathrm{Re}_L = 100$, $\theta = 0.8$. The values near the wall are neglected.

configuration of the flow. Here, we need a value of permeability for each x_3 in the porous zone. It is sampled for each x_1 in the cavity and then a mean value along the x_1 direction is extrapolated (solid and dotted lines of figure 5.23). It is clear that up to a distance $d = \mathcal{O}(\epsilon)$ from the interface the value of $\mathcal{K}_{ii}$ is constant; then it increases. In particular we observe that for the case $\mathrm{Re}_L = 100$ shown in figure 5.23 the component $\mathcal{K}_{11}$ has $d_1 = \frac{5}{2}\epsilon$, while for $\mathcal{K}_{33}$ it is $d_3 = \frac{3}{2}\epsilon$. This seems to indicate that $\mathcal{K}_{ii}^{-1}$ is proportional to d_i; in Table 5.1 this trend is further explored for varying values of Re_L. The distance d_i $(i = 1, 3)$ defines an interfacial layer whose thickness decreases slowly with the increase of the Reynolds number Re_L. In this it differs from the protrusion height δ of the fictitious interface approach. The agreement at the interface between the homogenized solution and the solution of the DNS is however not very good (cf. fig 5.24); this is probably due to the fact that near the interface Darcy's law is inappropriate and a model which accounts for inertia is needed.

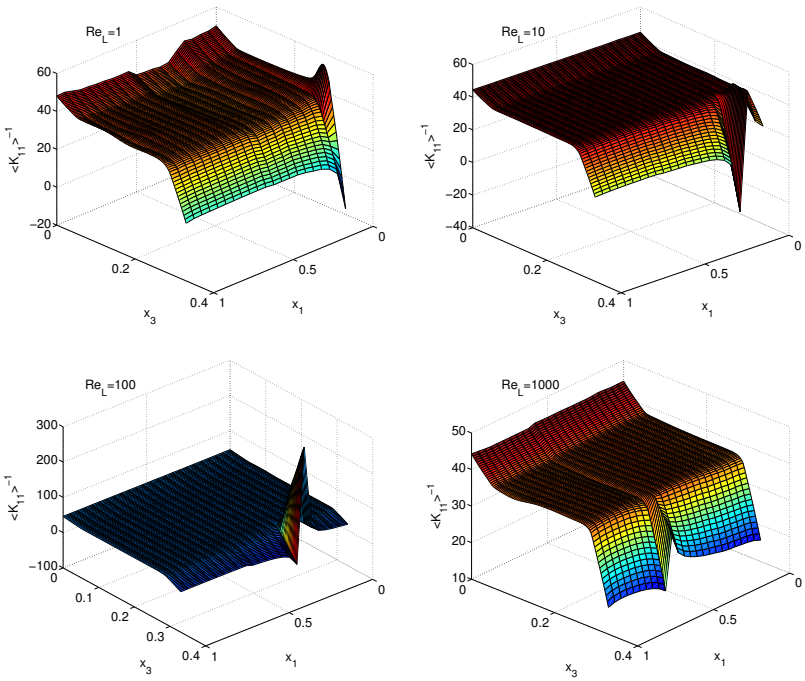

Figure 5.19: Pointwise values of $\mathcal{K}_{11}$ inside the porous region deduced from the DNS, for different Re_L.

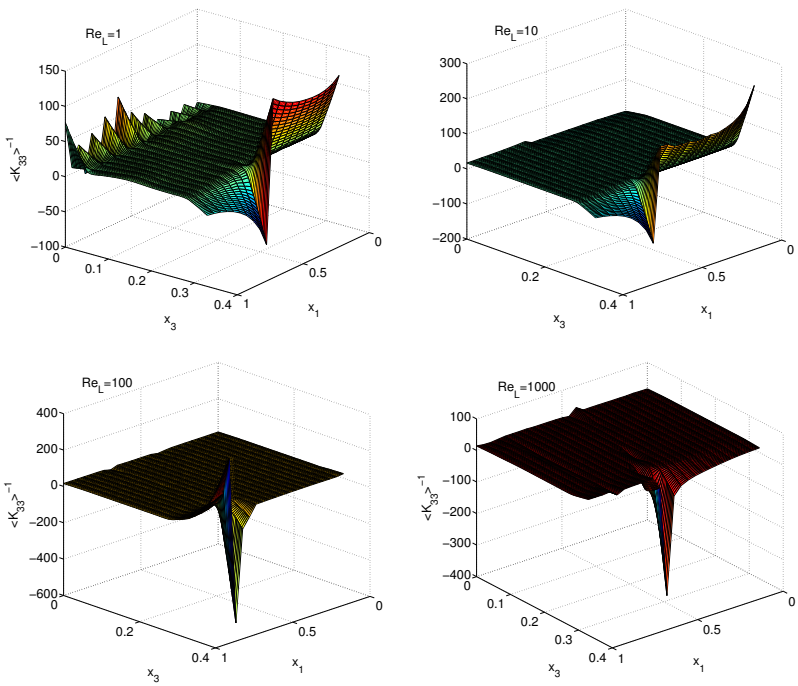

Figure 5.20: Pointwise values of $\mathcal{K}_{33}$ inside the porous region deduced from the DNS, for different Re_L.

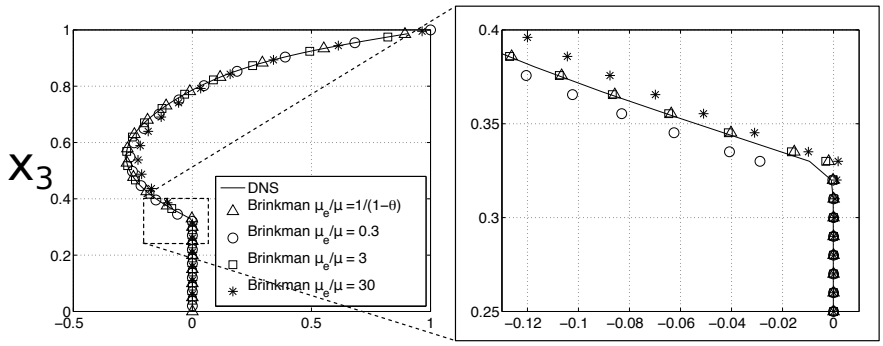

Figure 5.21: View of the macroscopic profile of u_1 for $x_1 = 0.5$ (middle of the cavity) for four choices of μ_e/μ ($\mathrm{Re}_L = 100$). A zoom is highlighted at the interface. Interface strategy: 3.4.

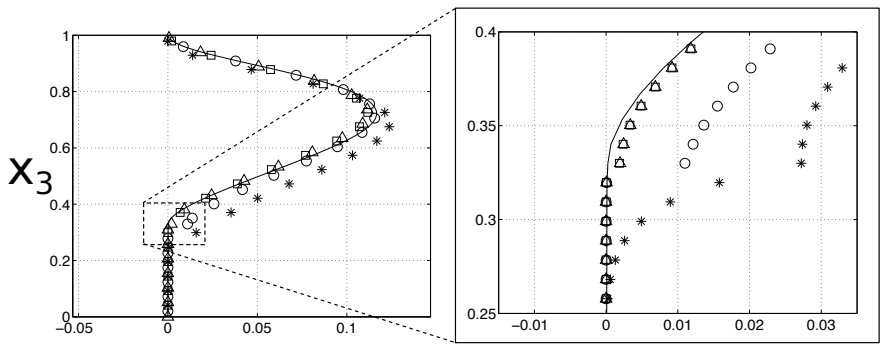

Figure 5.22: View of the macroscopic profile of u_3 for $x_1 = 0.5$ (middle of the cavity) for four choices of μ_e/μ ($\mathrm{Re}_L = 100$). Two zooms are highlighted at the interface.

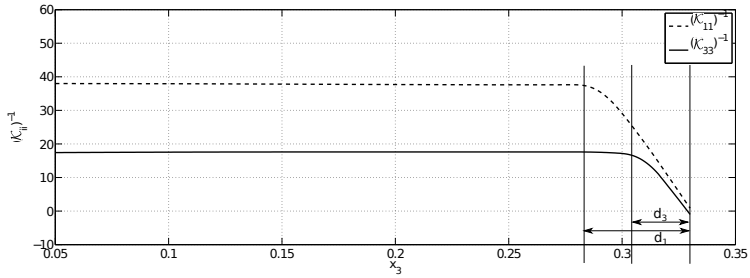

Figure 5.23: Inverse of the filtered permeability for the cases $\mathrm{Re}_L = 100$. The two lines (dotted and solid) arise from the DNS and are x_1-averaged values; d_1 and d_3 are the lengths over which the components of the permeability vary.

The pressure jump at the interface

The availability of the DNS renders it possible to assess the presence of, and quantify, the pressure jump across the physical interface. Arguments for the existence of a pressure jump have been put forward, using homogenization theory coupled with a boundary layer analysis near the interface, by Marciniak-Czochra & Mikelić (2012) for the Stokes flow over an anisotropic porous bed. Similarly, when inertia is present, a pressure slip at the interface has been reported by Saharoui & Kaviany (1994). The condition of Marciniak-Czochra & Mikelić (2012) in dimensionless form, reads:

$$-[p] = p_P(x_1, ITF^-) - p_F(x_1, ITF^+) = \frac{C}{\mathrm{Re}_L}\frac{\partial u_1}{\partial x_3}(x_1, ITF), \qquad (5.2.1)$$

with the first term above representing the pressure jump across the interface, positioned at $x_3 = ITF$, and C a constant which depends only on the porous bed geometry. We have evaluated precisely this jump on the basis of the DNS, by averaging the microscopic data, both in F and P, over cubic unit cells of size ϵ^3. Then, the pressure in the pure fluid is evaluated at $x_3 = ITF^+ = ITF + \frac{\epsilon}{2}$, and the average pressure in P is evaluated at $x_3 = ITF^- = ITF - \frac{\epsilon}{2}$. The left frame of 5.25 displays $|\mathrm{Re}_L[p]|$ along the interface at the three values of Re_L simulated; the right frame of the same figure reports a shear parameter defined as:

$$S = \frac{\partial u_1}{\partial x_3}(x_1, ITF) + \frac{\partial u_3}{\partial x_1}(x_1, ITF). \qquad (5.2.2)$$

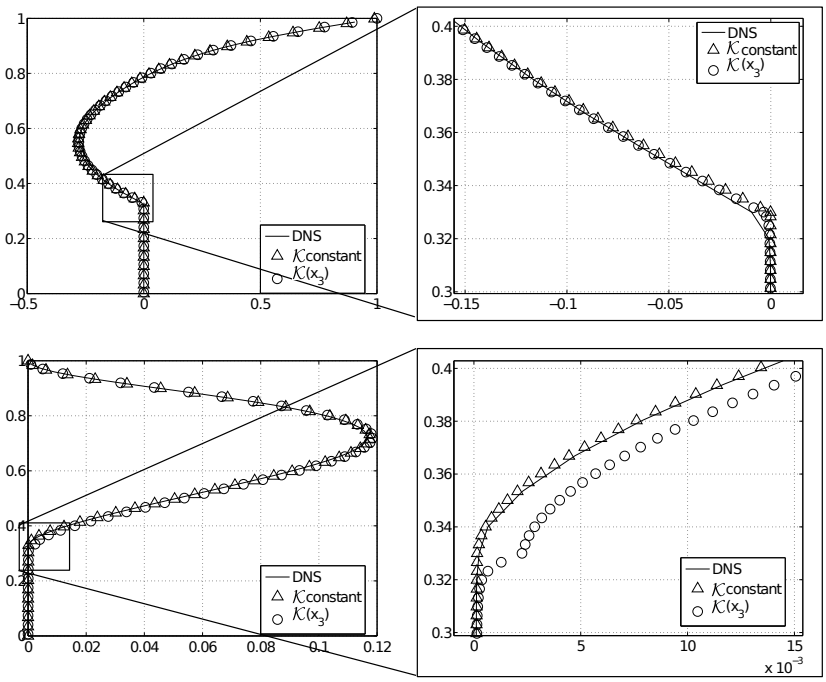

Figure 5.24: Macroscopic profile of u_1 and u_3 (lower frames) for $x_1 = 0.5$ computed using the filtered permeability shown in figure 5.23 ($\mathrm{Re}_L = 100$) and compared to the case in which the permeability components are maintained constant throughout the porous zone. Two zooms over the interfacial zone are highlighted on the right. Interface strategy: 3.5.

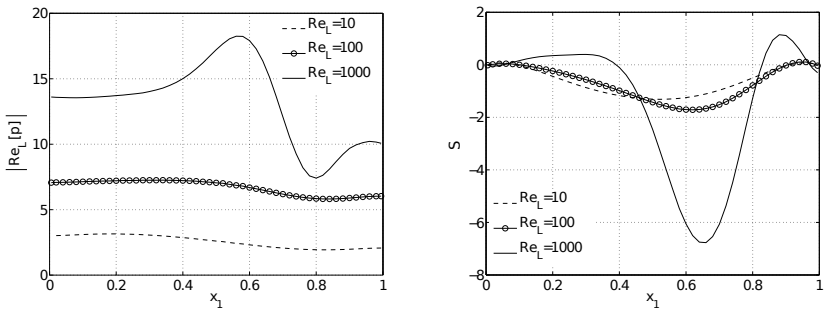

Figure 5.25: Left: pressure jump across the interface at three values of the Reynolds number. Right: shear parameters S at the interface. Both frames are based on DNS results.

In our simulations $\partial u_3/\partial x_1(x_1, ITF)$ at the interface is typically two orders of magnitude smaller than the $\partial u_1/\partial x_3(x_1, ITF)$ term, which thus dominates the parameter S. Comparison of the two frames makes it clear that, in the presence of inertia, a simple constant C cannot be found to satisfy the pressure jump condition, which is thus unsuited for use in the present case. Thus, although the pressure jump is present, condition (5.2.1) cannot be readily enforced.

A comparison for varying ϑ

We want now to assess how the microscopic structure affects the macroscopic flow field. In order to do this macroscopic homogenized simulations are performed for several values of the porosity and different geometries of the porous inclusions. Since we have already noted that the fictitious interface condition produces better results than the other two conditions tested, all the results shown here are computed using the first condition with $\delta = \epsilon/5 = 0.004$. The comparison is shown in figures 5.26 to 5.28 for the case of cylindrical inclusions and for different porosities. As one can see, the magnitude of the velocities are proportional to the permeability, so that the lower the porosity, the lower are the magnitudes of the horizontal and vertical velocity components. For this specific kind of inclusions, the vertical velocity is always greater than the horizontal because $\mathcal{K}_{33} > \mathcal{K}_{11}$. Figures 5.29 to 5.31 shows the flow when the porosity is maintained the same ($\vartheta = 0.8$), but the porous structure changes: cylinders, spheres and linked cylinders (the case of touching spheres can-

not be realized for this value of ϑ). As already underlined before, the intensity of the velocity depends on $\mathcal{K}_{ij}$; in the case of isotropic inclusions (spheres), $\mathcal{K}_{11} = \mathcal{K}_{33}$ so that u_1 and u_3 are of the same order. This behavior can also be observed in figure 5.32: looking at the streamlines for the case of simple cylinders and spheres it appears clear that in the former case the path of each streamline has a more vertical developement than in the latter case.

One of the advantages of the homogenized model is that in order to perform a macroscopic simulation for different porous structures the only thing to modify are the values of the parameters $\mathcal{K}_{ij}$ which appear in the macroscopic solver.

5.2.2 Poroelastic case

Results of the poroelastic system (5.1.1) are presented here. In all the cases the microscopic structure is composed by linked cylinders (to not encounter the problem explained in section 4.2.3 for unconnected fibers). The macroscopic configuration is the square cavity presented in the previous section. The results have been compared to one another and with the corresponding rigid cases. First of all, we introduce the interface conditions which allow to transfer information between the fluid and the homogeneous region.

The interface conditions

A similar to the real interface condition which is used by many authors (Barry *et al.*, 1991; Hoffmann *et al.*, 2004; Gopinath & Mahadevan, 2011; Alexiou & Kapellos, 2013) consists in imposing the continuity of normal and tangential stresses at the interface. In terms of homogenization this condition reads

$$\langle \Sigma_{ij}^{(0)} \rangle \cdot n_j = \langle \sigma_{ij}^{(1)} \rangle \cdot n_j. \tag{5.2.3}$$

In the particular case of a horizontal interface in the (x_1, x_3)-plane, the condition can be written as

$$\left(\mathcal{C}_{1313} \frac{\partial v_1}{\partial x_3} + \mathcal{C}_{1313} \frac{\partial v_3}{\partial x_1} \right) \Big|_P = \epsilon \left(\frac{\partial u_1}{\partial x_3} + \frac{\partial u_3}{\partial x_1} \right) \Big|_F \tag{5.2.4}$$

$$\left(\mathcal{C}_{3311} \frac{\partial v_1}{\partial x_3} + \mathcal{C}_{3333} \frac{\partial v_3}{\partial x_3} - \alpha'_{33} p \right) \Big|_P = \left(-p + 2\epsilon \frac{\partial u_3}{\partial x_3} \right) \Big|_F \tag{5.2.5}$$

where $|_P$ and $|_F$ denote the quantities in the porous and fluid region, respectively. This condition has to be considered together with the continuity of velocities at the

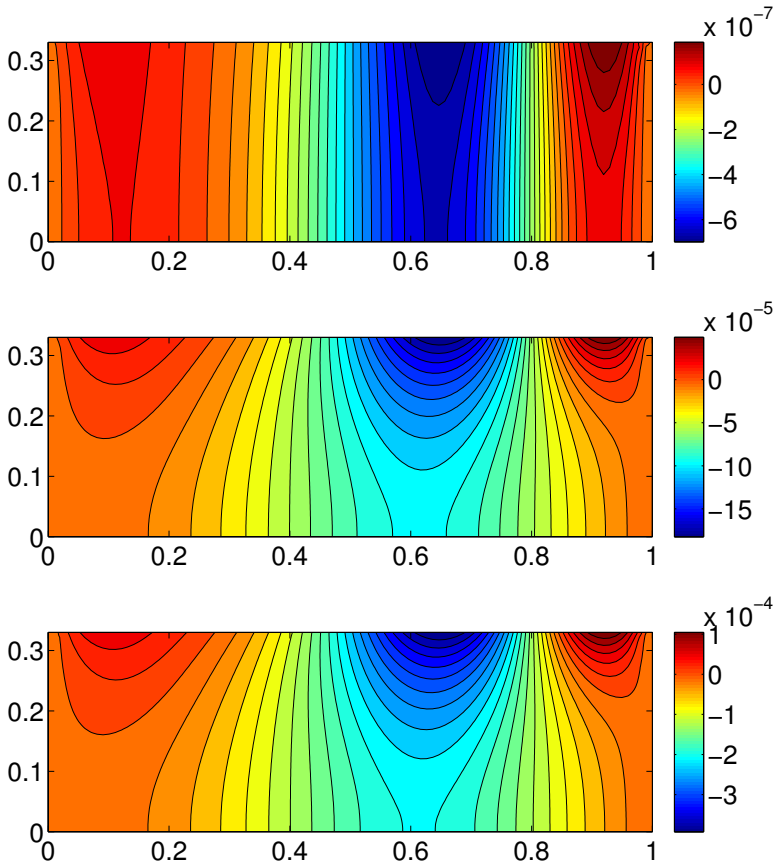

Figure 5.26: Isocontours of the horizontal velocity at Re $= 100$, for three different values of porosity: $\vartheta = 0.3, 0.8, 0.9$. Only the velocity in the porous region is shown. The microscopic structure of the porous medium is constituted by cylinders.

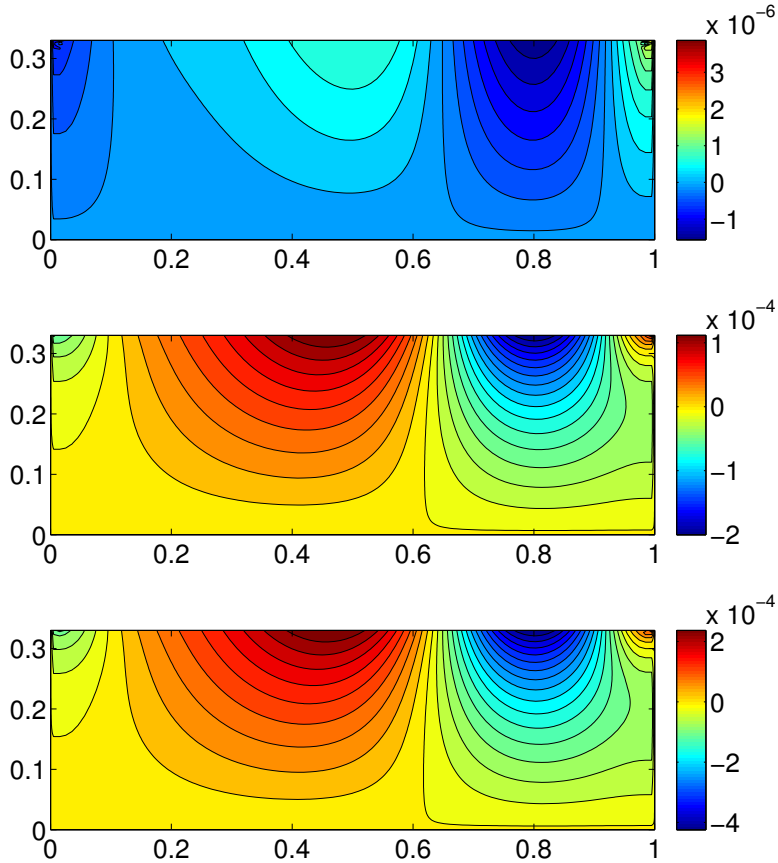

Figure 5.27: Isocontours of the vertical velocity at Re $= 100$, for three different values of porosity: $\vartheta = 0.3, 0.8, 0.9$. Only the velocity in the porous region is shown. The microscopic structure of the porous medium is constituted by cylinders.

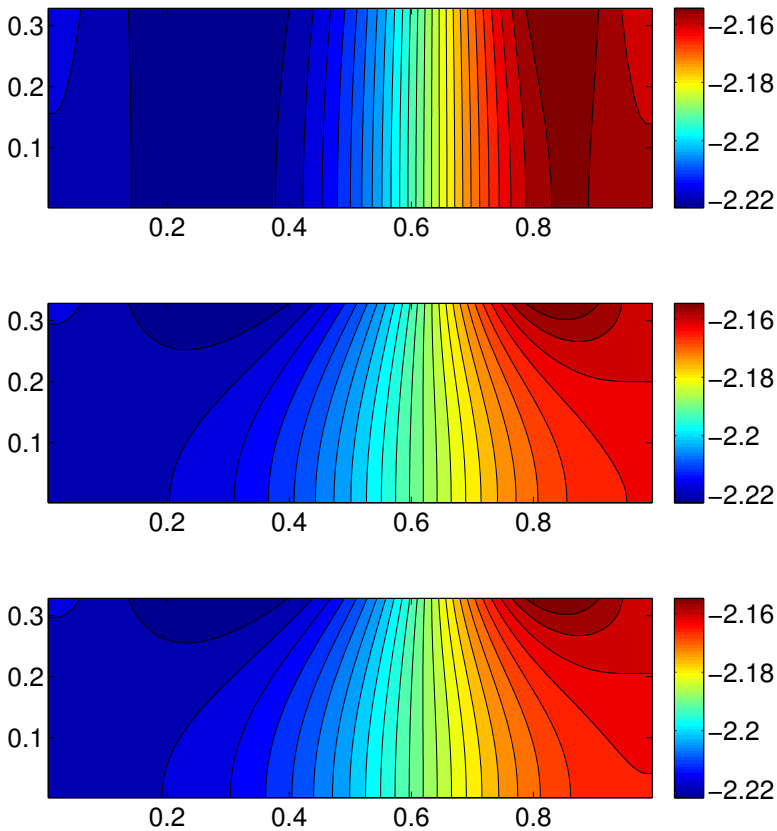

Figure 5.28: Isocontours of the pressure at Re $= 100$, for three different values of porosity: $\vartheta = 0.3, 0.8, 0.9$. Only the pressure in the porous region is shown. The microscopic structure of the porous medium is constituted by cylinders.

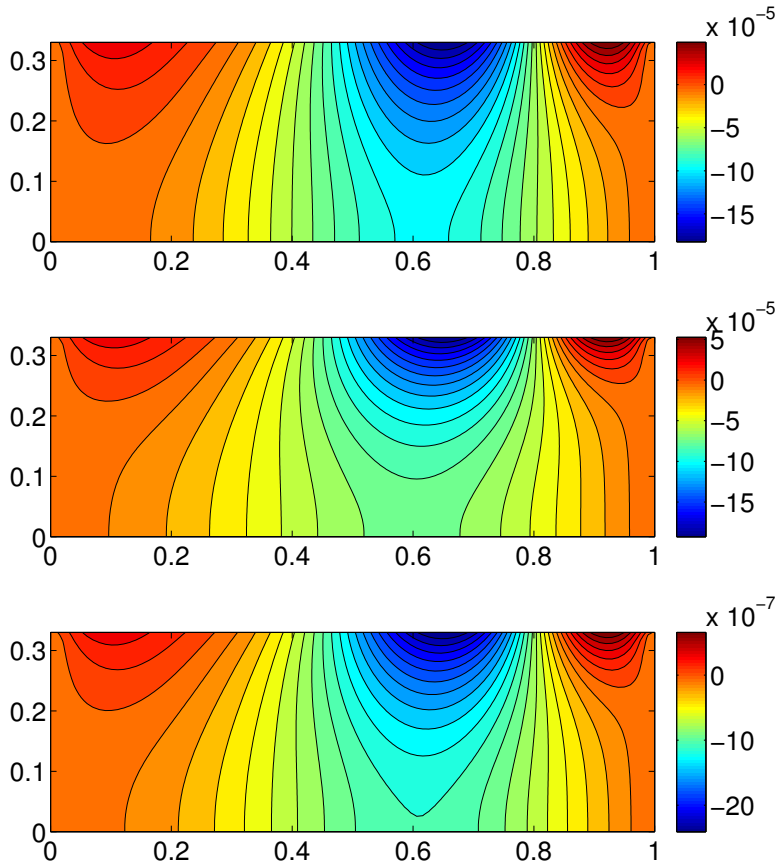

Figure 5.29: Isocontours of the horizontal velocity at Re $= 100$, for three different microscopic geometries: cylinders, spheres and linked cylinders (with $d/d_t = 2.5$). Only the velocity in the porous region is shown. The porosity is about 0.8.

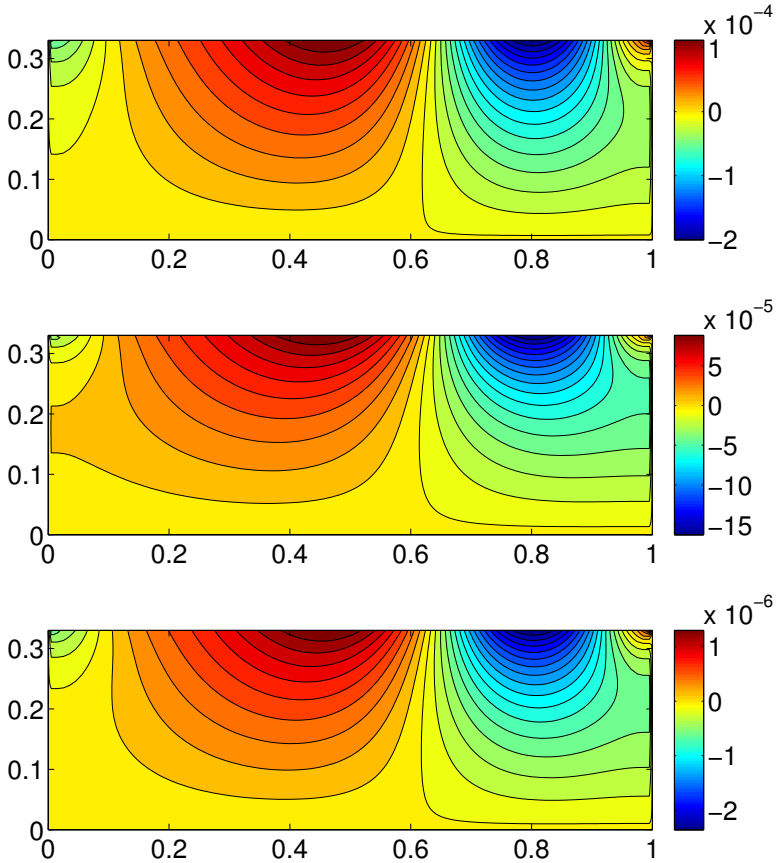

Figure 5.30: Isocontours of the vertical velocity at Re $= 100$, for three different microscopic geometries: cylinders, spheres and linked cylinders (with $d/d_t = 2.5$). Only the velocity in the porous region is shown. The porosity is about 0.8.

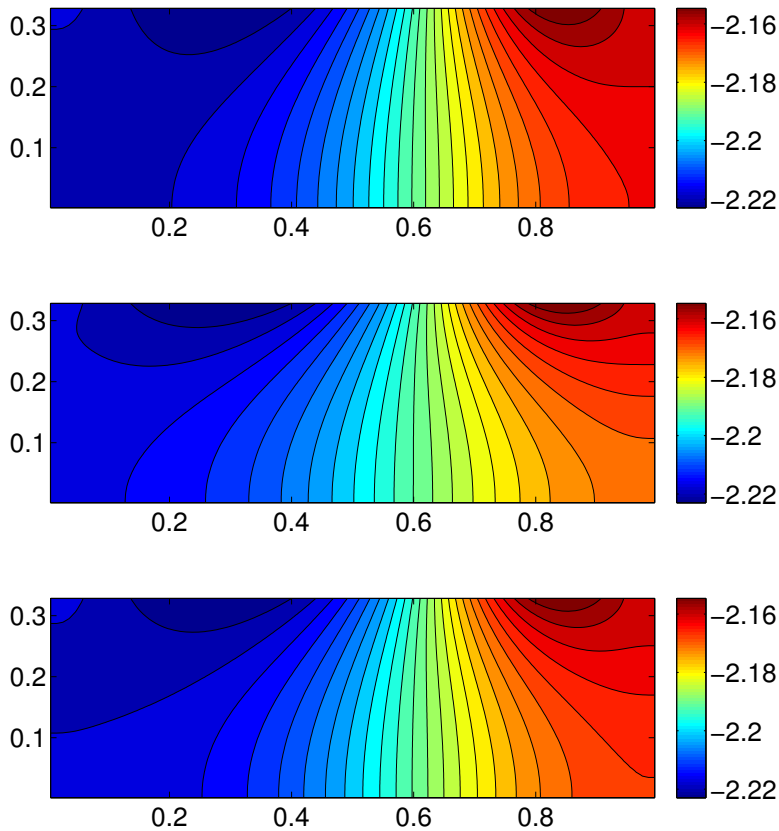

Figure 5.31: Isocontours of the pressure at Re $= 100$, for three different microscopic geometries: cylinders, spheres and linked cylinders (with $d/d_t = 2.5$). Only the velocity in the porous region is shown. The porosity is about 0.8.

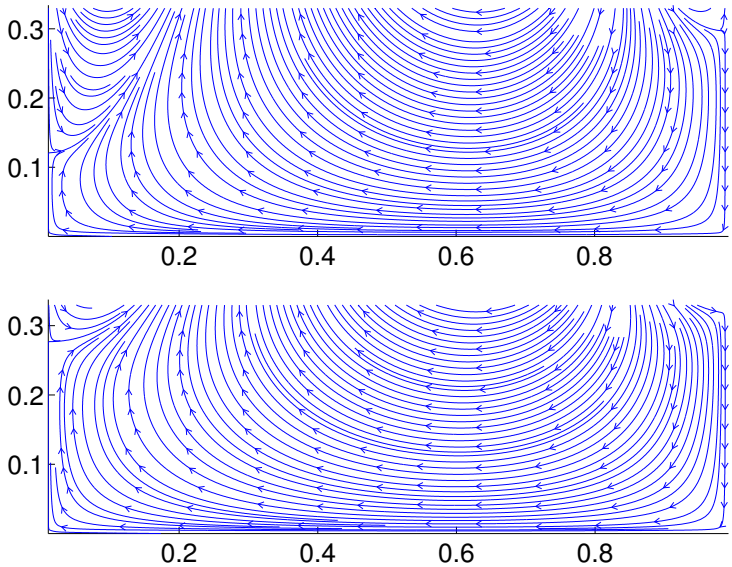

Figure 5.32: Streamlines of the flow field in case of cylindrical (up) and spherical (down) inclusions. Only the porous region is shown. The porosity is 0.8.

interface, i.e.

$$u_i|_P = u_i|_F. \tag{5.2.6}$$

Since in the P-region also the pressure is solved for, we need to impose one more condition. Gopinath & Mahadevan (2011) argue that one more boundary condition at the macroscopic interface can be formulated by assuming that the interface is bounded by a semipermeable thin skin of thickness d_f and isotropic permeability $\mathcal{K}_f$. The following fluid flux is present through the skin

$$\mathcal{K}_{33} \left.\frac{\partial p}{\partial x_3}\right|_P = \frac{\mathcal{K}_f}{d_f} P^*|_{F-P}, \tag{5.2.7}$$

where $P^*|_{F-P}$ is the difference of pressure calculated across the skin. The ratio $\mathcal{K}_f/d_f$ is *a priori* unknown and must be tuned for each configuration of the flow. Conditions (5.2.4), (5.2.5) and (5.2.7) are used to transfer information from F-region to P-region, equation (5.2.6), vice versa. For the discretization of these condition cf. Appendix A.2.

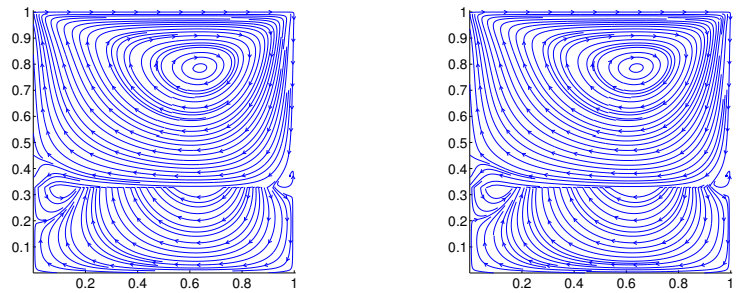

Figure 5.33: Streamlines inside the cavity. The porous medium has a microscopic structure made by linked cylinders. In the upper frame $d/d_t = 2.5$, in the lower $d/d_t = 7.5$.

A steady configuration: comparison with the rigid case

The simulations described below are made using a microscopic structure composed by linked cylinders (with $\vartheta = 0.8$ and $\epsilon = 0.02$) made of iron ($E = 210GPa$). $\mathrm{Re}_L = 100$ in all the cases. Several values of the parameter $\mathcal{K}_f/d_f$ have been tested, finding that the solution is weakly sensitive to the choice of this parameter (chosen equal to $\mathcal{K}_{33}/10^{-2}$ for the simulations shown in this section).

The results are normalized using the relations in (2.2.14) and (2.2.15), except for the effective velocity field which is normalized using relations (3.2.3) to be comparable with the rigid case. For comparison purposes, it has been necessary to perform simulations inside a square cavity of side equal to $1/\epsilon$ (which corresponds to a unitary cavity with the normalization in 3.2.3). In figures 5.33 to 5.38 a comparison between the poroelastic solutions for the cases $d/d_t = 2.5$ and $d/d_t = 7.5$ is shown. As in the rigid case, the effective velocities in the homogenized region are roughly proportional to the permeability. The displacement field is coherent with the velocity of the homogenized material (c.f. figures 5.34, 5.35 and 5.36). As one expects, the horizontal deformations are greater if the microscopic structure is "less" connected along x_1 (i.e. in case of $d/d_t = 7.5$). Since the configuration of the microscopic structure remains unchanged in x_3 for the cases $d/d_t = 2.5$ and $d/d_t = 7.5$, also the intensity of the vertical deformations are almost the same (cf. figure 5.35). In figures 5.39 to 5.41 the result of the poroelastic case for the parameters $\mathrm{Re}_L = 100$, $\vartheta = 0.8$ and $d/d_t = 2.5$ are presented against results of

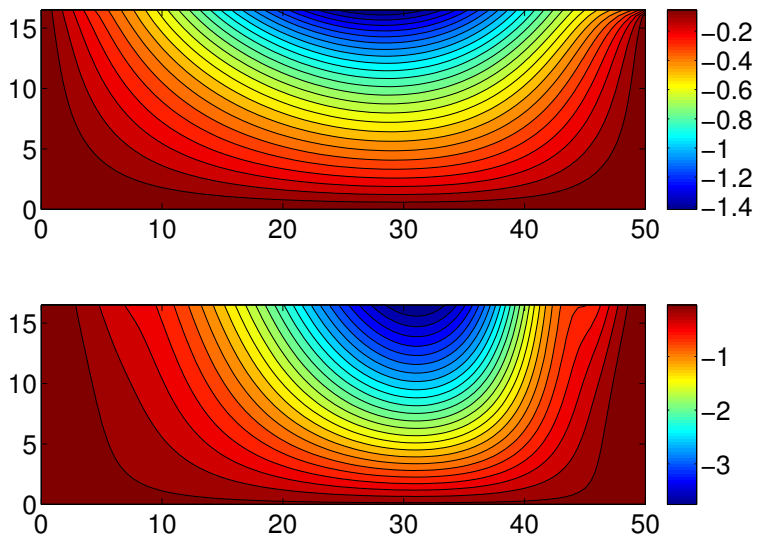

Figure 5.34: Contours of the displacement in the x_1 direction. In the upper frame $d/d_t = 2.5$, in the lower $d/d_t = 7.5$.

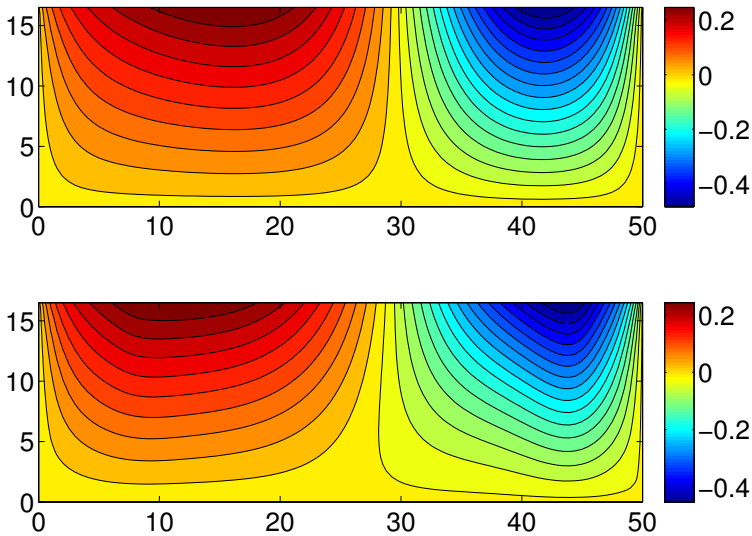

Figure 5.35: Contours of the displacement in the x_3 direction. In the upper frame $d/d_t = 2.5$, in the lower $d/d_t = 7.5$.

the rigid case for the same parameters. The effective velocity field inside the porous region is pretty much the same in both cases at steady-state.

An unsteady configuration: oscillating channel flow

Let us consider the oscillating flow of a Newtonian fluid with constant density ρ_f and viscosity μ in the plane channel sketched in figure 5.42. The flow is forced by an oscillating pressure gradient along the horizontal direction x_1,

$$\frac{\partial p}{\partial x_1} = A\Re(e^{i\omega t}), \tag{5.2.8}$$

where A is the real amplitude of the wave, ω its frequency and $\Re$ denotes the real part. The channel is filled over half of its height (L) by a porous medium whose microscopic structure is shown in figure 5.42.

In order to allow for periodicity along x_1, periodic conditions are imposed for the displacement and for the pressure gradient at the vertical boundaries of H.

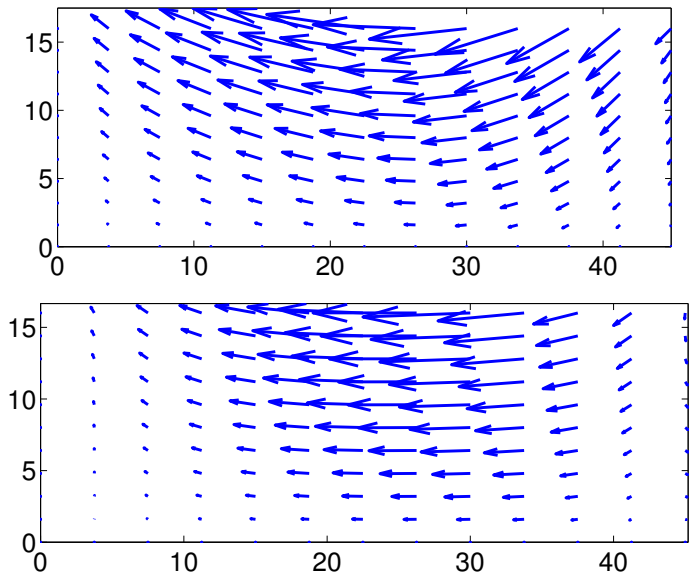

Figure 5.36: Representation of the displacement vector field. In the upper frame $d/d_t = 2.5$, in the lower $d/d_t = 7.5$.

The simulation shown here is done for the following conditions: the fluid is air ($\nu = 1.55 \times 10^{-5} m^2/s$), $\mathrm{Re}_L = 100$ and the material is a very soft and dense polyurethane foam with a microscopic structure organized as in figure 4.29 with $d/d_t = 2.5$. With these values $\mathrm{Ca} = 9.15 \times 10^{-8}$. The parameter ϵ is chosen equal to 4×10^{-5}, which, in other words, means that the microstructure is repeated about 2.5×10^4 times per unit length. The oscillating pressure gradient is characterized by non-dimensional amplitude A and frequency ω equal to 1.

The new fluid velocity in the F–region can be written as

$$\mathbf{u}^* = \mathbf{u} + \tilde{\mathbf{u}}, \tag{5.2.9}$$

where $\mathbf{u}$ is the solution computed imposing an impermeable wall at $x_3 = 0$ and $\tilde{\mathbf{u}}$ is the disturbance due to the effect of the poroelastic medium. The amplitude of such disturbances has the same order of magnitude of the effective velocity in the H–region defined as $\mathbf{u}^* - \dot{\mathbf{v}}$, i.e. about $\mathcal{O}(\epsilon \mathrm{Re}_l \mathcal{K}_{ij})$. In figure 5.43 the fluid flow disturbances at different instants during the periodic cycle are represented. The

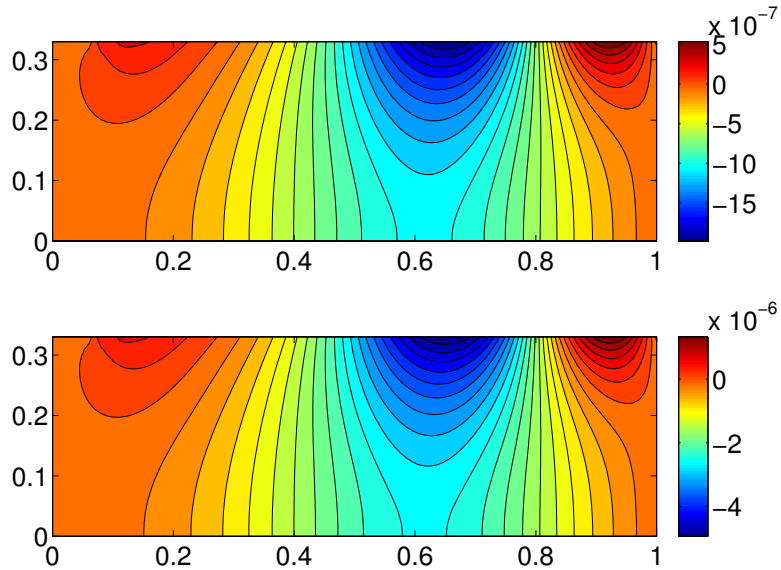

Figure 5.37: Contours of the velocity field in the x_1 direction. In the upper frame $d/d_t = 2.5$, in the lower $d/d_t = 7.5$.

contours represent the kinetic energy of $\tilde{\mathbf{u}}$, while the white arrows display the disturbance velocity field.

The effective fluid velocity field in the H–region is represented in figures 5.44, 5.45, normalized by the constants $\epsilon \mathrm{Re}_l(\mathcal{K}_{11})$ and $\epsilon \mathrm{Re}_l(\mathcal{K}_{33})$ for the x_1 and x_3 components of the velocity, respectively.

The displacement of the poroelastic structure is represented in figures 5.46, 5.47 and 5.48. Figure 5.46 shows how the displacement changes in time, along x_3 and for a fixed x_1 in the channel. Figure 5.47 shows the correlation in time between the horizontal and vertical displacements. After one cycle the curves overlap and the motion of the structure is fully periodic. In figure 5.48 the vertical position of the macroscopic fluid-structure interface is represented: even if the interface conditions (5.2.4, 5.2.5, 5.2.6, 5.2.7) have been imposed for a fixed $x_3 = 0$, thanks to the continuity of normal stresses, the procedure lets the interface to move in the vertical direction of a distance of order ϵ.

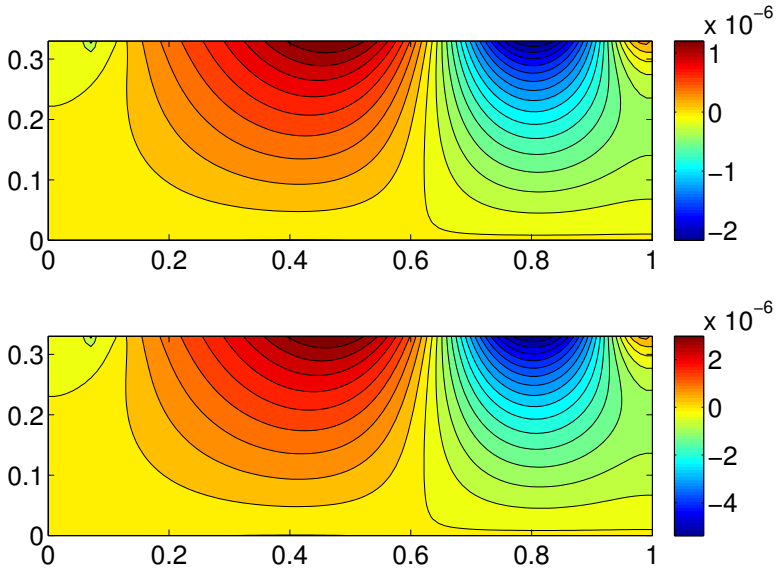

Figure 5.38: Contours of the velocity field in the x_3 direction. In the upper frame $d/d_t = 2.5$, in the lower $d/d_t = 7.5$.

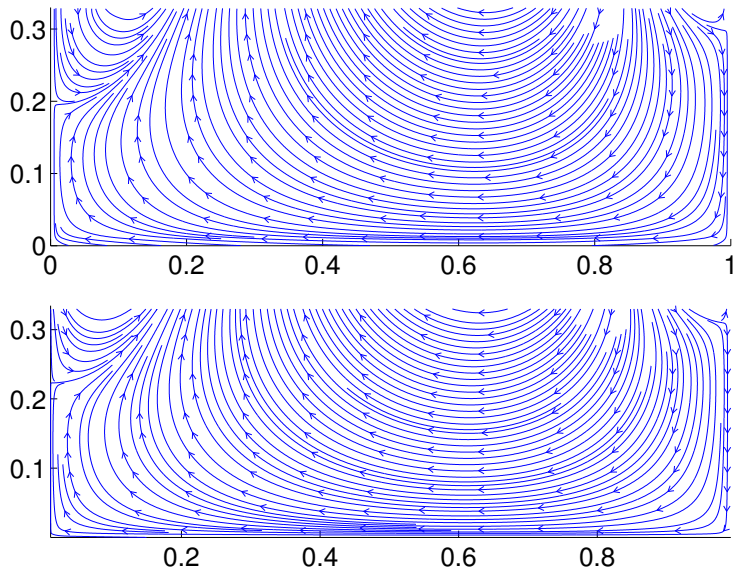

Figure 5.39: Streamlines inside the porous medium. The microscopic structure is made by linked cylinders with $d/d_t = 2.5$. The upper and lower frames show the deformable and rigid case respectively.

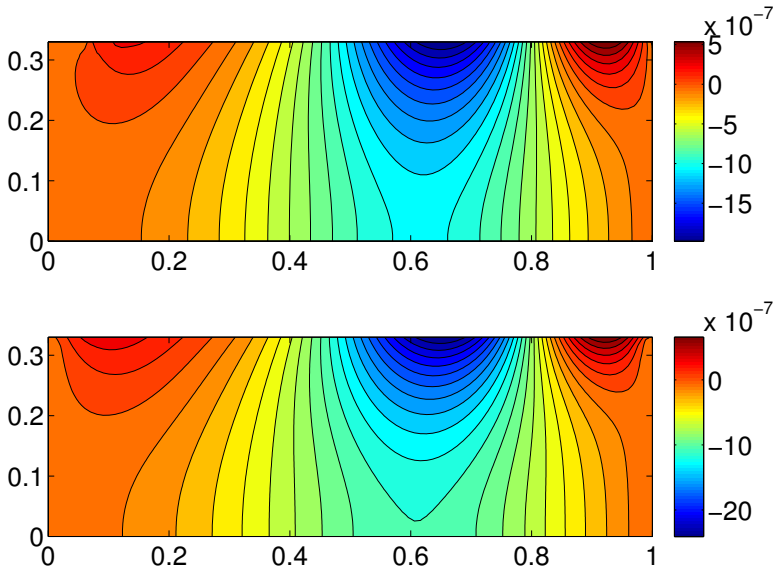

Figure 5.40: Contours of the velocity field in the x_1 direction. The microscopic structure is made by linked cylinders with $d/d_t = 2.5$. The upper and lower frames show the deformable and rigid case respectively.

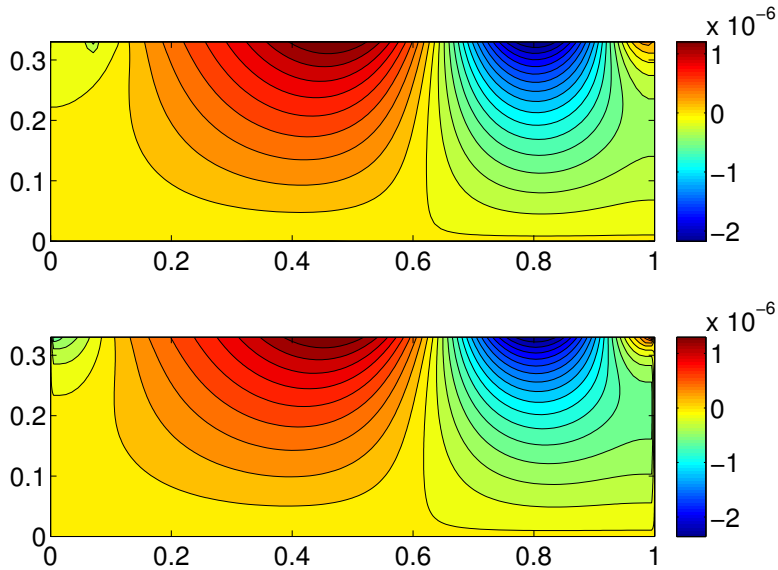

Figure 5.41: Contours of the velocity field in the x_3 direction. The microscopic structure is made by linked cylinders with $d/d_t = 2.5$. The upper and lower frames show the deformable and rigid case respectively.

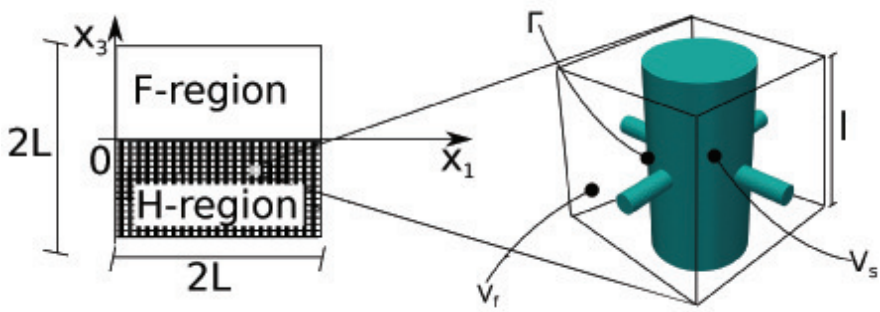

Figure 5.42: Configuration of the problem, no-slip and periodic conditions are imposed on the top and vertical boundaries of the fluid domain in the F–region, respectively. A zoom inside the homogenized, poroelastic H–region highlights the microscopic fibrous structure which constitutes the poroelastic medium with the usual notations.

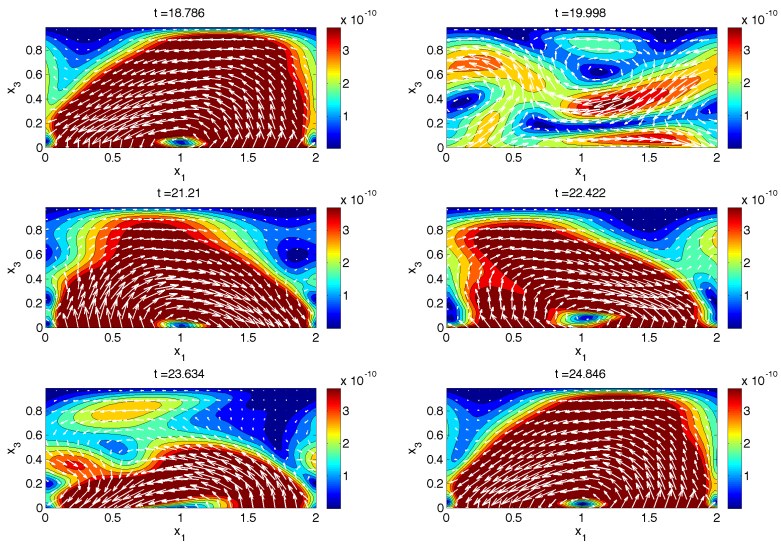

Figure 5.43: Disturbance velocity field $\tilde{\mathbf{u}}$ in the F–region at six different instants during the periodic cycle. The contours represent the local kinetic energy of the disturbance field and the arrows its velocity.

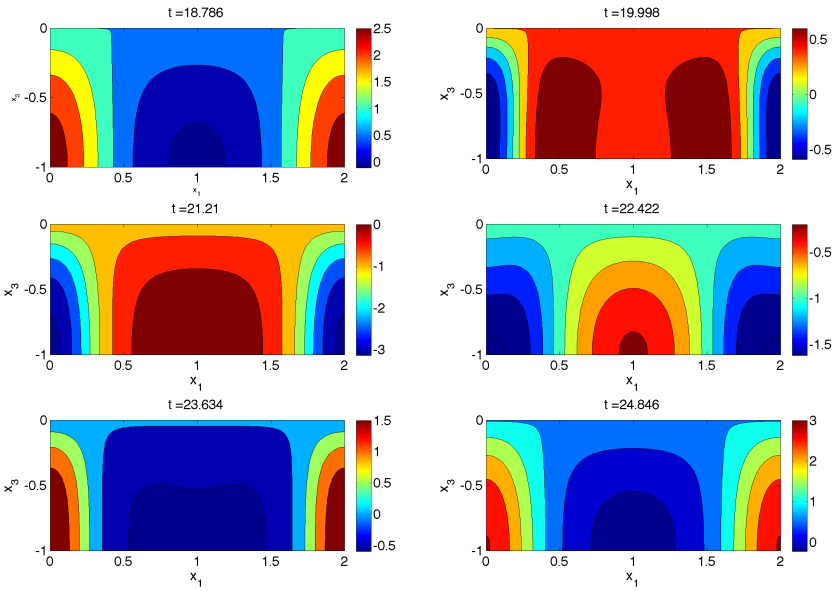

Figure 5.44: Horizontal component of the effective velocity field ($\mathbf{u}^* - \dot{\mathbf{v}}$) in the H–region at six different instants during the periodic cycle.

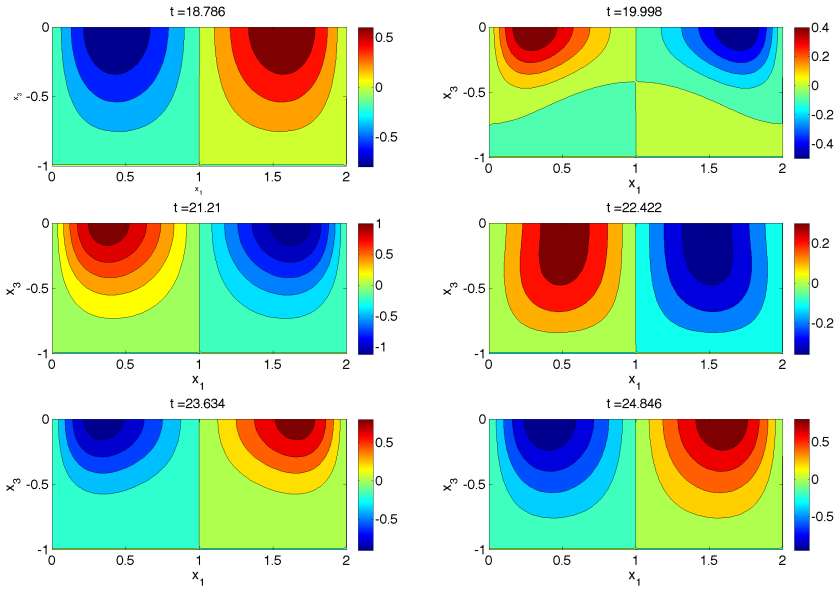

Figure 5.45: Vertical component of the effective velocity field ($\mathbf{u}^* - \dot{\mathbf{v}}$) in the $H-$ region at six different instants during the periodic cycle.

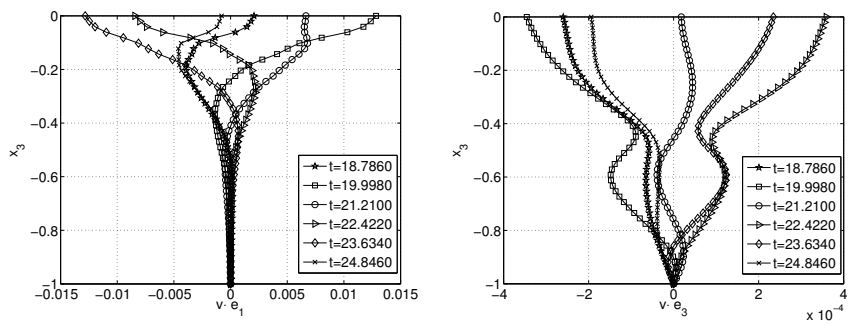

Figure 5.46: Horizontal (upper frame) and vertical (lower frame) displacement along x_3 for a fixed x_1 in the channel at six different instants during the period.

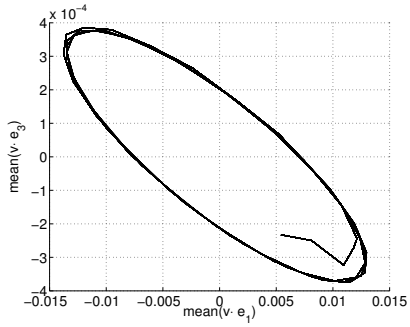

Figure 5.47: Mean horizontal displacement of the interface of the homogenized structure versus mean vertical displacement.

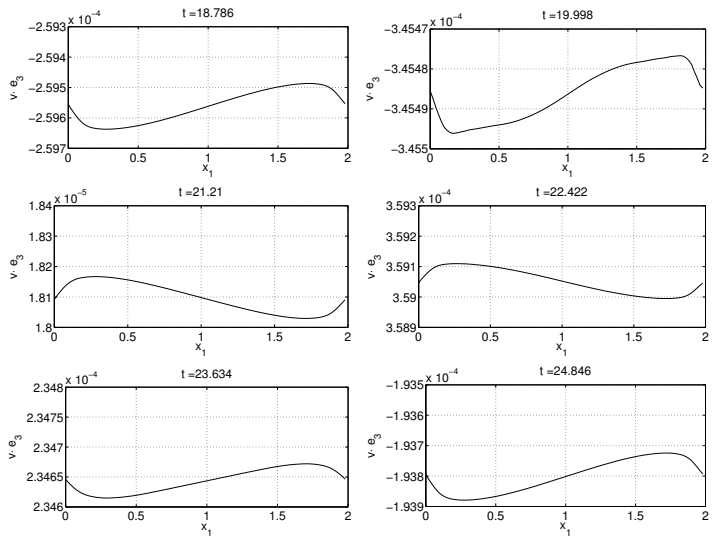

Figure 5.48: Vertical displacement of the interface for six different instants within a period.

5.3 Flow in a canopy

In this section we want to demonstrate that the model formed by equations (2.1.17), (4.2.2) plus the equations in the pure fluid domain and the interface conditions are adequate also to simulate a turbulent canopy flow. This kind of flow has been widely studied in the past since it develops very often in Nature (a recent review is provided by Nepf (2012)). Much literature (theoretical and experimental) is present to understand the mechanisms which induce the creation of a quasi-parallel mixing layer and the formation of honami and monami waves over canopies. Raupach *et al.* (1996) and Finnigan (2000) have classified the different structures which characterize the flow on the basis of the geometrical properties of the canopy (e.g. its density) and the parameters of the mixing layer.

In order to understand if the closure adopted for the $Re = \mathcal{O}(1)$ case in equation (4.2.2) makes sense we have used the experimental data of
Ghisalberti & Nepf (2004) where a fully developed turbulent flow of water over a submerged layer of vertical rigid fibres is studied. The setting of the problem

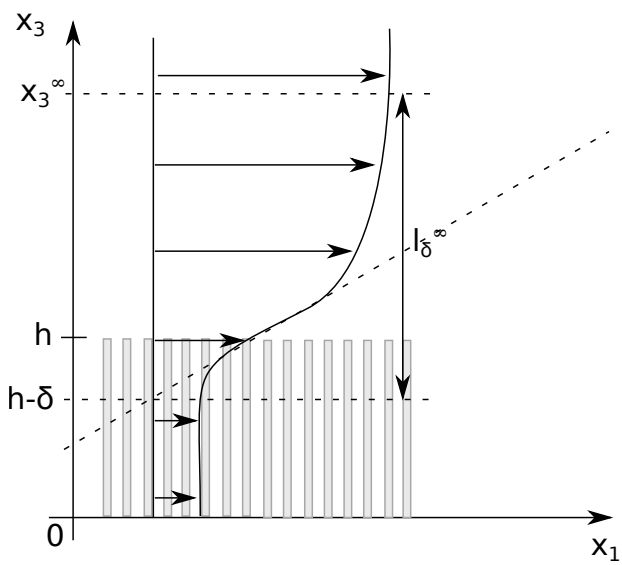

Figure 5.49: Setting of the experiments of Ghisalberti & Nepf (2004). Water flows over a layer of rigid cylindrical fibres. The whole system is slightly inclined at an angle α so that the fluid motion is driven by gravity.

is sketched in figure 5.49; the porosity ϑ in the experiments ranges from 0.96 to 0.99 and ε is about 0.2 (defined as the ratio between the diameter of the fibers and the height of the water column). The measurements of the mean velocity inside the canopy and the driving term are available so that the permeability $\mathcal{K}_{11}$ can be estimated a posteriori using Darcy's law which, in this case, can be written in dimensional variables as

$$\langle u_1^{(0)} \rangle = \mathcal{K}_{11} \frac{g \sin \alpha}{\nu}, \tag{5.3.1}$$

where $\nu = 0.94 \cdot 10^{-6} m^2/s$ is deduced using Re_{ml} in table 1 of Ghisalberti & Nepf (2004) and α is the slope of the inclined system. The use of equation (5.3.1) in the lower zone of the canopy, termed "wake zone", is justified on physical grounds since, as noted by Ghisalberti & Nepf (2009), such a region is 'governed by a simple balance of drag and hydraulic gradient, much like classical porous medium flow'.

Figure 4.22 and 5.50 display results for the microscopic permeability field K_{11} within the elementary volume, and the averaged values $\mathcal{K}_{11}$ for variable pore velocity. The gray band represents the range of permeability $\mathcal{K}_{11}$ computed using the homogenized model (4.2.2) for the corresponding porosities of each experiment. The experimental values are in reasonably good agreement with the homogenized values; discrepancies are of the same order as those shown in figure 4.21 and table 5.1.

We now consider the problem from a macroscopic point of view. Observing the sketch of the velocity profile in figure 5.49 it seems reasonable to impose continuity of the streamwise velocity at a distance δ (*the penetration depth*) below the top of the canopy. This is the fictitious interface and equation (5.3.1) is thus applicable for $x_3 \in [0, h - \delta]$. Since we are dealing with a fully developed turbulent flow, in the region above the fictitious interface ($x_3 \in [h - \delta, x_3^{\infty}]$), after using the Reynolds decomposition for the velocity (i.e. $u_i = U_i + u_i'$) plus temporal averaging ($\bar{\cdot}$), the streamwise momentum equation reads:

$$\frac{\partial \overline{u_1' u_3'}}{\partial x_3} = g \sin \alpha. \tag{5.3.2}$$

Thus, the turbulent stress balances the hydraulic gradient in the upper zone (termed the "exchange zone"), whereas the viscous term can be neglected. Assuming a constant mixing length model, such as that proposed by Ghisalberti & Nepf (2004), the Reynolds stress can be written as

$$-\overline{u_1' u_3'} = \left(c l_{\delta}^{\infty} \frac{\partial U_1}{\partial x_3} \right)^2, \tag{5.3.3}$$

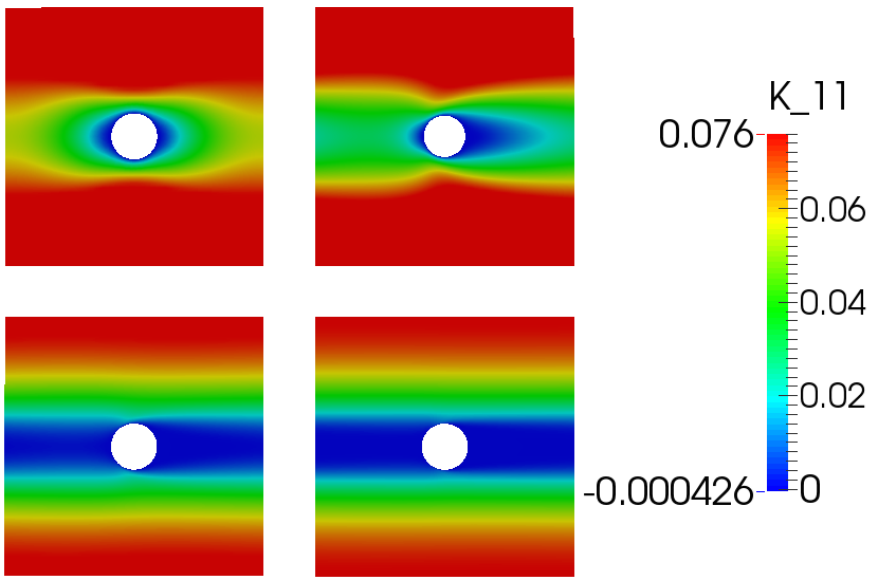

Figure 5.50: Horizontal component of the permeability K_{11} within a unit cell, for varying $\vartheta \mathrm{Re}_p = 0, 50, 500, 1500$. Increasing Re_p, the value of K_{11} is reduced and the distribution initially looses symmetry with respect to the vertical mid-plane through the cylinder, to eventually regain it because of periodicity for $\vartheta \mathrm{Re}_p$ above 500. Here $\vartheta = 0.975$.

where l_δ^∞ is shown in figure 5.49, c is a constant and their product is a "mixing length". Substituting equation (5.3.3) into equation (5.3.2), solving for the mean flow and determining the two constant of integration by imposing the value of U_1 at $h-\delta$ and $\left.\frac{\partial U_1}{\partial x_3}\right|_{h-\delta} = 0$, it is found:

$$U_1(x_3) = U_1(h-\delta) + \frac{2}{3}\frac{\sqrt{g\sin\alpha}}{c l_\delta^\infty}\left[(x_3^\infty - h + \delta)^{\frac{3}{2}} - (x_3^\infty - x_3)^{\frac{3}{2}}\right]. \quad (5.3.4)$$

The condition at the fictitious interface yields $U_1(h-\delta) = \langle u_i^{(0)}\rangle(h-\delta) = \mathcal{K}_{ij}\frac{g\sin\alpha}{\nu}$. As we can observe from figure 5.51 the proposed solution fits the experiments with the unique value of $c = 0.086$. Summing up, we can make the following two points:

- The values of the permeability deduced from the experiments slightly overestimate those evaluated via homogenization theory (cf. figure 4.22), and this is possibly due to the fact that in the experiments by Ghisalberti & Nepf (2004) the parameter ϵ is about 0.2, a value which is not much smaller than one.

- The agreement between the experimental and theoretical velocity profiles in figure 5.51 confirms that the interface condition **A** of Le Bars & Worster (2006) is suitable in this turbulent case. Moreover, for the four experiments analyzed, the order of magnitude of δ estimated from equation (3.3.3) matches that used here. However, if c in equation (3.3.3) were a simple constant, considering the trend of $\mathcal{K}_{11}$ in figure 4.22, also δ would decrease for increasing values of Re_p, contrary to observations (cf. the inset in fig. 5.51). Thus, the "constant" c in equation (3.3.3) should be rendered an increasing function of Re_p, for δ to increase monotonically with the increase of the pore velocity (at each given value of ϑ).

For ease of notation we denote $\mathbf{U} = (U, V, W)$, $x = x_1$, $y = x_3$.

5.3.1 Linear stability analysis

We have studied the linear stability of the profile defined by equation (5.3.4) which holds in the interval $[h-\delta, x_3^\infty]$ and the results have been compared with

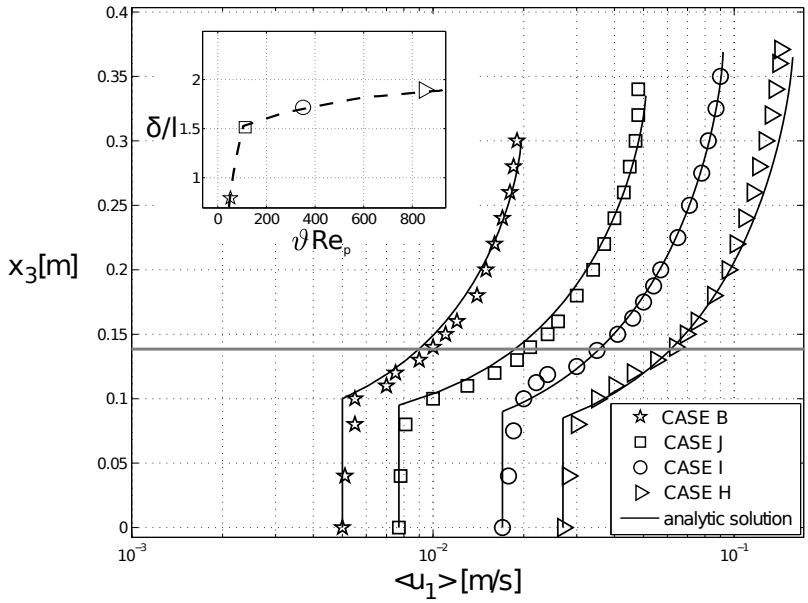

Figure 5.51: Analytical velocity profiles, in dimensional variables, against experimental results by Ghisalberti & Nepf (2004),Ghisalberti & Nepf (2006), Ghisalberti & Nepf (2009) for the turbulent flow over a layer of rigid fibres. The symbols represent the velocity measurements (with uncertainty of 5%) for cases B, H, I, and J of table 1 of Ghisalberti & Nepf (2004). The analytical solution, equation (5.3.4), is represented by the solid lines. Two horizontal gray lines, which appear overlapped in the scale of the figure, represent the physical interface h (in dimensional terms $h = 0.139\ m$ for case B and $h = 0.138\ m$ for the other cases). In the inset the values of δ, which define the fictitious interface at $x_3 = h - \delta$, are shown for the corresponding cases. The dashed line is drawn to guide the eye. In the four experiments we have used the following values for l_δ^∞: ☆: 0.202 m □: 0.245 m ◯: 0.279 m ▷: 0.286 m. Furthermore, the microscale l (used to normalize δ in the inset) is equal to 5.06 cm in experiment B (with $\vartheta = 0.99$) and 2.83 cm in the other cases (for which $\vartheta = 0.96$).

the linear stability results found by Pluvinage (2015) where a different method to find the mean flow and to take into account of the presence of the canopy is used. From now on, the approach of Pluvinage (2015) is named **A** and our approach is named **B**. We briefly present below the determination of the mean flow in approach **A**. It is assumed that the velocity profile ranges between two extreme values, one, U_1, which is found in the region from the lower plate at $y = 0$ to $y = y_1$ (the bottom, ininfluential boundary layer is neglected), and the other, U_2, which prevails for $y > y_2$ ($= x_3^\infty$ of the previous section). The distance t_{ml} is defined as the difference $y_2 - y_1$. The mean velocity is $U_m = (U_1 + U_2)/2$. Using Reynolds' decomposition for velocity and pressure, $u_i = U_i + u_i'$, $p = P + p'$, in the NSE and averaging (this operation is indicated by overbars), we have:

$$\frac{\partial U_i}{\partial x_i} = 0, \tag{5.3.5}$$

$$\rho(\frac{\partial U_i}{\partial t} + U_j \frac{\partial U_i}{\partial x_j} + \overline{u_j' \frac{\partial u_i'}{\partial x_j}}) = -\frac{\partial P}{\partial x_i} + \mu \frac{\partial^2 U_i}{\partial x_j \partial x_j} + f_i; \tag{5.3.6}$$

the last term in eq. (5.3.6) is the mean drag force of the canopy, proportional to the square of the velocity via two coefficients: one, denoted as a represents the frontal area of the vegetation per unit volume, i.e. the packing density of the elements (equal to $0.08\, cm^{-1}$ in the experiments by Ghisalberti & Nepf (2004, 2005)), while the second is the drag coefficient C_d of the canopy. The mean flow is parallel in the experiments, so that the equations reduce to:

$$\frac{\partial U}{\partial x} = 0, \tag{5.3.7}$$

$$\frac{\partial U}{\partial t} = -\frac{1}{\rho}\frac{\partial P}{\partial x} + (\nu + \nu_t)\frac{\partial^2 U}{\partial y^2} - \frac{1}{2} C_d a U^2, \tag{5.3.8}$$

$$0 = -\frac{1}{\rho}\frac{\partial P}{\partial y}. \tag{5.3.9}$$

In equation (5.3.8) it is assumed that the Reynolds stress can be modeled through a eddy viscosity and, henceforth, the constant mixing length $l = c l_\delta^\infty$ approach already introduced in eq. (5.3.3) is used. The pressure gradient depends on the surface slope $S = \sin\alpha$ of the lower plate (which is slightly inclined in the experiments, with $0.18 \times 10^{-5} < S < 10^{-4}$), i.e.

$$\frac{\partial P}{\partial x} = -\rho g S. \tag{5.3.10}$$

In the case of steady-in-the-mean flow, eq. (5.3.8) reads

$$\frac{\partial}{\partial y}\left[\left(\frac{\partial U}{\partial y}\right)^2\right] = \frac{1}{l^2}\left(\frac{1}{2}C_d a U^2 - \nu\frac{\partial^2 U}{\partial y^2} - gS\right), \tag{5.3.11}$$

and this equation can be easily solved numerically, for $0 < y < y_2$, as done, e.g., by Ghisalberti & Nepf (2004). In particular, they assume that $l = 0.22\,(h - y_1)$ within the canopy ($y_1 < y < h$) and $l = 0.095\,t_{ml}$ in the portion of the shear layer above the canopy ($h < y < y_2$). The coefficients 0.22 and 0.095 arise from experimental measurements and averaging over several configurations.

The drag coefficient C_d is deduced from the bulk drag coefficient C_{dA} of a random array of rigid cylinders. At large Reynolds numbers Re_d (based on the diameter d of a cylinder and U_1) this coefficient decreases with increasing cylinder density, $a\,d$, according to the best fit polynomial established by Nepf (1999):

$$C_{dA} = \left(1 + \frac{10}{Re_d^{2/3}}\right)[1.16 - 9.31ad + 38.6(ad)^2 - 59.8(ad)^3], \qquad (ad < 0.1) \tag{5.3.12}$$

with $C_d(y) = C_{dA}\eta(y)$ and $\eta(y)$ a function deduced experimentally by Ghisalberti & Nepf. Here, again, the profile of $\eta(y)$ is obtained via averaging over a large number of experimental runs. The vertical profile of the drag coefficient is displayed in fig. 5.53 for four cases, G, H, I and J taken from the papers by Ghisalberti & Nepf.

The methodology used to compute U is based on a procedure initiated by Ghisalberti & Nepf (2004) and allows to automatically determine the value of the mean velocity at the top of the canopy, $U(h)$. It involves two independent relationships to be satisfied iteratively:

- $h - y_1 = \dfrac{1}{8.7\,C_d\,a}\left(\dfrac{(\Delta U)^2}{U(h)^2 - U_1^2}\right)$, to evaluate the lower point of the mixing layer, y_1;
- $\dfrac{\Delta U}{U(h)} \approx 16(a\,d) + 1$ (for $0.016 < a\,d < 0.081$), to permit the evaluation of y_2.

The former equation stems from a balance between production and dissipation of shear-scale turbulent kinetic energy in a vegetated shear layer while the latter arises from the experimental correlation observed between $\Delta U/U(h)$ and the vegetation density in a range of values of $a\,d$
(Ghisalberti & Nepf (2004)). For an in deep description of this iterative method we refer to Pluvinage (2015).

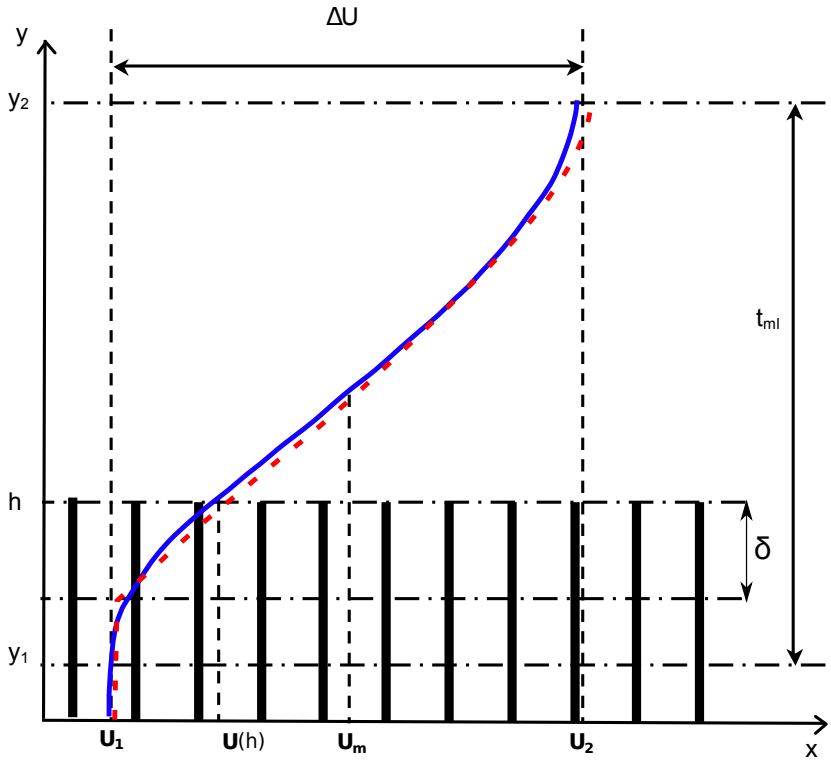

Figure 5.52: Mean flow velocity profile through a rigid canopy computed with method **A** and **B** (blue and red - dashed - curves, respectively).

Neglecting drag

Neglecting the canopy drag amounts to solving the inviscid stability equations within the flow domain to ascertain the effect of inflection points of the mean flow profile on the growth rate, frequency and wavelength of the most unstable mode which ensues. In the context of canopy flows this approach has been advocated by Raupach *et al.* (1996) on the argument that the mixing-layer analogy provides an explanation for many of the observed distinctive features of canopy turbulence.

We scale velocity with the mean flow velocity U_m, length with the canopy height h, pressure with $\rho {U_m}^2$ and time with h/U_m, so that the dimensionless Rayleigh

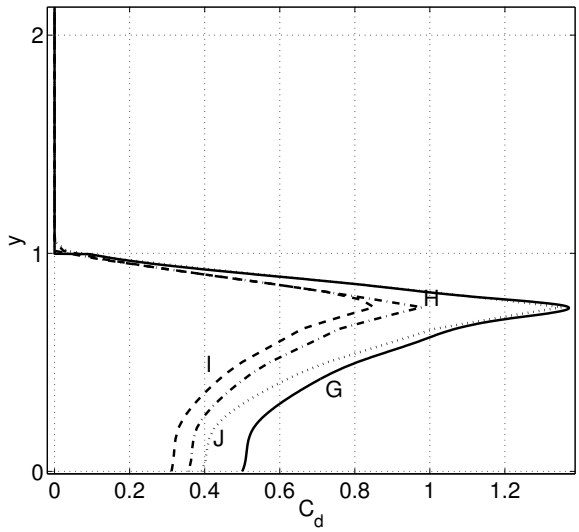

Figure 5.53: Vertical profile of the drag coefficient C_d for runs G, H, I and J.

equation reads:

$$\left[(U-c)(D^2-\alpha^2)-U''\right]v=0, \tag{5.3.13}$$

for the vertical velocity mode shape $v(y)$, with D and primes denoting d/dy; disturbances are taken to behave like $e^{i\alpha x-i\omega t}$ and $c=\omega/\alpha$ is the phase velocity of the wave. The temporal stability problem studied here requires finding complex eigenvalues c for each assigned value of the (real) wavenumber α. The boundary conditions are simply $v=0$ at $y=0$ and y_∞ in approach **A** and y_∞ is taken large enough for results not to be modified upon subsequent increments of y_∞.

The new approach pursued here is denoted as **B**. For the case of approach **B** a different condition must be imposed at the fictitious interface placed in $y=1-\delta$; it will be precisely this condition which will force the occurrence of one unstable mode, considering that the profile of the mean velocity in the interval $[1-\delta, y_\infty]$ presents no inflection points (under **B**). At $y=1-\delta$ we impose, like we have done in the corresponding determination of the mean flow, continuity of pressure and of the vertical velocity component. We thus need the expression of p and v deep within the canopy, where U is constant. It is simple to find that, for $y\leq 1-\delta$, equation

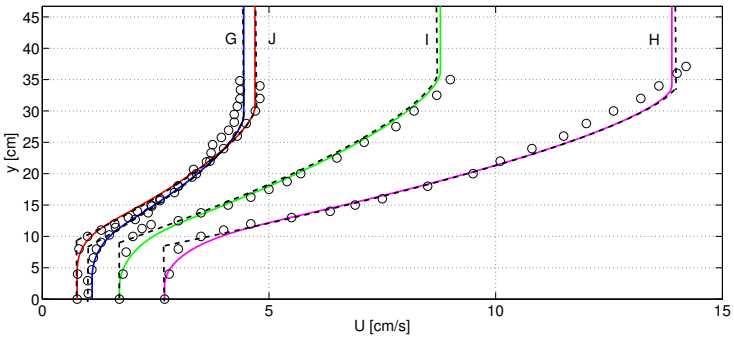

Figure 5.54: Mean velocity profiles of the flow through a rigid canopy, for various experimental runs (markers represent experimental datas from Ghisalberti & Nepf (2004, 2005)). Solid and dashed lines are the mean flow profiles built using approach **A** and **B**, respectively. In physical units it is $h = 13.8\,cm$ and the free surface is at $y_\infty = 46.7\,cm$.

CASE	Re_d	$\mathcal{K}_{11}$	$\mathcal{K}_{22}$
G	70.4	0.0045	0.0054
H	172.8	0.0014	0.0017
I	108.8	0.0027	0.0032
J	49.3	0.0032	0.0038

Table 5.2: Reynolds numbers, $\mathrm{Re}_d = U_1 d/\nu$, and dimensionless components of the apparent permeability tensor for the cases analyzed.

(5.3.13) reduces to the first term because U is constant, and its solution is

$$v_{canopy} = G\sinh(\alpha y), \quad p_{canopy} = -iG(U-c)\cosh(\alpha y), \tag{5.3.14}$$

where G is an integration constant. For $y \geq 1-\delta$ the following equation holds

$$p = \frac{i}{\alpha}\left[\left(\frac{\omega}{\alpha} - U\right) Dv + U'v\right], \tag{5.3.15}$$

deduced by combining the Rayleigh and continuity equation for the disturbances. Imposing continuity of p and v at $y = 1-\delta$ by substituting equation (5.3.14) in (5.3.15) the following boundary condition is found:

$$p|_{1-\delta}\tanh[\alpha(1-\delta)] + i(U-c)\,v|_{1-\delta} = 0. \tag{5.3.16}$$

The results, in terms of temporal growth rate ω_i as function of α, are shown for the four cases G through J in fig. 5.55. The amplification factors of approaches **A**

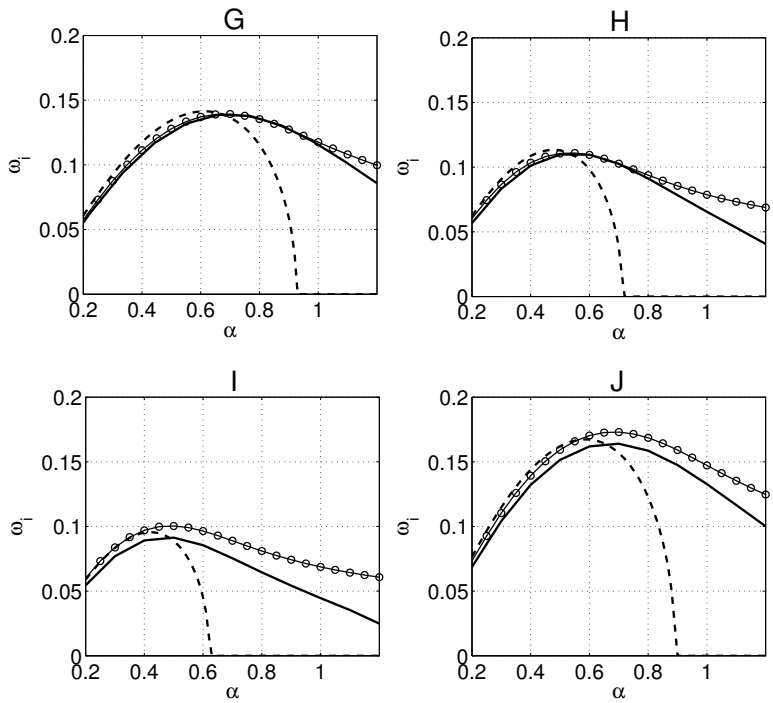

Figure 5.55: Temporal growth rate against wavenumber for the four cases, under Rayleigh's stability equation. Solid lines: numerical results (approach **B** with symbols); dashed lines: analytical results for piecewise-linear profiles.

and **B** are in very good agreement with each other; variations can be ascribed to the mild differences between the two velocity distributions. A further confirmation of the results in figure 5.55 is represented by the analytical solutions for the piecewise linear profiles in the semi-infinite domain $[0, \infty)$, the inclined piece of which is taken to be tangent to the numerical profile of approach **A** at the point of maximum

vorticity (cf. fig. 5.52). It is simple to find that

$$\omega_i(\alpha) = \alpha\, Im\left(\pm\sqrt{-\left(\frac{U_2-U_1}{2}\right)^2 + \frac{m}{2\alpha}(U_2-U_1)A - \frac{m^2}{16\alpha^2}B}\right),$$

with

$$A = \left(1 - \frac{e^{-2\alpha y_1} + e^{-2\alpha y_2}}{2}\right),$$

$$B = \left(e^{-4\alpha y_1} + e^{-4\alpha y_2} - 2e^{-2\alpha(y_2+y_1)} - 4e^{-2\alpha t_{ml}} - 4e^{-2\alpha y_1} + 4e^{-2\alpha y_2} + 4\right),$$

and $m = (U_2 - U_1)/t_{ml}$ the slope of the profile at the inflection point. The three families of curves in fig. 5.55 are very close to one another at low to moderate values of α. The results indicate that the preferred wavenumber should be in the range $0.4 \leq \alpha \leq 0.7$ (which means that wavelengths go from about $9h$ to $16h$).

To verify whether these values are reasonable we turn to the detailed measurements and analysis of coherent eddies by Raupach *et al.* (1996). Their results are for *honami* waves, i.e. for the oscillations of terrestrial canopies under the effect of wind, and thus apply to the case of a boundary layer (in their case the atmospheric boundary layer) which is much thicker than the vegetation height. As such, they are not directly applicable to the present case of aquatic canopies, but are nonetheless believed to provide relevant orders of magnitudes of the waves' characteristic features. The crucial parameter in the analysis by Raupach *et al.* (1996) is the *shear length scale* $L_s = U(h)/U'(h)$. L_s correlates well the streamwise spacing of the dominant canopy eddies; in particular, Raupach *et al.* (1996) state that

$$\alpha = \frac{2\pi h}{\gamma L_s},$$

with $\gamma = 8.1 \pm 0.3$, on the basis of observations from several experiments. We further note that L_s appears to be correlated also to the occurrence of *monami* waves in water: our analysis of the nine flow scenarios studied by Ghisalberti & Nepf (2002) suggests that *monami*s take place past a threshold value $L_s = 0.65h$, and the corresponding instabilities display a wavenumber α which is always below 1.4. Further confirmation of the relevance of L_s for the case of coherent eddies over aquatic vegetation is provided by Singh *et al.* (2015).

Another result by Raupach and colleagues, based on two-point u correlations of *honami* waves in a sparse wheat canopy, is that the dominant circular frequency is approximated by

$$\omega_r = \frac{\pi}{\epsilon}\frac{U(h)}{U_m},$$

with $\epsilon = 3 \pm 0.5$. A fit through the experimental data of Ghisalberti & Nepf (2002) for experiments in water provides a mean value of ϵ which is centered around 3.5.

A further correlation reported by Raupach *et al.* (1996) concerns the growth rate ω_i of the most unstable eddies, which is found to be proportional to $hU'(h)/U_m$.

Table 2 gives a summary of these predictions for the four experiments by Ghisalberti and Nepf analyzed here. On the basis of what stated above on L_s we might expect scenarios G, H and I to lead to *monami* waves. It is however somewhat unexpected to find that case J apparently displays the largest instability growth rate.

It is immediately apparent from the table that the most unstable wavenumbers of the inviscid stability analysis are 100% off the experimental correlations. Also, the frequencies of the most unstable mode at the peak value of α are underestimated by the numerical results. These facts justify a closer look at the effect of the drag force exerted by the canopy on the flow.

Accounting for drag

Drag is accounted for, in approach **A**, through a source term in the momentum equations, yielding a modified Rayleigh equation similar to that used by Singh *et al.* (2015) for the study of canopy flows. The difference from Singh et al.'s approach is that the drag coefficient C_d is not taken to be constant by Pluvinage (2015) within the canopy but variable, as shown in fig. 2. Another difference lies in the fact that is considered a shear layer extending to a large value of y_∞, whereas Singh *et al.* have limited the vertical extent of the domain to the actual size of the water channel of the experiments by Ghisalberti & Nepf (2002), enforcing at the free surface a no-shear condition. A final difference lies in the turbulence model used in Singh *et al.* (2015), based on a constant eddy viscosity through the canopy.

The equation used in approach **A** is:

$$(U - c)(D^2 - \alpha^2)v - U''v - \frac{ia}{\alpha} D(C_d U D v) = 0,$$

with $v = 0$ at $y = 0, y_\infty$.

Approach **B** couples Rayleigh's equation outside of the canopy to Darcy's equation within it, with a matching at the fictitious interface, $y = 1 - \delta$, on pressure and vertical velocity. Deep inside the porous zone the dimensional disturbance equations are

$$\frac{\partial u_i}{\partial x_i}, \quad u_i = -\frac{\kappa_{ij}}{\mu} \frac{\partial p}{\partial x_j}.$$

CASE	L_s/h	$U(h)[cms^{-1}]$	$U_m[cms^{-1}]$	$U'(h)[s^{-1}]$	α	ω_r	$hU'(h)/U_m$
G	0.73	2.22	2.75	0.22	1.06±0.04	0.87±0.14	1.104
H	0.73	5.95	8.29	0.59	1.06±0.04	0.77±0.13	0.982
I	0.76	3.60	5.24	0.35	1.02±0.04	0.74±0.12	0.922
J	0.55	1.88	2.73	0.25	1.42±0.05	0.74±0.12	1.835

Table 5.3: Significant parameters of the four experiments considered and characteristic wavenumber, frequency and growth rate of the coherent eddies which form above the canopy, according to estimates by Raupach *et al.* (1996).

Scaling the variables as in the previous section, the continuity equation remains unaltered and Darcy's equation becomes:

$$u_i = -\frac{\rho U_m h}{\mu}\,\frac{\kappa_{ij}}{h^2}\,\frac{\partial p}{\partial x_j} = -Re\,\mathcal{K}_{ij}\,\frac{d}{ah^2}\,\frac{\partial p}{\partial x_j},$$

with $Re = \rho U_m h/\mu$ the Reynolds number, $\mathcal{K}_{ij} = \kappa_{ij}/l^2$ the dimensionless permeability tensor (normalized with the square of the length l of the unit cell, i.e. the canonical normalization used elsewhere in this thesis), and $d/ah^2 = (l/h)^2$ a geometric coefficient related to the diameter ($d = 0.64cm$) of the cylindrical fibers forming the canopy. From now on, for simplicity, we will indicate the group $Re\,\mathcal{K}_{33}\,d/ah^2$ with the symbol ξ.

Given the orthotropic nature of the canopy, the off-diagonal terms of the permeability tensor $\mathcal{K}_{ij}$ vanish, and continuity yields

$$(D^2 - \tilde{\alpha}^2)p = 0,$$

with $\tilde{\alpha} = \alpha\sqrt{\mathcal{K}_{11}/\mathcal{K}_{33}}$. For the case of Stokes flow it is $\mathcal{K}_{11}/\mathcal{K}_{33} \approx 0.50$ (cf. fig. 4.12), but here we have chosen to use $\mathcal{K}_{11}/\mathcal{K}_{33} = 0.83$, as by computations in chapter 4, at the present values of the Reynolds number (cf. table 5.2). Upon application of the condition $v(0) = 0$, it is easy to find that p and v deep inside the canopy are given by:

$$p_{canopy} = \tilde{A}\cosh(\tilde{\alpha}y), \quad v_{canopy} = -\xi\tilde{\alpha}\tilde{A}\sinh(\tilde{\alpha}y).$$

Continuity of p and v at $y = 1 - \delta$ yields the boundary condition to be used when solving Rayleigh's equation in the domain $[1 - \delta, y_\infty]$, i.e.

$$v|_{1-\delta} + \xi\,\tilde{\alpha}\tanh[\tilde{\alpha}(1-\delta)]\,p|_{1-\delta} = 0. \tag{5.3.17}$$

The other condition is simply $v|_{y_\infty} = 0$.

Stability results are displayed as ω_i versus α in figure 5.56. For approach **A** the curves are very similar to those of the previous section, except for a damping effect experienced by the most unstable Helmholtz mode for all cases considered. This is precisely the effect predicted by Py *et al.* (2004) for the mixing layer instability over a flexible crop canopy. However, given that the wavenumber of largest growth seems still underestimated (at least against experimental correlations, cf. table 5.3) something seems to be missing from model **A**. A similar argument motivated Py *et al.* (2004) to study a coupled fluid-structure model, accounting for the flexibility of the

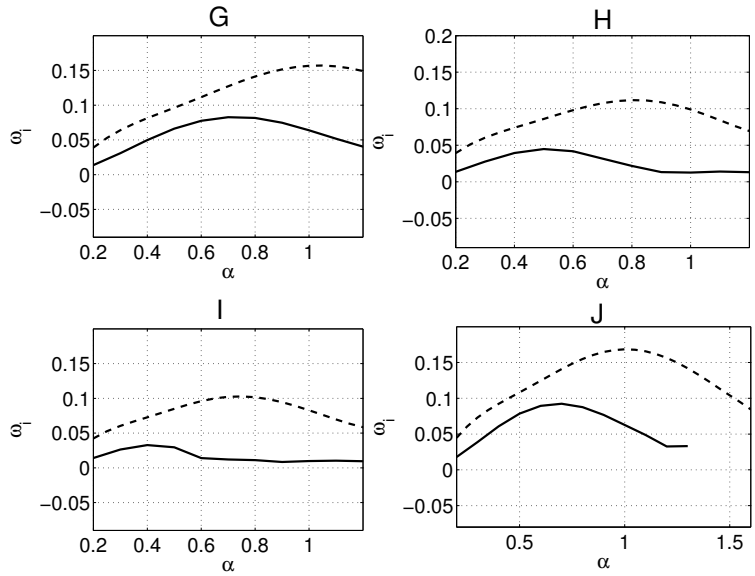

Figure 5.56: Stability curves for runs G, H, I and J, accounting for drag. The solid and the dashed lines are based, respectively, on approach **A** and **B**.

canopy via a wave equation (Doaré *et al.* (2004)). Py and colleagues demonstrated that, for realistic values of the crop flexibility, the characteristics of the mixing layer instability were significantly modified, in particular with an increase of the most amplified wavenumber. This explained, at least in qualitative terms, discrepancies with measurements of the size of coherent eddies over a variety of canopies, as reported by Finnigan (2000).

In cases G through J examined here the canopy is not flexible, which means that it is the model itself (Rayleigh equation plus drag in the canopy, expressed with a drag coefficient C_d) which might have to be questioned. Model **B** proposed here represents an alternative, never explored before, which shows some promise. In fact, the results based on the coupled Rayleigh-Darcy system provide most unstable wavenumbers which approaches the heuristic predictions by Raupach *et al.* (1996), as shown in table 5.4.

Also the growth rate of the most unstable mode is rather well correlated by the

CASE	$\alpha_{\mathbf{A}}$	$\alpha_{\mathbf{B}}$	$\omega_{i\mathbf{A}}$	$\omega_{i\mathbf{B}}$	$\omega_{r\mathbf{A}}$	$\omega_{r\mathbf{B}}$
G	0.73	1.05	0.083	0.157	0.68	1.225
H	0.50	0.8	0.045	0.112	0.45	0.929
I	0.43	0.75	0.034	0.103	0.38	0.867
J	0.70	1.00	0.092	0.168	0.63	1.182

Table 5.4: Most unstable modes for approaches **A** and **B**, accounting for drag throughout the canopy.

results of model **B** which indicate that

$$\frac{\omega_{i\mathbf{B}} U_m}{U(h)h} = 0.108 \pm 0.014,$$

i.e. the ratio above is constant to within about 10%. Conversely, the same ratio based on $\omega_{i\mathbf{A}}$ varies from 0.037 to 0.080.

The most unstable circular frequencies ω_r of the analysis, on the other hand, exceed those of Raupach et al.'s correlation (cf. table 5.3). On the basis of our results the coefficient ϵ should be about half the value quoted in Raupach *et al.* (1996) for the case of *honami*.

An example of mode shapes is provided in figure 5.57 for scenario G. For comparison purposes also the mode shapes of the no drag case are reported; all cases refer to a wavenumber equal to 0.7. As for the curves of the growth rate, in the case without drag the eigenfunctions of the two approaches are similar. The main difference is in the fact that we do not constrain the horizontal disturbance velocity to be continuous at the fictitious interface in approach **B**. Regarding the case with drag, instead, the main difference between the two approaches seems to be the non-smoothness of the vertical velocity at $y = 1 - \delta$.

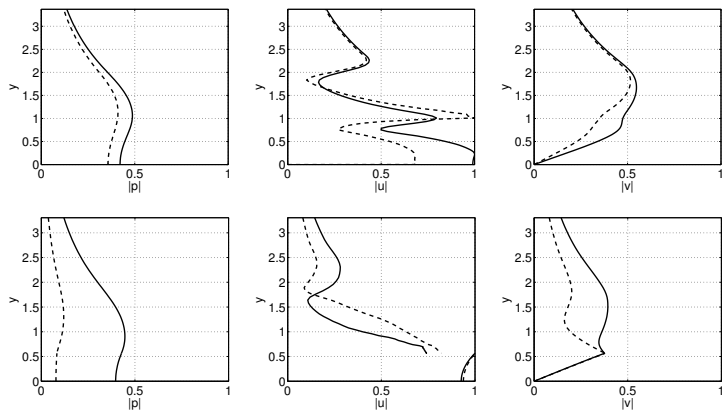

Figure 5.57: Modulus of the most unstable perturbation mode shapes for run G ($\alpha = 0.7$). Solid lines: Rayleigh equation. Dashed lines: including the drag force. Upper frames: approach **A**; lower frames: approach **B**.

Chapter 6

Conclusions and outlook

A homogenization approach has been used to study the flow over and through porous and poroelastic media, with a general strategy suitable for every kind of micro-periodic geometry. The work is developed essentially from two points of view: the microscopic and the macroscopic one. The microscopic equations provide a characterization of the particular geometry of the porous medium, resulting in an estimate for the components of the permeability and the effective elasticity tensors; the results for these tensors can be summarized in this way:

- the permeability tensor for spheres and touching spheres is isotropic (i.e. $\mathcal{K}_{ij} = \kappa\delta_{ij}$), as expected. In the case of spheres $\mathcal{K}_{ij}$ has been validated and a new correlation for the (scalar) permeability κ is provided as function of the porosity ϑ of the medium, correcting the classical relation by Kozeny-Carman.

- For transversely isotropic structures (cylinders and linked cylinders) only two diagonal components of this second order tensor ($\mathcal{K}_{11}$ and $\mathcal{K}_{33}$) are present since the terms relative to the plane normal to the vertical fibres' axes are equal. This result can be easily confirmed analytically (Milton, 2004). For cylindrical structures, $\mathcal{K}_{ij}$ has been compared with values from the literature, obtaining good agreement.

- In the presence of inertia within the porous region, an approach to estimate the permeability is proposed, based on the Oseen linearization of the equations in the unit cell, plus an iterative approach which alternates between the

microscopic and the macroscopic region. With this technique, the *apparent permeability* from the theory approaches the values found in experiments and direct numerical simulations, with the correct trend as function of the pore Reynolds number. The theoretical values do not precisely match those available from experiments or DNS because the fibres considered here are neither sufficiently slender nor packed densely enough for the first order equations of the multiple scale approximation to be fully adequate. To improve this one could possibly push the multiple scale theory up to higher order.

- The permeability tensor determined with the new three-scale approach for cylindrical structure is completely in agreement with that found in the two-scale approach. This allow us to consider simpler two-dimensional microscopic problems for every structure which is invariant in the x_3-axis.

- The effective elasticity tensor $\mathcal{C}_{ijkl}$ associated to the homogenized material has been computed. The assumption of periodicity over the REV gives good results for completely connected microscopic structures (linked cylinders and touching spheres), highlighting the properties of the transversely isotropic media. In case of unconnected fibers the homogenized material has strange properties which deserve further investigations (Hoffmann *et al.*, 2004).

- The tensor α'_{ij} depends directly on a geometrical assigned parameter (the porosity), so that no computational efforts must be made for its determination.

The coupling of the flow problem within the porous medium with that in a pure-fluid region neighboring it is particularly important. The main conclusion is that Darcy's law and its generalization to the poroelastic case provides a good approximation of the velocity inside the porous medium, also when inertia in the flow within the P-region is non-negligible. For rigid porous media, the DNS implemented inside the cavity has been fundamental since it has allowed us to explore in depth the different interface conditions to be imposed between the fluid and porous region. All of them contain some degree of arbitrariness and parameters which must be tuned. The interface condition of Le Bars & Worster (2006), which is an extension of the one by Beavers & Joseph (1967), is found to be the most suitable, both in the case of laminar and turbulent flow. The penetration depth δ which needs to be imposed satisfies the order estimate of Le Bars & Worster (2006), for fixed pore Reynolds number. When $\vartheta \mathrm{Re}_p$ increases also δ increases, and this should be accounted for when selecting δ in the model.

Conversely, the use of Brinkman's correction to Darcy's law should be avoided since, on the one hand, the estimation of the effective viscosity μ_e is uncertain and, on the other, results with this model appear to systematically overestimate the velocity near the interface.

Finally, also a condition which employs permeability components which vary as the interface is approached do not appear adequate. The distance over which the permeability approaches the infinite value of the pure fluid region has been estimated to be of order ϵ on the basis of DNS, and depends mildly on Reynolds numbers, for the range considered which spans three orders of magnitude. The use of permeability components which change smoothly (even according to DNS results) is, however, not sufficient in a coupled NSE-Darcy system to represent inertial effects within a small porous layer adjacent to the pure fluid region, and this suggests the inclusion of a Forchheimer term in a thin-layer interface model (Firdaouss *et al.*, 1997).

In case of poroelastic media the lack of a direct numerical simulation or other kind of available results to allow comparisons, weakens the conclusions which we reach, at least as far as the interface condition is concerned. The comparison with the rigid case is a preliminary validation of the model.

In section 5.3 the instability of shear layers generated by rigid canopies, is studied. A mean velocity profile (which fits in both cases the experimental data by Ghisalberti & Nepf, 2004, 2005) has been determined using the Prandtl mixing length assumption which appears to yield reasonable results. The presence of the canopy is rendered imposing a boundary condition at its fictitious edge, deduced by the governing homogenized equations.

A first step in stability analysis consists in neglect the canopy drag. The model displays the stability behavior in agreement with that described by Pluvinage (2015) and yield similar results as the theoretical model based on a piecewise-linear mean profile, at least for the case of long waves. Comparisons of the most unstable modes with the measurements by Raupach *et al.* (1996) and Ghisalberti & Nepf (2004) suggest that drag within the canopy must be accounted for (a fact which had been already suggested by Py *et al.* (2004)). We have thus tried to include the drag exerted by the canopy via a modified boundary condition at a canopy's fictitious edge. The second approach yields reasonable estimates of the wavenumber α and of the frequency ω_r, at least when compared to existing correlations. The growth rate of the most unstable mode is also found to be proportional to the quantity $hU'(h)/U_m$, with almost the same constant of proportionality for the four configurations studied, in agreement with experiments by Raupach *et al.* (1996). Some improvements could

be obtained using Brinkman's equation to model viscous effects within the canopy or Forchheimer's equation to account for inertial terms. In any case, only careful experimental measurements can justify the preference of a model over another and permit progress in the determination of the most appropriate interface condition to be imposed at the boundary of a porous (or poroelastic) medium and a pure fluid region.

Future developments This work has many pending points yet, which could give a deeper knowledge about the interaction between a fluid and a poroelastic medium characterized by a separation of scale. Some of them are listed here, inlight of the conclusions already reached:

- from a microscopic point of view, a strategy is needed to tackle unconnected microscopic structures. A way could be to develop an *ad hoc* three-scale approach which reduces the problem to the (x_1, x_2) plane, like in the rigid case. Another one could be to relax the periodicity assumption in the x_3-direction and consider new boundary conditions at the bottom and top of the fibers. This procedure should allow us to find some kind of response to horizontal deformations through the fact that the fibers are hinged at a wall.
- Since it is suitable to not consider periodic structures, the homogenization theory formalism must be extended to confined media, initially introducing weak (or statistical) periodicity for the microscopic problems. This extension could lead us to interface conditions directly deduced by homogenization.
- The preliminary study made using the Oseen's approximation to account for inertia in the permeability tensor should be parameterized finding a relation between the apparent permeability, the Reynolds number, the direction of the flow with respect to the principal axes of the microscopic structure and the porosity.
- The Oseen's approximation is only one strategy to include inertia in the model. Another strategy consists in the development of non-linear equations for the homogenized model, which can be deduced by higher order approximations in ϵ.
- A strategy to consider turbulent flows in poroelastic media could consist in the determination of microscopic problems for variables (e.g. eddy viscosity ν_t) which characterize the typical structures of turbulence.

Appendices

Appendix A

Numerical issues

A.1 The microscopic codes

The microscopic problems arising from homogenization have been solved with OpenFoam. The objective of this appendix is not to explain the finite volume method (FVM) on which OpenFoam is based, but to explain how this tool has been used to solve the PDE's introduced in chapter 2. For insights regarding FVM we refer to Versteeg & Malalasekera (2007) and for its implementation in OpenFoam to Moukalled *et al.* (2015). A simple scheme which describes how this FVM code works is presented here to make this appendix self-consistent. The `casedirectory` folder contains at least three subfolders: `0`, `constant` and `system`. The `0` folder contains the information about the initialization and boundary conditions for the unknown fields. The `constant` folder contains the definition of the discretized domain. To build a discretized domain we start from a CAD geometry of the physical domain. Then, this geometry is meshed (i.e. partitioned in cells whose shape depends on the meshing method). Each cell has a center and some faces over which the unknowns are evaluated on the basis of the spatial discretization scheme which is chosen. The numerical methods used for spatial and temporal discretization are set in the `system` folder. Now we are ready to present the strategies of resolution for the most used and meaningful microscopic tensors.

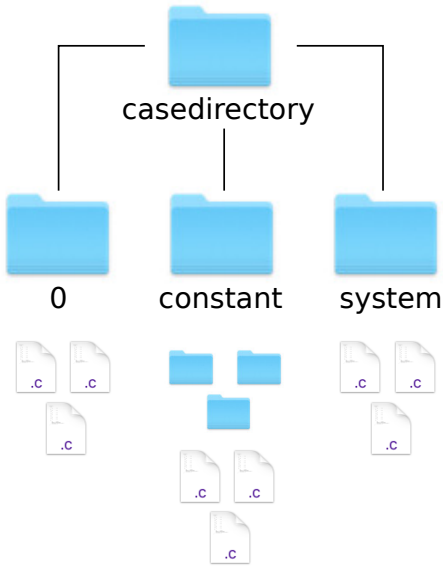

Figure A.1: Typical structure of an OpenFoam case.

A.1.1 Resolution of the problem for K_{ij} and A_j

Systems (4.0.3) or (4.0.5) (in case of Re $= \mathcal{O}(1)$), are boundary value problem defined over V_f, the domain occupied by the fluid inside the microscopic cell V. The boundary conditions are, in both cases, $K_{ij} = 0$ on Γ plus periodicity of the unknowns over V. We have a system of twelve equations and twelve unknown, plus the respective boundary conditions. Actually, the twelve governing equations can be grouped into three sets of four disjoined equations. The unknowns of each set are four: a vector field composed by the rows of the permeability tensor (K_{Ij}) and a scalar field represented by each entry of $\mathbf{A}$ (A_I, I fixed).

From this point of view, for Re $= \mathcal{O}(\epsilon)$, each of the three problems can be seen as a Stokes problem where K_{Ij} and A_I play the role of velocity and pressure, respectively. The solution of each set of equations satisfies exactly the same problem (the only difference is given by a volumetric source term represented in the equations, the vector field δ_{Ij}). In case of Re $= \mathcal{O}(1)$, the governing equations for K_{Ij} contain one more term which can be viewed as a linearized convective term.

A minimal effort is required to solve the problem since it is sufficient to delete

the convective term (for Re $= \mathcal{O}(\epsilon)$ or to linearize it for Re $= \mathcal{O}(1)$) of `icoFoam`, an existing solver for the NSE present in OpenFoam. In the programming language the equations for Re $= \mathcal{O}(1)$ read

```
// ************************************************************//
        fvVectorMatrix KEqn
        (
            fvm::ddt(K)
          + fvm::div(phiReU, K)
          - fvm::laplacian(nu, K)
        );

        solve(KEqn == DELTA -fvc::grad(A) );
// ************************************************************//
```

In order to solve the problem for Re $= \mathcal{O}(\epsilon)$ it is sufficient to delete the linearized convective term `fvm::div(phiReU, K)`. To better understand these equations we have to consider that:

- A time marching solver with Crank-Nicolson discretization in time (set in the file `casedirectory/system/fvSchemes.c`) is used to reach the steady-state; the time derivative is written in the solver as `fvm::ddt` where `ddt` is a member of the class `fvm` (`finite volume matrix`; this allows to build the matrices which discretize a partial differential operator) and double colon `::` is an access function to enter the classes.
- The spatial operators (which are members of `fvm`) has been discretized using a Gauss integration with different interpolation schemes for each operator.
- The gradient of A_I is taken into account in an explicit way (`grad` is a member of the class `fvc`, `finite volume calculus`, which allows to build the known term of the linear system associated to a given discretized PDE and, more in general, to apply differential operations to vector fields), because the PISO algorithm is used to decouple the equation for K_{Ij} and A_I, (for an explanation of the algorithm and its implementation, cf. Moukalled *et al.*, 2015).
- Once the spatial operators are discretized, the linear systems are solved using the `GAMG` (geometric-algebraic multi-grid) method for A_I and `PCG` (pre-conjugate gradient) method with `DIC` (Cholesky incomplete decomposition) preconditioner for $\mathcal{K}_{ij}$.

For each one of the geometries for which the equations have been solved, a grid convergence study has been performed (an example is shown in figure A.2 for Re $=$

# CELLS	$\mathcal{K}$
50^3	$2.07 \cdot 10^{-2}$
75^3	$2.10 \cdot 10^{-2}$
100^3	$2.08 \cdot 10^{-2}$

Table A.1: Scalar permeability in the case of spherical inclusions with $\vartheta = 0.8$. The base mesh is built with `blockMesh` with 50, 75, and 100 cells per unit length, respectively. The final mesh is built with `snappyHexMesh`.

# CELLS	$\vartheta \mathrm{Re}_p = 10^{-1}$	$\vartheta \mathrm{Re}_p = 1$	$\vartheta \mathrm{Re}_p = 10$	$\vartheta \mathrm{Re}_p = 50$
50^3	$1.89 \cdot 10^{-2}$	$1.89 \cdot 10^{-2}$	$1.80. \cdot 10^{-2}$	$1.59 \cdot 10^{-2}$
75^3	$1.85. \cdot 10^{-2}$	$1.85 \cdot 10^{-2}$	$1.80. \cdot 10^{-2}$	$1.57 \cdot 10^{-2}$
100^3	$1.89 \cdot 10^{-2}$	$1.89. \cdot 10^{-2}$	$1.82 \cdot 10^{-2}$	$1.61 \cdot 10^{-2}$

Table A.2: $\mathcal{K}_{11}$ for cylindrical inclusions with $\vartheta = 0.8$ and for different Re_p. The base mesh is built with `blockMesh` with 50, 75, and 100 cells per unit length, respectively. The final mesh is built with `snappyHexMesh`.

$\mathcal{O}(\epsilon)$ and $\vartheta = 0.8$). In table A.2 others grid convergence tests are shown in the case $\mathrm{Re} = \mathcal{O}(1)$.

Also L_{ijk} and M_{ijk} satisfy Stokes problems, forced by different volumetric constants. We omit the presentation of the corresponding codes which are analogous to those for the permeability tensor.

Solution for K_{ij} and A_j in the 3-scale approach The problems deduced by the three-scale homogenization (equations 2.3.22, 2.3.26 and 2.3.27) are defined over two-dimensional domains. The problems to be solved for the determination of K_{1j}, A_1 and K_{2j}, A_2 do not change from the two-scale approach, so that their resolution is the same as before. The problem for K_{33} is very simple: it consists of a Poisson's equation with a constant non-homogeneous forcing term in the whole domain, plus periodicity along x_1 and x_2. The routine `laplacianFoam`, already implemented in OpenFoam allows to easily determine K_{33}. In table A.3 the spatial convergence for K_{33} is shown.

Determination of the averaged tensors Once the microscopic permeability tensor is computed, to obtain the integral value over its domain it is sufficient to define a `functionObject` in the `system/controlDict` file of the present case.

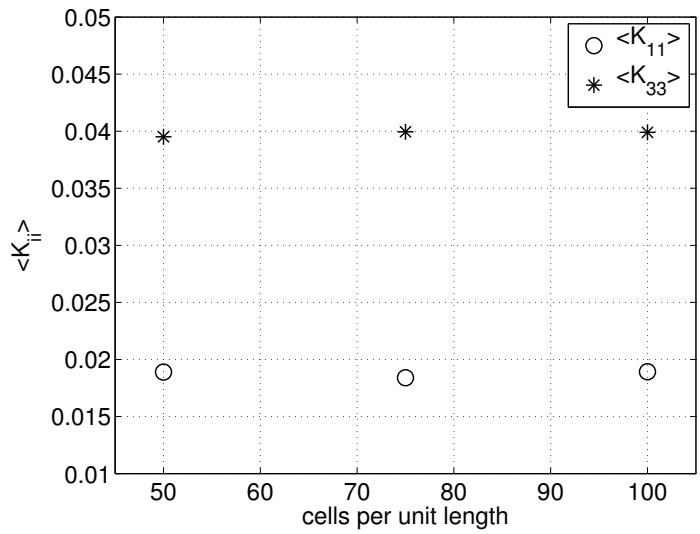

Figure A.2: Grid convergence evaluated looking at the integral of K_{11} and K_{33} over the domain, for three different grids, in the case of cylindrical inclusions and porosity 0.8.The mesh is built with `snappyHexMesh`.

```
// ************************************************************** //
    avgK
    {
        type cellSource;
        functionObjectLibs ("libfieldFunctionObjects.so");
        enabled true;
        outputControl timeStep;
        outputInterval 1;
        log true;
        valueOutput false;
        source all;
        operation volIntegrate;
        fields K;
    }
// ************************************************************** //
```

A.1.2 Resolution of the problems for χ_i^{pq} and η_i

System (4.0.1) is constituted by twenty-seven equations with the respective boundary conditions plus periodicity over the microcell. Upon inspection, the twenty-

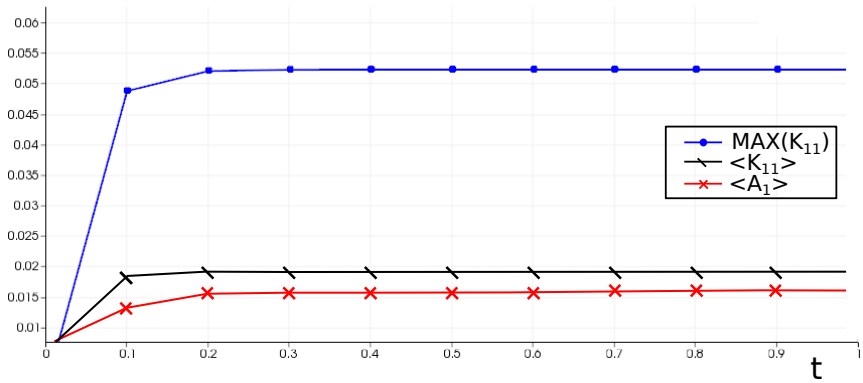

Figure A.3: Convergence in time of the time-marching solver for K_{1j}. A steady solution is reached in this case after about 0.25 time units. The case shown here is related to $\mathcal{K}_{11}$ with $\vartheta = 0.8$. Two indicators of the steady-state are shown: the maximum value reached by the solution and its integral value over the whole microscopic domain.

# CELLS	$\mathcal{K}_{33}$	$\mathrm{MAX}_V(\mathcal{K}_{33})$
50^3	$4.09 \cdot 10^{-2}$	$8.12 \cdot 10^{-2}$
150^3	$4.08 \cdot 10^{-2}$	$8.16 \cdot 10^{-2}$
200^3	$4.08 \cdot 10^{-2}$	$8.16 \cdot 10^{-2}$

Table A.3: Vertical permeability computed with the equations deduced by the three-scale approach, in case of cylindrical inclusions such that $\vartheta = 0.8$. The mesh is built with `NetGen` algorithm using 50, 150, and 200 cells per unit length, respectively.

seven unknown can be divided into nine independent groups of three unknowns which satisfy 9 disjoined sets of three equations plus boundary conditions. From this point of view, we have 9 unknown vector fields defined over the solid inclusions inside the microcell. Since the elastic material is isotropic these vector fields reduces to six, precisely, χ_i^{11}, χ_i^{22}, χ_i^{33}, χ_i^{12}, χ_i^{13} and χ_i^{23}. Each of the six unknown fields to be solved are ruled by equations which are linear combinations of the entries of the jacobian of $\boldsymbol{\chi}^{pq}$, $[J(\boldsymbol{\chi}^{pq})]_{ij} = \partial_j \chi_i^{pq}$. Each set of equations differs from the others because the coefficients of the linear combinations and source terms in the boundary conditions are different. These coefficients represent the elastic response of the material to compressions or expansions in each direction (i.e they are related to the entries of the microscopic elasticity tensor C).

To understand how the operators are discretized and solved, we write explicitly the equations for χ_i^{11}:

$$C_{1111}\frac{\partial^2 \chi_1^{11}}{\partial x_1^2} + C_{1122}\frac{\partial^2 \chi_2^{11}}{\partial x_1 \partial x_2} + C_{1133}\frac{\partial^2 \chi_3^{11}}{\partial x_1 \partial x_3} + \\ + C_{1212}\left(\frac{\partial^2 \chi_1^{11}}{\partial x_2^2} + \frac{\partial^2 \chi_2^{11}}{\partial x_1 \partial x_2}\right) + C_{1313}\left(\frac{\partial^2 \chi_1^{11}}{\partial x_3^2} + \frac{\partial^2 \chi_3^{11}}{\partial x_1 \partial x_3}\right) = 0,$$

$$C_{1212}\left(\frac{\partial^2 \chi_2^{11}}{\partial x_1^2} + \frac{\partial^2 \chi_1^{11}}{\partial x_1 \partial x_2}\right) \\ + C_{2211}\frac{\partial^2 \chi_1^{11}}{\partial x_1 \partial x_2} + C_{2222}\frac{\partial^2 \chi_2^{11}}{\partial x_2^2} + C_{2233}\frac{\partial^2 \chi_3^{11}}{\partial x_2 \partial x_3} + \\ + C_{2323}\left(\frac{\partial^2 \chi_2^{11}}{\partial x_3^2} + \frac{\partial^2 \chi_3^{11}}{\partial x_2 \partial x_3}\right) = 0,$$

$$C_{1313}\left(\frac{\partial^2 \chi_3^{11}}{\partial x_1^2} + \frac{\partial^2 \chi_1^{11}}{\partial x_1 \partial x_3}\right) + C_{2323}\left(\frac{\partial^2 \chi_3^{11}}{\partial x_2^2} + \frac{\partial^2 \chi_2^{11}}{\partial x_2 \partial x_3}\right) + \\ C_{3311}\frac{\partial^2 \chi_1^{11}}{\partial x_1 \partial x_3} + C_{3322}\frac{\partial^2 \chi_2^{11}}{\partial x_2 \partial x_3} + C_{3333}\frac{\partial^2 \chi_3^{11}}{\partial x_3^2} = 0.$$

The corresponding boundary conditions are

$$\left(C_{1111}\frac{\partial \chi_1^{11}}{\partial x_1} + C_{1122}\frac{\partial \chi_2^{11}}{\partial x_2} + C_{1133}\frac{\partial \chi_3^{11}}{\partial x_3} + 1\right) n_1 + \\ + C_{1212}\left(\frac{\partial \chi_1^{11}}{\partial x_2} + \frac{\partial \chi_2^{11}}{\partial x_1}\right) n_2 + C_{1313}\left(\frac{\partial \chi_1^{11}}{\partial x_3} + \frac{\partial^2 \chi_3^{11}}{\partial x_1}\right) n_3 = 0,$$

$$C_{1212}\left(\frac{\partial\chi_2^{11}}{\partial x_1}+\frac{\partial\chi_1^{11}}{\partial x_2}\right)n_1+$$
$$+\left(C_{2211}\frac{\partial\chi_1^{11}}{\partial x_1}+C_{2222}\frac{\partial\chi_2^{11}}{\partial x_2}++C_{2233}\frac{\partial\chi_3^{11}}{\partial x_3}+1\right)n_2+$$
$$+C_{2323}\left(\frac{\partial\chi_2^{11}}{\partial x_3}+\frac{\partial\chi_3^{11}}{\partial x_2}\right)n_3=0,$$

$$C_{1313}\left(\frac{\partial\chi_3^{11}}{\partial x_1}+\frac{\partial\chi_1^{11}}{\partial x_3}\right)n_1+C_{2323}\left(\frac{\partial\chi_3^{11}}{\partial x_2}+\frac{\partial\chi_2^{11}}{\partial x_3}\right)n_2+$$
$$\left(C_{3311}\frac{\partial\chi_1^{11}}{\partial x_1}+C_{3322}\frac{\partial\chi_2^{11}}{\partial x_2}+C_{3333}\frac{\partial\chi_3^{11}}{\partial x_3}+1\right)n_3=0.$$

These equations are valid only if the elasticity tensor has the form (4.2.5). They can be rewritten highlighting the laplacian of each component of χ_i^{11}:

$$C_{1111}\left(\frac{\partial^2\chi_1^{11}}{\partial x_1^2}+\frac{\partial^2\chi_1^{11}}{\partial x_2^2}+\frac{\partial^2\chi_1^{11}}{\partial x_3^2}\right)=-(C_{1122}+C_{1212})\frac{\partial^2\chi_2^{11}}{\partial x_1\partial x_2}+ \tag{A.1.1}$$
$$-(C_{1133}+C_{1313})\frac{\partial^2\chi_3^{11}}{\partial x_1\partial x_3}-(C_{1212}-C_{1111})\frac{\partial^2\chi_1^{11}}{\partial x_2^2}-(C_{1313}-C_{1111})\frac{\partial^2\chi_1^{11}}{\partial x_3^2},$$

$$C_{2222}\left(\frac{\partial^2\chi_2^{11}}{\partial x_1^2}+\frac{\partial^2\chi_2^{11}}{\partial x_2^2}+\frac{\partial^2\chi_2^{11}}{\partial x_3^2}\right)=-(C_{1212}+C_{2211})\frac{\partial^2\chi_1^{11}}{\partial x_1\partial x_2} \tag{A.1.2}$$
$$-(C_{2233}+C_{2323})\frac{\partial^2\chi_3^{11}}{\partial x_2\partial x_3}-(C_{1212}-C_{2222})\frac{\partial^2\chi_2^{11}}{\partial x_1^2}-(C_{2323}+C_{2222})\frac{\partial^2\chi_2^{11}}{\partial x_3^2},$$

$$C_{3333}\left(\frac{\partial^2\chi_3^{11}}{\partial x_1^2}+\frac{\partial^2\chi_3^{11}}{\partial x_2^2}+\frac{\partial^2\chi_3^{11}}{\partial x_3^2}\right)=-(C_{1313}+C_{3311})\frac{\partial^2\chi_1^{11}}{\partial x_1\partial x_3}+ \tag{A.1.3}$$
$$-(C_{2323}+C_{3322})\frac{\partial^2\chi_2^{11}}{\partial x_2\partial x_3}-(C_{1313}-C_{3333})\frac{\partial^2\chi_3^{11}}{\partial x_1^2}+$$
$$-(C_{2323}-C_{3333})\frac{\partial^2\chi_3^{11}}{\partial x_2^2}.$$

In the boundary conditions, the normal to the microscopic interface derivative of

each component of χ_i^{11} can be highlighted:

$$C_{1111}\left(\frac{\partial\chi_1^{11}}{\partial x_1}n_1+\frac{\partial\chi_1^{11}}{\partial x_2}n_2+\frac{\partial\chi_1^{11}}{\partial x_3}n_3\right)= \tag{A.1.4}$$

$$=-\left(C_{1111}+C_{1122}\frac{\partial\chi_2^{11}}{\partial x_2}+C_{1133}\frac{\partial\chi_3^{11}}{\partial x_3}\right)n_1+ \tag{A.1.5}$$

$$-\left[(C_{1212}-C_{1111})\frac{\partial\chi_1^{11}}{\partial x_2}+C_{1212}\frac{\partial\chi_2^{11}}{\partial x_1}\right]n_2+$$

$$-\left[C_{1313}\frac{\partial\chi_3^{11}}{\partial x_1}+(C_{1313}-C_{1111})\frac{\partial\chi_1^{11}}{\partial x_3}\right]n_3, \tag{A.1.6}$$

$$C_{2222}\left(\frac{\partial\chi_2^{11}}{\partial x_1}n_1+\frac{\partial\chi_2^{11}}{\partial x_2}n_2+\frac{\partial\chi_2^{11}}{\partial x_3}n_3\right)= \tag{A.1.7}$$

$$=-\left(C_{2211}+C_{2211}\frac{\partial\chi_1^{11}}{\partial x_1}+C_{2233}\frac{\partial\chi_3^{11}}{\partial x_3}\right)n_2+ \tag{A.1.8}$$

$$-\left[(C_{2121}-C_{2222})\frac{\partial\chi_2^{11}}{\partial x_1}+C_{2121}\frac{\partial\chi_1^{11}}{\partial x_2}\right]n_1+$$

$$-\left[C_{2323}\frac{\partial\chi_3^{11}}{\partial x_2}+(C_{2323}-C_{2222})\frac{\partial\chi_2^{11}}{\partial x_3}\right]n_3, \tag{A.1.9}$$

$$C_{3333}\left(\frac{\partial\chi_3^{11}}{\partial x_1}n_1+\frac{\partial\chi_3^{11}}{\partial x_2}n_2+\frac{\partial\chi_3^{11}}{\partial x_3}n_3\right)= \tag{A.1.10}$$

$$=-\left(C_{3311}+C_{3311}\frac{\partial\chi_1^{11}}{\partial x_1}+C_{3322}\frac{\partial\chi_2^{11}}{\partial x_2}\right)n_3+ \tag{A.1.11}$$

$$-\left[(C_{3131}-C_{3333})\frac{\partial\chi_3^{11}}{\partial x_1}+C_{3131}\frac{\partial\chi_1^{11}}{\partial x_3}\right]n_1+$$

$$-\left[C_{3232}\frac{\partial\chi_2^{11}}{\partial x_3}+(C_{3232}-C_{3333})\frac{\partial\chi_3^{11}}{\partial x_2}\right]n_2. \tag{A.1.12}$$

The equations, written in this way, lend themselves to an easy implementation with OpenFoam. Two things must be observed:

- the RHS of each governing equation and boundary condition can be written as the divergence of vectors whose entries are linear combinations of $[J(\boldsymbol{\chi}^{pq})]_{ij}$;
- the divergence operator is not implemented in OpenFoam as an implicit operator. In the programming language of OpenFoam, the `div` operator is not a member of the class `fvm`, but is a member of the `fvc` class.

On the basis of the previous considerations, the equations above are solved using a time-marching solver. The LHS of (A.1.1), (A.1.2) and (A.1.3) represent the implicit terms, while the RHS is completely explicit. In the OpenFoam notation this means

```
//***************************************************************//
        fvVectorMatrix ChiEqn
        (
            fvm::ddt(Chi) +
5           fvm::laplacian(diagC,Chi)  == - fvc::div(S)
        );
//***************************************************************//
```

where `diagC` is a vector which contains the first three entries on the diagonal of C_{ijkl} and `S` is defined as

```
//***************************************************************//
        S.replace(0,(C11.component(vector::Y) * GradChi.component(tensor::YY)
                + C11.component(vector::Z) * GradChi.component(tensor::ZZ)));
        S.replace(3,(Cmix.component(vector::X) * (GradChi.component(tensor::XY
                ))));
        S.replace(6,(Cmix.component(vector::Y) * (GradChi.component(tensor::XZ
                ))));
5       S.replace(1,(Cmix.component(vector::X) * (GradChi.component(tensor::YX
                ))));
        S.replace(4,(C22.component(vector::X) * GradChi.component(tensor::XX)
                + C22.component(vector::Z) * GradChi.component(tensor::ZZ)));
        S.replace(7,(Cmix.component(vector::Z) * (GradChi.component(tensor::YZ
                ))));
        S.replace(2,(Cmix.component(vector::Y) * (GradChi.component(tensor::ZX
                ))));
        S.replace(5,(Cmix.component(vector::Z) * (GradChi.component(tensor::ZY
                ))));
10      S.replace(8,(C33.component(vector::X) * GradChi.component(tensor::XX)
                + C33.component(vector::Y) * GradChi.component(tensor::YY)));
//***************************************************************//
```

where `GradChi` $= [J(\boldsymbol{\chi}^{pq})]_{ij}$, `C11`, `C22`, `C33` are vectors formed by the non-zero entries of the first, second and third row of C_{ijkl}, respectively, and `Cmix` is a vector which contains the last three entries on the diagonal of C_{ijkl}.

Since in OpenFoam it is possible to impose only boundary conditions on the value of the unknown fields (Dirichlet conditions) or on their normal to the boundary surface derivative (Neumann conditions), also the boundary conditions (A.1.4), (A.1.7), (A.1.10) are discretized in time, i.e.

$$LHS^{(N+1)} = RHS^{(N)} \tag{A.1.13}$$

where the superscript denotes the time index. These conditions are implemented using the extension `swak4Foam` which allows to customize initial and boundary

conditions. Conditions (A.1.4), (A.1.7) and (A.1.10) have been imposed during the initialization of $\boldsymbol{\chi}_{pq}$ in the following way:

```
boundaryField
{
    down
    {
        type            cyclic;
    }
    up
    {
        type            cyclic;
    }
    right
    {
        type            cyclic;
    }
    left
    {
        type            cyclic;
    }
    front
    {
        type            cyclic;
    }
    back
    {
        type            cyclic;
    }
    fil
    {
        type            groovyBC;
        value           uniform (0 0 0);
        valueExpression "vector(0,0,0)";
        gradientExpression "-oldTime(SBCs)&normal()";
        fractionExpression "0";
    }
}
```

where `down`, `up`, `left`, `right`, `front`, `back` represent the faces of the cubic microscopic cell over which periodic (`cyclic`) boundary conditions are imposed, and `fil` corresponds to Γ (the microscopic fluid-structure interface). The function `oldTime` allows the access to the solution at the previous time step, while the tensor `SBCs` represent the RHS of (A.1.4), (A.1.7) and (A.1.10). Note that here, the boolean variable `fractionExpression`, set equal to 0, switches to a Neumann boundary condition with known term equal to `gradientExpression`. We sum up the numerical schemes used:

- a time marching solver with Crank-Nicolson discretization in time is used to reach the steady-state;

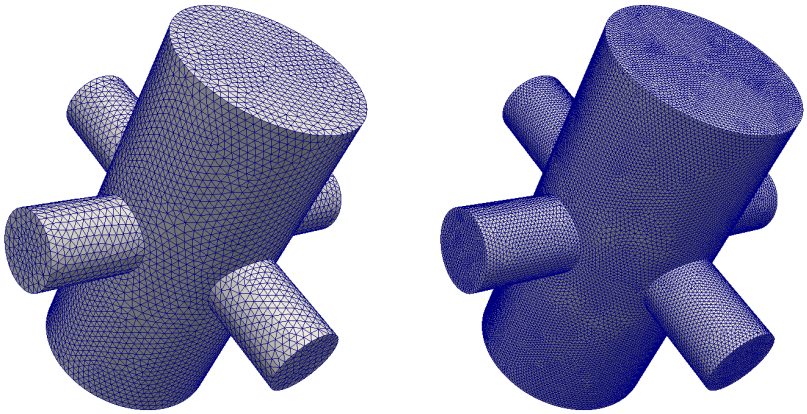

Figure A.4: Tetrahedral grids of linked cylinders such that $d/d_t = 2.5$ and $r = 0.252$. The grids are composed by about 2×10^5 (left) and 2×10^6 (right) tetrahedra.

- the spatial operators are discretized using a Gauss integration with different interpolation schemes for each operator;
- once the spatial operators are discretized, the linear systems are solved using the `PCG` method with `DIC` preconditioner for $\mathcal{K}_{ij}$.

It is clear that when the steady state is reached the original equations and boundary conditions are satisfied. For each one of the results shown in the thesis, both temporal and spatial convergence has been verified. The grid convergence is shown in figure A.5 for the particular case of a linked cylinder with $d/d_t = 2.5$; the relative error between the solution obtained with the coarser mesh (shown in the left frame of figure A.4) and that obtained with the finer mesh (shown in the right frame of figure A.4) is about 0.5% (evaluated as the mean of the relative errors between each dominant component of $\langle [J(\boldsymbol{\chi}^{pq})]_{ij} \rangle$). An example of temporal convergence is shown in figures A.6 and A.7 for $\boldsymbol{\chi}^{pq}$. The equations satisfied by η_i are analogous to those just analyzed and do not need further explanations.

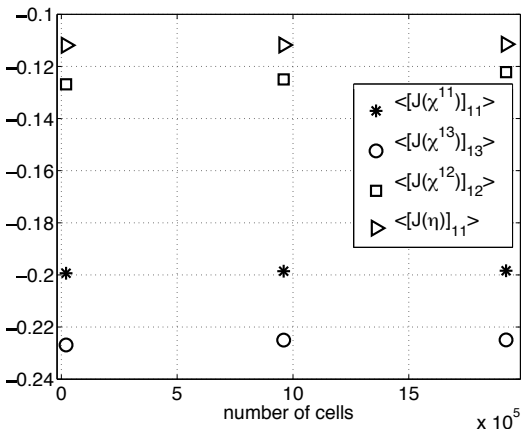

Figure A.5: Grid convergence using three different tetrahedral meshes (the coarser and finer are shown in figure A.5), for inclusions made of linked cylinders such that $d/d_t = 2.5$ and $r = 0.252$.

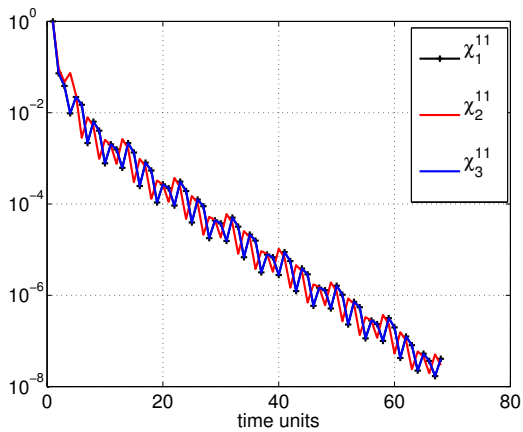

Figure A.6: Relative error for each component of $\boldsymbol{\chi}^{11}$, for varying time.

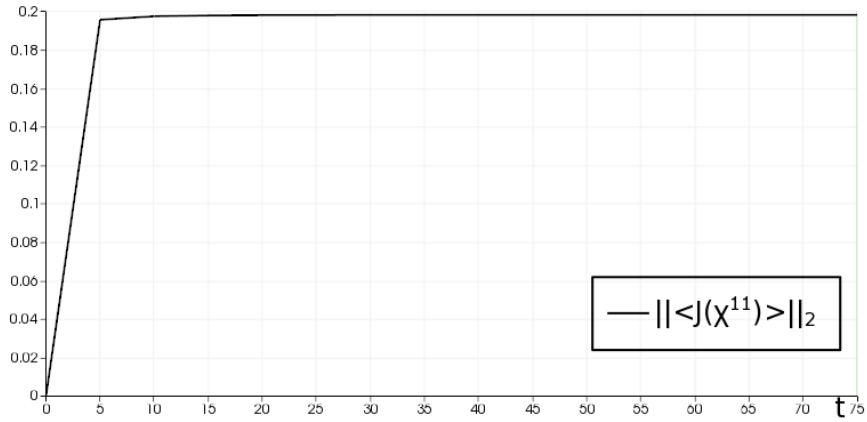

Figure A.7: Two-norm of the averaged Jacobian of χ^{pq} for varying time. After fifteen time units the norm reaches 99% of its final value.

A.2 The macroscopic codes

We briefly describe in this section the codes used to solve the macroscopic configuration. In order to do this we need a solver for the pure fluid region to be coupled with the solver in the porous homogenized region (based on Darcy's law, Brinkman equation or the generalization of Darcy's law in the deformable case). Each one of these codes are coupled in a proper way with the interface equations listed in chapter 3. All the codes have in common the following points:

- they are 2D codes, written in Matlab ®, which solve for the flow over rectangular domains discretized with cartesian non-uniform grids;
- the grid is staggered, the pressure is computed on the internal points (centers of the cells), the velocity is placed on the faces of the cells;
- the spatial operators are discretized using fourth-order finite differences.

Before presenting each solver we show how the spatial discretization is developed.

For ease of notation we restrict to a 1D case, supposing that the function f of which we want to calculate the first and second derivative is function of a single variable. In order to preserve the same order precision in each region of the domain, we need to define five different schemes for the first and second derivative of

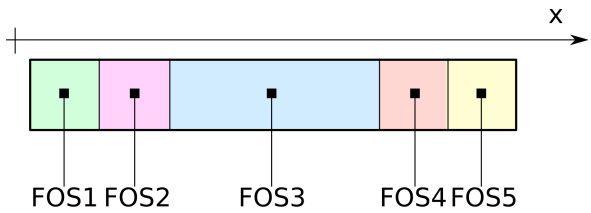

Figure A.8: Sketch of the position in the domain where each finite difference scheme is used.

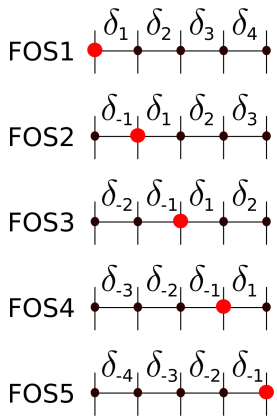

Figure A.9: Definition of each scheme and δ. The derivative are computed for the red point using the values of f in the black points.

f, one for each region highlighted in figure A.8; the five schemes are named FOSj, j=1,2,3,4,5 as can be seen in the same figure. In the internal points of the domain a centered scheme with 5 points is used (FOS3). Approaching the boundaries of the domain, in the second or second to last point, a one-backward-three-forward or three-backward-one forward scheme is employed (FOS2,FOS4). Over the boundaries, a fully forward or backward scheme is used (FOS1,FOS5). Since the grid is in principle non-uniform, we use the notation defined in figure A.9. We impose that first or second derivative of f (denoted here with $f^{(l)}$, $l = 1, 2$) can be written as a

linear combination of the value of f in the neighboring points i.e.

$$\text{FOS1} \qquad f^{(l)}(x) = af(x) + bf(x+\delta_1) + cf(x+\delta_1+\delta_2) + \\ +df(x+\delta_1+\delta_2+\delta_3) + ef(x+\delta_1+\delta_2+\delta_3+\delta_4),$$

$$\text{FOS2} \qquad f^{(l)}(x) = af(x-\delta_{-1}) + bf(x) + cf(x+\delta_1) + df(x+\delta_1+\delta_2) + \\ +ef(x+\delta_1+\delta_2+\delta_3),$$

$$\text{FOS3} \qquad f^{(l)}(x) = af(x-\delta_{-1}-\delta_{-2}) + bf(x-\delta_{-1}) + cf(x) + df(x+\delta_1) + \\ +ef(x+\delta_1+\delta_2),$$

$$\text{FOS4} \qquad f^{(l)}(x) = af(x-\delta_{-1}-\delta_{-2}-\delta_{-3}) + bf(x-\delta_{-1}-\delta_{-2}) + \\ +cf(x-\delta_{-1}) + df(x) + ef(x+\delta_1),$$

$$\text{FOS5} \qquad f^{(l)}(x) = af(x-\delta_{-1}-\delta_{-2}-\delta_{-3}-\delta_{-4}) + bf(x-\delta_{-1}-\delta_{-2}-\delta_{-3}) + \\ +cf(x-\delta_{-1}-\delta_{-2}) + df(x-\delta_{-1}) + ef(x),$$

where the coefficients a, b, c, d and e have to be determined. After writing the Taylor expansion for $f(x+\delta_1)$, $f(x-\delta_{-1})$, $f(x+\delta_1+\delta_2)$, $f(x-\delta_{-1}-\delta_{-2})$, $f(x+\delta_1+\delta_2+\delta_3)$, $f(x-\delta_{-1}-\delta_{-2}-\delta_{-3})$ and $f(x+\delta_1+\delta_2+\delta_3+\delta_4)$, $f(x-\delta_{-1}-\delta_{-2}-\delta_{-3}-\delta_{-4})$, substituting in the equations above, and imposing that they are equal to the desired derivative, the coefficients a, b, c, d and e solve the following systems:

FOS1

$$\begin{pmatrix} 1 & 1 & 1 & 1 & 1 \\ 0 & \delta_1 & \delta_1+\delta_2 & \delta_1+\delta_2+\delta_3 & \delta_1+\delta_2+\delta_3+\delta_4 \\ 0 & \delta_1^2 & (\delta_1+\delta_2)^2 & (\delta_1+\delta_2+\delta_3)^2 & (\delta_1+\delta_2+\delta_3+\delta_4)^2 \\ 0 & \delta_1^3 & (\delta_1+\delta_2)^3 & (\delta_1+\delta_2+\delta_3)^3 & (\delta_1+\delta_2+\delta_3+\delta_4)^3 \\ 0 & \delta_1^4 & (\delta_1+\delta_2)^4 & (\delta_1+\delta_2+\delta_3)^4 & (\delta_1+\delta_2+\delta_3+\delta_4)^4 \end{pmatrix} \cdot \\ \cdot \begin{pmatrix} a \\ b \\ c \\ d \\ e \end{pmatrix} = \begin{pmatrix} \delta_{1l} \\ \delta_{2l} \\ 0 \\ 0 \\ 0 \end{pmatrix}.$$

For the others schemes it is sufficient to modify the matrix of the coefficients of the system:

FOS2

$$\begin{pmatrix} 1 & 1 & 1 & 1 & 1 \\ -\delta_{-1} & 0 & \delta_1 & \delta_1+\delta_2 & \delta_1+\delta_2+\delta_3 \\ \delta_{-1}^2 & 0 & \delta_1^2 & (\delta_1+\delta_2)^2 & (\delta_1+\delta_2+\delta_3)^2 \\ -\delta_{-1}^3 & 0 & \delta_1^3 & (\delta_1+\delta_2)^3 & (\delta_1+\delta_2+\delta_3)^3 \\ \delta_{-1}^4 & 0 & \delta_1^4 & (\delta_1+\delta_2)^4 & (\delta_1+\delta_2+\delta_3)^4 \end{pmatrix},$$

FOS3

$$\begin{pmatrix} 1 & 1 & 1 & 1 & 1 \\ -(\delta_{-1}+\delta_{-2}) & -\delta_{-1} & 0 & \delta_1 & \delta_1+\delta_2 \\ (\delta_{-1}+\delta_{-2})^2 & \delta_{-1}^2 & 0 & \delta_1^2 & (\delta_1+\delta_2)^2 \\ -(\delta_{-1}+\delta_{-2})^3 & -\delta_{-1}^3 & 0 & \delta_1^4 & (\delta_1+\delta_2)^3 \\ (\delta_{-1}+\delta_{-2})^4 & \delta_{-1}^4 & 0 & \delta_1^4 & (\delta_1+\delta_2)^4 \end{pmatrix},$$

FOS4

$$\begin{pmatrix} 1 & 1 & 1 & 1 & 1 \\ -(\delta_{-1}+\delta_{-2}+\delta_{-3}) & -(\delta_{-1}+\delta_{-2}) & -\delta_{-1} & 0 & \delta_1 \\ (\delta_{-1}+\delta_{-2}+\delta_{-3})^2 & (\delta_{-1}+\delta_{-2})^2 & \delta_{-1}^2 & 0 & \delta_1^2 \\ -(\delta_{-1}+\delta_{-2}+\delta_{-3})^3 & -(\delta_{-1}+\delta_{-2})^3 & -\delta_{-1}^3 & 0 & \delta_1^3 \\ (\delta_{-1}+\delta_{-2}+\delta_{-3})^4 & (\delta_{-1}+\delta_{-2})^4 & \delta_{-1}^4 & 0 & \delta_1^4 \end{pmatrix},$$

FOS5

$$\begin{pmatrix} 1 & 1 & \dots \\ -(\delta_{-1}+\delta_{-2}+\delta_{-3}+\delta_{-4}) & -(\delta_{-1}+\delta_{-2}+\delta_{-3}) & \dots \\ (\delta_{-1}+\delta_{-2}+\delta_{-3}+\delta_{-4})^2 & (\delta_{-1}+\delta_{-2}+\delta_{-3})^2 & \dots \\ -(\delta_{-1}+\delta_{-2}+\delta_{-3}+\delta_{-4})^3 & -(\delta_{-1}+\delta_{-2}+\delta_{-3})^3 & \dots \\ (\delta_{-1}+\delta_{-2}+\delta_{-3}+\delta_{-4})^4 & (\delta_{-1}+\delta_{-2}+\delta_{-3})^4 & \dots \end{pmatrix}$$

$$\begin{pmatrix} \dots & 1 & 1 & 1 \\ \dots & -(\delta_{-1}+\delta_{-2}) & -\delta_{-1} & 0 \\ \dots & (\delta_{-1}+\delta_{-2})^2 & \delta_{-1}^2 & 0 \\ \dots & -(\delta_{-1}+\delta_{-2})^3 & -\delta_{-1}^3 & 0 \\ \dots & (\delta_{-1}+\delta_{-2})^4 & \delta_{-1}^4 & 0 \end{pmatrix}.$$

This kind of discretization allows to build the linear systems which discretize the PDE's for the determination of the flow field. In every solver developed, for the resolution of the linear systems, the Gauss elimination method already implemented

in Matlab ® is used. Since the code is 2D, we obtain a satisfying time efficiency even if *ad hoc* decomposition methods for the matrices built are not used.

A.2.1 Fluid solver

The fluid solver is based on the fractional step method in the formulation proposed by Perot (1993), a decomposition method to decouple the velocity and pressure in the NSE, linearizing the non-linear term. The main steps of this method are briefly presented:

- we discretize in space the NSE

$$\begin{cases} \dfrac{\partial u}{\partial t} + N(u) = -Gp + \dfrac{1}{\text{Re}} Lu \\ Du = 0 \end{cases}$$

  where N, G, L are the spatially discretized nonlinear term, gradient and laplacian operators respectively, plus the boundary conditions.

- Regarding the temporal discretization, we use a Crank-Nicolson scheme for the laplacian with an Adam-Bashfort approximation of the non-linear term after the first time step:

$$\begin{cases} \dfrac{u^{(n+1)} - u^{(n)}}{\Delta t} + \dfrac{3}{2} N(u^{(n)}) - \dfrac{1}{2} N(u^{(n-1)}) = -Gp^{(n+1)} + \dfrac{1}{\text{Re}} \dfrac{Lu^{(n+1)} + Lu^{(n)}}{2} \\ Du^{n+1} = 0 \end{cases}$$

  where n is the temporal index. If we define

$$r^{(n)} = \frac{u^{(n)}}{\Delta t} - \left[\frac{3}{2} N(u^{(n)}) - \frac{1}{2} N(u^{(n-1)}) \right] + \frac{Lu^{(n)}}{2\text{Re}}$$

  and

$$A = \frac{I}{\Delta t} - \frac{L}{2\text{Re}}$$

  the system can be rewritten as

$$\begin{cases} Au^{(n+1)} = -Gp^{(n+1)} + r^{(n)} \\ Du^{(n+1)} = 0. \end{cases} \tag{A.2.1}$$

- The gradient operator can be approximated in the following way

$$\Delta t A G = \left(I - \frac{\Delta t}{2\mathrm{Re}} \right) G \approx G$$

if $\Delta t/(2\mathrm{Re})$ is sufficient small. If this relation holds, system (A.2.1) can be rewritten as

$$\begin{cases} Au^* = r^{(n)} \\ \Delta t D G p^{(n+1)} = D u^* \\ u^{(n+1)} = u^* - \Delta t G p^{(n+1)}. \end{cases} \tag{A.2.2}$$

Each one of the equations in system (A.2.2) represent a single step of the fractional step method which consists of

- determine u^*;
- solve the Poisson equation for $p^{(n+1)}$ forced by the divergence of u^*;
- update u^* with $Gp^{(n+1)}$ to determine $u^{(n+1)}$.

The validation of this solver is initially performed using the results in a unitary square cavity present in Ghia *et al.* (1982) obtaining a perfect matching. However is not necessary to present this validation here since a more convincing validation has been already shown in figures 5.11 to 5.16 comparing the results obtained with this code with the DNS in the cavity. Figure A.10 show the temporal convergence when a steady solution inside the cavity is calculated. Figure A.11 shows the convergence with respect the grid. Figure A.12 shows the spatial and temporal convergence of the solution in the channel flow configuration with respect to the analytical solution of Landau & Lifshitz (1959).

A.2.2 Solver for the Darcy's law

In the porous region the homogenization technique yields system (5.1.3). Substituting the Darcy's law in the continuity equation we find

$$\epsilon^2 \mathrm{Re}_L \frac{\partial}{\partial x_j} \mathcal{K}_{ij} \frac{\partial p}{\partial x_i} = 0. \tag{A.2.3}$$

After this equation for the pressure is solved, the velocity can be deduced *a posteriori* applying Darcy's law. Equation (A.2.3) is a Laplace's equation weighted in each

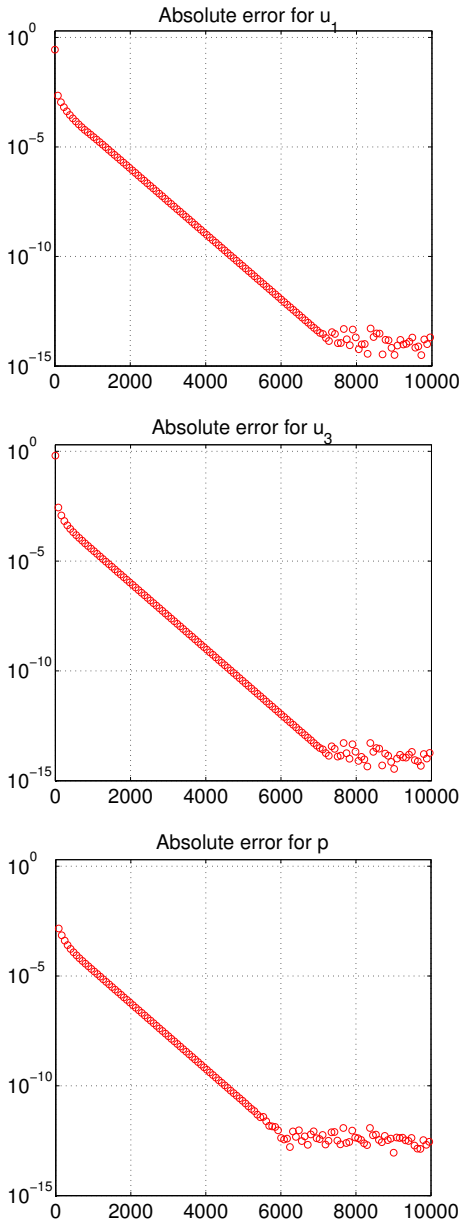

Figure A.10: Absolute error ($|f^{(n+1)} - f^{(n)}|$) for the velocity and pressure fields. Along the x-coordinate the number of iterations in time are shown. The scale in y is logarithmic. This test case is realized simulating a square unitary cavity with $\mathrm{Re}_L = 100$. The number of nodes per unit area are 6.4×10^3.

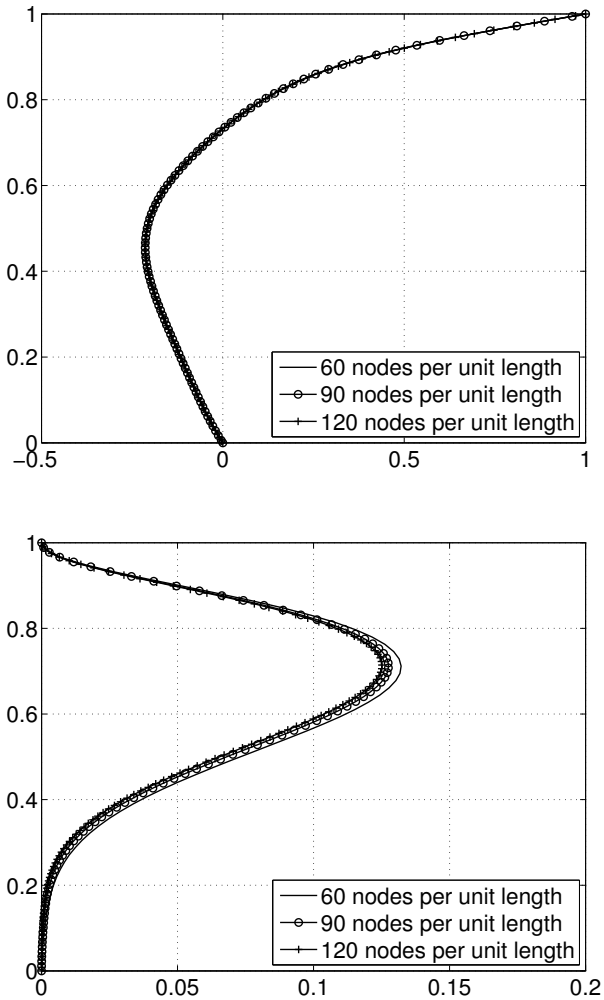

Figure A.11: Horizontal (upper frame) and vertical (lower frame) velocities at the center of the cavity ($x_1 = 0.5$), calculated using different numbers of nodes per unit area (3.6×10^3, 8.1×10^3 and 1.44×10^4). The Reynolds number Re_L is equal to 100.

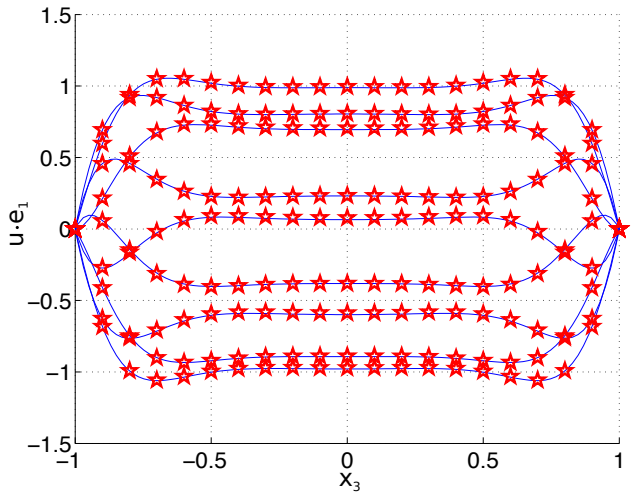

Figure A.12: Horizontal velocity profiles for $x_1 = 1$ at different instants during a cycle. Symbols ★ represent the analytical solution and the solid lines the numerical ones.

direction with respect to the entries of the permeability tensor. Actually, since $\mathcal{K}_{ij}$ is diagonal and not depends on the microscale, equation (A.2.3) becomes

$$\mathcal{K}_{11}\frac{\partial^2 p}{\partial x_1^2} + \mathcal{K}_{33}\frac{\partial^2 p}{\partial x_3^2} = 0. \tag{A.2.4}$$

The Laplacian is discretized using the fourth-order finite differences already described. Also in this case the pressure is computed over the centers of each cell. Since we solve for the pressure we cannot impose boundary conditions on the velocity directly. In order to prevent the impermeability of the walls, a homogeneous Neumann condition is imposed for the pressure. This fact causes that, even if the normal velocity is zero, there is a non-zero slip velocity over the walls, thing that is in accordance with the fact that we are solving a macroscopic model for an average velocity.

Coupling with NSE The coupling with NSE via the conditions described in 3.3 consists of the following iterative procedure

- run the fluid solver with a guess value for the velocity at the interface;
- determine and, since the grid is staggered, interpolate over the interface (linear and cubic fittings have been used without obtaining relevant differences) the pressure field in the fluid zone;
- impose a constant jump in the pressure as interface condition

$$p^{(n)}|_P = p^{(n)}|_F + constant \tag{A.2.5}$$

  where the superscript denotes the time index and the value of the *constant* is not important because both in the fluid momentum equation and in Darcy's equation only the gradient of the pressure appears;
- solve the pressure in the porous zone and recover the velocity $\mathbf{u}^{(n)}|_P$ at the interface via the Darcy's equation;
- impose the continuity of velocity at the interface

$$\mathbf{u}^{(n+1)}|_F = \mathbf{u}^{(n)}|_P \tag{A.2.6}$$

  as boundary condition for the NS solver;
- re-run the NS solver with the updated interface condition and iterate the procedure until the steady-state is reached.

A.2.3 Solver for the Brinkman's equation

To solve the Brinkman's equation we adopt a procedure similar to that used for the Darcy's solver. Substituting equation (3.2.6) in the continuity equation we obtain

$$-\epsilon^2 \mathrm{Re}_L \mathcal{K}_{ij} \frac{\partial^2 p}{\partial x_j \partial x_i} + \epsilon^2 \frac{\mu_e}{\mu} \mathcal{K}_{ij} \frac{\partial^3 u_j}{\partial x_i \partial x_k^2} = 0 \tag{A.2.7}$$

so that we can consider the new system

$$\begin{cases} \epsilon^2 \mathrm{Re}_L \mathcal{K}_{ij} \dfrac{\partial^2 p}{\partial x_j \partial x_i} = \epsilon^2 \dfrac{\mu_e}{\mu} \mathcal{K}_{ij} \dfrac{\partial^3 u_j}{\partial x_i \partial x_k^2} \\ u_i - \mathcal{K}_{ij} \epsilon^2 \dfrac{\mu_e}{\mu} \dfrac{\partial^2 u_j}{\partial x_k^2} = -\mathcal{K}_{ij} \epsilon^2 \mathrm{Re}_L \dfrac{\partial p}{\partial x_j}. \end{cases} \tag{A.2.8}$$

This set of equations has been solved with an iterative solver using the following discretization:

$$\begin{cases} LHS_1^{(n+1)} = RHS_1^{(n)} \\ LHS_2^{(n+1)} = RHS_2^{(n+1)}, \end{cases} \tag{A.2.9}$$

where the superscript represent the iteration's index and the subscript indicates either the first or the second of (A.2.8). The iterative procedure consists of two steps:

- solve for the pressure the first equation of system (A.2.9) with the velocity at the previous time step;
- use the pressure as known term in the second equation of system (A.2.9) and solve for the velocity; iterate until convergence.

This strategy appears not very intuitive, however it is justified by the interface conditions which we have presented in chapter 3. Conditions (3.4.3) and (3.4.4) can be seen as non-homogeneous Neumann conditions for u_1 and u_3 over the interface. In particular, in (3.4.4) the pressure appears directly, without any gradient operator applied to it. Since the pressure is determined, both in the fluid solver and in the porous solver, up to a constant, this could affect the solution. To pin this constant it is sufficient to use (3.4.4) as a boundary condition for the pressure in the first equation of system (A.2.9) and solve the Brinkman's model with the iterative procedure just explained.

Coupling with NSE The coupling of these equations with NSE has been implemented in a way similar to that of the Darcy's solver:

- run the fluid solver with a guess value for the velocity at the interface;
- save all the quantities which must be used in interface conditions (3.4.3–3.4.4) and interpolate them at the correct points, approaching the interface from the fluid region;
- impose conditions (3.4.3) and (3.4.4) discretized in time as

$$\left.\frac{\partial u_1^{(n+1)}}{\partial x_3}\right|_P = -\left.\frac{\partial u_3^{(n)}}{\partial x_1}\right|_P + \frac{\mu}{\mu_e}\left.\left(\frac{\partial u_1^{(n)}}{\partial x_3} + \frac{\partial u_3^{(n)}}{\partial x_1}\right)\right|_F \tag{A.2.10}$$

and

$$\left(-p^{(n+1)}+\frac{2\mu_e}{\mu \mathrm{Re}_L}\frac{\partial u_3^{(n+1)}}{\partial x_3}\right)\Bigg|_P=\left(-p^{(n)}+\frac{2}{\mathrm{Re}_L}\frac{\partial u_3^{(n)}}{\partial x_3}\right)\Bigg|_F; \tag{A.2.11}$$

- solve the Brinkman's model with the procedure outlined above;

- impose the continuity of velocity at the interface (A.2.6) as boundary condition for the NS solver;

- re-run the NS solver with the updated interface condition and iterate the procedure until the steady-state is reached.

A.2.4 Solver for the equations for poroelastic media

System (5.1.1) is composed by time-dependent equations, plus interface conditions (5.2.4) to (5.2.7). Since interface condition (5.2.5) presents the same problem as in equation (3.4.4) for the Brinkman's model, a similar approach has been adopted. Substituting the third equation (generalized Darcy's law) in the second equation (generalized continuity equation) of system (5.1.1), we obtain a set of three equations and three unknowns (pressure and displacement fields) for the poroelastic medium:

$$\begin{cases} (1-\vartheta)\dfrac{\partial^2 v_i}{\partial t^2}=\dfrac{\partial}{\partial x_j'}\left[\mathcal{C}_{ijpq}\varepsilon_{pq}'(\mathbf{v})-\alpha_{ij}'p\right], \\ \langle\dfrac{\partial \eta_i}{\partial x_i}\rangle\dfrac{\partial p}{\partial t}-\dfrac{\partial}{\partial x_i'}\left(\mathcal{K}_{ij}\dfrac{\partial p}{\partial x_j'}\right)=\langle\dfrac{\partial \chi_i^{pq}}{\partial x_i}\rangle\varepsilon_{pq}'(\dot{\mathbf{v}})-\dfrac{\partial}{\partial x_i'}\left(\mathcal{H}_{ij}\dot{v}_j\right), \end{cases} \tag{A.2.12}$$

where the superscript (0), which denotes the leading order in ϵ, is omitted for ease of notation. These equations have been discretized in time in the following way:

$$\begin{cases} \langle\dfrac{\partial\eta_i}{\partial x_i}\rangle\dfrac{p^{(n+1)}-p^{(n)}}{\Delta t}-\dfrac{1}{2}\dfrac{\partial}{\partial x'_i}\left(\mathcal{K}_{ij}\dfrac{\partial p^{(n+1)}}{\partial x'_j}\right)=\dfrac{1}{2}\dfrac{\partial}{\partial x'_i}\left(\mathcal{K}_{ij}\dfrac{\partial p^{(n)}}{\partial x'_j}\right)+ \\ +\langle\dfrac{\partial\chi_i^{pq}}{\partial x_i}\rangle\varepsilon'_{pq}\left(\dfrac{\mathbf{v}^{(n)}-\mathbf{v}^{(n-1)}}{\Delta t}\right)-\dfrac{\partial}{\partial x'_i}\left(\mathcal{H}_{ij}\dfrac{{v_j}^{(n)}-{v_j}^{(n-1)}}{\Delta t}\right), \\ (1-\vartheta)\dfrac{v_i^{(n+1)}+2v_i^{(n)}-v_i^{(n-1)}}{\Delta t^2}-\dfrac{1}{2}\dfrac{\partial}{\partial x'_j}\left[\mathcal{C}_{ijpq}\varepsilon'_{pq}(\mathbf{v}^{(n+1)})\right]= \\ =\dfrac{1}{2}\dfrac{\partial}{\partial x'_j}\left[\mathcal{C}_{ijpq}\varepsilon'_{pq}(\mathbf{v}^{(n)})-\alpha'_{ij}p^{(n)}\right]. \end{cases} \tag{A.2.13}$$

Coupling with NSE The coupling of these equations with NSE has been implemented in a way similar to that of the other homogenized solvers presented:

- run the fluid solver with a guess value for the velocity at the interface;
- save all the quantities which must be used in interface conditions (5.2.4–5.2.5–5.2.7) and interpolate them at the correct points, approaching the interface from the fluid region;
- impose condition (5.2.7) discretized in time as

$$\frac{\mathcal{K}_f}{d_f}p^{(n)}|_P+\mathcal{K}_{33}\left.\frac{\partial p}{\partial x_3}\right|_P=\frac{\mathcal{K}_f}{d_f}p^{(n)}|_F, \tag{A.2.14}$$

  to solve the first equation of system (A.2.13) for the pressure, with $K_f=\mathcal{K}_{33}$ and $d_f=10^{-2}$;
- impose conditions (5.2.4) and (5.2.5) discretized in time as

$$\left.\mathcal{C}_{1313}\frac{\partial v_1^{(n+1)}}{\partial x_3}\right|_P=-\left.\mathcal{C}_{1313}\frac{\partial v_3^{(n)}}{\partial x_1}\right|_P+\epsilon\left.\left(\frac{\partial u_1^{(n)}}{\partial x_3}+\frac{\partial u_3^{(n)}}{\partial x_1}\right)\right|_F \tag{A.2.15}$$

$$\left.\mathcal{C}_{3333}\frac{\partial v_3^{(n+1)}}{\partial x_3}\right|_P=-\left.\left(\mathcal{C}_{3311}\frac{\partial v_1^{(n)}}{\partial x_3}-\alpha'_{33}p^{(n)}\right)\right|_P+\left.\left(-p^{(n)}+2\epsilon\frac{\partial u_3^{(n)}}{\partial x_3}\right)\right|_F \tag{A.2.16}$$

  to solve for the displacement field the second equation of system (A.2.13);

- impose the continuity of velocity at the interface (A.2.6) as boundary condition for the NS solver;
- re-run the NS solver with the updated interface condition and iterate the procedure until the steady-state is reached.

A.2.5 Code for the linear stability analysis

A code for the linear stability has been developed with the following characteristics:

- the presence of the porous medium is simulated via boundary conditions (5.3.16) or (5.3.17) (without and with drag). The mean profile does not have inflection points, so that, in principle, it is stable. The boundary conditions, imposed at the fictitious interface, generate the unstable modes;
- the differentiation matrices are based on Chebyshev polynomials (cf. Canuto *et al.*, 1988; Weideman & Reddy, 2000);
- since the collocations points x over which these polynomial are evaluated ranges in the interval $[-1, 1]$, a linear map is used to map the Chebyshev space in the physical space ($[1-\delta, y_\infty]$); in this particular case we have employed

$$f(x) = \frac{y_\infty - (1-\delta)}{2}(1-x) + (1-\delta);$$

- the function `eigs` implemented in MatLab ® is used to solve the resulting generalized eigenvalue problem.

As shown by table A.4 for a particular case, convergence with respect to the number of collocations points is reached. In figure A.13, instead, the invariance of the solution with respect to the choice of y_∞ is shown.

# POINTS	c_r	ω_i
100	1.120	0.1646
150	1.169	0.1624
200	1.182	0.1684
300	1.195	0.1695
400	1.199	0.1708
600	1.201	0.1714
800	1.202	0.1715
1000	1.202	0.1715

Table A.4: Values of the most unstable eigenvalue for the case G (cf. section 5.3.1) with $\alpha = 1$ and $y_\infty = 15$, for varying number of collocations points.

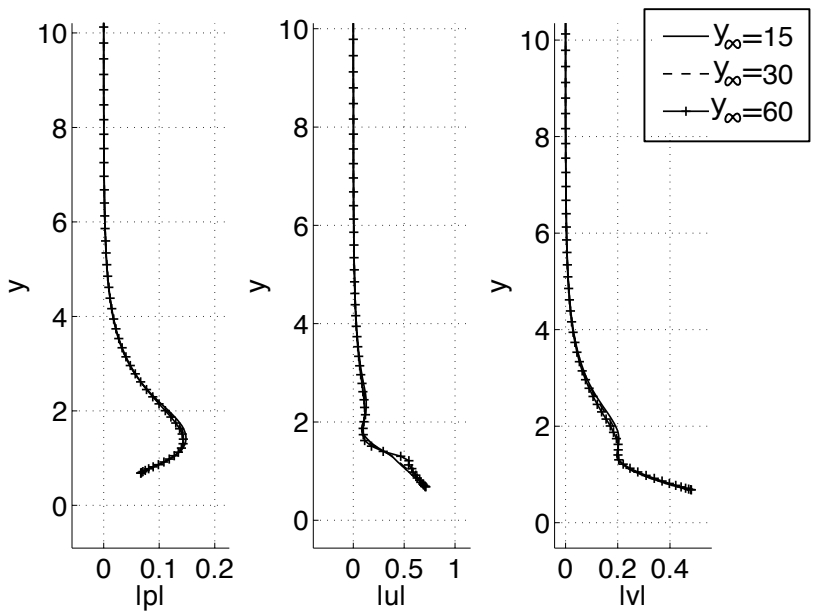

Figure A.13: Modulus of the eigenfunction associated to the most unstable eigenvalue for varying y_∞. Test case G with 200 collocation points and $\alpha = 1$.

Bibliography

Alexiou, T. S. & Kapellos, G. E. 2013 Plane Couette-Poiseuille flow past a homogeneous poroelastic layer. *Physics of fluid*, **25**, 073605,1–17.

Angot, P. & Bruneau C. H. & Fabrie P. 1999 A penalization method to take into account obstacles in incompressible viscous flows. *Numerische Mathematik,* **81**, (4), 497–520.

Auriault, J. L. 2009 On the domain of validity of Brinkman's equation. *Transport in Porous Media,* **79**, (2), 215–223.

Autumn, K. & Peattie, A. M. 2002 Mechanism of adhesion in geckos. *Integrative and Comparative Biology,* **42**, (6), 1081–1090.

Barry, S. I. & Parker, K. H. & Aldis, G. K. 1991 Fluid flow over a thin deformable porous layer. *Journal of Applied Mathematics and Physics*, **42**, 633–647.

Barthlott, W. & Neinhuis, C. 1997 Purity of the sacred lotus, or escape from contamination in biological surfaces. *Planta,* **202**, 1–8.

Battiato, I & Bandaru, P.R. & Tartakowsky, D.H. 2010 Elastic response of carbon nanotube forests to aerodynamic stresses. *Physical Review Letters,* **105**, 144504, 1–4.

Battiato, I. 2012 Self-similarity in coupled Brinkman/Navier–Stokes flows. *Journal of Fluid Mechanics,* **699**, 94–114.

Beavers, G. S. & Joseph, D. D. 1967 Boundary conditions at a naturally permeable wall. *Journal of Fluid Mechanics,* **30**, (1), 197–207.

Bechert, D. W. & Bruse, M. & Hage, W. & Meyer, R. 2000 Fluid mechanics of biological surfaces and their technological application. *Naturwissenschaften,* **87**, 157–171.

Bernhard, C. G. & Miller, W.H. & Moller, A. R. 1965 The insect corneal nipple array. A biological broad-band impendance transformer that acts as a antireflection coating. *Acta Physiologica Scandinavica,* **63**, 1–79.

Biot, M. A. 1955 Theory of elasticity and consolidation for a porous anisotropic solid. *Journal of Applied Physics*, **26**, (2), 182–185

Breugem, W. P. & Boersma, B. J. 2005 Direct numerical simulations of turbulent flow over a permeable wall using a direct and a continuum approach. *Physics of Fluids,* **17**, 025103.

Breugem, W. P. & Boersma, B. J. & Uittenbogaard, R. E. 2004 Direct numerical simulations of plane channel flow over a 3D cartesian grid of cubes. *Applications of Porous Media, (ICAPM 2004)*, 27–35.

Brinkman, H. C. 1949 A calculation of the viscous force exerted by a flowing fluid on a dense swarm of particles. *Applied Scientific Research,* **1**, (1), 27–34.

Bruneau, C. H. & Mortazavi, I. 2008 Numerical modelling and passive flow control using porous media. *Computers & Fluids,* **37**, (5), 488–498.

Burridge, R. & Keller, J.B. 1981 Poroelasticity equations derived from microstructure. *Journal of Acoustic Society of America*, **70**, (4), 1140–1146.

Canuto, C. & Hussaini, M. Y. & Quarteroni, A. & Zang, T. A. 1988 *Spectral Methods in Fluid Dynamics*, Springer-Verlag, Berlin, Germany.

Carman, P. C. 1939 Permeability of saturated sands, soils and clays. *The Journal of Agricultural Science,* **29**, (02), 262–273.

Carraro, T. & Goll, C. & Marciniak-Czochra, A. & Mikelić, A. 2013 Pressure jump interface law for the Stokes–Darcy coupling: confirmation by direct numerical simulations. flows. *Journal of Fluid Mechanics,* **732**, 510–536.

Cheng, A. H. D. 1997 Material coefficients of anisotropic poroelasticity. *International Journal of Rock Mechanics*, **34**, (2), 199–205.

Chandesris, M. & Jamet, D. 2008 Jump conditions and surface-excess quantities at a fluid/porous interface: a multi-scale approach. *Transport in Porous Media,* **78**, 419–438.

Cimolin, F. & Discacciati, M. 2013 Navier–Stokes/Forchheimer models for filtration through porous media. *Applied Numerical Mathematics* **72**, 205–224.

Cowin, S. 2013 *Continuum Mechanics of Anisotropic Materials*. Springer Science+Business Media, New York.

Darcy, H. 1856 *Les fontaines publiques de la ville de Dijon* Victor Dalmont Editeur, Paris, France.

Davit, Y. & Quintard, M. & Bell, C. G. & Byrne, H. M. & Chapman, L. A. C. & Kimpton, L. S. & Lang, G. E. & Oliver, J. M. & Pearson, N. C. & Waters, S. L. & Leonard, K. H. L. & Whiteley, J. P. & Shipley, R. J. & Wood, B. D. 2013 Homogenization via formal multiscale asymptotics and volume averaging: How do the two techniques compare? *Advances in Water Resources,* **62**, 178–206.

De Langre, E. 2008 Effect of wind on plants. *Annual Review of Fluid Mechanics*, **40**, 141-168.

Doaré, O. & Moulia, B. & De Langre, E. 2004 Effect of plant interaction on wind-induced crop motion. *Journal of Biomechanical Engineering*, **126**, (2), 146–151.

Edwards, D. A. & Shapiro, M. & Bar-Yoseph, P. & Shapira, M. 1990 The influence of Reynolds number upon the apparent permeability of spatially periodic arrays of cylinders. *Physics of Fluids,* **2**, (1), 45–55.

Ene, H. I. & Sánchez-Palencia, E. 1975 Equations et phénomènes de surface pour l' écoulement dans un modèle de milieu poreux. *J. Mécanique,* **14**, 73–108.

Firdaouss, M. & Guermond, J. & Le Quéré, P. 1997 Nonlinear correction to Darcy's law at low Reynolds numbers. *Journal of Fluid Mechhanic,* **343**, 331–350.

Finnigan, J. J. 2000 Turbulence in plant canopies. *Annual Review of Fluid Mechanics,* **32**, 519–571.

Geim, A. K. & Dubonos, S. V. & Grigorieva, I. V. & Novoselov, K. S. & Zhukov, A. A. & Shapoval, S. Y. 2003 Micro-fabricated adhesive mimicking gecko foot-hair. *Nature Materials,* **2**, 461–463.

Ghia, U. & Ghia, K. N. & Shin, C.T. 1982 High-Re solutions for incompressible flow using Navier-Stokes equations and a multigrid method. *Journal of Computational Physics*, **48**, 387–411.

Ghisalberti, M & Nepf, H.M. 2002 Mixing layers and coherent structures in vegetated aquatic flows. *Journal of Geophysical Research: Oceans (1978–2012)*, **107**, (C2), 3–1.

Ghisalberti, M. & Nepf, H. M. 2004 The limited growth of vegetated shear layers. *Water Resources Research,* **40**, (7),1–12.

Ghisalberti, M. and Nepf, H. 2005 Mass transport in vegetated shear flows. *Environmental Fluid Mechanics*, **5**, (6):527–551, 2005.

Ghisalberti, M. & Nepf, H. M. 2006 The structure of the shear layer over rigid and flexible canopies. *Environmental Fluid Mechanics,* **6**, (3), 277–301.

Ghisalberti, M. & Nepf, H. M. 2009 Shallow flows over a permeable medium: the hydrodynamics of submerged aquatic canopies. *Transport in Porous Media,* **78**, (2), 309–326.

Givler, R. C. & Altobelli, S. A. 1994 A determination of the effective viscosity for the Brinkman-Forchheimer flow model. *Journal of Fluid Mechanics,* **258**, 355–370.

Goldstein, H. 1980 *Classical Mechanics* Addison-Wesley series in physics, New York.

Gopinath, A. & Mahadevan, L. 2011 Elastohydrodynamics of wet bristles, carpets and brushes. *Proceedings of the Royal Society*, **467**, (2130), 1–21.

Gosselin, F.P. & de Langre, E. 2011 Drag reduction by reconfiguration of a poroelastic system. *Journal of Fluid and Structures,* **27**, 1111–1123.

Gray, W. G. 1975 A derivation of the equations for multi-phase transport. *Chemical Engineering Science,* **30**, (2), 229–233.

Gustafsson, J. & Protas, B. 2013 On Oseen flows for large Reynolds numbers. *Theoretical and Computational Fluid Dynamics,* **27**, (5), 665–680.

Hill, A. A. & Straughan, B. 2008 Poiseuille flow in a fluid overlying a porous medium. *Journal of Fluid Mechanics,* **603**, 137–149.

Hoffmann, K. H. & Botkin, N. D. & Starovoitov, V. N. Homogenization of interfaces between rapidly oscillating fine elastic structures and fluids. *SIAM Journal of Applied Mathematics*, **65**, (3), 983–1005.

Hussong, J. & Breugem W. P. & Westerweel J. 2011 A continuum model for flow induced by metachronal coordination between beating cilia. *Journal of Fluid Mechanics,* **684**, 137-162.

Jackson, G. W. & James, D. F. 1986 The permeability of fibrous porous media. *The Canadian Journal of Chemical Engineering,* **64**, (3), 364–374.

Jäger, W. & Mikelić, A. 1996 On the boundary conditions at the contact interface between a porous medium and a free fluid. *Annali Scuola Normale Superiore di Pisa, Classe Fisiche e Matematiche-Serie IV,* **23**, 403-465.

Jäger, W. & Mikelić, A. 2000 On the interface boundary condition of Beavers, Joseph, and Saffman. *SIAM Journal of Applied Mathematics,* **60**, (4), 1111–1127.

James, D. F. & Davis, A. M. J. 2001 Flow at the interface of a model fibrous porous medium. *Journal of Fluid Mechanics,* **426**, 47–72.

Jamet, D. & Chandesris, M. 2009 On the intrinsic nature of jump coefficients at the interface between a porous medium and a free fluid region. *International Journal of Heat and Mass Transfer,* **52**, 289–300.

Jones, D. R. H. & Ashby, M. F. 2005 *Engineering Materials I*. Butterworth-Heinemann, Oxford, UK.

Kaviany, M. 1995 *Principles of Heat Transfer in Porous Media*. Springer, New York.

Kroeger, R. A. & Grushka, H. D. & Helvey, T. C. 1972 Low Speed Aerodynamics for Ultra-Quiet Flight. *Tech. Rep. of Air Force Flights Dynamics Laboratory,*. Wright-Patterson AFB.

KUTTANIKKAD, S. P. 2009 Pore-scale direct numerical simulation of flow and transport in porous media. Ph.D thesis, Ruprecht-Karls-Universität Ruprecht-Karls-Universität, Heidelberg, Germany.

LAKHTAKIA, A. & MARTÍN–PALMA, R. J. 2013 *Engineered biomimicry*. Elsevier, Oxford, UK.

LE BARS, M. & WORSTER, M. 2006 Interfacial conditions between a pure fluid and a porous medium: implications for binary alloy solidification. *Journal of Fluid Mechanics,* **550** (1), 149–173.

LEE, D. W. 1986 Unusual strategies of light absorption in rain forest herbs. In *On the economy of plant form and function* (ed. T. J. Givnish), pp. 149–173 *Cambridge University Press*, Cambridge, UK.

LI. J. Q. & SUN, J. R. & REN, L. Q. & CHEN, B. C. 2004 Sliding resistance of plates with bionic bumpy surface against soil. *Journal of Bionics Engineering*, **1**, 207–214.

LUCHINI, P. & MANZO, F. & POZZI, A. 1991 Resistance of a grooved surface to parallel flow and cross-flow. *Journal of Fluid Mechanics*, **228**, 87–109.

LUHAR, M. & NEPF, H.M. 2011 Flow-induced reconfiguration of buoyant and flexible aquatic vegetation. *Limnology and Oceanography*, **56**, (6), 2003–2017.

MARCINIAK-CZOCHRA, A. & MIKELIĆ, A. 2012 Effective pressure interface law for transport phenomena between an unconfined fluid and a porous medium using homogenization. *SIAM Multiscale Modeling and Simulation,* **10**, (2), 285–305.

MARTYS, N. S. & TORQUATO, S. & BENTZ D.P. 1994 Universal scaling of fluid permeability for sphere packings. *Physical Review,* **50**, (1), 403–409.

MATSUMURA, Y. & JACKSON, T. L. 2014 Numerical simulation of fluid flow through random packs of cylinders using immersed boundary method. *Physics of Fluids (1994-present),* **26** (4) 043602.

MEI, C. C. & AURIAULT, J. L. 1991 The effect of weak inertia on flow through a porous medium. *Journal of Fluid Mechanics,* **222**, 647–663.

MEI, C. C. & VERNESCU, B. 2010 *Homogenization methods for multiscale mechanics*. World Scientific, Singapore.

Milton, G. W. 2004 *The theory of composites*. Cambridge University Press, Cambridge.

Mityushev, V. & Adler, P. M. 2002*a* Longitudinal permeability of spatially periodic rectangular arrays of circular cylinders I. A single cylinder in the unit cell. *Zeitschrift für Angewandte Mathematik und Physik,* **82**, (5), 335–346.

Mityushev, V. & Adler, P. M. 2002*b* Longitudinal permeability of spatially periodic rectangular arrays of circular cylinders II. An arbitrary distribution of cylinders inside the unit cell. *Zeitschrift für Angewandte Mathematik und Physik,* **53**, (3), 486–514.

Moukalled, F. & Mangani, L. & Darwish, M. 2015 *The Finite Volume Method in Computational Fluid Dynamics. An advanced introduction with OpenFoam and Matlab.* Springer international publishing, Switzerland.

Nepf, H. M. 1999 Drag, turbulence, and diffusion in flow through emergent vegetation. *Water Resources Research*, **35**, (2), 479– 489.

Nepf, H. M. 2012 Flow and transport in regions with aquatic vegetation. *Annual Reviews of Fluid Mechanics,* **44**, 123–142.

Nield, D. A. & Bejan, A. 2013 *Convection in porous media*. Springer-Verlag, New York.

Ochoa-Tapia, J. A. & Whitaker, S. 1995 Momentum transfer at the boundary between a porous medium and a homogeneous fluid, I. Theoretical development. *International Journal of Heat and Mass Transfer,* **38**, (14), 2635–2646.

Park, J. H. & Yoon, K. J. 2008 Designing a biomimetic ornithopter capable of sustained and controlled flight. *Journal of Bionic Engeneering,* **5**, (1), 39–47.

Penta, R. & Ambrosi, D. 2013 Effective governing equations for poroelastic growing media. *The Quarterly Journal of Mechanics and Applied Mathematics*, **67**, (1), 69–91.

Perot, J. B. 1993 An Analysis of the Fractional Step Method. *Journal of Computational Physics,* **108**, 51–58.

Pluvinage, F. 2015 *Effets d'interfaces poroélastiques sur la stabilité d'un écoulement incompressible cisaillé.* Ph.D Thesis, University of Orléans.

Py, C. & De Langre, E. & Moulia, B.2004 The mixing layer instability of wind over a flexible crop canopy. *Comptes Rendus Mécanique*, **332**, (8), 613–618.

Quarteroni, A. & Valli, A. 1999 *Domain decomposition methods for partial differential equations*. Oxford University Press, Oxford.

Quintard, M. & Whitaker, S. 1994 Transport in ordered and disordered porous media II: Generalized volume averaging. *Transport in Porous Media,* **14** (2), 179–206.

Raupach, M. R. & Finnigan, J. J. & Brunet, Y. 1996 Coherent eddies and turbulence in vegetation canopies: the mixing-layer analogy. *Boundary-Layer Meteorology,* **78**, 351–382.

Rice, J. R. & Cleary, M. P. 1976 Some basic stress diffusion solutions for fluid-saturated elastic porous media with compressible costituents. *Reviews of Geophysics and Space Physics*, **14**, (2), 227–241.

Rosti, M. & Cortelezzi, L. & Quadrio M. 2015 Direct numerical simulation of turbulent channel flow over porous walls. *Journal of Fluid Mechanics,* **784**, 396–442.

Sadiq, T. A. K. & Advani, S. G. & Parnas, R. S. 1995 Experimental investigation of transverse flow through aligned cylinders. *International Journal of Multiphase Flow,* **21**, (5), 755–774.

Saffman, P. G. 1971 Boundary condition at the surface of a porous medium. *Studies in Applied Mathematics,* **50**, (2), 93–101.

Saharoui, M. & Kaviany, M. 1988 Slip and no–slip temperature boundary conditions at the interfaceof porous, plain media: convection. *Journal of Heat Mass Tranfer,* **37**, (6), 1029–1044.

Sangani, A. S. & Yao, C. 1988 Transport processes in random arrays of cylinders. II. Viscous flow. *Physics of Fluids (1958-1988),* **31**, (9), 2435–2444.

Sarradj, E. & Fritzsche, C. & Geyer, T. 2011 Silent owl flight: flyover noise measurements. *American Institute of Aeronautics and Astronautics Journal,* **49**, (4), 769–779.

Singh, R. & Bandi, M. M. & Mahadevan, A. & Mandre, S. 2015 Monami as an oscillatory hydrodynamic instability in a submerged sea grass bed. *ArXiv*, arXiv:1411.0365v2.

Sirohi, J. 2013 Bioinspired and biomimetic microflyers. In *Engeneered Biomimicry* (ed. Lakhtakia & Martín–Palma), Elsevier, Oxford, UK.

Sharma, M. D. 2007 Wave propagation in a general anisotropic poroelastic medium: Biot's theories and homogenization theory. *Journal of Earth System Science*, **116**, (4), 357–367.

Skartsis, L. & Kardos, J. L. 1990 The newtonian permeability and consolidation of oriented carbon fiber beds. In *Proceedings of the American Society for Composites. Fifth Technical Conference: Composite Materials in Transition, E. Lansing, Michigan*, pp. 548–556.

Skjetne, E. & Auriault, J. L. 1999 New insights on steady, non-linear flow in porous media. *European Journal of Mechanics-B/Fluids* **18** (1), 131–145.

Stoddart, P. R. & Cadusch, P. J. & Boyce, T. M. & Erasmus, R. M. & Comins J. D. 2006 Optical properties of chitin: surface enhanced Raman scattering substrates based on antireflection structures on cicada wings. *Nanotechnology,* **17**, 680-686.

Sueki, T. & Takaishi, T & Ikeda, M. & Arai, N. 2010 Application of porous material to reduce aerodynamic sound from bluff bodies. *Fluid Dynamics Research,* **42**, (1), 015004.

Tamayol, A. & Bahrami, M. 2009 Analytical determination of viscous permeability of fibrous porous media. *International Journal of Heat and Mass Transfer,* **52** (9), 2407–2414.

Vafai, K. & Kim, S. J. 1990 Fluid mechanics of the interface region between a porous medium and a fluid layer—an exact solution. *International Journal of Heat and Fluid Flow,* **11**, (3), 254–256.

van der Westhuizen, J. & du Plessis, J. P. 1996 An attempt to quantify fibre bed permeability utilizing the phase average Navier-Stokes equation. *Composites Part A: Applied Science and Manufacturing,* **27**, (4), 263–269.

VERSTEEG, H. K. & MALALASEKERA, W. 2007 *An introduction to Computational Fluid Dynamics. The Finite Volume Method.* Pearson Education Limited, Harlow, Essex UK.

VINCENT, J.F.V. & BOGATYREVA, O.A. & BOGATYREV, N.R. & BOWYER, A. & PAHL, A.K. 2006 Biomimetics: its practice and theory. *Journal of the Royal Society Interface*, **3**, 471–482.

VOIGT, W. 1889 Ueber die beziehung zwischen den beiden elasticitätsconstanten isotroper körper. *Annalen der Physik*, **274**, (12), 573–587.

WAGNER, T. & NEINHUIS, C. & BARTHLOTT, W. 1996 Wettability and contaminability of insect wings as a function of their surface sculptures. *Acta Zoologica*, **76**, 213–225.

WEIDEMAN, J. A. C. & REDDY, S. C. 2000 A MATLAB Differentiation Matrix Suite *ACM Transactions on Mathematical Software*, **26**, (4), 465–519.

WEN, L. & WEAVER, J.C. & LAUDER, G.V. 2014 Biomimetic shark skin: design, fabrication and hydrodynamic function *The Journal of Experimental Biology*, **217**, 1656–1666.

WHITAKER, S. 1986 Flow in porous media I: A theoretical derivation of Darcy's law. *Transport in Porous Media,* **1**, (1), 3–25.

WHITAKER, S. 1996 The Forchheimer equation: a theoretical development. *Transport in Porous Media,* **25**, (1), 27–61.

WHITAKER, S. 1998 *The method of volume averaging*, Jacob Bear, Technion - Israel Institute of Technology, Haifa, Israel.

YAZDCHI, K. & SRIVASTAVA, S. & LUDING, S. 2011 Microstructural effects on the permeability of periodic fibrous porous media. *International Journal of Multiphase Flow,* **37**, (8), 956–966.

ZICK, A. A. & HOMSY, G. M. 1982 Stokes flow through periodic arrays of spheres. *Journal of Fluid Mechanics,* **115**, 13–26.